

**Technical Report  
1100**

**Standoff Polarimetric Aerosol  
Detection (SPADE) for Biodefense**

J.W. Snow  
W.E. Bicknell  
A.T. George  
H.K. Burke

1 February 2005

---

**Lincoln Laboratory**  
MASSACHUSETTS INSTITUTE OF TECHNOLOGY  
LEXINGTON, MASSACHUSETTS

---



Prepared for the Office of the Secretary of Defense  
under Air Force Contract F19628-00-C-0002.

Approved for public release; distribution is unlimited.

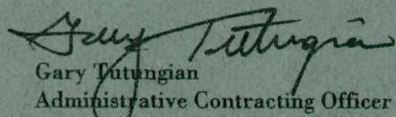
This report is based on studies performed at Lincoln Laboratory, a center for research operated by Massachusetts Institute of Technology. This work was prepared for the Office of the Secretary of Defense under Air Force Contract F19628-00-C-0002.

This report may be reproduced to satisfy needs of U.S. Government agencies.

The ESC Public Affairs Office has reviewed this report, and it is releasable to the National Technical Information Service, where it will be available to the general public, including foreign nationals.

This technical report has been reviewed and is approved for publication.

FOR THE COMMANDER



Gary Tutungian  
Administrative Contracting Officer  
Plans and Programs Directorate  
Contracted Support Management

Non-Lincoln Recipients

PLEASE DO NOT RETURN

Permission has been granted by the Contracting Officer to destroy this document, when it is no longer needed.

**Massachusetts Institute of Technology  
Lincoln Laboratory**

**Standoff Polarimetric Aerosol Detection (SPADE)  
for Biodefense**

*J.W. Snow  
W.E. Bicknell  
H.K. Burke  
Group 97*

*A.T. George  
Group 902*

**Technical Report 1100**

1 February 2005

Approved for public release; distribution is unlimited.

**Lexington**

**Massachusetts**

## EXECUTIVE SUMMARY

The topic of this concept-development report is the polarization characteristics of light elastically scattered by small particles. The specific objective is the remote (standoff) detection of bio-aerosol presence within typical ambient background aerosols. The information source is small-particle scattering code computations – not actual measurements. The particles are disperse, i.e., single-scattering is the operative scattering mode, and they are distributed in sizes. Two separate types of particles are combined, each having its own mode-radius, size distribution, particle shape, and refractive index – one representative of natural ambient background aerosols, the other of bio-aerosols. In this study, the mixing ratio of bio-aerosol particles per unit volume to number of ambient background aerosol particles is  $1/100 - 1 \text{ cm}^{-3}$  of bio-aerosol to  $100 \text{ cm}^{-3}$  of ambient particles. The objective is to assess the feasibility of detecting the introduction of the bio-aerosols into the ambient aerosol backgrounds at this relative concentration by analyzing the polarization state of laser light scattered by the combination of particles.

The incident laser light is assigned two elementary linear polarization states, oriented either parallel to or at  $+45^\circ$  relative to the scattering plane. The state of polarization of the laser light redirected through various scattering angles, mostly in the backscatter hemisphere, is specified by four (of at least six possible) polarimetric quantities that are developed from single Stokes parameters or the difference between two Stokes parameters. (This report is limited to four polarimetric quantities obtainable from the two basic incident polarization states.) The polarization-state changes caused by the ambient background aerosols alone are assessed in comparison to changes caused by the combination of ambient background plus bio-aerosols.

Incoherent laser and receiver specifications are employed to evaluate the feasibility of such a concept for standoff polarimetric aerosol detection (SPADE) specifically for bio-aerosol detection. Three SPADE application scenarios are considered: outdoor stadium, indoor auditorium, and building heating-ventilating-air-conditioning (HVAC) system. Of these, the HVAC application is very feasible with current laser and detector technology. The indoor application (range on order 50 m) is feasible, reliably providing at least two different polarimetric quantities. However, for the outdoor application (range on order 1500 m), conventional optical components can provide one quantity, the scattered intensity, which is necessary but generally not sufficient information to detect the introduction of bio-aerosols. Employment of coherent laser and advanced photodiode detector technologies does enhance SPADE performance especially in the outdoor application.

## PREFACE

This project report is intended as an introduction to the technology of polarimetric detection of aerosols for the purpose of biodefense. The feasibility of a standoff polarimetric aerosol detection (SPADE) system to remotely sense bio-aerosols is assessed given elementary scattering theory and current laser and detector engineering. Linear (meaning single-scattering) radiative transfer is sufficient. The operative scattering equation is simply the traditional lidar equation with a coefficient matrix replacing the scalar volume backscattering coefficient. Each section of the report is somewhat autonomous and can be dealt with separately. Abundant cross-references are included to pertinent items in other sections of the report and to original explanations or clarifications in the technical literature (reference format [AB, p #], AB author abbreviation, page number). The reader may skip-over such references initially.

Polarization is an attribute of electromagnetic radiation that is not readily appreciated by humans because we are almost completely insensitive to it. Although we are acutely aware of light intensity and have moderate acumen in discriminating color, we are practically polarization blind. Without a sophisticated electronic receiver we are unaware that every light scattering event has its own polarization state. However, considerable information concerning the object doing the scattering—aerosol particles in this report—is contained in the altered polarization state of scattered light. The information is gleaned by illuminating the particles with laser light of known polarization while measuring the intensity of light scattered through specific angles with a full-Stokes-parameter receiver, i.e., with a polarimeter.

The theory of particle light scattering needs to guide the engineering of an effectual laser-and-polarimeter aerosol detection system. Fundamental to polarimetric measurement is the bi-static configuration, i.e., different locations for the laser-transmitter and the polarimetric receiver. Since the magnitudes of all scattering characteristics depend on the scattering angle—the angle through which light is redirected by the scattering event—the angular variation in scattered intensity contains exploitable information on the scatterer. The physical properties of the scattering aerosols are therefore assessable from multi-angle polarimetric measurements. Change in any aerosol physical property leads to some detectable polarimetric change.

Key physical properties of particles are: (1) number-concentration, (2) size, (3) shape, (4) orientation, and (5) refractive index. According to linear scattering theory, corresponding polarimetric properties are found in certain elements (or element combinations) of the  $4 \times 4$  scattering coefficient matrix. Each of the 16 matrix elements varies directly with (1). Whereas all four diagonal elements are immune to (4), all 12 off-diagonal elements are sensitive to it. The upper left block of four matrix elements reacts strongly to changes in (2) and (3). The lower right block of four matrix elements contains information on (5).

The monitoring in time of specific locations to assess the introduction of new aerosols involves complex coordination of the bistatic lidar transmitter direction-and-range vis-à-vis the receiver direction-and-range. Practical laser power and the limiting noise of detectors are the optical engineering constraints. These are challenges to a feasible SPADE system, especially over long distances. But particle scattering theory indicates that the payoff is substantial—definitive and non-obtrusive remote detection of suspicious aerosol introduction.

The majority of the small-particle scattering codes employed in this research were developed and freely provided by Dr. M.I. Mishchenko, NASA Goddard Institute for Space Studies in New York, NY. We appreciate especially his generous provision via the world-wide-web of the very versatile T-matrix numerical code.

## TABLE OF CONTENTS

	<b>Page</b>
Executive Summary	iii
Preface	v
List of Illustrations	ix
List of Tables	xi
 1. INTRODUCTION	1
1.1 Objective	1
1.2 Concept of Operation	2
1.3 Delineation of Tasks	5
 2. SCATTERING EQUATION	7
2.1 Scattering Matrix	8
2.2 Volume Scattering Coefficient Matrix	9
2.3 Polarimetric Properties	12
 3. MODEL AEROSOLS	15
3.1 Population Scattering Matrix Elements	15
3.2 Aerosol Size Distribution	16
3.3 Physical and Optical Parameters	16
 4. SCATTERING COMPUTATIONS	21
4.1 Sensitivity Studies	22
4.1.1 Wavelength Sensitivity	22
4.1.2 Matrix Element Sensitivity	27
4.1.3 Concentration Sensitivity	29
4.2 Non-Spherical Particles	31
4.3 Retardation Polarimetric Property	37
 5. SYSTEM DESIGN CONCEPTS	41
5.1 Bistatic Lidar Equation	42
5.2 Signal-to-Noise Ratio	45
5.2.1 SNR Equation	45
5.2.2 System Parameters	46
5.2.3 Polarimetric SNR Estimates	50
5.3 Signal-to-Noise Backscatter-Angle Profiles	53
5.4 Biodefense Configuration Designs	57
5.4.1 Loci of Constant Scattering Angle	57
5.4.2 Perimeter and Area Defense Scenarios	60

6. DETECTION PROCEDURE	61
6.1 Data Processing Functions	61
6.2 Total Volume Scattering Coefficient	64
6.3 Photometric Analysis	65
6.4 Polarimetric Analysis	67
7. SUMMARY AND CONCLUSIONS	71
7.1 Environmental Signals	71
7.2 Signal-to-Noise for Three Scenarios	73
APPENDIX A. SCATTERING MATRIX	75
A.1 Scattering Equation	75
A.2 Ensemble-Average Scattering Matrix	77
A.3 Normalized Scattering Matrix	77
A.4 Combined Scattering Matrix	80
A.5 Volume Scattering Coefficient Matrix	81
A.6 Polarimetric Properties	82
A.7 Scattering Cross Section	84
APPENDIX B. PARAMETERS OF PARTICLE POPULATIONS	87
B.1 Number-, Area-, and Volume-Concentration	87
B.2 Area-Equivalent Sphere Radii of Spheroids	88
B.3 Particle Attenuation Size Parameters	89
B.4 Ensemble Averaging	89
B.5 Effective Radius and Effective Variance	92
APPENDIX C. SCATTERING CODES AND CODE COMPARISONS	95
C.1 Particle Scattering Codes	95
C.2 Mie Code Comparisons	97
APPENDIX D. SIGNAL-TO-NOISE RATIOS	99
D.1 Shot-Noise SNR	99
D.2 Thermal-Noise SNR	101
APPENDIX E. SCATTERING MATRIX ELEMENT INTERPRETATIONS	103
E.1 Optical Devices and Aerosol Analogs	104
E.2 Element Determination	111
E.3 Element Associations	114
GLOSSARY OF SYMBOLS [UNITS]	115
REFERENCES	121

## LIST OF ILLUSTRATIONS

<b>Figure</b>	<b>Page</b>
1.1. SPADE Bistatic Backscatter Configuration	2
1.2. SPADE 95% Probability-of-Detection (PD) – Notional Diagram	3
2.1. Overlapping Coincident Volumes at Scattering Site	7
3.1. Size Distributions of Aerosol Particles	17
3.2. Bacillus Spores – Scanning Electron Microscope Images	19
4.1. Profiles of <i>Intensity</i> Volume Scattering Coefficient at Four Wavelengths	24
4.2. Profiles of <i>Linear Polarization</i> Volume Scattering Coefficient at Four Wavelengths	25
4.3. Profiles of <i>Intensity</i> and <i>Linear Polarization</i> Volume Scattering Coefficients for Two Bio-Aerosol Number-Concentrations	30
4.4. Profiles of <i>Intensity</i> and <i>Linear Polarization</i> Volume Scattering Coefficients for Bio-Aerosol Introduction vs. Increased Ambient Background Aerosol	32
4.5. Profiles of Volume Scattering Coefficients for Five Axis Ratios of Oblate and Prolate Bio-Aerosols	34
4.6. Profiles of <i>Non-Sphericity</i> Indicators: <i>Non-Sphericity</i> Ratio and <i>Non-Sphericity</i> Volume Scattering Coefficient	36
4.7. Profiles of <i>Retardation</i> Volume Scattering Coefficients	39
5.1. Bistatic Lidar Geometric Configuration	41
5.2. Bistatic Lidar Surveillance System Modular Diagram	46
5.3. Signal-to-Noise Ratio ( $\text{SNR}_{\text{tn}}$ ) Profiles at Far-Backscatter Angles	55
5.4. <i>Non-Sphericity</i> Signal-to-Noise Ratio Profiles at Far-Backscatter Angles, $\lambda = 1.50 \mu\text{m}$	56
5.5. Same as Fig 5.4 Except for Laser Wavelength $\lambda = 2.12 \mu\text{m}$	56
5.6. Bistatic Lidar Geometry	58
5.7. Composite Constant- $\Theta$ Coverage	59
5.8. Defense Designs: Perimeter and Area	60
6.1. Detection Procedure Component of SPADE System	62
6.2. Hierarchy of SPADE Bio-Aerosol Decision Process	65
C.1. Comparative Spherical Scattering Code Computations of Profiles of <i>Intensity</i> and <i>Linear Polarization</i> Volume Scattering Coefficients	98
E.1. Stokes Parameter Receiver (Polarimeter) – Conceptual Design	111
E.2. Polarimetric Measurement Employing Variable Incident Polarization States	112

## LIST OF TABLES

<b>Table</b>	<b>Page</b>
2.1 Scattering Matrix Forms	11
2.2 Polarimetric Quantities of Scattered Light	12
3.1 Modified-Gamma and Physical Parameters of Aerosol Types	18
3.2 Spectral Values of Refractive Index	18
4.1 Volume Scattering Coefficients for Spherical Particles at Far-Backscatter Angle $\Theta = 170^\circ$ for Various Polarimetric Properties	23
4.2 Volume Scattering Coefficients for Spherical Particles at Near-Forward Angles $\Theta = 5$ or $6^\circ$ for Various Polarimetric Properties	27
4.3 Volume Scattering Coefficients for Prolate Spheroid Bio-Aerosols at Backscatter Angle $\Theta = 170^\circ$ for Various Polarimetric Properties	33
4.4 Volume Scattering Coefficients for Prolate Spheroid Bio-Aerosols at Near-Forward Scattering Angles $\Theta = 5$ or $6^\circ$ for Four Polarimetric Properties	37
5.1 Component Efficiencies and Transmittances at $\lambda = 1.50 \mu\text{m}$	47
5.2 SPADE Parameters for Three Biodefense Scenarios	47
5.3 Qualitative Review of Feasibility for $2.12 \mu\text{m}$ and $1.50 \mu\text{m}$ Lasers	49
5.4 Laser and Receiver Parameters for Outdoor, Indoor, and HVAC Systems	49
5.5 Aerosol Volume Scattering Coefficients for $\lambda = 1.50 \mu\text{m}$	51
5.6 Gain-Enhanced Signal-to-Noise Ratios $^7\text{SNR}_i$ for Outdoor Stadium, Indoor Auditorium, and HVAC System	52
5.7 Parameters for Thermal-Noise Limited SNR Computations	54
5.8 Maximum Perpendicular Distance Y Scaled by $L=1$ , vs. Scattering Angle	59
6.1 Synopsis of Bio-Aerosol Detection Procedure	66
7.1 Relative Rankings of Bio-Aerosol Signal Strengths	72
7.2 Physical vis-à-vis Polarimetric Bio-Aerosol Properties – Detection Protocol	73
A.1 Various Scattering Matrix Forms	80
A.2 Polarimetric Properties of Scattered Light	83

## 1. INTRODUCTION

The fact that every small-particle elastic light scattering event has its own distinct polarization allows remote detection of small amounts of bio-aerosol within background aerosols of considerably higher number-concentrations. Two exploitable polarization signatures are the spectral ( $\lambda$ ) and scattering-angle ( $\Theta$ ) variations of polarimetric quantities. Spectral variation means change in the value of such quantities with illumination wavelength—measurements at multiple wavelengths do enhance polarimetric information, especially for combinations of particle types having different mode radii. (Spectral variation in this report does not signify fluorescence or Raman effects since only elastic scattering is considered.) However in this concept development report, the type of polarimetric signature exploited is primarily scattering-angle change in quantities such as the extent of linear polarization.

### 1.1 OBJECTIVE

This is the record document of an internal research project entitled Standoff Polarimetric Aerosol Detection (SPADE). The objective of the SPADE project was to assess the phenomenological and technical feasibility of remote detection of bio-aerosols by analyzing the polarization state of scattered laser illumination. Numerical simulation vs. measurement is the information source utilized here. Specific polarization characteristics of light scattered by bio-aerosols versus ambient background aerosols are investigated, especially at backscatter angles. State-of-technology small-particle scattering-code computations are employed. In the numerical simulations physical and optical properties of typical background aerosols and of one bio-aerosol simulant are used. The practicality of the SPADE concept depends on the signal strength of the bio-aerosol induced changes in polarimetric quantities relative to those caused by expected temporal variations in the ambient background aerosols alone. Included in this report are both scattering-code findings and the results of signal-to-noise calculations.

Scattering-angle signatures (angular profiles) of four quantities ( $P_X$ ) are used to remotely detect bio-aerosols co-located with ambient background aerosols. These four quantities, as a group referred to as polarimetric quantities, are: 1)  $P_I$  – scattered intensity, 2)  $P_L$  – partial linear polarization, 3)  $P_N$  – non-sphericity, and 4)  $P_R$  – retardation. All four are spectral and vary with the scattering angle  $\Theta$  – variations that can be evaluated using small-particle scattering theory, given the scattering particle physical and optical properties.

Each quantity is related to Stokes parameters of the scattered light vector  $\mathbf{I}_{\text{sca}}(\Theta) = [I_{\text{sca}}(\Theta), Q_{\text{sca}}(\Theta), U_{\text{sca}}(\Theta), V_{\text{sca}}(\Theta)]^T$ , where  $T$  means the transpose. Specifically, in this report,  $P_I(\Theta) \sim {}^+ I_{\text{sca}}(\Theta)$ ,  $P_L(\Theta) \sim {}^+ Q_{\text{sca}}(\Theta)$ ,  $P_N(\Theta) \sim [{}^P I_{\text{sca}}(\Theta) - {}^P Q_{\text{sca}}(\Theta)]$ , and  $P_R(\Theta) \sim {}^+ V_{\text{sca}}(\Theta)$ , where the lead-superscript indicates the orientation of the incident linearly polarized light relative to the scattering plane:  ${}^+$  is  $+45^\circ$  and  ${}^P$  is parallel to the horizontal scattering plane. So defined,  $P_I(\Theta)$  is not a polarization sensitive quantity, specific, the relative magnitude (intensity) of light angularly scattered is independent of incident polarization state. Yet, for convenience,  $P_I(\Theta)$  is referred to as a polarimetric quantity. (As seen in Section 2, each  $P_X$  is related to a specific volume scattering coefficient.)

Of the four polarimetric quantities,  $P_I(\Theta)$  is the most researched – being the single-scattering phase function for unit intensity incident light. The seminal publication of Wyatt in 1968 proposed using angular profiles of  $P_I(\Theta)$  to non-disruptively identify specific bacterial species

[WY, Figures 8–18]. When normalized by the incident light intensity,  $P_L(\Theta)$  is the degree of linear polarization that is known to be the polarimetric quantity most sensitive to the effective size and refractive index for spherical aerosol particles [MTL, p 272; or MT7, p 17,000]. The  $P_N(\Theta)$  quantity, similar to the depolarization ratio used in lidar research of clouds [SA, eq (2)], is a sensitive discriminator between spherical and non-spherical particles, especially at backscattering angles. The quantity  $P_R(\Theta)$ , called here retardation, quantifies the phase-shift difference in orthogonal incident electric field components effected by living aerosols, esp. by bio-aerosols [VHB, p 5053; also BDV].

## 1.2 CONCEPT OF OPERATION

The concept of operation of SPADE is change detection and evaluation. In particular, remotely sensed aerosol optical characteristics in any area of interest are continuously monitored and the temporal variations in these serve as the basis for the decision regarding whether the change is due to natural variability of the ambient background aerosol or is due to bio-aerosol introduction.

A SPADE system operating in a bistatic lidar configuration is illustrated in Figure 1.1. The scattering volume that contains both background and possibly biological types of aerosols is illuminated by a pulsed laser transmitter of specified polarization state. Radiation scattered by both types of aerosols being irradiated is monitored by the receiver. The receiver is a polarimeter, able to measure the four Stokes parameters of the scattered light.

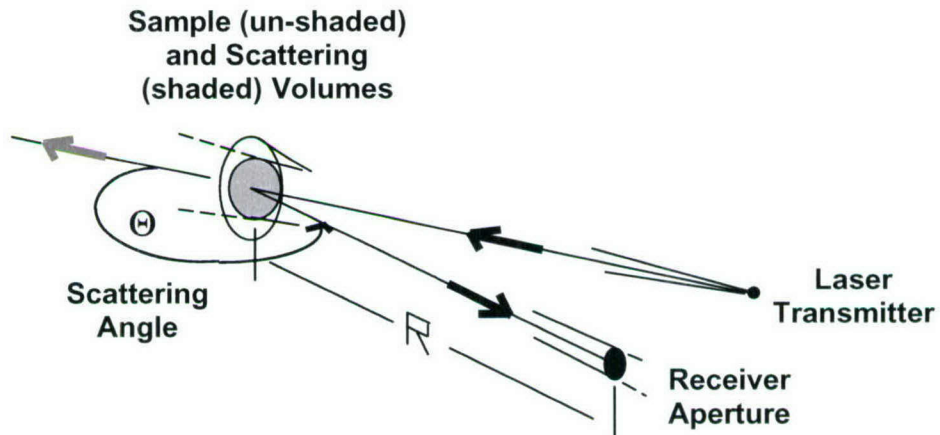


*Figure 1.1. SPADE Bistatic Backscatter Configuration. Azimuth-adaptable transmitter irradiating scattering volume (shaded) and coordinated receiver sensing scattered light from sample volume (un-shaded) located at range  $R$  and scattering angle  $\Theta$ .*

The sample volume is defined by the receiver aperture field-of-view solid angle and the particular range-gate (detector integration time increment) that includes the centroid of the laser pulse. Individually, both transmitter and receiver could execute coordinated azimuth changes providing for variation in scattering angle  $\Theta$ . These changes, along with the pulsed format of the transmitter and the range-gate of the receiver, then determine the range  $R$  from sample volume to receiver. Added receivers (not shown in Figure 1.1) could enhance the  $(R, \Theta)$  surveillance of an area of interest.

In this report, the four polarimetric quantities,  $P_l(\Theta)$ ,  $P_L(\Theta)$ ,  $P_N(\Theta)$ , and  $P_R(\Theta)$ , together, measured at more than one scattering angle or spectral wavelength, provide the information for detecting the introduction of a bio-aerosol. The physical conditions of the bio-aerosol vis-à-vis the ambient background aerosol, under which such detection is possible, can be specified in terms of the number-concentration mixing ratio,  $R_N \equiv N_b/N_a$ . It specifies the relative abundance of the bio-aerosol as the number of bio-aerosol particles  $N_b[\text{cm}^{-3}]$  per unit volume of air to the number of ambient particles  $N_a[\text{cm}^{-3}]$  per same unit volume. In this study  $R_N = 1/100$  ( $\log R_N = -2$ ) is assigned, unless otherwise stated.

In Figure 1.2 are shown hypothetical 95% probability-of-detection solid curves ( $PD = 95\%$ ) in the variable-space defined by the number of polarimetric quantities employed (ordinate) vs. the logarithm of the number-concentration mixing ratio; with the number of different angular or spectral measurements used as the parameter. Notional lines of constant probability-of-false-detection (PFD[%]) are the light dashed lines.

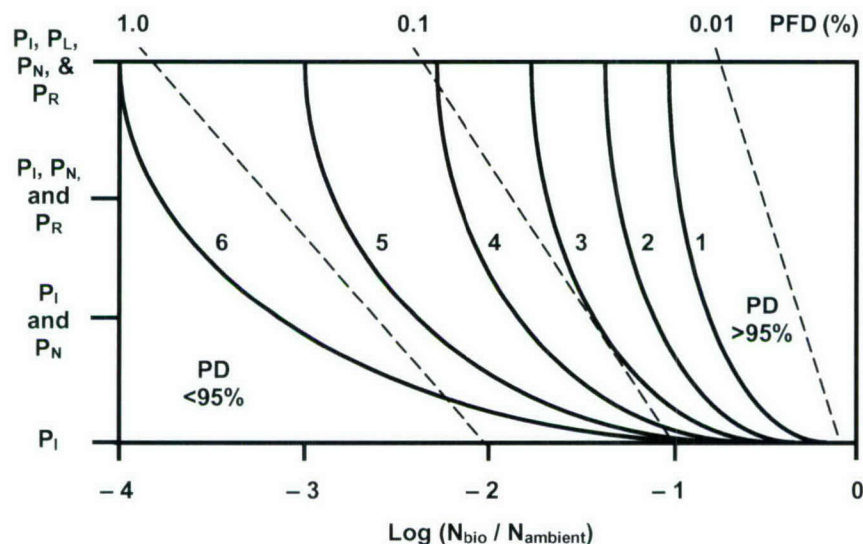


Figure 1.2. SPADE 95% Probability-of-Detection (PD) – Notional Diagram. Solid isopleths of  $PD = 95\%$  on plot of number of polarimetric quantities (ordinate) versus logarithm of number-concentration ( $\log R_N$ ). Parameter is number of scattering angles and/or wavelengths at which polarimetric measurements are made. Dash isolines of constant probability of false detection PFD(%).

Operationally, the detection of bio-aerosol introduction in a sample volume is a rare event in comparison to the very large number of interrogations of that same sample volume containing only benign ambient background aerosols. The false-positive-detection problem, namely, wrongly interpreting one or more of the myriad truly background measurements as positive for containing bio-aerosol, is inevitably present in such rare-event detection scenarios. The probability-of-false-detection (PFD) naturally increases as the relative concentration  $R_N$  decreases, i.e., PFD increases toward the left in the variable-space of Figure 1.2. However, PFD decreases with increasing number of polarimetric properties – the ordinate in Figure 1.2. The purely hypothetical constant PFD dashed lines purport to incorporate these dependencies – PFD decreases upward and toward the right.

As indicated in the purely notional Figure 1.2, if measurements are made at 5 or more angle/spectral conditions with  $R_N = 1/10$  ( $\log R_N = -1$ ), then the  $P_1$  quantity alone appears to be sufficient for bio-aerosol detection at  $PD \geq 95\%$ ; but with  $PFD \cong 0.1\%$ . To lower the PFD, more polarimetric properties need to be used. With five polarimetric properties (top border) and the same  $R_N = 1/10$ ,  $PFD \cong 0.02\%$ . In the range  $1/10 > R_N \geq 1/10,000$  ( $-1 > \log R_N > -4$ ), additional polarimetric quantities and angle/spectral measurements are essential to attain the same probability of detection. At the higher concentration mixing ratios these added information sources lower the PFD, but at the lowest concentrations PFD remains high even with multiple properties and angular measurements. As bio-aerosol relative concentration decreases (to the left in Figure 1.2), the solid isopleths indicate that the PD-multiplier for the SPADE technique is additional angle/spectral measurements, whereas the PFD-reducer is additional polarimetric quantities. (In Section 5, are considered the effects of range, laser power, and receiver aperture on SPADE effectiveness.)

Measurements of scattered light could be made over the entire range  $\Theta \in [0^\circ, 180^\circ]$ , but this is usually neither practical nor necessary. Ideally, one optimally located measurement in each of the three sectors: forward scatter  $\Theta \in [0^\circ, 60^\circ]$ , side-scatter  $\Theta \in [60^\circ, 120^\circ]$ , or backscatter  $\Theta \in [120^\circ, 180^\circ]$  might adequately quantify the three generic scattering phenomena – diffraction, refraction, and reflection – prevalent in each sector, respectively. But specific angle-varying quantities like  $P_L$  or  $P_N$ , being determined by refraction/reflection, are better quantified by multiple measurements in the backscattering region ( $90^\circ < \Theta \leq 180^\circ$ ). In fact, the SPADE strategy is to concentrate measurements in the sector where the polarization of bio-aerosol scattering most differs from that of the background aerosols. While adjacent angle measurements are not independent, their differences – varying from one interrogation time to the next – are useful indicators of altered scattering-particle conditions.

Since bio-aerosols tend to be larger than most ambient background aerosols, the backscatter sector should be especially informative. There photons backscattered from larger particles have been redirected both by the outer convex surface and also, after refraction, by the inner concave surface of such particles. Polarization signatures are distinctive in this sector, as long as other bio-aerosol properties (esp. shape or absorption) do not offset the size advantage. For example, introduction of large but non-spherical particles can diminish otherwise expected backscatter polarization features.

Regarding exploitation of any spectral variation in polarimetric signatures, the size and the distribution of aerosol particle sizes – bio-aerosols vis-à-vis ambient background aerosols – determines that, at backscattering angles, short-wave infrared (SWIR) wavelengths provide in most cases the optimal discrimination between these two aerosol types. With regard to scattered intensity specifically, the relatively large and quite narrowly distributed bio-aerosol particles individually scatter SWIR light more efficiently [e.g. MTL, Figure 9.12] and differently [MTL, Plate 9.4] than the individual ambient background particles, which tend to be of smaller and more broadly distributed sizes. (Aerosol size-related parameters are defined in Section 3.2 and Appendix B.3.) In the present research the emphasis is on two wavelengths, 1.50 or 2.12  $\mu\text{m}$ , although the implications of shorter wavelength are included.

The smaller ambient aerosols increasingly become more efficient and distinctive scattering particles at shorter – visible or near-infrared (NIR) – wavelengths. While this compromises bio-aerosol detection per se, the use of a second shorter wavelength, in addition to the primary SWIR

wavelength, is recommended to specifically monitor temporal changes in the ambient background aerosol condition.

### **1.3 DELINEATION OF TASKS**

Four SPADE development tasks were carried out during this research project. These tasks, discussed in Sections 3, 4, 5, and 6, respectively, are:

- Background and bio-aerosol (simulant) database compilation,
- Enhancement and execution of particle-population scattering codes,
- Identification and evaluation of potential SPADE system designs,
- Data utilization in an elementary detection procedure.

Section 2 of this report is a brief discussion of the scattering matrix, which is the basis for polarimetric detection of trace aerosols. (Appendix A is a more complete explanation of the scattering matrix.) The physical and optical properties of the aerosols used in scattering code computations are discussed in Section 3. The results of scattering code simulations of both spherical and non-spherical bio-aerosols, co-located with spherically shaped background aerosols, are presented in Section 4. Section 5 discusses the bistatic lidar equation and includes conceptual SPADE designs that exploit polarimetric signatures for both perimeter and area surveillance. These SPADE designs, which are scalable to different scenarios by the distance between transmitter and receiver, include computation of signal-to-noise for specific optical system parameters and realistic bio-aerosol vis-à-vis ambient background conditions. Section 6 contains the decision logic—the detection procedure that is followed in order to identify introduction of bio-aerosols. Strengths and limitations of SPADE concepts are summarized in Section 7. Five appendices, Appendices A–E, provide detailed information on relevant topics directly associated with Sections 2–6, respectively.

## 2. SCATTERING EQUATION

Radiation singly scattered by particles is the measured quantity. In any SPADE application particle concentrations are low enough so that single-scattering theory applies and the operative geometry is one scattering plane – typically the horizontal plane. As seen in Figure 1.1, the laser transmitter, the sample volume, and the receiver establish the scattering plane in which the scattering angle  $\Theta$  is defined. In particular, the temporal change in the scattering-angle profile of the scattered light vector is the SPADE information source. The scattered light vector is basically the product of the incident light vector and the 4x4 matrix specifying the capability of the illuminated particles to redirect and re-orientate that radiation into any and all scattering angles. The fundamental scattering relationship is, therefore,

$$\mathbf{I}_{\text{sca}}(\Theta) \sim \mathbf{F}(\Theta) \mathbf{I}_{\text{inc}} \quad (1A)$$

The angle-varying Stokes parameters of  $\mathbf{I}_{\text{sca}}(\Theta)$  are the measured variables. The incident laser irradiance  $\mathbf{I}_{\text{inc}}$  [ $\text{W m}^{-2}$ ] has known and selectable states of polarization. Given the illumination wavelength, the 16 elements  $F_{ij}(\Theta)$  of the *volume scattering matrix*  $\mathbf{F}(\Theta)$ , each with dimensions of area, completely describe all the angular scattering properties of the combination of illuminated particles in a volume. The volume scattering matrix  $\mathbf{F}(\Theta)$  quantifies the environment part of the scattering relationship. It is the environmental Mueller matrices – one of those needed for Eq (1A) to be an equality [MHT, 2000, p 50, eq (2)].

Eq (1A) applies at the scattering site, the location of the two overlapping volumes depicted in Figure 2.1. The *scattering volume*, shaded cylinder of length  $c\tau_L$  in Figure 2.1, contains all particles irradiated during the laser pulse duration  $\tau_L$ ;  $c$  is speed of light. In distinction, the volume interrogated by the receiver during that time interval  $\tau_L$  is the *sample volume*  $V$ , unshaded truncated cone-section also of length  $c\tau_L$  in Figure 2.1. The fraction of  $V$  that is illuminated is the geometrical overlap factor  $\xi \leq 1$ , discussed in Section 5.1. The scattering volume,  $\xi V$ , is the source of receiver light – source of detected signal.

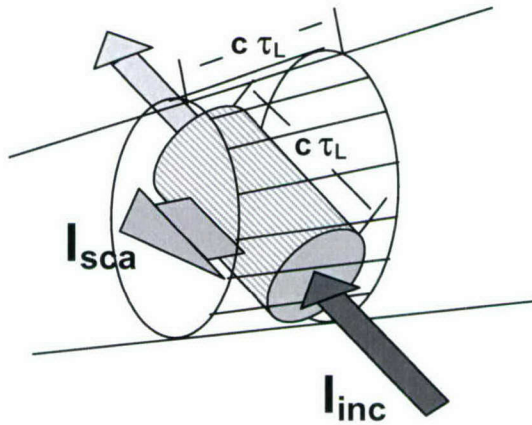


Figure 2.1. Overlapping Coincident Volumes at Scattering Site. Scattering volume irradiated during laser pulse duration  $\tau_L$ —shaded cylinder. Sample volume interrogated by receiver during  $\tau_L$ —unshaded conic sector. Laser light incident at scattering site  $I_{\text{inc}}$  [ $\text{W m}^{-2}$ ]; portion of laser light scattered toward receiver  $I_{\text{sca}}$  [ $\text{W m}^{-2}$ ].

Properly, Eq (1A) becomes the elastic-scattering active remote-sensing equation by including the matrices quantifying the optical components of the illumination laser and the receiver-detector, the geometric size of the sample volume  $V$ , the overlap factor  $\xi$ , and ultimately, the range  $R$  shown in Figure 1.1. At  $\Theta = 180^\circ$ , this equation is the well-known mono-static lidar equation of laser remote sensing [Measures, 1984, p 241]. For the SPADE application it is extended to include any scattering angle  $\Theta$ , not just the lidar angle. Eq (1A) then becomes the bistatic lidar equation developed in Section 5.1. In this section, only the basic geometric variables are incorporated.

## 2.1 SCATTERING MATRIX

Appendix A contains more comprehensive details on the scattering matrix – its normalized form and its configuration when different types of scattering particles concurrently occupy the sample volume. Specific forms of the scattering matrix, developed in Appendix A, are presented and applied in this subsection with only minimum explanation not to impede the primary goal of the report – the presentation of SPADE ACC project results.

If all  $\square$  particles in the sample volume  $V$  are the same type, then the concept of ensemble-average scattering matrix per particle  $\langle \mathbf{F}(\Theta) \rangle$  is straightforward. (Ensemble averaging is defined in Appendix B.4, esp. Eq (B.5B).) The fraction of  $\square$  being irradiated is taken to be the same as the fraction of  $V$  that is occupied by the scattering volume, i.e., the overlap factor  $\xi$ . Including the decrease in scattered intensity due to separation between the scattered light source ( $\sim$  point source) and receiver,  $R$  in Figure 1.1, Eq (1A) becomes the basic *scattering equation*

$$\mathbf{I}_{\text{sca}}(R, \Theta) = [\xi/R^2] \square \langle \mathbf{F}(\Theta) \rangle \mathbf{I}_{\text{inc}} \quad (1B)$$

Separating  $\langle \mathbf{F}(\Theta) \rangle$  into integral photometric and directional polarimetric parts (Appendix A.6) means that  $\langle \mathbf{F}(\Theta) \rangle = [\langle C_{\text{sca}} \rangle / 4\pi] \mathbf{F}(\Theta)$ . The polarimetric part, matrix  $\mathbf{F}(\Theta)$  referred to as the *normalized scattering matrix* [MTL, p 100], isolates angular variations in scattering from the spherical average of the total (all-angle) scattering magnitude,  $\langle C_{\text{sca}} \rangle / 4\pi$ . The photometric quantity  $\langle C_{\text{sca}} \rangle [\text{cm}^2]$  is the per-particle-average scattering cross-sectional area. The dimensionless quantity  $\mathbf{F}(\Theta)$  is the per-particle-average angular scattering function – the average being made over all laser-illuminated aerosol particles in the scattering volume. Since  $\square[-] = (N[\text{cm}^{-3}] V[\text{cm}^3])$ , where  $N$  is number-concentration, then the normalized form of Eq (1B) is,

$$\mathbf{I}_{\text{sca}}(R, \Theta) = [\xi V/R^2] N [\langle C_{\text{sca}} \rangle / 4\pi] \mathbf{F}(\Theta) \mathbf{I}_{\text{inc}} \quad (1C)$$

As introduced by Perrin [1942], the elements of the normalized scattering matrix are assigned simple single-subscript letter designations, specifically,  $F_{11}(\Theta) \equiv a_1(\Theta)$ ,  $F_{12}(\Theta) \equiv b_1(\Theta)$ ,  $F_{22}(\Theta) \equiv a_2(\Theta)$ , etc. (The convenience of this abbreviated notation is better appreciated in Appendices A and E.) For either spherical particles or for non-spherical particles that have an axis of symmetry and are randomly orientated and isotropically dispersed throughout the sample volume, the normalized scattering matrix simplifies considerably. It is block diagonal and cross-diagonal pairs are equal in magnitude. The normalized scattering matrix is then reduced to at-most six non-zero elements.

$$\mathbf{F}(\Theta) = \begin{vmatrix} a_1(\Theta) & b_1(\Theta) & 0 & 0 \\ b_1(\Theta) & a_2(\Theta) & 0 & 0 \\ 0 & 0 & a_3(\Theta) & b_2(\Theta) \\ 0 & 0 & -b_2(\Theta) & a_4(\Theta) \end{vmatrix} \quad (2A)$$

In particular,  $a_1(\Theta)$  is the familiar *single-scattering phase function* [MTL, p 101] and  $b_1(\Theta)$  is called the polarized phase function [HDD].

Whenever two different types of particles are co-located in the same sample volume  $V$ , the *combined scattering matrix* for all particles present in  $V$  is  $\mathbf{F}_c(\Theta)$ , which then determines the transformation of the incident light vector into the scattered light vector. For ambient background aerosols and bio-aerosols of number-concentrations  $N_a$  and  $N_b$ , respectively, the combined number of particles in the sample volume is  $\mathbb{N}_c = VN_a + VN_b$  and the combined normalized scattering matrix is  $\mathbf{F}_c(\Theta) = V [N_a \langle \mathbf{F}_a(\Theta) \rangle + N_b \langle \mathbf{F}_b(\Theta) \rangle]$ . (Subscripts ‘a’ – ambient and ‘b’ – bio-aerosol are in no way related to Eq (2A) abbreviated normalized scattering-matrix element symbols,  $a_1$ ,  $b_1$ , etc.)

In terms of the individual normalized matrices,  $\mathbf{F}_a(\Theta)$  and  $\mathbf{F}_b(\Theta)$ , the combined scattering matrix is  $\mathbf{F}_c(\Theta) = [V/4\pi] [N_a \langle C_{sca} \rangle_a \mathbf{F}_a(\Theta) + N_b \langle C_{sca} \rangle_b \mathbf{F}_b(\Theta)]$ . But, by definition,  $\mathbf{F}_c(\Theta) = [V/4\pi] [N_a \langle C_{sca} \rangle_a + N_b \langle C_{sca} \rangle_b] \mathbf{F}_c(\Theta)$ , which results in

$$\mathbf{F}_c(\Theta) = [N_a \langle C_{sca} \rangle_a \mathbf{F}_a(\Theta) + N_b \langle C_{sca} \rangle_b \mathbf{F}_b(\Theta)] / [N_a \langle C_{sca} \rangle_a + N_b \langle C_{sca} \rangle_b] \quad (3)$$

This is the *combined normalized scattering matrix* that depends on the relative presence of each type of particle but is independent of the total number of particles. (Eq (3) is the same as Eq (4.74) developed in MTL, pp 102, 103. In comparing equations, the dimensionless particle number used here,  $VN_a$ , is the same as  $N_1$  found in MTL. Also, the factors ( $V/4\pi$ ) that are in both numerator and denominator of Eq (3) obviously cancel.)

The individual elements of the combined normalized scattering matrix are usually symbolized by the same  $a_1(\Theta)$ ,  $b_1(\Theta)$ , etc, appearing in Eq (2A); but the expressions for each of these combined normalized scattering matrix elements differ from those for a single aerosol type (Appendix A.4 and A.5). Eq (3) is applied repeatedly in the scattering computations discussed in Section 4.

## 2.2 VOLUME SCATTERING COEFFICIENT MATRIX

From Eq (1C) and the definition of  $\mathbb{N}$ , and for simplicity assigning  $\xi = 1$ , the scattered light vectors produced by the ambient background and bio-aerosol separately are

$$\mathbf{I}_{sca}(R, \Theta) = [V/4\pi R^2] [N_a \langle C_{sca} \rangle_a \mathbf{F}_a(\Theta) \mathbf{I}_{inc}] \quad (4A)$$

and

$$\mathbf{I}_{sca}(R, \Theta) = [V/4\pi R^2] [N_b \langle C_{sca} \rangle_b \mathbf{F}_b(\Theta) \mathbf{I}_{inc}] \quad (4B)$$

Similarly, the introduction of Eq (3) into Eq (1C) results in the combined-aerosol scattered light vector expressed in the normalized form of the scattering equation

$$\mathbf{I}_{sca}(R, \Theta) = [V/4\pi R^2] [N_a \langle C_{sca} \rangle_a + N_b \langle C_{sca} \rangle_b] \mathbf{F}_c(\Theta) \mathbf{I}_{inc} \quad (4C)$$

The *volume scattering coefficient matrix* for each type of aerosol and for unit solid angle is made up of all the particle-related factors on the right sides of Eqs (4A) and (4B), i.e.,

$$\mathbf{B}_a(\Theta) = [1/4\pi] [N_a \langle C_{sca} \rangle_a] \mathbf{F}_a(\Theta) \quad (5A)$$

and

$$\mathbf{B}_b(\Theta) = [1/4\pi] [N_b \langle C_{sca} \rangle_b] \mathbf{F}_b(\Theta) \quad (5B)$$

Similarly, on the right side of Eq (4C)

$$\mathbf{B}_c(\Theta) = [1/4\pi][N_a \langle C_{sca} \rangle_a + N_b \langle C_{sca} \rangle_b] \mathbf{F}_c(\Theta) \quad (5C)$$

Given the incident laser wavelength,  $\mathbf{B}_c(\Theta)$  is a function only of the scattering particle properties – the remote sensing objective here. Presence of the scattering angle argument ( $\Theta$ ) indicates direction into which light is scattered relative to the incident light direction. The quantity  $\mathbf{B}_c(\Theta)$  is then the directional scattering ability [ $\text{cm}^2$ ] of all particles in a unit volume [ $\text{cm}^{-3}$ ] to redirect incident photons through the angle  $\Theta$ , i.e., it is the *directional volume scattering coefficient matrix* [ $\text{cm}^{-1}$ ]. The complete set of values for all  $\Theta \in [0^\circ, 180^\circ]$  is the scattering-angle profile of  $\mathbf{B}_c(\Theta)$ .

In terms of  $\mathbf{B}_c(\Theta)$ , Eq (4C) is simply

$$\mathbf{I}_{\text{sca}}(R, \Theta) = [V/R^2] \mathbf{B}_c(\Theta) \mathbf{I}_{\text{inc}} \quad (4D)$$

The condition of random-oriented isotropically dispersed particles allows the same reduced form as Eq (2A) for the volume scattering coefficient matrix. Thus, all of the matrices  $\mathbf{F}_a(\Theta)$ ,  $\mathbf{F}_b(\Theta)$ , and  $\mathbf{F}_c(\Theta)$ , and also  $\mathbf{B}_a(\Theta)$ ,  $\mathbf{B}_b(\Theta)$ , and  $\mathbf{B}_c(\Theta)$  are likewise block-diagonal. In general, elements of any  $\mathbf{B}$ -matrix are the *directional volume scattering coefficients*  $\beta_{ij}(\Theta)$ . Here, the name for any  $\beta_{ij}(\Theta)$  is abridged to *volume scattering coefficient*, which in some references is called volume scattering function. Specifically,

$$\mathbf{B}(\Theta) = \begin{vmatrix} \beta_{11}(\Theta) & \beta_{12}(\Theta) & 0 & 0 \\ \beta_{21}(\Theta) & \beta_{22}(\Theta) & 0 & 0 \\ 0 & 0 & \beta_{33}(\Theta) & \beta_{34}(\Theta) \\ 0 & 0 & \beta_{43}(\Theta) & \beta_{44}(\Theta) \end{vmatrix} \quad (2B)$$

Similar to Eq (2A) for axisymmetric particles, it is anticipated that  $\beta_{21}(\Theta) = \beta_{12}(\Theta)$  and  $\beta_{43}(\Theta) = -\beta_{34}(\Theta)$ , meaning at most six non-zero elements. However, the matrix element notation in Eq (2B) is maintained to identify (in Section 4 and Appendix E) which matrix position is associated with each polarimetric quantity.

Five directional scattering variables have now been introduced. As a convenient reference, Table 2.1 relates each individual form of the scattering matrix, in particular its elements, to the other four forms. For example, it is evident from Table 2.1 that the volume scattering coefficient matrix  $\mathbf{B}(\Theta)$  is in fact the unit-volume volume scattering matrix  $\mathbf{F}(\Theta)/V$ . For simplicity of notation in Table 2.1, the scattering angle variation  $f(\Theta)$  of each element (and matrix) is not explicitly included.

**Table 2.1. Scattering Matrix Forms.**

All matrices and elements are directional; all vary with scattering angle ( $\Theta$ ).

Descriptor	Symbol	Units	Element:	$= F_{ij}$	$= \langle F_{ij} \rangle$	$= F_{ij}$	$= a_k, b_k$	$= \beta_{ij}$
Volume	<b>F</b>	[cm <sup>2</sup> ]	$F_{ij} x$	1	1/D	$4\pi/D\langle C_{sca} \rangle$	$4\pi/D\langle C_{sca} \rangle$	$N/D$
Ensemble-Ave.	$\langle F \rangle$	[cm <sup>2</sup> ]	$\langle F_{ij} \rangle x$	D	1	$4\pi/\langle C_{sca} \rangle$	$4\pi/\langle C_{sca} \rangle$	N
Normalized	<b>F</b>	[–]	$F_{ij} x$	$D\langle C_{sca} \rangle/4\pi$	$\langle C_{sca} \rangle/4\pi$	1	1	$N\langle C_{sca} \rangle/4\pi$
Abbreviated	<b>F</b>	[–]	$a_k, b_k x$	$D\langle C_{sca} \rangle/4\pi$	$\langle C_{sca} \rangle/4\pi$	1	1	$N\langle C_{sca} \rangle/4\pi$
Vol. Scattering Coefficient	<b>B</b>	[cm <sup>-1</sup> ]	$\beta_{ij} x$	D/N	1/N	$4\pi/N\langle C_{sca} \rangle$	$4\pi/N\langle C_{sca} \rangle$	1

D [–] – number of particles in sample volume V [cm<sup>3</sup>], D = NV, D/N = V. N [cm<sup>-3</sup>] – number of particles per unit physical volume.  $\langle C_{sca} \rangle$  [cm<sup>2</sup> = 10<sup>8</sup> μm<sup>2</sup>] – ensemble-average scattering cross section. Examples:  $\beta_{ij} = (N\langle C_{sca} \rangle/4\pi)F_{ij}$ ;  $a_k = (4\pi/\langle C_{sca} \rangle)\langle F_{ij} \rangle$ ;  $F_{ij} = (D\langle C_{sca} \rangle/4\pi)b_k$ .

Referring specifically to the volume scattering coefficients, as with the matrix, so with its elements (the individual coefficients) – given the incident wavelength, each  $\beta_{ij}(\Theta)$  is a function only of particle properties. In particular, the values of these coefficients are independent of the polarization state of the incident light (except for ‘optically active’ particles; refer Appendix E.) Different incident polarization states only determine which coefficients are available for measurement.

Given commonly used incident polarization states, not all elements of the volume scattering coefficient matrix  $B_c(\Theta)$  appear in the scattered light vector. As an example, for randomly oriented axisymmetric particles the scattered light vector resulting from incident light linearly polarized parallel  $P$  to the scattering plane,  $P\mathbf{I}_{inc} = [1 \ 1 \ 0 \ 0]^T I_o$ , has only two non-zero Stokes parameters. ( $I_o$  is the magnitude of incident light, considered below.) Ignoring the initial geometric factor, Eq (4D) gives,  $P\mathbf{I}_{sca}(\Theta) \sim [P\mathbf{I}_{sca}(\Theta) \ P\mathbf{Q}_{sca}(\Theta) \ 0 \ 0]^T \sim \{[\beta_{11}(\Theta) + \beta_{12}(\Theta)] \ [\beta_{21}(\Theta) + \beta_{22}(\Theta)] \ 0 \ 0\}^T I_o$ . The two Stokes parameter are  $P\mathbf{I}_{sca}(\Theta) \sim [\beta_{11}(\Theta) + \beta_{12}(\Theta)] I_o$  and  $P\mathbf{Q}_{sca}(\Theta) \sim [\beta_{21}(\Theta) + \beta_{22}(\Theta)] I_o$ , the difference being the non-sphericity polarimetric property discussed in Section 2.3. For the case of + 45° linear incident polarization,  $L\mathbf{I}_{inc} = [1 \ 0 \ 1 \ 0]^T I_o$ , all four Stokes parameters are present in the scattered radiation and are specified by the four volume scattering coefficients  $\beta_{11}(\Theta)$ ,  $\beta_{21}(\Theta)$ ,  $\beta_{33}(\Theta)$ , and  $\beta_{43}(\Theta)$ , respectively. Other incident polarization states provide for different elements and element combinations, but for the purposes of this study, only two linear polarization states are used, parallel to the scattering plane, also called 0° polarization, and + 45° polarization.

The convenient notation  $I_o$  for the magnitude, i.e., the intensity of the incident light is explained for these two states. In general,  $I_o = \langle E_o E_o^* \rangle$ , the dot-product of  $E_o$  the magnitude of the total electric field vector and  $E_o^*$  its complex conjugate, with  $\langle \rangle$  here indicating time-average over periods that are long compared to the approximately 100 THz of optical fields. For incident light linearly polarized parallel (0°) to the scattering plane, which is the plane of measurement – taken here to be the x-plane – then,  $I_o = \langle E_x E_x^* \rangle$ , since the electric field temporal oscillations are entirely in the x-plane,  $E_x(t) \equiv E_o(t)$ . For incident light linearly polarized at + 45° to the scattering plane, the total electric field vector is considered as made up of two equal and orthogonal field components,  $E_o = E_x + E_y$ , so that  $I_o = \langle E_x E_x^* \rangle + \langle E_y E_y^* \rangle = 2\langle E_x E_x^* \rangle$  [e.g., CO, p 40]. Since  $E_x(t) = E_y(t) = E_o(t)/(\sqrt{2})$ , then the general definition still applies,  $I_o = \langle E_o E_o^* \rangle$ .

## 2.3 POLARIMETRIC PROPERTIES

The four polarimetric quantities, defined in terms of the scattered radiation Stokes parameters in Section 1.1, are now expressed in their constituent forms, i.e., in terms of the incident radiation as affected by the scattering particles. In Table 2.2 the four polarimetric quantities applied in this report are listed along with their various associated Stokes parameters and matrix elements; these are subsequently explained.

**Table 2.2. Polarimetric Quantities of Scattered Light.  
All entries vary with scattering angle  $\Theta$ .**

Name	Symbol	Stokes Parameter	Normalized Element*	Vol. Scat. Coefficient*
Intensity	$P_I$	${}^+I_{\text{sca}}$	$a_1$	$\beta_{11}$
Partial Linearity	$P_L$	${}^+Q_{\text{sca}}$	$b_1$	$\beta_{21}$
Non-Sphericity	$P_N$	${}^P I_{\text{sca}} - {}^P Q_{\text{sca}}$	$a_1 - a_2$	$\beta_{11} - \beta_{22}$
Retardation	$P_R$	${}^+V_{\text{sca}}$	$-b_2$	$\beta_{43}$

\* Valid for spheres or for randomly oriented isotropically dispersed spheroids.

When quantified by the appropriate volume scattering coefficients, the four measurable scattered radiation *polarimetric quantities* can be referred to as *polarimetric properties* because the scattering properties of the particles in the sample volume are explicitly included. Since the incident laser light vector is completely known, the scattering properties of the particles can, in theory, be retrieved from the polarimetric measurements. It is, in fact, the inference, from the measured Stokes parameters, of the changes in specific terms and factors comprising the volume scattering coefficient matrix elements  $\beta_{ij}(\Theta)$  that enables detection of bio-aerosols in the sample volume.

The four polarimetric properties for the combination of two aerosol types are expressed using  $a_1$ ,  $b_1$ ,  $a_2$ , and  $b_2$  in Eq (2A). Specifically, for the incident light vector  $\mathbf{I}_{\text{inc}}$  of magnitude  $I_o$  that is linearly polarized parallel to (at  $0^\circ$ ) and at  $+45^\circ$  counterclockwise from the upward normal of the scattering plane (as seen by the detector), the four polarimetric properties are related simply as:

$$\begin{aligned} P_I(\Theta) &= {}^+I_{\text{sca}}(\Theta)/I_o \sim a_1(\Theta) \\ P_L(\Theta) &= {}^+Q_{\text{sca}}(\Theta)/I_o \sim b_1(\Theta) \\ P_N(\Theta) &= [{}^P I_{\text{sca}}(\Theta) - {}^P Q_{\text{sca}}(\Theta)]/I_o \sim [a_1(\Theta) - a_2(\Theta)] \\ P_R(\Theta) &= {}^+V_{\text{sca}}(\Theta)/I_o \sim -b_2(\Theta) \end{aligned} \quad (6A)$$

The simplicity of these expressions recommends the two states of incident linear polarization indicated by superscripts,  ${}^+$  and  ${}^P$ . Then, three polarimetric properties are single Stokes parameter measurements, the fourth a Stokes parameter difference. Each property is a Stokes parameter(s) normalized by the magnitude of the incident light, meaning that the properties are dimensionless.

Only the polarimetric portion of the normalized Stokes parameters—the polarimetric properties—appears in Eq (6A). Applying Eq (4C), the properties used here are expressed as:

$$\begin{aligned} P_I(\Theta) &= [V/4\pi R^2][N_a \langle C_{\text{sca}} \rangle_a + N_b \langle C_{\text{sca}} \rangle_b] a_1(\Theta) \\ P_L(\Theta) &= [V/4\pi R^2][N_a \langle C_{\text{sca}} \rangle_a + N_b \langle C_{\text{sca}} \rangle_b] b_1(\Theta) \\ P_N(\Theta) &= [V/4\pi R^2][N_a \langle C_{\text{sca}} \rangle_a + N_b \langle C_{\text{sca}} \rangle_b][a_1(\Theta) - a_2(\Theta)] \\ P_R(\Theta) &= [V/4\pi R^2][N_a \langle C_{\text{sca}} \rangle_a + N_b \langle C_{\text{sca}} \rangle_b] b_2(\Theta) \end{aligned} \quad (6B)$$

Although simple in form, Eq (6B) contains the four combined normalized elements,  $a_1$ ,  $b_1$ ,  $a_2$ , and  $b_2$ , which themselves are compound expressions that are given in Appendix A.6 as Eq (A.7).

Finally, in terms of Eq (5C) volume scattering coefficient elements, Eq (6B) is

$$\begin{aligned} P_I(\Theta) &= [V/R^2] \beta_{11}(\Theta) \\ P_L(\Theta) &= [V/R^2] \beta_{21}(\Theta) \\ P_N(\Theta) &= [V/R^2] [\beta_{11}(\Theta) - \beta_{22}(\Theta)] \\ P_R(\Theta) &= [V/R^2] \beta_{43}(\Theta) \end{aligned} \quad (6C)$$

Table 2.2 summarizes Eqs (6A), (6B), and (6C). Either Eqs (6B) or (6C) quantify how the scattering properties of particles determine the values  $P_I$ ,  $P_L$ ,  $P_N$ , and  $P_R$ . Eqs (6B), in particular, explicitly separate those particle properties that are angle-independent from the angle-dependent polarimetric ones. The explicit formulations of the angle variation of the normalized scattering matrix elements,  $a_i(\Theta)$ ,  $b_i(\Theta)$ ,  $a_2(\Theta)$ ,  $b_2(\Theta)$ , are quite complex. However, a number of readily employed small-particle scattering codes are now available on the world-wide-web; addresses are given in Appendix C.

Clearly, the normalized elements (the  $a$ 's and  $b$ 's) and the volume scattering coefficients (the  $\beta$ 's) are linearly related by the particle ensemble-average scattering cross-section and number-concentration. In Section 4 the results of small-particle scattering computations, which give all  $a_i(\Theta)$ ,  $b_i(\Theta)$ , and the  $\langle C_{\text{sca}} \rangle$  values, are extensively considered. There the Eq (6C) identity is assumed between polarimetric properties and volume scattering coefficients.

In application of the SPADE concept of operations, the introduction of bio-aerosol into the ambient environment is detected by continuously monitoring temporal changes in polarimetric properties, in this report confined to the four defined in Eq (6C). Any of the various aerosol physical properties indicated in Eq (6B) could change with time: number-concentrations  $N_a$  and  $N_b$ , both average scattering cross-sections  $\langle C_{\text{sca}} \rangle_a$  and  $\langle C_{\text{sca}} \rangle_b$ , and possibly all four normalized scattering matrix elements for each of the two types of particles:  $a_1(\Theta) \sim [F_{a,11}(\Theta), F_{b,11}(\Theta)]$ ,  $b_1(\Theta) \sim [F_{a,12}(\Theta), F_{b,12}(\Theta)]$ ,  $a_2(\Theta) \sim [F_{a,22}(\Theta), F_{b,22}(\Theta)]$ ,  $b_2(\Theta) \sim [F_{a,34}(\Theta), F_{b,34}(\Theta)]$  – 12 variables in total. From the five measured quantities, Stokes parameters  ${}^+I_{\text{sca}}(\Theta)$ ,  ${}^+Q_{\text{sca}}(\Theta)$ ,  ${}^+V_{\text{sca}}(\Theta)$ ,  ${}^P I_{\text{sca}}(\Theta)$ , and  ${}^P Q_{\text{sca}}(\Theta)$ , that constitute the four polarimetric properties considered here, the question is: How are all 12 variables separated and accounted for? The answer is considered in Section 6 that deals with the detection procedure.

### 3. MODEL AEROSOLS

In the atmosphere, ambient background aerosol are never of a single size; rather they are distributed over a range of sizes that—for their light scattering effects—can be characterized by an effective radius  $r_{\text{eff}}$ , an effective variance  $v_{\text{eff}}$ , and an analytical size-distribution function  $n(r)$  describing the number of particles per unit volume as a function of size  $r$  [HT, p 558]. For spherical particles the meaning of  $r$  is evident; for non-spherical particles, it is the area equivalent-sphere radius, which is defined in Appendix B.2. Also, the relative intensity of the light scattered by any particle population varies with the total number of particles per unit of spatial volume, i.e., with the number-concentration  $N$  [ $\text{cm}^{-3}$ ].

#### 3.1 POPULATION SCATTERING MATRIX ELEMENTS

The traditional scattering matrix for a single particle of size  $r$  and refractive index  $m$  can be symbolized as  $\mathbf{F}(\Theta; r, m)$ . (Wavelength dependence can be included if  $r$  is replaced by the size parameter  $x = 2\pi r/\lambda$ , see Appendix B.3) Extending the meaning of such a matrix to more generally specify the scattering characteristics of a population of variously-sized particles within a unit physical volume ( $D \equiv N$  in Table 2.1), all having the same refractive index  $m$ , then the population parameters become  $\mathbf{F}(\Theta; N, r_{\text{mo}}, n(r), m)$ , where  $r_{\text{mo}}$  is the mode size of the particles. Often the specific form of the size distribution function  $n(r)$ , given population parameters  $r_{\text{eff}}$  and  $v_{\text{eff}}$  (defined in Appendix B.5), is not critical [MTL, p 285, or MT4b, p 7209, or HT p 559]. Adopting these two size-related parameters the complete-arguments form of the scattering matrix in Eq (1A) is  $\mathbf{F}(\Theta; N, r_{\text{eff}}, v_{\text{eff}}, m)$ . Similarly, the form of the normalized scattering matrix in Eq (1C), with the particle population indicated by the same two parameters, is  $\mathbf{F}(\Theta; r_{\text{eff}}, v_{\text{eff}}, m)$ ; and in Eq (2A) the normalized scattering matrix elements are,  $a_1(\Theta; r_{\text{eff}}, v_{\text{eff}}, m)$ , etc. These are, then, the normalized scattering matrix elements (meaning the  $F_{ij}$ 's in Table 2.1 divided by  $\langle C_{\text{sca}} \rangle / 4\pi$  and also by  $N$ ), or equivalently the volume scattering coefficients, the  $\beta_{ij}$ 's, similarly normalized.

The scattering matrix particle dependencies are again extended—this time to include non-spherical particles, in particular, spheroids (particles having a circular plane of symmetry) that are randomly oriented. The new particle parameter is the axis ratio  $\varepsilon$  (defined in Appendix B.2). Resulting is the ensemble-average normalized per-particle scattering matrix elements, the  $a_1$ ,  $b_1$ ,  $a_2$ , etc. in Eq (2A), each having the argument list  $(\Theta; r_{\text{eff}}, v_{\text{eff}}, \varepsilon, m)$ . Therefore, the traditional phase function for an ensemble of spheroid particles is  $a_1(\Theta; r_{\text{eff}}, v_{\text{eff}}, \varepsilon, m)$ .

The properties of an ensemble of similarly shaped particles ( $r_{\text{eff}}$ ,  $v_{\text{eff}}$ ,  $\varepsilon$ ,  $m$ ) constitute the necessary input parameters for any scattering code that computes the phase function or any other scattering matrix element. In more versatile non-spherical particle scattering codes (esp. the T-matrix code of Mishchenko [M91, M93, and MT8] considered in Appendix C), one additional input parameter is allowed—the specific particle size-distribution function  $n(r)$  is selectable from a list of common distribution functions. (While the particular form of  $n(r)$  may not much influence the final values of elements, it does significantly affect computation time.) The input parameters of the Mishchenko T-matrix code depend somewhat on the distribution function selected. Specifically, initial routines of the code convert the actual input parameters, which are the minimum and maximum particle size,  $r_{\text{min}} \leq r \leq r_{\text{max}}$ , into the needed  $r_{\text{eff}}$  and  $v_{\text{eff}}$ , according to the form of the selected distribution function  $n(r)$ .

Wherever populations of two different types of particles are co-located in the same sample volume, as with ambient plus bio-aerosol, the weighted sum in Eq (3) is formed for each combined normalized scattering matrix element. The influence of the two particle populations is

explicitly indicated by replacing the single argument ( $\Theta$ ) in individual normalized scattering matrices in Eq (3) by ( $\Theta; r_{\text{eff},a} v_{\text{eff},a}, \epsilon_a, m_a$ ) and ( $\Theta; r_{\text{eff},b} v_{\text{eff},b}, \epsilon_b, m_b$ ), where, it is reemphasized, subscripts refer to the ambient and bio-aerosol, and not to the conventional normalized matrix element symbols introduced in Eq (2A).

### 3.2 AEROSOL SIZE DISTRIBUTION

All SPADE scattering computations reported on in Section 4 use a single-mode particle size distribution. Specifically, the functional form is the *modified-gamma distribution*, originally publicized by Deirmendjian in 1969 [DE, eq 82]; further explained by Thomas and Duncan [TD, eq 1.216] or by Modest [MT, eq 11.34]. This form describes especially well the positively skewed size distributions of cloud particles and of larger aerosol particles–bio-aerosols being such. The modified-gamma size-distribution function is

$$n(r) = A r^\alpha \exp(-Br^\gamma) \quad (7A)$$

which has four positive-valued parameters: two coefficients,  $A$  and  $B$ , and two exponents,  $\alpha$  and  $\gamma$ . The standard gamma distribution function has  $\gamma = 1$  [DE, p 76].

In this research, the distribution function is normalized, meaning that the integral of  $n(r)$ , i.e., the number-concentration  $\int n(r) dr = 1 \text{ cm}^{-3} \equiv N_o$ . This unit number-concentration determines the value of  $A$  used here. Therefore,  $n(r)$  is a *probability density function* for particle size (Appendix B.2) that is further described in Section 3.3. Other values of number-concentration  $N$  are applicable by replacing  $A$  in Eq (7A) with the product  $(NA)$ , where  $\int n_N(r) dr = N$ .

For the modified-gamma distribution

$$A = \gamma B^\mu [1/\Gamma(\eta)] \quad (7B)$$

where, for convenience,  $\mu = (\alpha+1)/\gamma$ . The gamma function in Eq (7B) is the basis for the name of this distribution.

The value of the mode radius of the modified-gamma distribution [e.g., TD, eq 1.218] is

$$r_{\text{mo}}[\mu\text{m}] = [\alpha/(B\gamma)]^{(1/\gamma)} \quad (7C)$$

which indicates that the parameter quotient  $(\alpha/B)$  is associated with the average size of the particles. That modified-gamma parameters are not all independent is apparent from Eqs (7B) and (7C), e.g., the dimension of  $A$  depends on exponent  $\alpha$ , that of  $B$  on  $\gamma$ . In practice, both  $B$  and then  $A$  are determined from Eqs (7B) and (7C) once the values of the positive exponents, integer  $\alpha$  and half-integer  $\gamma$  are specified and the mode radius  $r_{\text{mo}}$  is known. With values for  $r_{\text{mo}}$ ,  $\alpha$ , and  $\gamma$ , Eq (7C) is solved for  $B$ . Given  $B$ , the value of  $A$  is determined from Eq (7B). In Table 3.1, as indicated earlier, all  $A$ 's are determined for unit number-concentration,  $N_o = \int n(r) dr = 1 \text{ cm}^{-3}$ .

### 3.3 PHYSICAL AND OPTICAL PARAMETERS

Three background aerosols and one bio-aerosol are used in the present study; these are depicted in Figure 3.1. The modified-gamma size-distribution function, Eq (7A), is used to generate each of the curves in Figure 3.1. For the background aerosols the number-concentrations – related to the area under each curve – are assigned as  $N = 100 \text{ cm}^{-3}$ ; for the bio-aerosol,  $N = 1 \text{ cm}^{-3}$ .

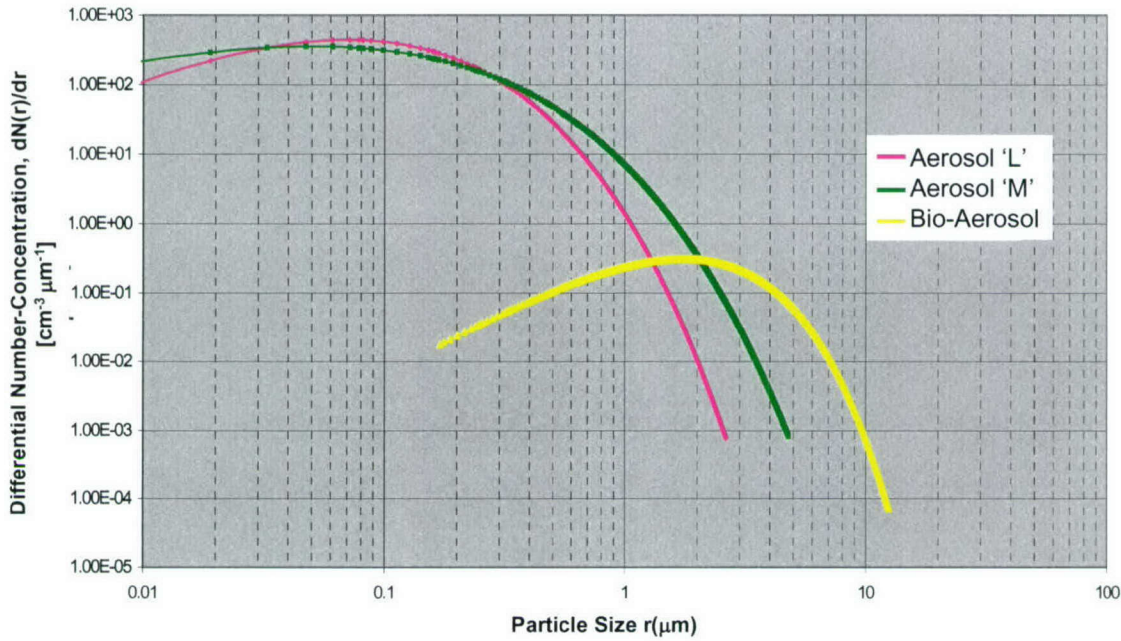


*Figure 3.1. Size Distributions of Aerosol Particles. Two types of ambient background aerosols, continental 'L' and maritime 'M', and one bio-aerosol 'BS'. Log-log plots of modified-gamma distribution function (parameters in Table 3.1) for total number-concentration (area under curve): background aerosols  $N_a = 100 \text{ cm}^{-3}$ , bio-aerosol  $N_b = 1 \text{ cm}^{-3}$ . Ordinate: differential number-concentration, number of particles per unit spatial volume per unit interval of particle radius [cm<sup>-3</sup> μm<sup>-1</sup>].*

To aid in interpreting Figure 3.1, the definitions and interrelationships among the various measures of particle size, number-concentration, and distribution are summarized.  $N$  is the total number of all particles per unit volume [cm<sup>-3</sup>], irrespective of size.  $N(r)$  is the accumulated total number of particles per unit volume having radius smaller than or equal to  $r$ . In the normalized condition,  $N_o = 1 \text{ cm}^{-3}$ , then  $N_o(r)$  is the fraction of many hypothetical unit volumes that contains particles with radius  $\leq r$ . The ordinate in Figure 3.1,  $dN(r)/dr$  is the number having sizes between  $r$  and  $(r + dr)$ ; units are [cm<sup>-3</sup> μm<sup>-1</sup>]. The relation with the size-distribution function  $n(r)$ , considered in Appendix B.1, is  $dN(r)/dr = N n(r) \equiv n_N(r)$ . Thus, for  $N = N_o = 1$ ,  $dN_o(r)/dr = n(r)$ .

Given in Table 3.1 are the specific values of the four parameters and the mode radius used in the modified-gamma form of  $n(r)$  for each aerosol type. Also listed are the effective radius  $r_{\text{eff}}$  and effective variance  $v_{\text{eff}}$ , both of which are output parameters from preliminary routines of the scattering code applied in Section 4 (the Mishchenko T-matrix scattering code, referred to in Appendix C.3). Finally,  $x_{\text{eff}}$  the effective size-parameter (Appendix B.5) is included for 2.12 μm – the illumination wavelength most utilized in Section 4 computations.

**Table 3.1. Modified-Gamma and Physical Parameters of Aerosol Types.  
Ambient backgrounds ‘M’, ‘L’, ‘D’; bio-aerosol simulant ‘Bacillus subtilis’.**

Aerosol Type	N (cm <sup>-3</sup> )	α	γ	r <sub>mo</sub> (μm)	B	A [N = 1]	r <sub>eff*</sub> (μm)	v <sub>eff*</sub> (–)	x <sub>eff</sub> <sup>#</sup> (μm)
Maritime ‘M’	1	1	½	0.05	8.9443	5.3333x10 <sup>2</sup>	0.86	0.429	2.55
Continental ‘L’	1	2	½	0.07	15.1186	4.9757x10 <sup>4</sup>	0.48	0.415	1.42
Desert Dust ‘D’	1	2	½	0.47	5.8346	1.6438x10 <sup>2</sup>	3.19	0.384	9.45
B. Subtilis ‘BS’	1	2	1	1.75	1.1429	0.74644	4.36	0.195	12.92

\* Radius ranges used:  $0.0 \geq r \geq 3.0 \mu\text{m}$  for ‘M’ and ‘L’;  $0.0 \geq r \geq 12.5 \mu\text{m}$  for ‘D’ and ‘BS’.

\*\* Effective size parameter:  $x_{\text{eff}}^{\#} = 2\pi r_{\text{eff}}/\lambda$  for  $\lambda = 2.12 \mu\text{m}$ .

For the ambient backgrounds ‘M’ and ‘L’, the  $\alpha$ ,  $\gamma$ , and  $r_{\text{mo}}$  values in Table 3.1 are from [DE, table 5]. For the desert dust ‘D’ the mono-modal value of  $r_{\text{mo}}$  is from [DKS, table 4.2], and for the agent ‘BS’ it is from a measured Bacillus subtilis aerosol distribution [2001, internal Lincoln Laboratory measurement]. The value of  $\alpha$  is assigned according to the size of the most common particles relative to the range of sizes – small mode radius but wide range indicated by  $\alpha = 1$ , intermediate mode and more narrow range by  $\alpha = 2$  [DE, Figure 20]. The value of  $\gamma$  is prescribed by the distribution skewness [SP, Figure 7.11] – highly skewed by  $\gamma = ½$ , moderately skewed by  $\gamma = 1$ .

The analytical form of  $n(r)$ , given the Table 3.1 parameters, means that the entire particle size distribution is known. For each aerosol type, these are needed to compute the scattering matrix elements, especially, their angular variations that are emphasized in Section 4. The normalization,  $N = N_o = 1 \text{ cm}^{-3}$ , enables computation of scattering matrix element values that are applicable to any concentration of ambient background or agent aerosol by multiplying each element at each angle by the appropriate N-value, as, for example, in Eqs (4A) and (4B).

In Table 3.1, the particle-population parameters of the bio-aerosol simulant ‘BS’ are different from those of common ambient background aerosols. In general, the bio-aerosol particles are larger ( $r_{\text{eff},b} \cong 4.0 \mu\text{m}$ ) and more narrowly distributed ( $v_{\text{eff},b} \cong 0.2$ ) than ‘M’ or ‘L’ ambient backgrounds, which are smaller ( $r_{\text{eff},a} \cong 0.7 \mu\text{m}$ ) and more broadly distributed ( $v_{\text{eff},a} \cong 0.4$ ).

With regard to the complex refractive index  $m$ , Table 3.2 contains the spectral variation for the aerosols employed in this study. Generally, the larger the real (imaginary) part, the larger (smaller) the relative scattering intensity, especially in backscattering directions.

**Table 3.2. Spectral Values of Refractive Index ( $m = m_{\text{real}} - i m_{\text{imag}}$ ) and  $\langle C_{\text{sca}} \rangle$  at 2.12 μm for ambient background and ‘BS’ aerosols.**

Wavelength (μm)	0.532		1.06		1.50		2.12		2.12
Aerosol Type:	m <sub>real</sub>	m <sub>imag</sub>	$\langle C_{\text{sca}} \rangle (\mu\text{m}^2)$						
Maritime ‘M’	1.381	5.5e-9	1.369	9.3e-5	1.360	0.0011	1.337	0.0056	0.5214
Continental ‘L’	1.530	0.0056	1.518	0.0163	1.420	0.0225	1.420	0.0090	0.0954
Desert Dust ‘D’	1.530	0.0080	1.506	0.0080	1.410	0.0080	1.260	0.0080	18.87
B. Subtilis ‘BS’	1.520	0.0178	1.520	0.0126	1.520	0.0097	1.520	0.0089	58.88 <sup>#</sup>

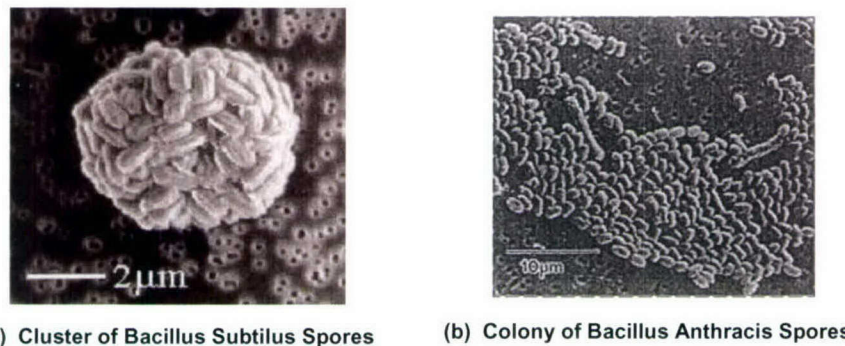
\* Values interpolated from d’Almeida, Koepke, and Shettle [DKS, table 4.3] with ‘oceanic’ = ‘M’, ‘water-soluble’ = ‘L’, ‘dust-like’ = ‘D’. ‘BS’ values from [TAK, table 1, spores in water].

<sup>#</sup> Spherical particles; average of all ε for prolate spheroids – 59.07, average of all ε for oblate – 59.34 μm<sup>2</sup>.

A particular feature, in the visible, is that ‘L’, ‘D’, and ‘BS’ aerosols all have nearly the same real index, but ‘BS’ has a larger imaginary index, which tends to diminish detectability in the backscattering directions. However, in the SWIR ( $\lambda = 2.12 \mu\text{m}$ ), the real parts are significantly different, as seen in Table 3.2. The interpretation is that the more effective surface scattering by ‘BS’ could aid in the differentiation of ‘BS’ from an ambient ‘D’ aerosol even though photons that enter either type of particle are about equally likely to be absorbed. The implication is that ‘BS’ and ‘D’ are more likely to be distinguished at forward scattering angles than at back-scattering angles. (Relevant additional reference is [MTK, p 16,831].)

Regarding particle shape, as presented in Section 4.1, the initial SPADE scattering computations are carried out for spherical particle shapes for both the ambient background and bio-aerosol – traditional Mie scattering codes are therefore applicable (Appendix C.2). Naturally occurring aerosol particles that contain acids or salts tend to be spherical because they usually form aqueous solutions with readily condensed water vapor. Also, regardless of shape, very small aerosol particles ( $r < 0.01 \mu\text{m}$ ) interact with visible and longer wavelength radiation as if they were spheres (the Rayleigh approximation).

But naturally occurring aerosol comprised of soil fragments or other non-hygrosopic materials are usually non-spherical. Furthermore, individual bio-aerosol spores have rather characteristic prolate morphologies. Figure 3.2 shows scanning electron microscope images of two species of *Bacillus* spores.



(a) Cluster of *Bacillus Subtilis* Spores      (b) Colony of *Bacillus Anthracis* Spores

*Figure 3.2. Bacillus Spores – Scanning Electron Microscope Images.*

(a) *Cluster of *Bacillus subtilis* spores formed by evaporation of liquid solution containing individual spores [from HPC, Figure 2].* (b) *Colony of individual *Bacillus anthracis* spores, two elongated, grown aerobically on animal blood substratum; imprint scale 10  $\mu\text{m}$ .* [Photograph of colony by J. Ezzell, US Army Medical Research Inst, Fort Detrick, Frederick, MD.]

In Figure 3.2, (a) is a cluster of approximately 350 individual *Bacillus subtilis* ‘BS’ spores and (b) is a colony of nearly the same number of separate *Bacillus anthracis* spores. The cluster, which results from dehydration of a larger aqueous droplet containing spores, is slightly oblate with the shorter rotation axis directed perpendicular to the page. The colony in Figure 3.2 (b) was grown on a gelatinous animal-blood substrate. Such bio-aerosols when prepared as a weapon consist of somewhat non-spherical clusters, typically in the size range of  $0.5 < r_A < 10 \mu\text{m}$  (equivalent-sphere radius  $r_A$  is defined in Appendix B.2).

In Section 4.2, more extensive and realistic computations for bio-aerosol particles having spheroid shapes are considered. The particle shape parameter is the axis ratio  $\epsilon$ , which is defined in Appendix B.2. The bio-aerosol particle shape is varied over axis-ratio values for prolate spheroids of  $\epsilon = 1.0/1.3, 1.0/1.4, 1.0/1.5, 1.0/2.0$ , and for oblate spheroids  $1.3/1.0, 1.4/1.0, 1.5/1.0$ , and  $2.0/1.0$ .

## 4. SCATTERING COMPUTATIONS

Numerical computations using scattering codes are an efficient method for evaluating the feasibility of the SPADE concept. In the research reported on here, scattering computations are carried out for size-distributed populations of ambient background and bio-aerosols. In all cases, ambient background aerosols are treated as spherical particles, whereas bio-aerosol particles can have either spherical or non-spherical shapes. Bio-aerosols are spheres for the purpose of sensitivity analysis (Section 4.1) and spheroids for the purpose of environmental signal-strength comparisons (Section 4.2).

The scattering computations for spherical particles in Section 4.1 result from the Mie scattering code contained in Thomas and Duncan [TD, pp 136-147], which is an extension to populations of spheres of the Bohren and Huffman [BH, pp 479-482] individual-sphere BHMIE code. (Mie scattering codes are available at internet addresses given in Appendix C.1.) In Section 4.2, all non-spherical bio-aerosol particle computations, including the spherical limit of axis ratio  $\epsilon = 1.0/1.0$ , and all spherical background particle computations use the M.I. Mishchenko T-matrix scattering code, extended-precision version (documented in [MTL, Section 5.11] and available via internet; Appendix C.1).

Computations are made twice—once for ambient background particles alone, and then for the combination of background plus bio-aerosol particles. The modified-gamma size distribution function (Section 3.2) is applied separately to the background and bio-aerosol particles. The modified-gamma parameters and the physical properties of each aerosol type are given in Table 3.1. Except for Section 4.1.3, the number-concentration for ambient backgrounds is  $N_a=100 \text{ cm}^{-3}$  and for the bio-aerosols it is  $N_b=1 \text{ cm}^{-3}$ , i.e., the number-concentration mixing ratio is  $R_N = 10^{-2}$ .

The specific purpose of scattering computations is to assess the size of any environmental ‘signal’ that might indicate the introduction of bio-aerosols. The signal magnitude for a specific polarimetric property is the difference between the value for the condition of combined background and bio-aerosols versus the condition of no bio-aerosols, i.e., the ambient background alone. Recalling Figure 2.1, the ‘signal’ dealt with here is the environmental signal only—that of the irradiated scattering-volume aerosols themselves, the scattering source—and does not include effects of path transmission, optical devices, or receiver components; factors that are added in Section 5.

Environmental signal, for a polarimetric property, is quantified as the difference between the volume scattering coefficient matrices for the two aerosol conditions. Eq (5C) is the relevant matrix for the combined condition; Eq (5A) being the matrix for the ambient aerosol alone – the  $N_b = 0$  case. Ultimately, it is the magnitude of the difference between individual elements of those matrices that quantifies the environmental signal, specifically,

$$\Delta\beta_{ij}(\Theta) = |\beta_{ij,c}(\Theta) - \beta_{ij,a}(\Theta)| \quad (8A)$$

The row-column subscript  $_{ij}$  identifies the individual volume scattering coefficient element needed in the Eq (6C) expressions for the polarimetric properties  $P_l(\Theta)$ ,  $P_L(\Theta)$ ,  $P_N(\Theta)$ , and  $P_R(\Theta)$ . Subscript ‘a’ is for the ambient background aerosol alone, and is derived using Eq (2A) in Eq (5A). Subscript ‘c’ is for the combined aerosol, derived from Eq (2A) in Eq (3) and then in Eq (5C). Both are formulated in terms of the expressions for the  $\beta_{ij}(\Theta)$  quantities provided in Appendix A.6, specific, Eqs (A.8) are used in Eqs (A.9).

For constant ambient background, it is clear from Eqs (3) and (5C) that the environmental signal is, indeed, the bio-aerosol  $\beta$ -value. Eq (8A) is, then

$$\Delta\beta_{ij}(\Theta) = \beta_{ij,b}(\Theta) \quad (8B)$$

Values of  $\Delta\beta_{ij}(\Theta)$  are here determined from scattering-code computations of  $\beta_{ij,c}(\Theta)$  and  $\beta_{ij,a}(\Theta)$ . Computed  $\beta_{ij,b}(\Theta)$ -values confirm Eq (8B) in all cases.

Implicitly, differences in the polarimetric properties are analyzed:

$$\begin{aligned}\Delta\beta_{11} &\sim (P_{l,c} - P_{l,a}) \\ \Delta\beta_{21} &\sim (P_{L,c} - P_{L,a}) \\ \Delta(\beta_{11} - \beta_{22}) &\sim (P_{N,c} - P_{N,a}) \\ \Delta\beta_{43} &\sim (P_{R,c} - P_{R,a})\end{aligned}\quad (9)$$

In this section only the environmental signal values, the  $\Delta\beta_{ij}$ 's ( $= \beta_{ij,b}$ 's), are analyzed. In Sect 5 specific bi-static lidar measurement scenarios allow assessments of signal-to-noise of the  $\beta_{ij,b}$ 's or from Eq (9) of polarimetric property differences themselves, the  $(P_{X,c} - P_{X,a})$ 's. Importantly, values of  $\beta_{ij,b}$ 's, not of ratios like  $\beta_{ij,b}/\beta_{11,b}$  are essential to carry out signal-to-noise computations.

In applying the SPADE concept-of-operations, Eq (8A) is a diagnostic fact and not a-priori useful, unless a detailed database of  $\beta_{ij,b}(\Theta)$  is developed to utilize Eq (8B). In particular, from prior measurement the volume scattering coefficient of the ambient background  $\beta_{ij,a}(\Theta)$  is available for comparison with the presently measured, potentially combined quantity  $\beta_{ij,c}(\Theta)$ . Uncertainties in  $\Delta\beta_{ij}(\Theta)$  attributable to realistic measurement system effects are evaluated in Section 5. In Section 6 is addressed the central question for SPADE feasibility – When and where are the values of  $\Delta\beta_{ij}(\Theta)$  sufficiently distinct from naturally occurring temporal variation in the ambient background, specific, from  $\Delta\beta_{ij,a}(\Theta)/\Delta t$ , that they can be confidently identified as evidence of  $\beta_{ij,b}(\Theta)$ ?

## 4.1 SENSITIVITY STUDIES

Scattering computations are most readily made for populations of spherical particles because only one orientation of the particles is needed. Also, only three normalized scattering matrix elements in Eq (2A) have to be evaluated, since for spheres at every scattering angle,  $a_2 = a_1$ ,  $a_4 = a_3$ , and  $a_1^2 = b_1^2 + a_3^2 + b_2^2$  [e.g., BH, p 113]. Furthermore, the expansion coefficients in each matrix element angular expression have the familiar Lorentz-Mie form (refer to Appendices A.1 and C.2), and calculation of the needed photometric quantity  $\langle C_{sca} \rangle$  is done expediently [e.g., SP, p 1184]. For these reasons, spherical particles are assumed for both ambient background and bio-aerosols in the following sensitivity analyses: 1) illumination wavelength, 2) matrix element, and 3) number-concentration mixing ratio ( $R_N = N_b/N_a$ ) versus the magnitude of the environmental signals—the  $\Delta\beta_{ij}$ s.

### 4.1.1 Wavelength Sensitivity

In Figures 4.1 and 4.2, values of  $\Delta\beta_{11}(\Theta)$  and  $\Delta\beta_{21}(\Theta)$  are represented by the vertical separations between the blue (background plus bio) and the red (background alone) curves. The  $\Delta\beta_{ij}$  analyses are presented in Table 4.1. The data—the Mie-code computed values of the  $\beta_{ij}$ 's at  $\Theta = 170^\circ$  backscatter angle—are for the maritime ‘M’ background, used to generate Figures 4.1 and 4.2, and

similar computed values for the continental ‘L’ background aerosol (not depicted). At 1.50  $\mu\text{m}$ ,  $\Delta\beta_{11}(170) = 21.09 \times 10^{-9} \text{ cm}^{-1}$ ; whereas in the 2.12  $\mu\text{m}$  panel its value is  $25.72 \times 10^{-9} \text{ cm}^{-1}$ . The implication is that, for the maritime ‘M’ background aerosol comprised of spherical particles of concentration  $N_a = 100 \text{ cm}^{-3}$ , within which is present spherical ‘BS’ particles of concentration  $N_b = 1 \text{ cm}^{-3}$ , the signal-strength at  $\Theta = 170^\circ$  is marginally greater at the longer wavelength. The reason, as seen in Figure 4.1, is mostly the lower intensity of the background aerosol backscattering at 2.12  $\mu\text{m}$ . Similarly with the ‘L’ background  $\Delta\beta_{11}(170)$  is, as anticipated, somewhat greater at 2.12  $\mu\text{m}$ . These examples illustrate the employment of scattering computations in sensitivity analyses.

**Table 4.1. Volume Scattering Coefficients ( $10^{-9} \text{ cm}^{-1}$ ) for Spherical Particles at Far-Backscatter Angle  $\Theta = 170^\circ$  for Various Polarimetric Properties.**

Background aerosols: maritime ‘M’ and continental ‘L’ each of concentration  $N_a = 100 \text{ cm}^{-3}$ . Bio-aerosol: ‘BS’ of concentration  $N_b = 1 \text{ cm}^{-3}$ . All particles are spheres of size distributions as in Figure 3.1.

Wavelength:		$\lambda = 1.50 \mu\text{m}$			$\lambda = 2.12 \mu\text{m}$		
Bkg	Property $\sim$ Coeff.	$ \beta_{ij,c} - \beta_{ij,a}  = \Delta\beta_{ij} \equiv \beta_{ij,b}$			$ \beta_{ij,c} - \beta_{ij,a}  = \Delta\beta_{ij} \equiv \beta_{ij,b}$		
‘M’	$P_I \sim \beta_{11}$	29.80	8.71	<b>21.09</b>	29.90	4.18	<b>25.72</b>
‘M’	$P_L \sim \beta_{21}$	-0.91	0.76	<b>1.67</b>	4.66	0.25	<b>4.41</b>
‘M’	$P_N \sim (\beta_{11} - \beta_{22})$	0.00	0.00	<b>0.00</b>	0.00	0.00	<b>0.00</b>
‘M’	$P_R \sim \beta_{43}$	9.92	0.99	<b>8.93</b>	6.51	0.35	<b>6.16</b>
‘L’	$P_I \sim \beta_{11}$	23.24	2.18	<b>21.06</b>	26.96	1.20	<b>25.76</b>
‘L’	$P_L \sim \beta_{21}$	-1.52	0.15	<b>1.67</b>	4.40	-0.01	<b>4.41</b>
‘L’	$P_N \sim (\beta_{11} - \beta_{22})$	0.00	0.00	<b>0.00</b>	0.00	0.00	<b>0.00</b>
‘L’	$P_R \sim \beta_{43}$	9.02	0.09	<b>8.93</b>	6.18	0.02	<b>6.16</b>

For these computations Eq (8B),  $\Delta\beta_{ij} \equiv \beta_{ij,b}$ , must apply—as is evident from the bold entries in Table 4.1. The differences are unaffected by the type of ambient background aerosol. They are the volume scattering coefficient values for the bio-aerosol only. (The slight differences between the ‘M’ vs. ‘L’ values of  $\beta_{11}$  are caused either by rounding errors in table data or by approximations made in the Mie-code.)

Although the Table 4.1 differences between the  $\Delta\beta_{11}(170)$  values at 1.50 vs. 2.12  $\mu\text{m}$  are not great, it is evident from Figure 4.1 that the differences between the visible 0.53  $\mu\text{m}$  or near-infrared 1.06  $\mu\text{m}$  and either short-wave infrared (SWIR) wavelength, 1.50 or 2.12  $\mu\text{m}$ , are very significant in the backscatter region ( $130^\circ < \Theta \leq 180^\circ$ ). For out-of-doors standoff detection of bio-aerosols using intensity in the backscatter region, the SWIR wavelength region has an evident advantage.

Turning to Figure 4.2 that illustrates  $P_L(\Theta)$ , the linearity polarization property\*, the  $\Delta\beta_{21}(\Theta)$  curves contain many interesting features. For instance, at the visible and near-infrared wavelengths there is essentially no backscattering signal,  $\Delta\beta_{21}(150^\circ < \Theta < 180^\circ) \approx 0$ ; whereas at the SWIR wavelengths the signal is very apparent. The sign of  $\beta_{21,c}(170)$  changes as wavelength changes from 1.50 to 2.12  $\mu\text{m}$ , but for the purpose of signal-strength assessment only the magnitude  $|\Delta\beta_{21}(170)|$  is of concern. From the Table 4.1 entries, specifically for 1.50  $\mu\text{m}$ ,  $|\Delta\beta_{21}(170)| = 1.67 \times 10^{-9} \text{ cm}^{-1}$  and at 2.12  $\mu\text{m}$  it is  $4.41 \times 10^{-9} \text{ cm}^{-1}$ , irrespective of the background aerosol type.

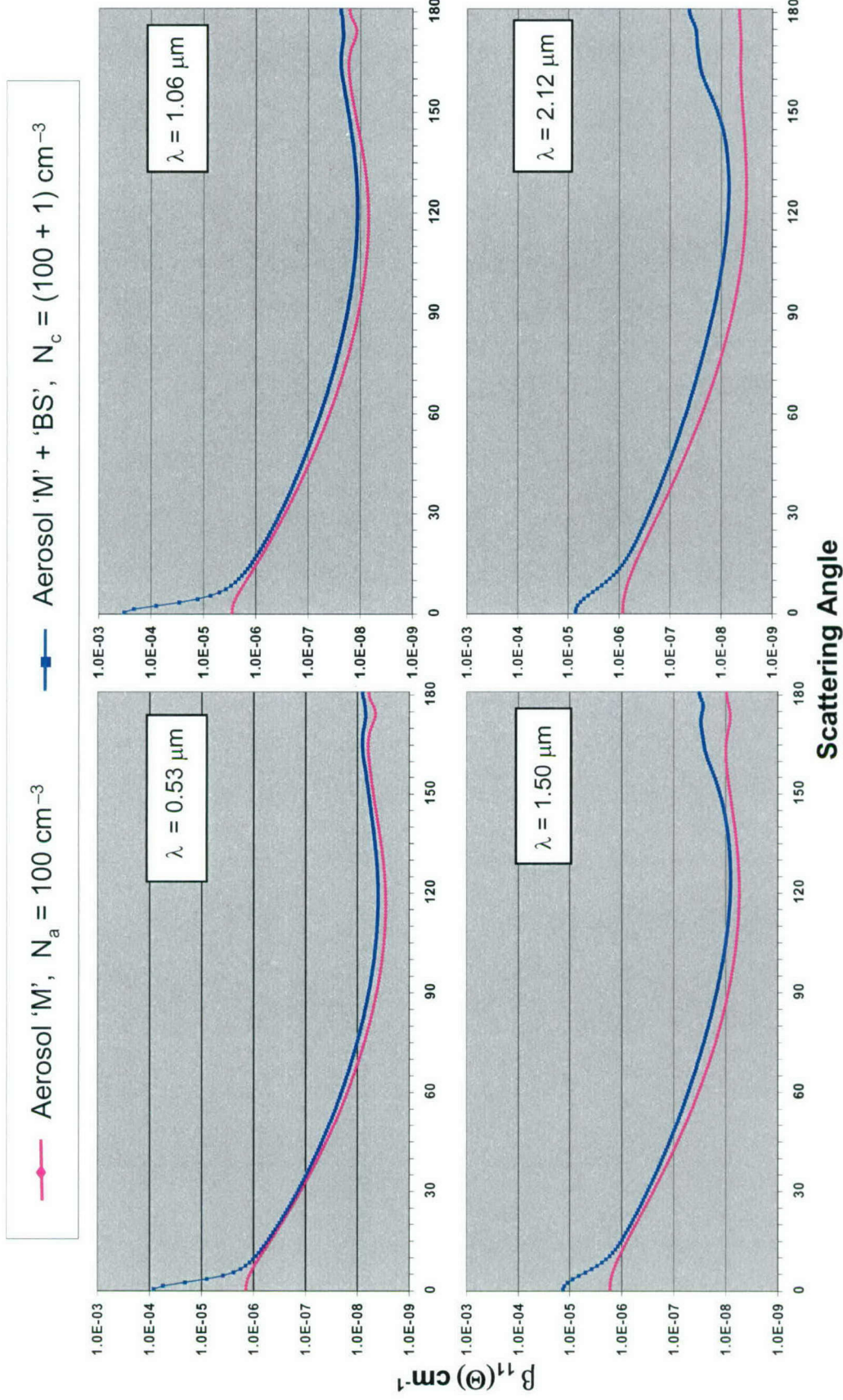


Figure 4.1. Profiles of Intensity Volume Scattering Coefficient at Four Wavelengths. (Red) Scattering-angle variations of  $\beta_{11,a}(\Theta)$  for maritime 'M' ambient background aerosol. (Blue) Scattering-angle variations of  $\beta_{11,c}(\Theta) = [\beta_{11,a}(\Theta) + \beta_{11,b}(\Theta)]$  for ambient aerosol 'M' plus *Bacillus subtilis* 'BS'. Number concentrations: 'M' is  $N_a = 100 \text{ cm}^{-3}$ , 'BS' is  $N_b = 1 \text{ cm}^{-3}$ . Aerosol particle sizes distributed as in Fig 3.1. All particles spherical.

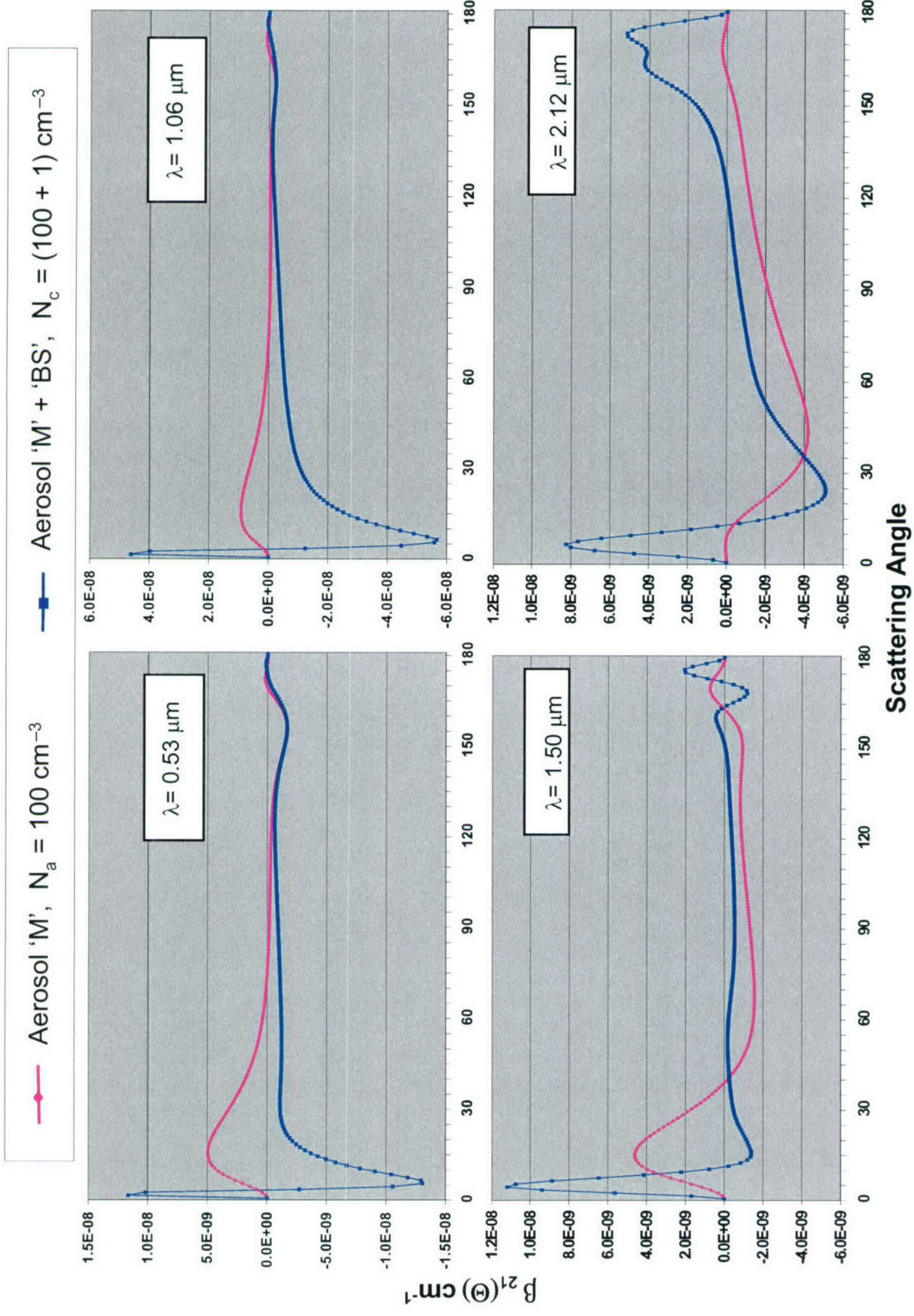


Figure 4.2. Profiles of Linear Polarization Volume Scattering Coefficient at Four Wavelengths. Same as Fig 4.1 except: (Red) Scattering-angle variations of  $\beta_{21,a}(\Theta)$ . (Blue) Scattering-angle variations of  $\beta_{21,c}(\Theta) = [\beta_{21,a}(\Theta) + \beta_{21,b}(\Theta)]$ .

---

\* Explanatory note relating to sign of  $P_L(\Theta)$ : As in Eq (6A),  $P_L(\Theta) = {}^+Q_{\text{sca}}(\Theta)/I_o \sim b_1(\Theta)$ . In order for Rayleigh (blue sky) polarization to be positive – the common convention – the degree of linear polarization varies with  $[-Q_{\text{sca}}(\Theta)]$ , the negative of the 2<sup>nd</sup> Stokes parameter, e.g., [HT, eq 2.17 and Figures 16–18], or [MTL, pp 246, 271]. In all plots of  $\beta_{21}(\Theta)$  shown here, negative values indicate Rayleigh-like polarization. For example, in Figure 4.2, lower right 2.12  $\mu\text{m}$  panel, the polarization of light scattered by the background (red curve) is negative at almost all  $\Theta$ ; this polarization is preferentially perpendicular to the plane of scattering, i.e., Rayleigh-like. For the ambient background plus bio-aerosols (blue curve) the backscatter polarization is dominated by the larger bio-aerosols, i.e., Mie-like, with maxima occurring in ‘bow’ regions near  $\Theta \cong 162^\circ$  and  $\Theta \cong 174^\circ$ .

---

Furthermore, the magnitude of the  $P_L(170)$  signal, for ‘BS’ in either ‘M’ or ‘L’ background, is smaller than the  $P_l(170)$  signal by a factor of twelve at 1.50  $\mu\text{m}$ , but is smaller by only a factor of less than six at 2.12  $\mu\text{m}$ . Such ratios of properties effectively remove the direct dependence of polarimetric property magnitudes on the geometric factors of measurement and the particle number-concentration, but not on the particle type. Since volume scattering coefficients are independent of incident polarization state (Section 2.2), these ratios also effectively emphasize the distinctive angular scattering traits of the aerosols themselves.

From the analyses of the Figures 4.1 and 4.2 curves, along with the Table 4.1 volume backscattering coefficients, it is apparent that SWIR wavelengths offer increased signal-strength at backscattering angles – at least for the aerosol conditions specified in Table 3.1.

Since spherical particles are used here for both the background and bio-aerosols, all  $P_S(\Theta)$  values, i.e., all  $(\beta_{11} - \beta_{22})$ , are necessarily zero ( $a_1 \equiv a_2$ ). Also, the somewhat larger  $P_R(170)$  at 1.50  $\mu\text{m}$  will be discussed in Section 4.2.

Table 4.2 contains  $\Delta\beta_{ij}$  analyses in the near-forward directions where the polarization feature in Figure 4.2 is maximum, specific,  $\Theta = 5^\circ$  for  $\lambda = 1.50 \mu\text{m}$ ,  $\Theta = 6^\circ$  for  $\lambda = 2.12 \mu\text{m}$ . The enhancement in intensities,  $P_l(5,6)$  over  $P_l(170)$  values in Table 4.1, is clearly evident. From Figure 4.1, the effect of Mie-scattering on near-forward intensity is even more distinct in the visible and near-infrared. The enhanced diffraction of visible (0.53  $\mu\text{m}$ ) and near-infrared (1.06  $\mu\text{m}$ ) light around the ‘BS’ spheres ( $r_{\text{eff}} = 4.36 \mu\text{m}$ , Table 3.1) leads to the nearly order-of-magnitude enhancement in  $\beta_{11,c} (\cong 0^\circ)$ , and also in  $\Delta\beta_{11} (\cong 0^\circ)$ , over that occurring at either of the SWIR wavelengths, 1.50 or 2.12  $\mu\text{m}$ . This forward enhancement is caused by particles larger than the illuminating wavelength scattering preferentially forward – the Mie-scattering pattern. At  $\Theta = 0^\circ$ ,  $P_l$  varies as  $(2\pi r_{\text{eff}}^2/\lambda)^2$  [BH, pp 110, 111; also MTL, eq (7.16) and Figure 7.3], which is in accord with the  $\beta_{11,c}(0^\circ)$ -values in Figure 4.1.

Also evident in Table 4.2 is the larger (relative to  $\Theta = 170^\circ$ ) partial linear polarization signal at the near-forward directions. However, relative to intensity, the  $P_L(5,6)$  signals are about 300 times smaller than near-forward  $P_l$  signals (the polarization state of forward scattering is largely unchanged).

Though forward scattering features are not readily measured in standoff configurations like that seen in Figure 1.1, for more localized bio-aerosol monitoring scenarios, considered in Section 5.2.2, the large forward-scattering intensity increase in the visible recommends such wavelengths for any remote aerosol detection technique based on diffraction or on small- $\Theta$  refractions. In distinction to the backscatter region, the near-forward signal strengths at 1.50  $\mu\text{m}$  are somewhat

greater than at 2.12  $\mu\text{m}$ . Regarding spectral variation in environmental signal-strength, the conclusion is that for relatively large bio-aerosol particles contained in relatively small-particle backgrounds, maximum near-forward signal for any intensity-related polarimetric property is at visible or near-infrared (NIR) wavelengths rather than at SWIR wavelengths.

**Table 4.2. Volume Scattering Coefficients ( $10^{-9} \text{ cm}^{-1}$ ) for Spherical Particles at Near-Forward Angles  $\Theta = 5$  or  $6^\circ$  for Various Polarimetric Properties.**

Background aerosols: maritime ‘M’ and continental ‘L’ each of concentration  $N_a = 100 \text{ cm}^{-3}$ . Bio-aerosol: ‘BS’ of concentration  $N_b = 1 \text{ cm}^{-3}$ . All particles are spheres of size distributions as in Fig 3.1.

Bkg	Wavelength	$\lambda = 1.50 \mu\text{m}$ ( $\Theta = 5^\circ$ )			$\lambda = 2.12 \mu\text{m}$ ( $\Theta = 6^\circ$ )		
		$ \beta_{ij,c} - \beta_{ij,a}  = \Delta\beta_{ij} \equiv \beta_{ij,b}$	$ \beta_{ij,c} - \beta_{ij,a}  = \Delta\beta_{ij} \equiv \beta_{ij,b}$	$ \beta_{ij,c} - \beta_{ij,a}  = \Delta\beta_{ij} \equiv \beta_{ij,b}$	$ \beta_{ij,c} - \beta_{ij,a}  = \Delta\beta_{ij} \equiv \beta_{ij,b}$	$ \beta_{ij,c} - \beta_{ij,a}  = \Delta\beta_{ij} \equiv \beta_{ij,b}$	$ \beta_{ij,c} - \beta_{ij,a}  = \Delta\beta_{ij} \equiv \beta_{ij,b}$
‘M’	$P_I \sim \beta_{11}$	5050.00	1510.00	<b>3540.00</b>	3290.00	760.00	<b>2530.00</b>
‘M’	$P_L \sim \beta_{21}$	10.74	1.69	<b>9.05</b>	8.26	0.05	<b>8.21</b>
‘M’	$P_N \sim (\beta_{11} - \beta_{22})$	0.00	0.00	<b>0.00</b>	0.00	0.00	<b>0.00</b>
‘M’	$P_R \sim \beta_{43}$	-155.00	-9.61	<b>145.39</b>	-109.00	-4.87	<b>104.13</b>
‘L’	$P_I \sim \beta_{11}$	3742.00	199.70	<b>3542.30</b>	2600.00	67.42	<b>2532.58</b>
‘L’	$P_L \sim \beta_{21}$	8.94	-0.10	<b>9.04</b>	8.05	-0.16	<b>8.21</b>
‘L’	$P_N \sim (\beta_{11} - \beta_{22})$	0.00	0.00	<b>0.00</b>	0.00	0.00	<b>0.00</b>
‘L’	$P_R \sim \beta_{43}$	-146.00	-0.68	<b>145.32</b>	-104.50	-0.25	<b>104.25</b>

The overall conclusion regarding wavelength sensitivity is that at backward scattering angles SWIR wavelengths are better than visible or NIR for detecting relatively large particles. For remote sensing employing forward scattering directions, the opposite is true; visible and NIR signals are stronger than those at SWIR wavelengths. Since outdoor standoff detection (implying backscatter measurements) is the application of primary interest in this report, the research considered herein primarily emphasizes the SWIR wavelengths.

#### 4.1.2 Matrix Element Sensitivity

For spherical particles or randomly oriented spheroids illuminated by  $+45^\circ$  linearly polarized light,  ${}^+I_{\text{inc}} = [1, 0, 1, 0]^T I_o$ , the four Stokes parameters of the scattered light vector  ${}^+I_{\text{sca}}(\Theta) = [{}^+I_{\text{sca}}(\Theta), {}^+Q_{\text{sca}}(\Theta), {}^+U_{\text{sca}}(\Theta), {}^+V_{\text{sca}}(\Theta)]^T$  are simply proportional to four different non-zero scattering matrix elements (Appendix A.2). For incident magnitude  $I_o$ , in the normalized matrix form of Eq (2A), this means  ${}^+I_{\text{sca}}(\Theta) = [a_1(\Theta), b_1(\Theta), a_3(\Theta), -b_2(\Theta)]^T I_o$ . So far, in terms of Eq (6A), only  $a_1(\Theta)$  and  $b_1(\Theta)$  have been used; in terms of volume scattering coefficients, only  $\beta_{11}(\Theta)$  and  $\beta_{21}(\Theta)$ . Also, for spheres,  $a_1(\Theta) \equiv a_2(\Theta)$ , so that incident polarization of  $0^\circ$  (parallel to the scattering plane,  ${}^P I_{\text{inc}} = [1, 1, 0, 0]^T I_o$ ) does not enhance the aerosol polarimetric information beyond that provided by  $P_I$  and  $P_L$ .

Additional polarimetric properties based on  $a_3(\Theta)$  and  $b_2(\Theta)$  can be developed. In volume scattering coefficient terminology, these involve  $\beta_{33}$  and  $\beta_{43}$ . To enhance detection of bio-aerosols, any additional polarimetric property should result in a value of  $\Delta\beta_{ij}$  that is: 1) to a large extent independent of  $P_I$  and  $P_L$ , and 2) greater in magnitude than the smaller of these two, i.e., greater than the  $\Delta\beta_{21}$  cases in Tables 4.1 and 4.2.

The additional information comes from  ${}^+U_{\text{sca}}$  or  ${}^+V_{\text{sca}}$ . In the backward (bwd) scattering region ( $140^\circ < \Theta < 180^\circ$ ), values of the diagonal scattering-matrix elements,  ${}^+U_{\text{sca}}(\text{bwd}) \sim a_3(\text{bwd})$  in particular, are reduced due to even small amounts of absorption by scattering particles. In the forward (fwd) scattering region ( $0^\circ < \Theta < 40^\circ$ ), the change in polarization state of incident linear polarized light is expected to be relatively small due mainly to the large diffraction contribution to the forward peak. In effect,  ${}^+U_{\text{sca}}(\text{fwd}) \cong {}^+I_{\text{sca}}(\text{fwd})$  and  ${}^+Q_{\text{sca}}(\text{fwd}) \ll {}^+I_{\text{sca}}(\text{fwd})$ . Therefore, any new and pseudo-independent information in the scattered light vector from spherical particles resulting from  $+45^\circ$  polarized incident light is not expected to be from  ${}^+U_{\text{sca}}$  in either bwd or fwd regions. Rather, it is expected to be from  ${}^+V_{\text{sca}}$ .

In terms of the normalized scattering matrix elements, new information is therefore in  $b_2$  (vis-à-vis  $a_3$ ). The  $b_2$  element is especially sensitive to change in particle refractive index – both the real and imaginary parts [see MTL, plate 9.6]. The polarimetric property associated with  ${}^+V_{\text{sca}}(\Theta)$  is  $P_R(\Theta)$ , here called retardation because the distinguishing element of the quarter-wave plate retarder is  $b_2$  [e.g., CO, Section 5.3, eq 28]. From Eq (6C), it is expressed in terms of the associated volume scattering coefficient as  $P_R(\Theta) = [V/R^2] \beta_{43}(\Theta)$ . Presented in Table 4.1 ( $\Theta = 170^\circ$ ) and Table 4.2 ( $\Theta = 5$  or  $6^\circ$ ) are analyses of the  $\beta_{43}$  environmental signal. As expected, the values of  $\Delta\beta_{43}$  in these environment-only sensitivity analyses are identically  $\beta_{43,b}$ , i.e., are the same for either ‘M’ or ‘L’ backgrounds. What is different is that for both scattering angles–near-forward and near-backward—the  $P_R$  property has somewhat greater signal strength at  $1.50 \mu\text{m}$  than at  $2.12 \mu\text{m}$ . (The physical interpretation of  $P_R$  is given in Section 4.3.)

Probability-of-detection (PDE), introduced in Section 1.2, is directly related to the environmental signal, i.e., to the values of  $\Delta\beta_{ij}$  ( $= \beta_{ij,b}$ ). From Table 4.1, therefore, a backscatter SWIR-wavelength SPADE configuration would have larger PDE using, individually, the  $P_L$  property vis-à-vis the  $P_R$  property. Considered as independent measures of a common polarimetric property,  $P_L$  and  $P_R$  used together would hardly increase the combined PDE. Specifically, at  $\lambda = 2.12 \mu\text{m}$  with the ‘M’ background,  $\{[\Delta\beta_{11}(170)]^2 + [\Delta\beta_{21}(170)]^2\}^{1/2} = 26.10 \times 10^{-9} \text{ cm}^{-1}$ , versus  $25.72 \times 10^{-9} \text{ cm}^{-1}$  using  $\Delta\beta_{11}(170)$  alone. Including  $\Delta\beta_{21}(170)$ , in spite of the prominent backscatter feature in Figure 4.1, only enhances the combined signal-strength by  $1\frac{1}{2}\%$  over that attributable to intensity alone. (As will be seen in Section 4.2, any non-sphericity of particles decreases the  $P_L$  backscatter polarization feature, further decreasing the combined  $\Delta\beta(170)$  signal.) Similarly, using the retardation polarization signal, i.e.,  $\Delta\beta_{43}$ , along with  $\Delta\beta_{11}$  results in  $26.45$  vs.  $25.72 \times 10^{-9} \text{ cm}^{-1}$ , which is still only a  $3\%$  increase over  $P_L$  alone. From the Table 4.1 information, the best two-property enhancement is at  $1.50 \mu\text{m}$  using  $P_R$  and  $P_L$  – an  $8\frac{1}{2}\%$  increase.

At the near-forward scattering angles in Table 4.2,  $\Delta\beta_{21}$  has even less environmental signal relative to  $\Delta\beta_{11}$  than at the far-backscatter angle, and even the substantial size of  $\Delta\beta_{43}$  does not increase combined intensity and retardation environmental signal by more than  $0.1\%$  over intensity ( $\Delta\beta_{11}$ ) alone. But, each polarimetric property emphasizes a different aerosol physical characteristic, especially when measured at the most discriminating scattering angles. As long as signal-to-noise values are sufficient (Section 5.2), then each polarimetric property, e.g.,  $P_R \sim \Delta\beta_{43} = \beta_{43,b}$ , does provide new information useful in identifying the scattering particles, that is not shared in common with other properties. Referring specifically to Appendix E.2 and allowing that these relationships are not exclusive, the basic associations between aerosol polarimetric properties and aerosol physical characteristics are the following.

Backscattering angles –  $P_L$  : size,  $P_R$  : size,  $P_N$  : shape,  $P_R$  : index  
 Forward scatter angles –  $P_L$  : size,  $P_R$  : shape,  $P_N$  : shape,  $P_R$  : size

Forward scatter angles offer less diverse particle information overall. (More detailed interpretations of the scattering matrix elements are in Appendix E.)

Examining the results of scattering computations for spherical particles in Tables 4.1 and 4.2, the conclusion is that the scattering matrix elements and their related polarimetric properties ranked by environmental signal from highest to lowest are:  $a_1 : P_1$ ,  $b_2 : P_R$ ,  $b_1 : P_L$ , in both the backward and forward scatter regions. (Non-sphericity elements and property,  $(a_1 - a_2) : P_N$ , cannot yet be ranked for the general aerosol case because only spherical particles have so far been considered. In Section 4.2, the utility of  $P_N$  is shown.)

#### 4.1.3 Concentration Sensitivity

It is to be expected from Eqs (5B) and (8B) that  $\beta_{ij,b}(\Theta) \sim N_b$ . In Figure 4.3 this is confirmed, for both the  $P_1$  and  $P_L$  properties; vertical separation between green and red curves vs. separation between blue vs. red curves. Using as an example the  $P_1$  property at  $\lambda = 1.50 \mu\text{m}$ , for bio-aerosol number-concentrations of  $N_b = 100 \text{ cm}^{-3}$  (not shown in Figure 4.3), 10 and  $1 \text{ cm}^{-3}$  with ‘M’ background of  $N_a = 100 \text{ cm}^{-3}$ , the computation results are:  $\beta_{11,c}(170) = 2.11 \times 10^{-6}$ ,  $2.19 \times 10^{-7}$ , and  $2.98 \times 10^{-8} \text{ cm}^{-1}$ , respectively (numerical values from scattering code output files). For the ‘M’ background alone  $\beta_{11,a}(170) = 8.71 \times 10^{-9} \text{ cm}^{-1}$  (Table 4.1). From Eqs (8),  $\Delta\beta_{11}(170) = \beta_{11,b}(170) = 2101.3 \times 10^{-9}$ ,  $210.3 \times 10^{-9}$ ,  $21.1 \times 10^{-9} \text{ cm}^{-1}$ , correlating precisely with the corresponding  $N_b$ -values – as they must.

In Figure 4.3, similarly, the values of  $\Delta\beta_{21}(\Theta)$ , and thus the  $P_L$  property values, vary directly with number-concentration of bio-aerosol particles. At  $1.50 \mu\text{m}$  for the same values of  $N_b = 100$ , 10, and  $1 \text{ cm}^{-3}$  with background the same as before, corresponding results are:  $\beta_{21,c}(170) = -16.61 \times 10^{-8}$ ,  $-15.92 \times 10^{-9}$ , and  $-9.06 \times 10^{-10} \text{ cm}^{-1}$ . For ‘M’ background alone  $\beta_{21,a}(170) = 7.63 \times 10^{-10}$  (as in Table 4.1). From Eqs (8),  $\beta_{21,b}(170) = 166.87 \times 10^{-9}$ ,  $16.69 \times 10^{-9}$ ,  $1.67 \times 10^{-9} \text{ cm}^{-1}$ , again varying directly with the  $N_b$  number-concentration values.

As expected, all environmental signal strengths, the  $\Delta\beta$ s in Eq (9), vary directly with the number-concentration of the bio-aerosol  $N_b (\text{cm}^{-3})$ . The obvious corollary is that, for a SPADE area surveillance system, bio-aerosols are most confidently detected nearest to the release point.

It is likewise evident from Eqs (5B) that  $\beta_{ij,b}(\Theta) \sim \langle C_{\text{sca}} \rangle_b$ . This total (all-angle) quantity, the ensemble average scattering cross section  $\langle C_{\text{sca}} \rangle = f(\lambda; r_{\text{mo}}, n(r), m)$  [e.g., BH, eq 4.61; also SP, eq 22.13]. Therefore, at a given wavelength, and for fixed values of refractive index, mean size, and size distribution function  $n(r)$  of bio-aerosols, then the environmental signal varies directly as the product  $N_b \langle C_{\text{sca}} \rangle_b$ , called here the *total volume scattering coefficient*, which is further explained in Section 6.2. In Section 6.3 a procedure is given for separating the two quantities using single and bi-spectral measurements.

The concept-of-operations for any SPADE configuration is to monitor the ambient background aerosol concentration including its natural temporal variation. It is necessary to discriminate between these natural background variations ( $N_a + \Delta N_a$ ) and the effect of introducing bio-aerosols ( $N_a + N_b$ ). In simulations reported here the concentration mixing ratio is  $R_N = N_b/N_a = 10^{-2}$ . The question now is: Can  $N_b/N_a = 10^{-2}$  be distinguished from  $\Delta N_a/N_a = 10^{-2}$ ?

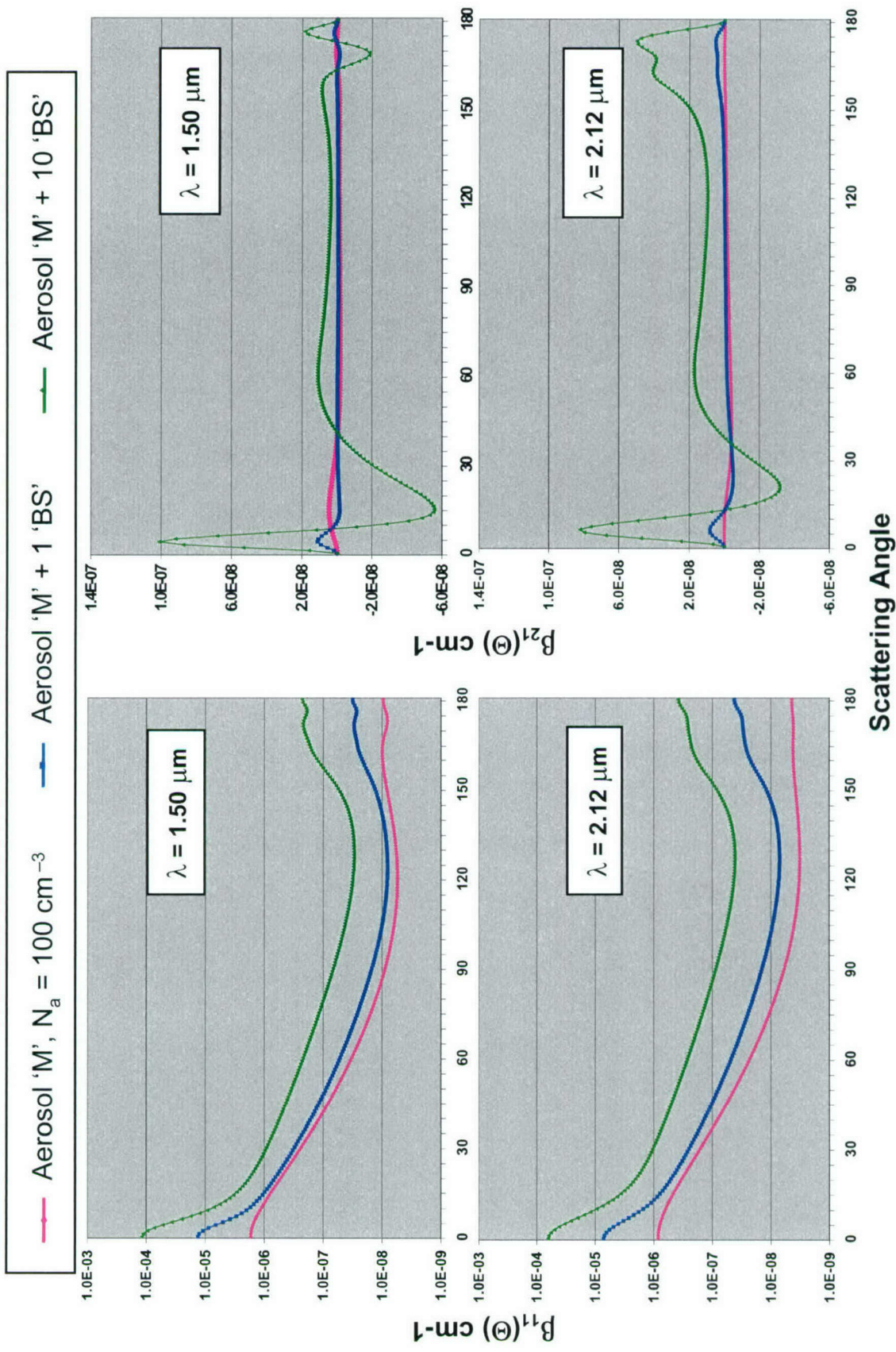


Figure 4.3. Profiles of Intensity and Linear Polarization Volume Scattering Coefficients for Two Bio-Aerosol Number-Concentrations;  $\lambda = 1.50 \mu\text{m}$  (Top) and  $\lambda = 2.12 \mu\text{m}$  (Bottom). Same aerosols as Figures 4.1 and 4.2 except (Blue) number-concentration for 'BS' bio-aerosol  $N_b = 1 \text{ cm}^{-3}$ ,  $R_N = 10^2$ ; (Green)  $N_b = 10 \text{ cm}^{-3}$ ,  $R_N = 10^1$ .

To simulate such variation, the background aerosol concentration is allowed to increase from  $N_a = 100$  to  $(N_a + \Delta N_a) = 101 \text{ cm}^{-3}$ . But the newly added background particles  $\Delta N_a$  are assigned the same mode radius and size distribution as the bio-aerosols in Table 3.1, in particular,  $r_{mo} = 1.75 \mu\text{m}$  and the same ‘BS’-values for A, B,  $\alpha$ , and  $\gamma$ . But, the new background aerosols remain compositionally the same as the ambient background—same refractive index. Even with the same refractive index (and illumination wavelength), these new particles affect scattering through the scattering cross section (mentioned above) and through the scattering matrix elements themselves [e.g. MTL, p 139], which have dependencies on  $r_{mo}$  and  $n(r)$ . Basically, larger particles scatter more efficiently and proportionally scatter more in forward directions. These effects enhance  $\beta$ -values and affect their angular profiles beyond any straight-forward increase due to increased number-concentration (in the present case,  $N_a + \Delta N_a = 101 \text{ cm}^{-3}$ ).

The effects on  $\beta_{11}(\Theta)$  and  $\beta_{21}(\Theta)$ , at the two SWIR wavelengths, are shown in Figure 4.4 for the continental ‘L’ type of background aerosol. As expected, the additional  $\Delta N_a = +1 \text{ cm}^{-3}$  ‘large’ background aerosol does increase the intensity at all scattering angles (green-curve versus red-curve) – but most strongly in the near-forward directions because of enhanced diffraction and more near-axial transmission by larger particles.

The second incrementing by  $N_b$ ,  $N_c = N_a + \Delta N_a + N_b = 102 \text{ cm}^{-3}$ , the blue curves in Figure 4.4, simulates adding bio-aerosol to a large-particle enhanced background condition. Particularly at  $2.12 \mu\text{m}$ , the presence of the bio-aerosol is still easily distinguished in both  $\beta_{11}(\Theta)$  and  $\beta_{21}(\Theta)$ , at least in the backscatter region due to the larger bio-aerosol refractive index. The decision sequence to distinguish ambient background variation from bio-aerosol introduction, based on results like those in Figure 4.4, is explained in Section 6.

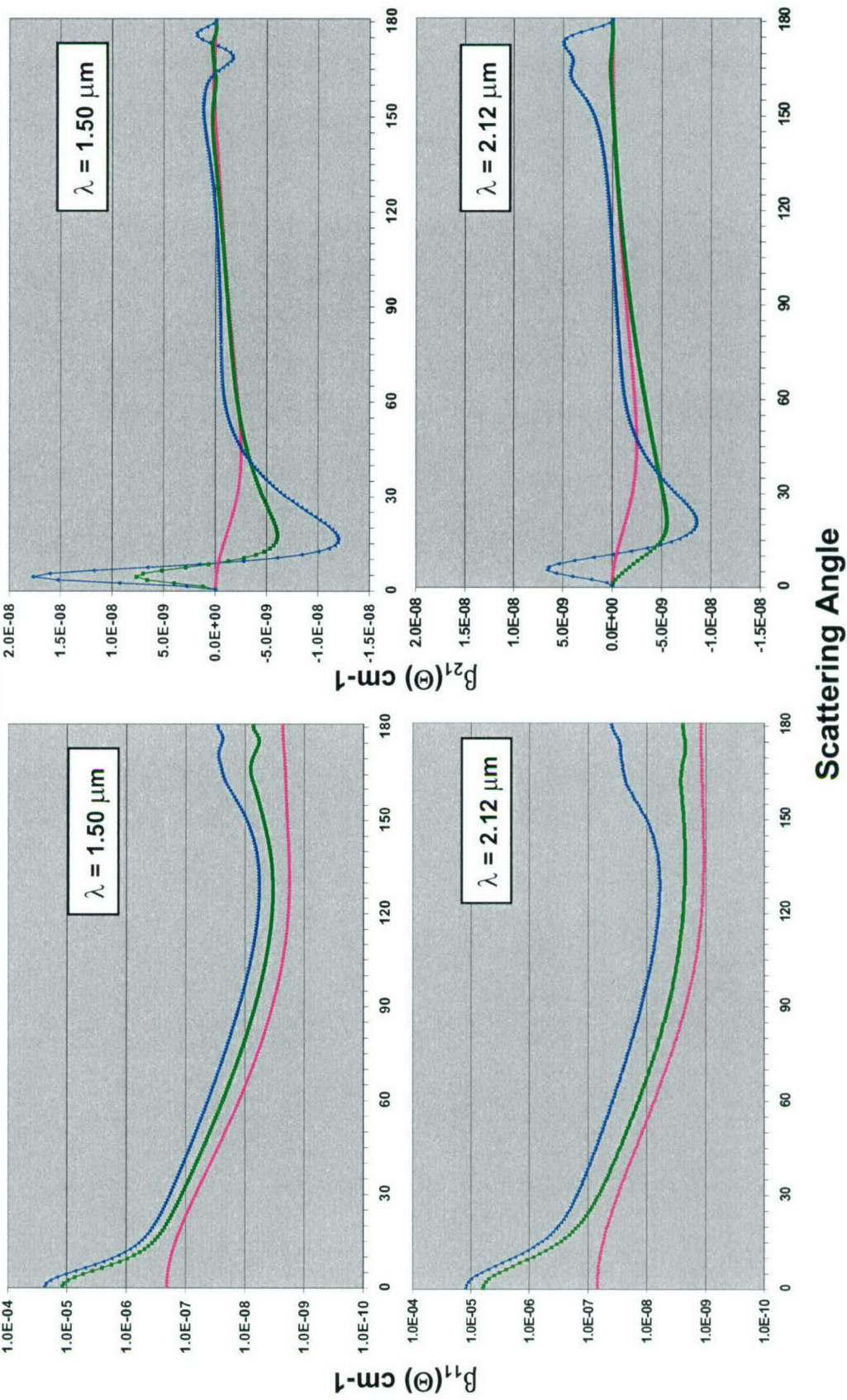
The conclusion is that the environmental signal strength increases directly with number-concentration. Similarly it varies directly with the average scattering cross section, which involves physical and optical properties of the scattering particles. It is also found that distinctive polarimetric features, based primarily on different refractive indices for comparably sized aerosol particles, allow discrimination between similar concentration ratios resulting from adding large background particles vs. adding bio-aerosols.

## 4.2 NON-SPHERICAL PARTICLES

More realistically, the bio-aerosol particles are expected to be somewhat non-spherical, e.g., individual spores in the ‘BS’ cluster or anthrax colony shown in Figure 3.2. The shape of the individual ‘BS’ spores that make up the cluster is similar to a prolate spheroid–polar axis longer than equatorial axis—with axis ratio  $\epsilon = 1.0/2.0$  ( $= 0.25/0.50$  [HPC, Figure 2(a)]). The ‘BS’ cluster itself is also prolate but with axis ratio  $\epsilon \approx 1.0/1.2$  (Figure 3.2(a) measurements: 4.7/5.5). The individual *Bacillus anthracis* spores pictured in Figure 3.2(b) are also prolate with  $\epsilon \approx 1.0/1.5$ ; the elongated spores have  $\epsilon \approx 1.0/5.0$ .

A polarimetric property quantifying non-sphericity is  $P_N$ , which from Eq (6C) is determined as  $(\beta_{11} - \beta_{22})$ . It is emphasized that only the bio-aerosol, present in amount  $N_b = 1 \text{ cm}^{-3}$ , is non-spherical; the  $N_a = 100 \text{ cm}^{-3}$  ambient aerosols remain spherical in all cases. Although  $P_N$  is the primary metric of interest in this section, the introduction of non-spherical bio-aerosols also affects the  $P_L$  and  $P_R$  signals and modifies the angular profile of the  $P_I$  signal as well. Since the non-spherical bio-aerosol particles are randomly oriented, then the common ‘bow’ and ‘glory’ backscatter features of spheres, e.g.,  $\beta_{21}(\Theta > 160)$ , right panels of Figures 4.3 (green curves) and 4.4 (blue curves), are compromised by the variety of surface curvatures of non-spherical particles.

— Aerosol 'L',  $N_a = 100 \text{ cm}^{-3}$  — Aerosol 'L' + 1 lg 'L' — Aerosol 'L' + 1 lg 'L' + 1 'BS'



## Scattering Angle

Figure 4.4. Profiles of Intensity and Linear Polarization Volume Scattering Coefficients for Bio-Aerosol Introduction vs. Increased Ambient Background Aerosol;  $\lambda = 1.50 \mu\text{m}$  (Top) and  $\lambda = 2.12 \mu\text{m}$  (Bottom). (Red) Ambient background – continental 'L' in Table 3.1 ( $N_a = 100 \text{ cm}^{-3}$ ). (Green) Same 'L' ambient aerosol as (Red) plus  $N_b = 1 \text{ cm}^{-3}$  of 'L' type aerosol distributed like 'Bio-Aerosol' in Figure 3.1. (Blue) Same 'L' ambient aerosol as (Red) plus  $N_b = 1 \text{ cm}^{-3}$  of 'L' plus  $N_b = 1 \text{ cm}^{-3}$  of 'L' plus  $N_b = 1 \text{ cm}^{-3}$  of 'BS' aerosol in Table 3.1, both distributed like 'Bio-Aerosol' in Figure 3.1. All particles spherical.

Alternatively, polarimetric properties that emphasize non-spherical shape are strengthened, in particular the volume scattering coefficient difference that constitutes  $P_N$ .

Plotted in Figure 4.5 are the angular profiles of  $\beta_{11,c}(\Theta)$  and  $\beta_{21,c}(\Theta)$  for oblate or prolate spheroid bio-aerosol particles collocated with continental ‘L’ ambient background aerosols. The extent of bio-aerosol non-sphericity is indicated by the departure of the spheroid axis ratio  $\varepsilon$  from the sphere value of  $\varepsilon = 1.0/1.0$ . Profiles for various  $\varepsilon$ -values (different colors) are plotted in Figure 4.5 and for comparison profiles for spherical bio-aerosol (blue) are included.

The ‘flattening’ of the intensity profile within the backscattering range ( $70^\circ < \Theta < 170^\circ$ ) is evident in Figure 4.5, for both oblate (bun-like) and prolate (roll-like) spheroids [also see MTL, plate 10.7]. For prolate spheroids, backscatter polarization  $\beta_{21,c}(\Theta)$  diminishes markedly for even the smallest departure from sphericity, as is shown in Figure 4.5 ( $\varepsilon = 1.0/1.3$ ). In Figure 4.5 the vertical difference between the blue and any other color quantifies the effect on  $\Delta\beta_{11} (= \beta_{11,b})$  and  $\Delta\beta_{21} (= \beta_{21,b})$  attributable to the bio-aerosol particle non-sphericity.

In Table 4.3 are presented environmental signal analyses at a far-backscatter angle, i.e.,  $\Delta\beta_{ij}(170)$ , for prolate ‘BS’ in the continental ‘L’ background—the ‘BS’ prolate spheroids having  $\varepsilon = 1.0/1.1$ ,  $1.0/1.4$ , and  $1.0/2.0$ . Comparable values for spherical ‘BS’,  $\varepsilon = 1.0/1.0$ , are in the lower portion of Table 4.1. Although tabulations for oblate ‘BS’ are not included in this report, relative values for oblate spheroids of comparable eccentricities can be seen in Figure 4.5.

**Table 4.3. Volume Scattering Coefficients ( $10^{-9}$  cm $^{-1}$ ) for Prolate Spheroid Bio-Aerosols at Backscatter Angle  $\Theta = 170^\circ$  for Various Polarimetric Properties.**

Background aerosol is spherical continental ‘L’, concentration  $N_a = 100$  cm $^{-3}$ . Bio-aerosol is ‘BS’,  $N_b = 1$  cm $^{-3}$ . ‘BS’ particles have  $\varepsilon = 1.0/1.1$ ,  $1.0/1.4$ , and  $1.0/2.0$ . Particle size distributions as in Figure 3.1.

$\varepsilon$	Wavelength	$\lambda = 1.50$ $\mu\text{m}$			$\lambda = 2.12$ $\mu\text{m}$		
		$ \beta_{ij,c} - \beta_{ij,a}  = \Delta\beta_{ij} \equiv \beta_{ij,b}$			$ \beta_{ij,c} - \beta_{ij,a}  = \Delta\beta_{ij} \equiv \beta_{ij,b}$		
1.0/1.1	$P_1 \sim \beta_{11}$	23.82	2.18	<b>21.64</b>	23.35	1.20	<b>22.15</b>
1.0/1.1	$P_L \sim \beta_{21}$	3.75	0.15	<b>3.60</b>	3.68	– 0.01	<b>3.69</b>
1.0/1.1	$P_N \sim (\beta_{11} - \beta_{22})$	3.70	0.00	<b>3.70</b>	3.82	0.00	<b>3.82</b>
1.0/1.1	$P_R \sim \beta_{43}$	3.78	0.09	<b>3.69</b>	3.80	0.02	<b>3.78</b>
1.0/1.4	$P_1 \sim \beta_{11}$	10.49	2.18	<b>8.31</b>	14.63	1.20	<b>13.43</b>
1.0/1.4	$P_L \sim \beta_{21}$	0.45	0.15	<b>0.30</b>	0.37	– 0.01	<b>0.38</b>
1.0/1.4	$P_N \sim (\beta_{11} - \beta_{22})$	3.52	0.00	<b>3.52</b>	5.61	0.00	<b>5.61</b>
1.0/1.4	$P_R \sim \beta_{43}$	– 0.06	0.09	<b>0.15</b>	– 0.43	0.02	<b>0.41</b>
1.0/2.0	$P_1 \sim \beta_{11}$	6.65	2.18	<b>4.47</b>	9.41	1.20	<b>8.21</b>
1.0/2.0	$P_L \sim \beta_{21}$	0.31	0.15	<b>0.16</b>	0.71	– 0.01	<b>0.72</b>
1.0/2.0	$P_N \sim (\beta_{11} - \beta_{22})$	1.20	0.00	<b>1.20</b>	2.24	0.00	<b>2.24</b>
1.0/2.0	$P_R \sim \beta_{43}$	0.09	0.09	<b>0.00</b>	– 0.15	0.02	<b>0.13</b>

The specific polarimetric property employed in this research to assess the influence of non-sphericity is  $P_N(\Theta) \sim [\beta_{11}(\Theta) - \beta_{22}(\Theta)]$ , defined in Eq (6C). For the SPADE configuration ( $\Theta =$

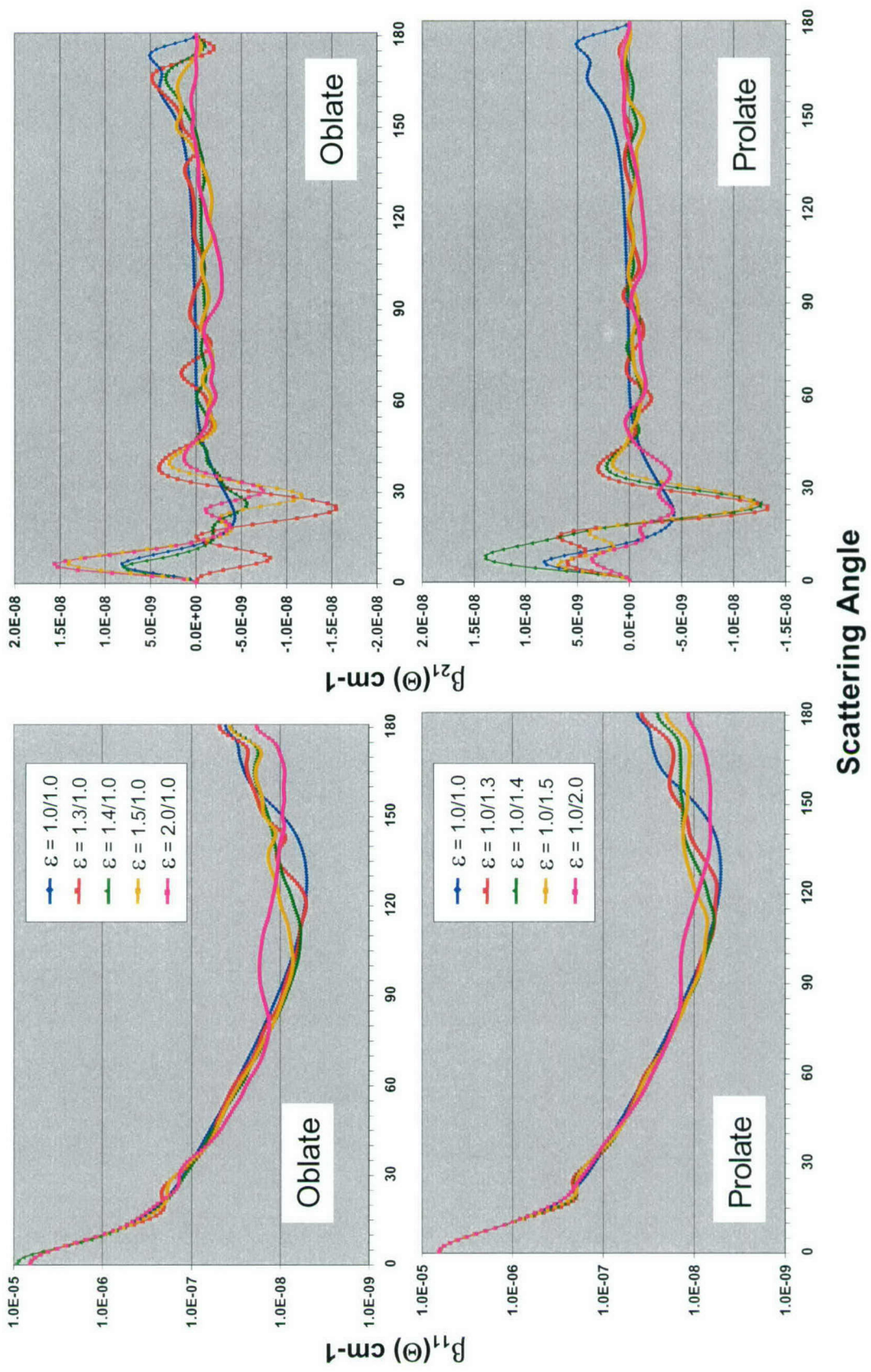


Figure 4.5. Profiles of Volume Scattering Coefficients for Five Axis Ratios of Oblate and Prolate Bio-Aerosols: Intensity (Left) and Linear Polarization (Right), at  $\lambda = 2.12 \mu\text{m}$ . Colors indicate axis ratio  $\epsilon$  for oblate (Top) and prolate (Bottom) spheroid bio-aerosol 'BS' ( $N_b = 1 \text{ cm}^{-3}$ ) and spherical ambient background aerosol 'L' ( $N_a = 100 \text{ cm}^{-3}$ ).

$170^\circ$ ) simulated in Table 4.3, the non-sphericity indicator  $P_N(170)$  for prolate ‘BS’ is significantly greater than zero and is the polarimetric parameter in magnitude second-only to the intensity  $P_I$  for all the prolate spheroid shapes (all  $\epsilon \leq 1.0/1.1$ ).

Regarding the responses of other polarimetric properties to  $\epsilon$ , the partial linear polarization signal  $P_L(170)$  at  $\lambda = 1.50 \mu\text{m}$  for prolate ‘BS’ roughly doubles as  $\epsilon$  goes from  $1.0/1.0$  to  $1.0/1.1$ , but then drops rapidly to very small values for more non-spherical particles (cf.  $\beta_{21}$  rows in Table 4.1 for  $\epsilon=1.0/1.0$ , vs.  $\beta_{21}$  rows in Table 4.3 for  $\epsilon=1.0/1.1$ ,  $1.0/1.4$ ,  $1.0/2.0$ ). Likewise, backscattering  $P_I(170)$  signal drops off as  $\epsilon$  departs from unity.

Finally, as seen from the data in Table 4.3, the retardation signal  $P_R(170)$  is strongly reduced as particles become more non-spherical. (The polarimetric property  $P_R$  is investigated further in Section 4.3.) The reduction in both  $P_L(170)$  and  $P_R(170)$  as  $\epsilon$  departs from unity seriously compromises these polarimetric properties as discriminators in standoff configurations.

However, the difference between the first two diagonal elements of the volume scattering matrix is a very sensitive indicator of non-sphericity, especially at the backscattering angles. In Figure 4.6 are depicted the angular profiles of  $[\beta_{11}(\Theta) - \beta_{22}(\Theta)]$  along with the ratio most often used as a non-sphericity index  $a_2(\Theta)/a_1(\Theta) \sim \beta_{22}(\Theta)/\beta_{11}(\Theta)$ . (The ratio emphasizes the polarimetric vs. photometric effects of particle nonsphericity; see Section 6.1.) Non-sphericity is strongly manifest in the backscatter hemisphere. In fact at the lidar angle,  $P_N(180) = [\beta_{11,b}(180) - \beta_{22,b}(180)]$ , like  $a_2(180)/a_1(180)$ , is at its maximum for all non-spherical particles—oblate or prolate—except for the most eccentric prolate spheroids. Whereas particle size tends to sustain the backscatter phase function  $a_1$ , particle shape (non-sphericity) negatively affects  $a_2$  leading to the strong signals seen especially for  $\Theta > 140^\circ$  in Figure 4.5.

A procedure for detecting introduction of non-spherical particles, independent of backscattered light magnitude, is  $P_N(170)/P_I(170) = 1 - a_2(170)/a_1(170)$ , which in Table 4.3 and in lower half of Table 4.1 is seen to increase from 0.00 for spheres to a maximum close to 0.50 for the intermediate prolate values ( $\epsilon \cong 1.0/1.5$ ) before decreasing to 0.25 for ( $\epsilon = 1.0/2.0$ ). At standoff backscatter angles,  $P_N$  is a very useful polarimetric property to confirm non-spherical particle introduction that might otherwise be suspected from the rather flat  $P_I$  signature (seen in Figure 4.5). (Utilization of  $P_N$  in the detection procedure is discussed more completely in Section 6.3).

In Table 4.4 are presented environmental signal analyses for non-spherical particles at the near-forward angles, specific,  $\Delta\beta_{ij}(5$  or  $6$ ), for the same background and prolate bio-aerosol particle conditions as in Table 4.3. The near-forward angles in Table 4.4 are selected based on where (from Figure 4.3) the spherical  $P_L$  signals attain maximum values for  $\lambda = 1.50$  and  $2.12 \mu\text{m}$ , i.e.,  $\Theta = 5^\circ$  and  $\Theta = 6^\circ$ , respectively.

As expected the near-forward  $P_I$  signals are very strong, but the non-sphericity signals, the  $P_N$ -values, are relatively weak. However from Table 4.4, the near-forward retardation signals  $P_R$  remain strong even for the most eccentric ‘BS’ shape ( $\epsilon = 1.0/2.0$ ), contrary to far-backscatter signals (Table 4.3).

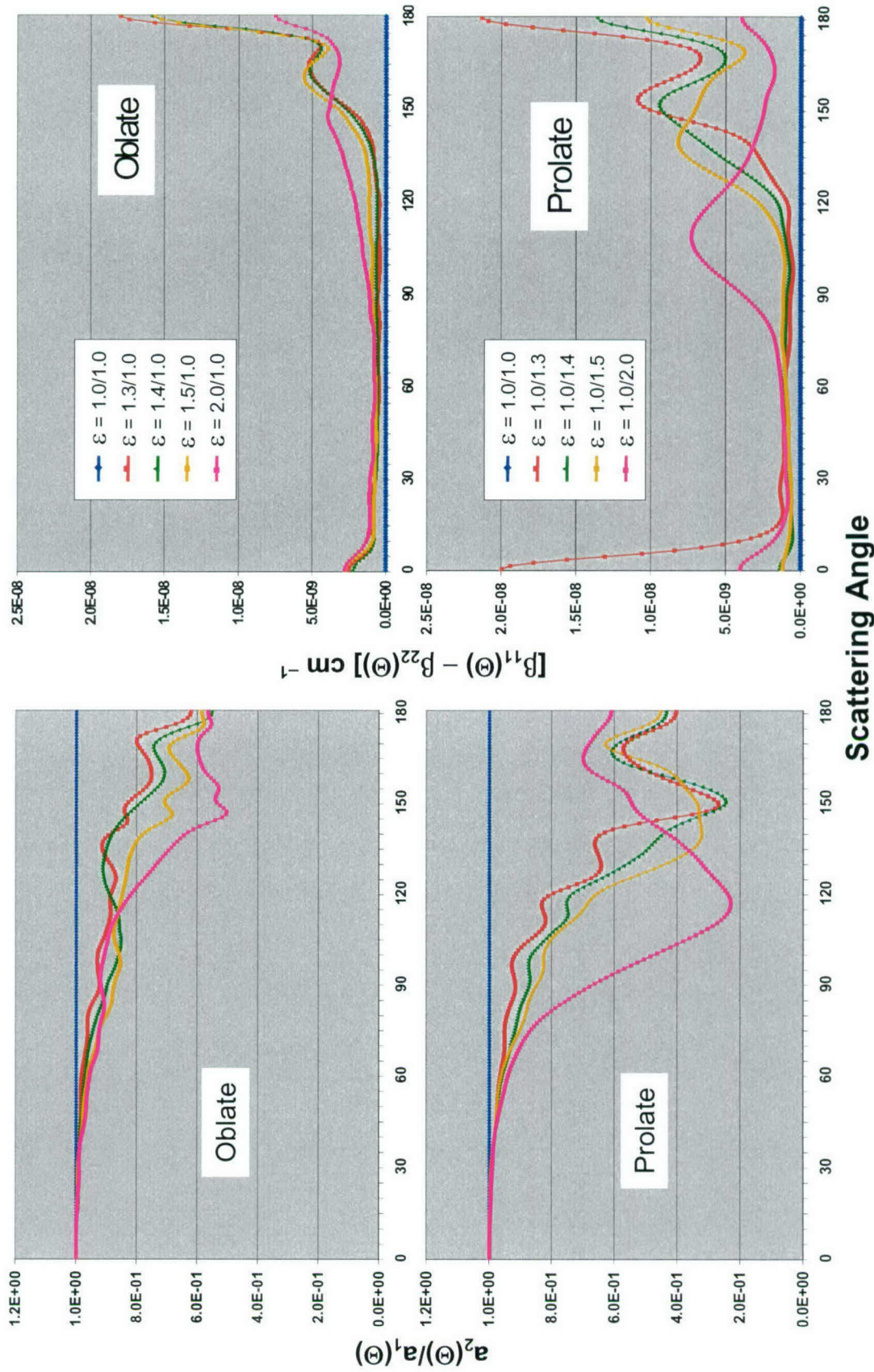


Figure 4.6. Profiles of Non-Sphericity Indicators: Non-Sphericity Ratio  $a_2/a_1$  (Left) and Non-Sphericity Volume Scattering Coefficient (Right), at  $\lambda=2.12\text{ }\mu\text{m}$ . Colors indicate axis ratios  $\varepsilon$  for oblate (Top) and prolate (Bottom) spheroid bioaerosol 'BS' ( $N_b=1\text{ cm}^{-3}$ ) and spherical ambient aerosol 'L' ( $N_a=100\text{ cm}^{-3}$ ).

**Table 4.4 Volume Scattering Coefficients ( $10^{-9} \text{ cm}^{-1}$ ) for Prolate Spheroid Bio-Aerosols at Near-Forward Scattering Angles  $\Theta = 5$  or  $6^\circ$  for Four Polarimetric Properties.**

Background aerosol is spherical continental ‘L’ with  $N_a = 100 \text{ cm}^{-3}$ . Bio-aerosol is ‘BS’,  $N_b = 1 \text{ cm}^{-3}$ . ‘BS’ particles have  $\epsilon = 1.0/1.1, 1.0/1.4$ , and  $1.0/2.0$ . Particle size distributions as in Figure 3.1.

$\epsilon$	Wavelength	$\lambda = 1.50 \mu\text{m}$ ( $\Theta = 5^\circ$ )			$\lambda = 2.12 \mu\text{m}$ ( $\Theta = 6^\circ$ )		
		$ \beta_{ij,c} - \beta_{ij,a}  = \Delta\beta_{ij} \equiv \beta_{ij,b}$			$ \beta_{ij,c} - \beta_{ij,a}  = \Delta\beta_{ij} \equiv \beta_{ij,b}$		
1.0/1.1	$P_I \sim \beta_{11}$	3498.10	199.96	<b>3298.14</b>	2709.20	67.27	<b>2641.93</b>
1.0/1.1	$P_L \sim \beta_{21}$	11.94	-0.10	<b>12.04</b>	12.54	-0.16	<b>12.70</b>
1.0/1.1	$P_N \sim (\beta_{11} - \beta_{22})$	-3.70	0.00	<b>3.70</b>	1.04	0.00	<b>1.04</b>
1.0/1.1	$P_R \sim \beta_{43}$	-99.32	-0.68	<b>98.64</b>	-109.37	-0.25	<b>109.12</b>
1.0/1.4	$P_I \sim \beta_{11}$	3948.20	199.96	<b>3748.24</b>	2609.30	67.27	<b>2542.03</b>
1.0/1.4	$P_L \sim \beta_{21}$	-4.69	-0.10	<b>4.59</b>	13.14	-0.16	<b>13.30</b>
1.0/1.4	$P_N \sim (\beta_{11} - \beta_{22})$	1.00	0.00	<b>1.00</b>	0.79	0.00	<b>0.79</b>
1.0/1.4	$P_R \sim \beta_{43}$	-128.41	-0.68	<b>127.73</b>	-93.06	-0.25	<b>92.81</b>
1.0/2.0	$P_I \sim \beta_{11}$	3372.5	199.96	<b>3172.54</b>	2540.00	67.27	<b>2472.73</b>
1.0/2.0	$P_L \sim \beta_{21}$	4.93	-0.10	<b>5.03</b>	3.51	-0.16	<b>3.67</b>
1.0/2.0	$P_N \sim (\beta_{11} - \beta_{22})$	1.90	0.00	<b>1.90</b>	2.63	0.00	<b>2.63</b>
1.0/2.0	$P_R \sim \beta_{43}$	-94.12	-0.68	<b>93.44</b>	-68.47	-0.25	<b>68.22</b>

Conclusions are now drawn from the environmental signal information for non-spherical, specific, for spheroid bio-aerosols, presented as  $\beta_{ij}(\Theta)$  profiles in Figures 4.5 and 4.6, and as scattering-computation summaries in Tables 4.3 and 4.4. Of the four polarimetric properties presented, intensity  $P_I$  is the best discriminator in both backward and forward scattering directions at both SWIR wavelengths. The next-best discriminator is non-sphericity  $P_N$  in backward, but retardation  $P_R$  in forward directions. Interestingly, partial linear polarization  $P_L$  is a very weak discriminator in backward directions if particles are even slightly non-spherical. In forward directions  $P_L$  has increased magnitude but is there quite small relative to  $P_R$ . Regarding the better of the two SWIR wavelengths, for the conditions of the computations (background  $r_{\text{eff}} = 0.48 \mu\text{m}$ , bio-aerosol  $r_{\text{eff}} = 4.36 \mu\text{m}$ ), at the backward directions the longer SWIR wavelength is somewhat better, whereas at near-forward scattering directions  $1.50 \mu\text{m}$  is better for the two properties  $P_I$  and  $P_R$  that are there dominant.

### 4.3 RETARDATION POLARIMETRIC PROPERTY

Of the polarimetric quantities outlined in Table 2.2,  $P_R$  called retardation (Section 4.1.2) attains the largest environmental signals except for  $P_I$  itself. From Eqs (6A) & (6B), the scattering-angle variation in the retardation property is directly associated with the scattering matrix element  $b_2(\Theta)$ , which relates to  $\beta_{43}(\Theta)$  (see Eq (A.8), Appendix A.6). Element  $b_2$ , and therefore the volume scattering coefficient  $\beta_{43}$ , is associated with the optical constants of the scattering particles – the refractive index  $m = m_{\text{real}} - i m_{\text{imag}}$ . The sensitivity of  $b_2$  to any change in particle refractive index has been recognized and studied [e.g., SI, Figure 7, or VHB, Figure 6 (implicitly due to optical constants)]. In this report the refractive index varies with the wavelength of incident light (refer to Table 3.2) but does not vary with the polarization state of incident light, i.e.,  $m(\lambda)$  is single valued. Thus, no effects are considered of ‘optically active’ particles.

When the aerosol's refractive index (vs. concentration, size, shape) affects the polarization of the scattered beam, the scattering aerosols then function, in general, like a polarizing waveplate retarder – using the optical device analogs mentioned in Appendix E.1. As such, the scattering cross-section portion (Eqs (A.9)) of the volume scattering coefficient  $\beta_{43}$  (equal to  $-\beta_{34}$ ) varies as the optical dimension  $\delta[-]$ , a quantity varying, in turn, as the product ( $m x_{\text{eff}}$ ).

In Figure 4.7 are plotted the scattering-angle profiles of  $\beta_{43}(\Theta)$  for spherical continental 'L' ( $N_a = 100 \text{ cm}^{-3}$ ) background aerosols plus bio-aerosol particles ( $N_b = 1 \text{ cm}^{-3}$ ) of various oblate and prolate non-spherical shapes (various colors); these at both 1.50 and 2.12  $\mu\text{m}$ . Also plotted are the corresponding profiles for the ambient background aerosol 'L' alone (brown curve).

As with any scattering coefficient derived from b-elements in the Eq (2A) matrix,  $\beta_{43}(180) = \beta_{43}(0) = 0$ . Also, in the side-scattering region  $40^\circ < \Theta < 140^\circ$ , the signal is limited – there the bio-plus-background appears to be nearly indistinguishable from the background alone, except for the most eccentric oblate spheroids. For spherical 'BS' (Table 4.1), in the far-backscatter region  $160^\circ < \Theta < 170^\circ$ ,  $\beta_{43} \geq 6.0 \times 10^{-9} \text{ cm}^{-1}$  at 2.12  $\mu\text{m}$  and nearly  $9.0 \times 10^{-9} \text{ cm}^{-1}$  at 1.50  $\mu\text{m}$ . This far-backscatter region is the aerosol 'bow' (as in 'rainbow') region where rays have undergone two refractions and one internal reflection. There the influence of particle refractive index  $m$  is great because of the double transit of the particle interior. However as seen in Table 4.3 and Figure 4.7, any non-sphericity of the 'BS' sharply reduces  $\beta_{43}$  to very small values – only spherical particles form 'bows'. Shape tends to overwhelm index polarimetric effects in non-spherical particle backscatter.

Yet backscatter intensity is at some angles enhanced. The backscatter configuration of SPADE may benefit from increased values of  $P_l(\sim 140)$  brought about by introducing non-spherical particles (as in Figure 4.5, left panels). However, the far-backscatter environmental signal of both  $P_L$  and  $P_R$  especially collapse for prolate spheroids (as in Figure 4.5, lower right panel, and Figure 4.7, right panels). For oblate spheroids (not tabulated in this report, but plotted in Figure 4.7, left panels), in the backscatter region  $150^\circ < \Theta < 175^\circ$ ,  $P_R$  does have significant magnitudes – comparable to the spherical 'BS' (Table 4.1) and is easily distinguished from the near-zero value for the background aerosol alone.

In the near-forward region  $2^\circ < \Theta < 20^\circ$ ,  $P_R$  is especially large for spherical bio-aerosols (Table 4.2) with maximum values of  $\beta_{43} \geq 10.0 \times 10^{-8} \text{ cm}^{-1}$  at 2.12  $\mu\text{m}$ ,  $\geq 14.0 \times 10^{-8}$  at 1.50  $\mu\text{m}$ . Importantly, even for very eccentric spheroid aerosols,  $P_R$  signal strengths are maintained, as Figure 4.7 clearly shows. In fact as given in Table 4.4, the largest  $\beta$ -values except for  $\beta_{11}$  itself occur for all non-spherical shaped bio-aerosols,  $\beta_{43} > 100 \times 10^{-9} \text{ cm}^{-1}$  near  $\Theta = 5^\circ$ .

This strong retardation signal is likely due to the larger bio-aerosol particles functioning as a quarter-waveplate (Appendix E.1, Eq (E.4A)) on rays that transit the particles once while twice being refracted in the near-forward direction. The large near-forward  $b_2$  effect is due to a combination of the bio-aerosol particle size–larger obstacle–and differing index of refraction that affects polarization state change by retarding one electric field component more than the other. A SPADE configuration that can make use of the ratio of properties  $P_R/P_l$  ( $|\beta_{43}|/\beta_{11}$ ) in the near-forward direction should reliably detect the introduction of bio-aerosol.

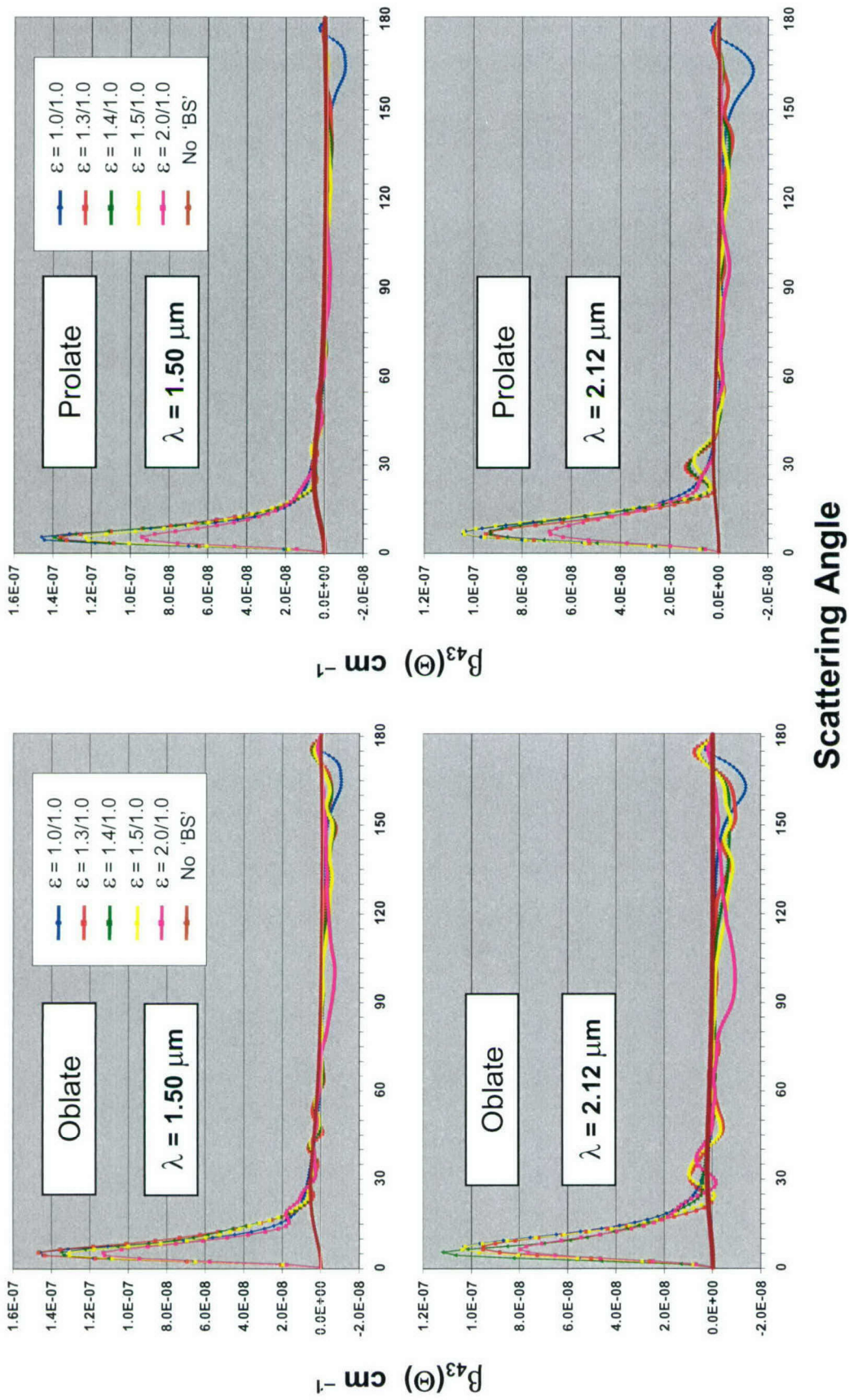


Figure 4.7. Profiles of Retardation Volume Scattering Coefficients at  $\lambda=1.50 \mu\text{m}$  (Top) and  $\lambda=2.12 \mu\text{m}$  (Bottom). Colors indicate axis ratio  $\varepsilon$  for oblate (Left) and prolate (Right) spheroid bio-aerosol 'BS' ( $N_b=1 \text{ cm}^{-3}$ ) and spherical ambient background aerosol 'L' ( $N_a=100 \text{ cm}^{-3}$ ). Brown—ambient background 'L' alone (no 'BS').

## Scattering Angle

The summary conclusion regarding the retardation polarimetric property for non-spherical particles is that shape dominates in the far-backscatter region and refractive index dominates in the near-forward direction. It is evident from the far-backscatter analyses in Tables 4.1 vs. Table 4.3 that as long as the large particles are spherical  $P_R$  signals are quite sizeable, but fall to insignificance if large particles are even slightly prolate. In contrast, the near-forward analyses in Tables 4.2 and Table 4.4 indicate that the retardation signal is immune to large particle shape. The robustness of the near-forward  $\beta_{43,c}$  feature (depicted in Figure 4.7)—in terms of magnitude, immunity to particle eccentricity, scattering-angle extent ( $5^\circ \leq \Theta \leq 15^\circ$ ), and of distinctiveness from the ambient background—all these recommend it as a prime property for any SPADE scenario in which near-forward measurement can be carried out.

## 5. SYSTEM DESIGN CONCEPTS

The SPADE system must accomplish measurements at more than one scattering angle, i.e., at multiple  $\Theta$ s. Operational configurations to achieve multi-angle measurements can be that of one fixed orientation laser-transmitter and one angle-adaptable receiver, as in the standard nephelometer [e.g., QHH, p 535; earlier, HG, pp 1115-1117]. Alternatively, multiple transmitters and receivers that execute, in pairs, coordinated azimuth reorientations are considered in Section 5.3. In any case, the transmitter beam axis and the receiver field-of-view axis are not aligned as they are (very nearly) in the conventional monostatic lidar configuration. In the bistatic configuration these axes are separated by the angle ( $\pi-\Theta$ ) and are within a single plane—the scattering plane—considered here to be the horizontal plane.

In this chapter, first, the lidar equation is developed in Section 5.1 for the variable scattering-angle configuration that is key to the SPADE system. Unless interested in this derivation, the reader can go immediately to Eq (10E) and then to Section 5.2. Next, expressions for the signal-to-noise ratio (SNR) under two different system constraints are considered: shot-noise limited SNR in Section 5.2, thermal-noise limited SNR in Section 5.3. The variation with the range from scattering aerosols to detector,  $R$  in Figure 5.1, is different for these two constraints; specifically,  $\text{SNR} \sim 1/R$  in the shot-noise limited case,  $\text{SNR} \sim 1/R^2$  in the thermal-noise limited case. SNRs for both constraints are produced from the volume-scattering coefficient values developed in Section 4, using existing laser and receiver component specifications. Finally, two particular standoff biodefense designs are addressed in Section 5.4—perimeter and area defense.

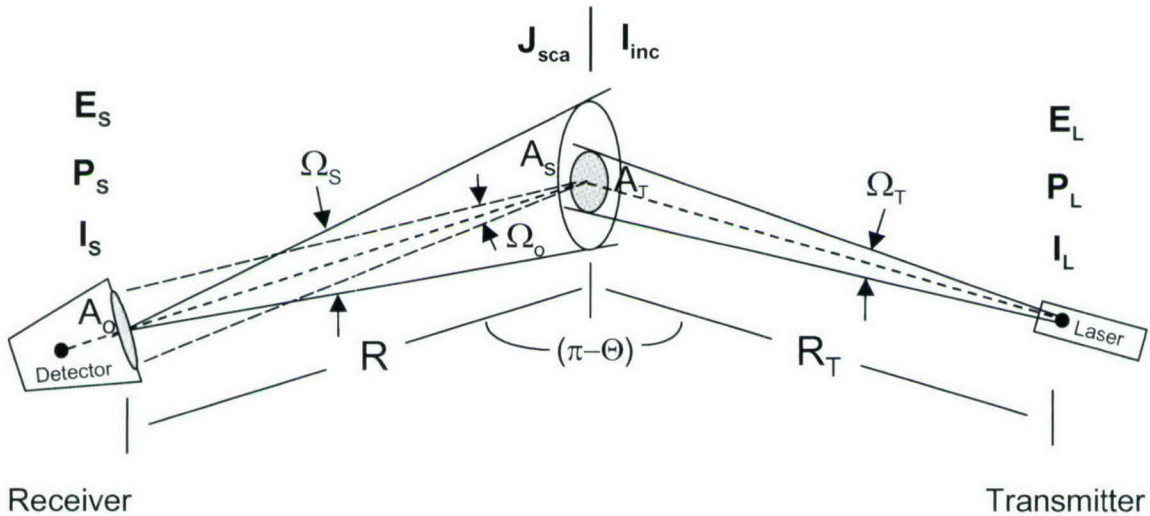


*Figure 5.1. Bistatic Lidar Geometric Configuration. Scattering angle is  $\Theta$ . Ranges:  $R$  – receiver to target,  $R_T$  – transmitter to target. Cross-sectional areas:  $A_o$  – receiver aperture,  $A_S$  – receiver field-of-view at  $R$ ,  $A_T$  – laser beam at  $R_T$ . Solid angles:  $\Omega_o$  – aperture-from-source,  $\Omega_S$  – receiver field-of-view,  $\Omega_T$  – laser divergence. Energy or power per integration time or pulse, and irradiance:  $E_s$ ,  $P_s$ ,  $I_s$  – received signal;  $E_L$ ,  $P_L$ ,  $I_L$  – laser output. Irradiance incident at  $R_T$ ,  $I_{inc}$  [ $\text{W m}^{-2}$ ]. Scattered irradiance per unit pulse length at  $R$ ,  $J_{sca}$  [ $\text{W m}^{-3}$ ].*

## 5.1 BISTATIC LIDAR EQUATION

The following development follows closely that of Measures [ME, Section 7.1]. But here, only elastic scattering is considered so allowance for different wavelengths—laser vs. signal—is not needed. What is needed, however, is modification to the basic scattering lidar equation [ME, eq 7.14] so it applies to angle-dependent scattering in the bistatic lidar configuration. The bistatic measurement setup is depicted in Figure 5.1. The objective is the energy version of the bistatic lidar equation, Eq (10E).

The bistatic lidar equation is the formulation of the received signal, having as its source the radiation scattered by particles located in one specific range interval within the receiver field of view, i.e., in one *sample volume*  $V(R)$ . (In Figure 2.1 the sample volume is the unshaded conic sector.) The instantaneous (superscript ') signal power [W] arriving at the receiver aperture from the sample volume at  $R$  is

$$P_s'(R, \Theta) = \int_{AT} J_{sca}(R; \Theta, R_T) p[V:A_o] \Delta R_T dA_T \quad (10A)$$

The transmitter range  $R_T$  can differ in the bistatic configuration from  $R$ , but the two ranges, as indicated in Figure 5.1, share one common terminus. The laser beam cross-section area, which may vary somewhat with range  $A_T(R_T)$ , is located within the sample volume defined by the receiver range interval corresponding to  $R$ . The receiver's radiant source  $J_{sca}(R; \Theta, R_T)$  [ $\text{W m}^{-3}$ ] is the scattered laser-induced irradiance at  $R$  (here, position  $R$  is a parameter) per unit laser pulse length located within the range  $R_T$  and  $R_T \pm 1/2 \Delta R_T$ , that is redirected through the scattering angle  $\Theta$ . ( $J_{sca} = I_{sca}/c\tau_L$  in Figure 2.1.) The probability,  $p[V:A_o]$ , that any scattered radiation originating within the sample volume arrives at the receiver aperture  $A_o$  depends on the solid angle of the aperture seen from the source, illustrated in Figure 5.1 as  $\Omega_o = A_o/R^2$ . It also depends on the fraction of the sample volume occupied by the laser-irradiated *scattering volume*  $V_T(R_T)$ , namely, on the *overlap factor* that in this report is defined simply as  $\xi(R, R_T) = V_T(R_T)/V(R)$ . As seen in Figures 2.1,  $\xi(R, R_T) < 1$ .

Furthermore, any receiver-directed radiation is reduced by path attenuation along the receiver range (atmospheric absorption and scattering out of  $\Omega_o$ ), which is quantified by the path-transmittance  $t(R)$ , and by losses specific to the receiver system—indicated here by the symbol  $T$  (and explained in Section 5.2). Using Figure 5.1 as a rough receiver-to-transmitter guide to the various factors involved, the instantaneous detected signal power is

$$P_s'(R, \Theta) = T A_o/R^2 t(R) \int_{AT} J_{sca}(R; \Theta, R_T) \xi(R, R_T) \Delta R_T dA_T \quad (10B)$$

The laser-induced scattered irradiance per unit range interval,  $J_{sca}(R; \Theta, R_T)$ , is the product of  $I_{inc}(R_T)$ , the transmitter irradiance incident on  $V_T(R_T)$  times the volume scattering coefficient for the particles that are located at  $R$  (and within  $V_T$ ) and which are scattering laser radiation from the laser axis direction into the receiver axis direction, i.e.,

$$J_{sca}(R; \Theta, R_T) = B(R; \Theta) I_{inc}(R_T) \quad (11A)$$

The volume scattering coefficient matrix  $B(R; \Theta)$  has been introduced already in Section 2.2. It quantifies elastic scattering as a function of  $\Theta$  by the particles at the location specified by  $R$ . It has the dimension of inverse length, in this report the unit used is [ $\text{cm}^{-1}$ ]. The transmitter irradiance incident at  $R_T$  is the laser-leaving pulse irradiance  $I_L$  [ $\text{W m}^{-2}$ ] as attenuated by the atmosphere, namely,  $I_{inc}(R_T) = t(R_T) I_L$ . Eq (10B) is

$$P_s'(R, \Theta) = T A_o/R^2 t(R) B(R; \Theta) \xi(R, R_T) \Delta R_T t(R_T) A_T(R_T) I_L \quad (10C)$$

For the transmit-beam cross-section area integration in Eq (10B),  $\xi$  and  $\Delta R_T$  are fixed and it has been assumed that laser irradiance is uniform across  $A_T$ , thus removing all factors from the integral except the area increment itself, resulting in  $\int_{A_T} dA_T = A_T(R_T)$ .

The meaning of the range interval  $\Delta R_T$  in the rectangular-pulse monostatic lidar setup is unambiguous [ME, p 240]; it is expressible as half of the laser pulse length  $c\tau_L$ , where  $\tau_L$  is the laser pulse duration. In the general bistatic lidar case, the meaning is more problematic [ZIK, p 139], involving the definitions of both the scattering and sample volumes in terms of  $\tau_L$  and the detector integration time  $\tau_D$ , respectively, and the specification of their overlap in space and time. If the scattering volume is entirely contained within the sample volume, as is depicted in Figure 2.1, then the limits on the range interval are  $c\tau_L/2 \leq \Delta R_T \leq c\tau_L$  for any bistatic configuration. This range increment along with the value of the overlap factor  $\xi(R, R_T)$  restricts the source of detected signal to be the irradiated portion of the sample volume. It is expedient here to use the monostatic lidar value of  $\Delta R_T = c\tau_L/2$ .

The total output energy per laser pulse  $\mathbf{E}_L$  [J] is used to define the average power per pulse  $\mathbf{P}_L \equiv \mathbf{E}_L/\tau_L$  [ME, p 243], which for small  $\tau_L$  is usually called the laser *peak power*. The portion of this peak power that arrives at  $V_T(R_T)$  is  $\mathbf{P}_{inc}(R_T) = t(R_T) \mathbf{P}_L = t(R_T) \mathbf{E}_L/\tau_L$ . By irradiance definition,  $\mathbf{I}_{inc}(R_T) = \mathbf{P}_{inc}(R_T)/A_T(R_T)$ ; the dark-stippled ellipse in Figure 5.1 depicts the laser beam area  $A_T(R_T)$ . Thus,

$$\mathbf{I}_{inc}(R_T) = t(R_T) \mathbf{P}_L/A_T(R_T) = t(R_T) \mathbf{E}_L/[\tau_L A_T(R_T)] \quad (11B)$$

But, since the laser irradiance at  $R_T$  is  $\mathbf{I}_{inc}(R_T) = t(R_T) \mathbf{I}_L$ , then  $\mathbf{P}_L = \mathbf{I}_L A_T(R_T)$ . Substitution in Eq (10C) gives the basic *bistatic lidar power equation*

$$\mathbf{P}_S(R, \Theta) = T A_o/R^2 t(R) \mathbf{B}(R; \Theta) \xi(R, R_T) t(R_T) (c\tau_L/2) \mathbf{P}_L \quad (10D)$$

where  $\mathbf{P}_S(R, \Theta)$  is the pulse-average value and no longer the instantaneous value because  $\Delta R_T$  is now specified in terms of  $\tau_L$ .

The signal energy is physically the integral over the detector integration time  $\tau_D$  of the instantaneous radiant power  $\mathbf{P}_S'(R, \Theta, t)$  incident on the detector [ME, eq 7.13], i.e.,  $\mathbf{E}_S(R, \Theta) = \int_{\tau_D} \mathbf{P}_S'(R, \Theta, t) dt$ . A  $\tau_D$ -average detected power is formed, analogous to laser peak power, as  $\mathbf{P}_S(R, \Theta) = \mathbf{E}_S(R, \Theta)/\tau_D$ . Therefore, the energy version of Eq(10D) is obtained, either heuristically, by multiplying through with the time-increments product ( $\tau_D\tau_L$ ), or by using Eq (11B) and the definition of total signal energy received during the detector integration time  $\mathbf{E}_S$  [J] =  $\tau_D \mathbf{P}_S$ . The *bistatic lidar energy equation* is, then,

$$\mathbf{E}_S(R, \Theta) = T A_o/R^2 (c\tau_D/2) t(R) \mathbf{B}(R; \Theta) \xi(R, R_T) t(R_T) \mathbf{E}_L \quad (10E)$$

With the flexibility that the signal energy can vary with  $\Theta$ - and that the range axes  $R$  and  $R_T$  have different orientations and lengths, Eq (10E) is the same as the basic lidar scattering equation [ME, eq 7.14].

Comments regarding the bistatic lidar equations, Eq (10D) and (10E) are:

1. The development of an analytical expression for the overlap factor, indicated here as only varying with ranges,  $\xi(R, R_T)$ , can be problematic; it varies with, among other factors, the axes separation angle ( $\pi - \Theta$ ).

2. The Beer's law atmospheric path transmittance expressions are  $t(R) = \exp[-\kappa R]$  and  $t(R_T) = \exp[-\kappa R_T]$ , with  $\kappa$  being the assumed-uniform atmospheric extinction coefficient ( $m^{-1}$ ) at the laser wavelength. (The extinction length  $1/\kappa$  is sometimes encountered.)
3. The detection quantum efficiency (Section 5.2) is included in the receiver parameter  $T$ , so that both  $\mathbf{P}_S$  and  $\mathbf{E}_S$ , while still in radiant-source units, are already reduced by the less-than-complete detector conversion of input photons to output photo-generated electrons.
4. Even though energy is physically a scalar quantity, each of the  $\mathbf{E}$ 's in Eq (10E) retains the polarization vector (Stokes parameter) form of the irradiances involved.
5. The signal-to-noise computations in Section 5.2 are more readily carried out using the energy version of the bistatic lidar equation, Eq (10E).

The bistatic lidar equation is now related to the basic scattering equation that was developed in Section 2.2 as it applies to a combination of two different aerosol types mixed together in the same sample volume. For simplicity, there the assumption was made that  $\xi(R, R_T) = 1$ . The basic equation, Eq (4D), is here restated with the range dependencies of  $\mathbf{I}_{inc}$ ,  $\mathbf{I}_{sca}$ , and  $V$  all explicitly indicated and with place-to-place variation of the combined volume scattering coefficient indicated by argument  $R$ .

$$\mathbf{I}_{sca}(R, \Theta) = V(R)/R^2 \mathbf{B}_c(R; \Theta) \mathbf{I}_{inc}(R_T) \quad (4D)$$

The incident irradiance in Eq (4D) is at the common terminus of the two ranges, i.e. it applies at the collocated volumes indicated in center of Figure 5.1. For that reason, not included in Eq (4D) are atmospheric path-transmittance of the laser beam  $t(R_T)$ , atmospheric transmittance to the receiver  $t(R)$ , and all receiver losses. By including all these factors, along with the overlap factor, then Eq(4D) would be the *bistatic lidar irradiance equation* and  $\mathbf{I}_{sca}(R, \Theta)$  would then be identically  $\mathbf{I}_s(R, \Theta)$ , at left in Figure 5.1. On the other hand, Eqs (10D) and (10E) already specify detected signals in terms of laser output radiation as it is affected by scattering within those partially overlapping volumes, including transmission losses in propagating to and from them, and inefficiencies inherent in any detector. For total-system signal-to-noise computation, the complete laser-to-detector specification is needed as in Eq (10D), and not just the redirection of light within the volumes as in Eq (4D).

In order to use the polarimetric scattering properties (in particular, the Section 4 values of the volume scattering coefficient matrix elements) to carry out system signal-to-noise evaluations, the irradiance vectors in Eq (4D) need to be expressed in terms of the complete bistatic system. But already, Eq (11B) specifies the path and transmitter parameters that determine  $\mathbf{I}_{inc}(R_T)$ . One parameter, the beam area  $A_T$ , is by design very nearly independent of range. Furthermore, the path and receiver performance parameters that link  $\mathbf{I}_{sca}(R, \Theta)$  to the measured signal,  $\mathbf{E}_S$  or  $\mathbf{P}_S$ , are incorporated. (It is also noted that  $V(R) = c\tau_D A_S(R) = c\tau_D \Omega_S R^2$ ; the receiver field-of-view  $\Omega_S$  being fundamentally determined by dimensions of the receiver and detector components, esp. detector area and focal length.) With  $\mathbf{P}_L$  from Eq (11B) used in Eq (10D), and then including Eq (4D) with  $\xi(R, R_T) \neq 1$ ,

$$\mathbf{P}_S(R, \Theta) = T/2 A_o t(R) [c\tau_L A_T/V(R)] \mathbf{I}_{sca}(R, \Theta)$$

But the square bracket is  $V_T(R_T)/V(R)$ , which in this report is the overlap factor  $\xi(R, R_T)$ , so that the detector radiant power and signal energy in Eq (10E) are related to Eq (4D) scattered irradiance as:

$$\begin{aligned} \mathbf{P}_S(R, \Theta) &= T/2 A_o t(R) \xi(R, R_T) \mathbf{I}_{sca}(R, \Theta) \\ \mathbf{E}_S(R, \Theta) &= T/2 A_o \tau_D t(R) \xi(R, R_T) \mathbf{I}_{sca}(R, \Theta) \end{aligned} \quad (10F)$$

## 5.2 SIGNAL-TO-NOISE RATIO

The ideal upper limit, the shot-noise limit, for achievable lidar single-pulse return signal-to-noise ratio (SNR) is the topic here. In Appendix D.1, the shot-noise limited equation for  $\text{SNR}_{\text{sn}}$  is explained and inherent assumptions are described. The  $\text{SNR}_{\text{sn}}$  is the ideal case conventionally achieved by the use of optical heterodyne lidar techniques—meaning coherent laser and, more recently, Geiger-mode avalanche photodiode detector (APD) [BW]. With that in mind, the  $\text{SNR}_{\text{sn}}$  equation is applied using the following information: 1) optical performance of theoretical  $\lambda = 1.50 \mu\text{m}$  coherent laser and heterodyne receiver, 2) bistatic lidar system parameters applicable to three biodefense scenarios of outdoor stadium, indoor auditorium, or heat-ventilation-air-conditioning (HVAC) system, and 3) the volume scattering coefficient matrix values tabulated in Section 4.

### 5.2.1 SNR Equation

It is assumed that a shot-noise limited photodiode detector is employed. The maximum SNR value attainable with such a detector is

$$\text{SNR}_{\text{sn}} \leq [1/(2)^{1/2}] [\langle \mathbf{n}_q(t) \rangle]^{1/2} = [1/(2)^{1/2}] [(\lambda/hc)\mathbf{E}_s]^{1/2} \quad (12A)$$

This is the ideal performance that cannot be exceeded—all other noise sources being ignored. Eq (12A) is the *signal photon shot-noise limited SNR equation*, in which  $\langle \mathbf{n}_q(t) \rangle$  is the average number of photons detected during any one laser pulse (see also Appendix D.1). In terms of the single-pulse detected energy  $\langle \mathbf{n}_q(t) \rangle = \mathbf{E}_s/h\nu = \lambda\mathbf{E}_s/hc$ , with  $h$  as Planck's constant  $6.626 \times 10^{-34} \text{ [J s]}$ , and  $\nu (= c/\lambda)$  as the laser frequency [Hz],  $c = 2.998 \times 10^8 \text{ [m s}^{-1}\text{]}$  being speed of light.

Comments relevant to Eq (12A) are:

1. The polarization vector (Stokes parameter) form of  $\text{SNR}_{\text{sn}}$ ,  $\mathbf{n}_q$ , and  $\mathbf{E}_s$  is noteworthy. The polarization state of the photons incident on the detector (of which  $\mathbf{n}_q$ , are detected) means that  $\text{SNR}_{\text{sn}}$  has a Stokes parameter form.
2. SNR is typically a ratio of some type of electrical quantity. The SNR being employed here is the ‘current’ or ‘voltage’ [WO3, Sect 25.4] version (also called ‘square-root’ version), in distinction to the ‘radar’ or ‘power’ [e.g., KI, eq 2.12] version.
3. Eq (12A) provides single-pulse values of  $\text{SNR}_{\text{sn}}$ , given appropriate polarimetric measurement of the received energy  $\mathbf{E}_s$ .
4. The signal photon shot-noise limited SNR equation applies at the output of the detector but is here expressed in detector input radiant energy units and not in detector output electronic units. This radiant energy form is convenient for assessing SNR exclusively in radiation terms.

Allowing for pre-amplifier noise that adds to otherwise existing shot noise another factor  $1/(2)^{1/2}$  (pre-amp noise-figure of 3 dB), the not-to-exceed limit is reduced to

$$\text{SNR}_{\text{snpn}} \leq \frac{1}{2} [\langle \mathbf{n}_q(t) \rangle]^{1/2} = \frac{1}{2} [(\lambda/hc)\mathbf{E}_s]^{1/2} \quad (12B)$$

As before, Eq (12B) is the ideal receiver SNR expressed in detector input radiant energy units but now as found at the output of the pre-amplifier.

Using Eq (10E) in Eq (12B), with  $r_o$  as the radius of the receiver aperture  $A_o$ ,

$$\text{SNR}_{\text{snpn}} \leq \frac{1}{2} [(\lambda/hc) \mathbf{E}_S]^{1/2} = \frac{1}{2} [r_o/R] [(\pi/2h)(\lambda T \tau_D t^2 \mathbf{B} \xi \mathbf{E}_L)]^{1/2} \quad (12C)$$

where the detector quantum efficiency is included in the receiver efficiency factor  $T$ . For simplicity, in Eq (12C) the complete path transmittance is written  $t^2 = t(R) t(R_T)$  and the argument lists for the overlap factor  $\xi$  and the volume scattering coefficient matrix  $\mathbf{B}$  are suppressed. Attention is directed to the  $(1/R)$  dependence of SNR for shot-noise-limited detectors.

### 5.2.2 System Parameters

Figure 5.2 depicts the essential modules of a bistatic lidar surveillance system: transmitter (top row); receiver (middle row); recorder, timing, and control (bottom row). Singled-out are the receiver optical components and their interrelations.

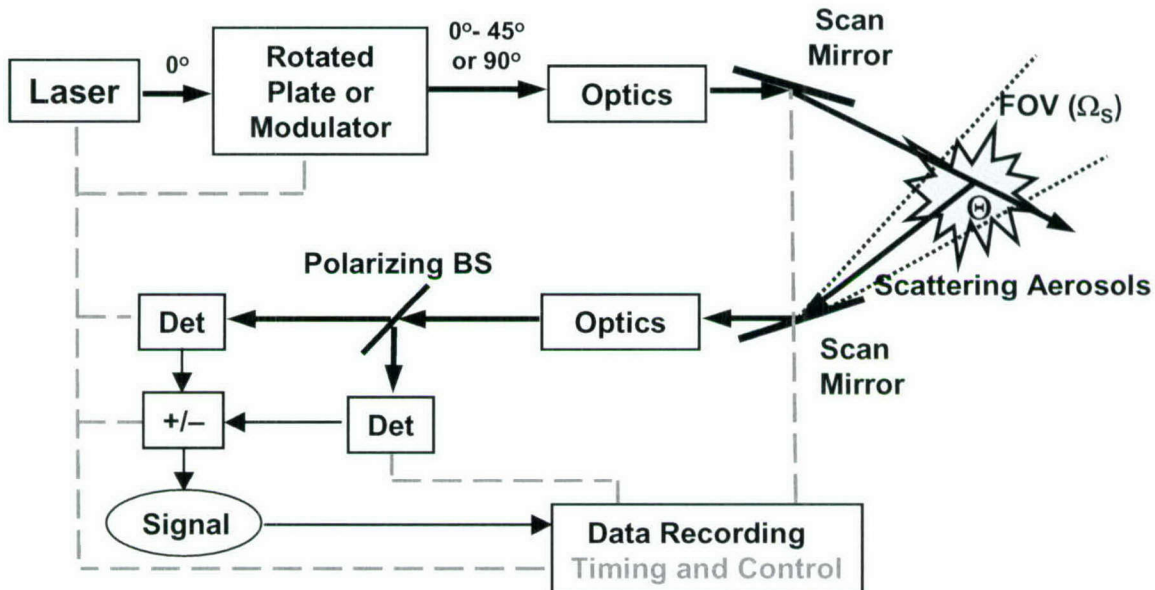


Figure 5.2. Bistatic Lidar Surveillance System Modular Diagram. Optical paths – thick arrows, electronic paths – thin arrows, timing and control routes – dashed lines. Initial state of incident polarization  $0^\circ$ .

The laser light incident on the scattering aerosols needs to be rapidly switched between at least two polarization states, e.g.,  $0^\circ$  and  $45^\circ$ . Mechanical rotation of optical devices or electro-optical modulation can effect this change. The scattering angle variation is shown in Figure 5.2 to result from coordinated repositioning of two scan-mirrors. (In this report no further details on the control-timing-data-recording module are given.)

A number of the receiver-components' efficiencies and transmittances are factors in the parameter represented by  $T$  in the various forms of Eq (10) and in Eq (12C). Among these independent factors are the detector quantum efficiency  $\eta$ , a polarizer efficiency factor  $q$ , and product of transmittances and reflectances of receiver optical-train components–beamsplitter, mirrors, optical filter, etc.

Specific,  $T = \eta q t_{bs} (r_{mr})^2 t_{fl}$ . In Table 5.1 are listed the values used here along with an initial source reference for each. The overlap factor  $\xi$  and the atmospheric transmittance  $t$  both depend on range so that only nominal values are given in Table 5.1. Combining values, the receiver parameter is  $T = 0.027$ ; and furthermore,  $(T \xi t^2) = 0.006 < 1\%$ .

**Table 5.1. Component Efficiencies and Transmittances at  $\lambda = 1.50 \mu\text{m}$ .**

Factor	Value	Reference
Detector quantum efficiency	$\eta = 0.30$	[DKB; Table 3.2]
Polarizer efficiency factor	$q = 0.73$	[SH, Figure 4.6, P( $k_1$ )]
Beamsplitter transmittance	$t_{bs} = 0.30$	[CH, generic value]
Mirror(s) reflectance	$(r_{mr})^2 = (0.78)^2$	[WO8; WO6; Figure 10-4(vis)]
Filter transmittance	$t_{fl} = 0.68$	[MA, Figure 3.11(c)]
Volumes overlap factor	$\xi = 0.30$	[ME, Figure 7.12 (A = 5, $\delta = 0.05$ , $z = 4$ )]
Atmospheric transmittance(s)	$t^2 = 0.77$	[MC, Figure 6.2]

Three biodefense scenarios are considered for the purpose of assessing SPADE feasibility in terms of SNR. These scenarios are: outdoor stadium, indoor auditorium, and HVAC system. Each poses different requirements on the bistatic lidar system in terms of range, receiver aperture size, and lidar pulse duration. Table 5.2 gives estimates of possible system parameters associated with the three scenarios.

**Table 5.2. SPADE Parameters for Three Biodefense Scenarios.**

Biodefense Scenario	$L_L$ (m)	$\tau_L$ (ns)	$r_o$ (m)	R (m)	$r_o/R$ (-)	$\theta_s$ (deg)
Outdoor Stadium	30	100	0.125	1600	$7.8 \times 10^{-5}$	1.1
Indoor Auditorium	3	10	0.050	50	$1.0 \times 10^{-3}$	3.4
HVAC System	0.1	0.33	0.025	1	$2.5 \times 10^{-2}$	5.7

Table 5.2 is constructed by first considering the physical length of the laser pulse,  $L_L$ . This basically sets the spatial resolution of the lidar coverage. For outdoor situations, a resolution on-order 30 m is commensurate with the large area-surveillance application. This, in turn, determines the laser pulse duration,  $\tau_L$ , since  $L_L = c\tau_L$ . It is judged that a fairly large 25-cm diameter aperture receiving system could be employed for the outdoor application. This gives a receiver aperture radius  $r_o = 0.125$  m. The range is not unequivocally set, but  $R = 1600$  m (about 1 mile) is representative of outdoor aerial coverage. The  $(1/R)$ effect of operating at longer ranges can readily be estimated from Eq (12C).

For an indoors auditorium, higher spatial resolution is required;  $L_L = 3$  m is chosen. This is adequate to distinguish possible aerosol-agent release points. The receiver aperture size is also reduced to  $r_o = 0.050$  m (about 2 inches). A large receiver telescope would likely be obtrusive (and obvious) in an indoor auditorium. The indoor range is taken to be  $R = 50$  m.

Finally, in an HVAC system the pulse must be very short to detect only aerosol scattered light and not light that strikes and reflects from boundaries of the ventilation system. Unless light absorbers

are installed, multiple boundary reflections would seriously contaminate an HVAC measurement. A pulse length of  $L_L = 0.1$  m (about 4 inches) is therefore selected. The aperture size would also have to be small to be compatible with an HVAC duct system; the choice of  $r_o = 0.025$  m is made. The HVAC range is also small, e.g.,  $R = 1$  m.

The stringency of timing required for synchronization between the receiver and transmitter and of the overall timing bandwidth, increase significantly in proceeding from the outdoor stadium to the HVAC scenario. For the SNR evaluation purpose, the topic need not be pursued beyond stipulating that the detector integration time  $\tau_D = \tau_L$ , the laser pulse duration. Nevertheless, synchronization may be a technical challenge in bistatic lidar applications.

The receiver two-dimensional field-of-view angle,  $\theta_S$ , is estimated by considering the geometry at scattering angle  $\Theta = 90^\circ$ , i.e.,  $\theta_S = 2 \tan^{-1}[(L_L/2)/R]$ . ( $\theta_S$  is the in-scattering-plane projection of the field-of-view solid angle  $\Omega_s$  in Figure 5.1.) This is a simplifying approximate value since in space the overlap is a straightforward but tedious geometrical calculation that depends on  $\theta_S$ , on the laser-to-receiver direction change,  $(\pi - \Theta)$  in Figure 5.1, and on the in-scattering-plane laser beam divergence angle  $\theta_T$ .

In Table 5.2 the values of  $\theta_S$  are listed. For the outdoor application, its value is suitable for uncomplicated design of a narrow-band filter. For the indoor scenario, the larger value is of some concern. For the HVAC scenario, fabrication of a narrow-band filter could be difficult. This trend in  $\theta_S$  is mitigated by the fact that the need for a narrow-band filter will be most stringent for outdoors and, likely, least stringent for an HVAC application.

At this point, Eq (12C) is formulated using the values of the ratio  $r_o/R$  and the spatial parameters for the three biodefense scenarios from Table 5.2. Component parameters  $T$  and  $\xi$  are taken directly from Table 5.1. However, assuming the range from target-aerosol to receiver is the same as that from laser to target-aerosol ( $R = R_T$  in Figure 5.1), the two-way atmospheric transmittance is then recomputed for the widely varying ranges in Table 5.2. The atmospheric extinction coefficient for  $\lambda = 1.50$   $\mu\text{m}$  is assigned as  $\kappa = 8.0 \times 10^{-5}$   $\text{m}^{-1}$  [MC, Figure 6.2,  $v = 2.25$ ], which is the sum of aerosol scattering  $7.5 \times 10^{-5}$   $\text{m}^{-1}$ , aerosol absorption  $0.2 \times 10^{-5}$   $\text{m}^{-1}$ , and molecular absorption  $0.3 \times 10^{-5}$   $\text{m}^{-1}$ . Since in Eq (12C) the root of  $t^2$  is taken, the Beer's law t-values themselves are sufficient, specific,  $t = 0.880, 0.996, 1.000$  for the outdoor, indoor, and HVAC scenarios.

In Eq (12C), for  $\tau_D = \tau_L(s)$ ,  $\mathbf{B}(\text{cm}^{-1})$ , and  $\mathbf{E}_L(J)$ , the SNR expressions for the three scenarios (outdoor, indoor, HVAC) are, respectively,

$$\mathbf{SNR}_{\text{snpn}} \leq [18.55 \times 10^8, 26.88 \times 10^9, 6.75 \times 10^{11}] [\tau_L \mathbf{B} \mathbf{E}_L]^{1/2} \quad (13A)$$

with units on the factor being  $[\text{cm}/\text{J s}]^{1/2}$ .

Eq (13A) provides single-pulse SNR values. Pulse-averaging increases SNR. In theory, the lidar SNR can be increased by  $\sqrt{K}$ , where  $K$  is the number of pulses averaged. In practice, improved SNR limits are reached due to low-level correlated noise (e.g., 1/f-noise, not considered here). The pulse-averaging improvement limit is often encountered for  $K < 100$ .

Regarding the near-term feasibility of a bistatic lidar system configured to detect bio-aerosol presence, two key laser parameters are the magnitude of the laser energy per pulse ( $E_L$ ) and the pulse repetition frequency (PRF). A survey of near-term laser capabilities in 2.1- and 1.5- $\mu\text{m}$  wavelength regions are contained in Table 5.3 based on these parameters. (Near-term: early 2005.)

**Table 5.3. Qualitative Review of Feasibility for (a) 2.12 μm and (b) 1.50 μm Lasers.**(a)  $\lambda = 2.12 \mu\text{m}$ 

$E_L \setminus \text{PRF}$	1 Hz	10 Hz	100 Hz	1 kHz
1 mJ	Feasible	Feasible	Challenging	Difficult
10 mJ	Feasible	Feasible	Difficult	Development req.
100 mJ	Challenging	Difficult	Development req.	R&D effort
1 J	Difficult	Development req.	R&D effort	Major R&D effort

(b)  $\lambda = 1.50 \mu\text{m}$ 

$E_L \setminus \text{PRF}$	1 Hz	10 Hz	100 Hz	1 kHz
1 mJ	Feasible	Feasible	Feasible	Feasible
10 mJ	Feasible	Feasible	Challenging	Difficult
100 mJ	Feasible	Challenging	Difficult	Development req.
1 J	Challenging	Very difficult	Development req.	Major R&D effort

Any assessment like Table 5.3 is subject to revision and its interpretation is changed some by the purpose to which the assessment is put. Nonetheless, at this time (mid 2004), it appears that obtaining a 2.12-μm laser with much greater energy than 10 mJ per pulse at 10 Hz PRF with good beam quality and suitable spectral stability is about at the limit of near-term feasibility. Alternatively, for a  $\lambda = 1.50 \mu\text{m}$  laser, due to rapid progress in optical communications, 10 mJ at 100 Hz pushes the near-term limit.

For the SNR computations reported on here, the 1.50-μm laser with the highest near-term feasible PRF is selected. Table 5.4 lists the parameters of such a laser along with attendant system parameters for each of the three SPADE application scenarios (Table 5.2).

**Table 5.4. Laser and Receiver Parameters for Outdoor, Indoor, and HVAC Systems.**

Parameter	Value
Laser wavelength	$\lambda = 1.50 \mu\text{m}$
Laser average power	$\bar{P} = 1 \text{ W}$
Laser pulse repetition frequency	PRF = 1 kHz
Laser energy per pulse	$E_L = 1 \text{ mJ}$
Laser pulse duration	$\tau_L = 100, 10, 0.33 \text{ ns}$
Laser pulse length	$L_L = 30, 3, 0.1 \text{ m}$
Laser peak power	$P_L = 0.01, 0.10, 3.0 \text{ MW}$
Receiver aperture area	$A_o = 490, 78, 20 \text{ cm}^2$
Detector integration time	$\tau_D = 100, 10, 0.33 \text{ ns}$

The 1.50-μm, 1-mJ, 1-kHz laser operating with pulse durations appropriate for outdoor, indoor, and HVAC scenarios results in Eq (13A) becoming

$$\text{SNR}_{\text{snpn}} \leq [18.55 \times 10^3, 85.00 \times 10^3, 387.6 \times 10^3] [\mathbf{B} \mathbf{s}_L]^{1/2} \quad (13B)$$

A binary Stokes vector  $\mathbf{s}_L$  can for convenience be used to apportion among the four components a unit of pulse-energy leaving the laser transmitter. It is  $\mathbf{E}_L$  normalized by its magnitude  $E_L$  (in the present case, 1 mJ), i.e.,  ${}^z\mathbf{E}_L / E_L \equiv {}^z\mathbf{s}_L$ , with  ${}^z$  indicating incident polarization state. For unpolarized

laser light,  ${}^0\mathbf{s}_L = [1 \ 0 \ 0 \ 0]^T$  is the unit-valued vector of binary Stokes parameters. For horizontal ( $0^\circ$ ) polarized laser light  ${}^h\mathbf{s}_L = \frac{1}{2} [1 \ 1 \ 0 \ 0]^T$ , vertical ( $90^\circ$ ) polarized light  ${}^v\mathbf{s}_L = \frac{1}{2} [1 \ -1 \ 0 \ 0]^T$ ,  $+45^\circ$  polarized  ${}^+\mathbf{s}_L = \frac{1}{2} [1 \ 0 \ 1 \ 0]^T$ ,  $-45^\circ$  polarized  ${}^-\mathbf{s}_L = \frac{1}{2} [1 \ 0 \ -1 \ 0]^T$ , right-hand circular polarized  ${}^r\mathbf{s}_L = \frac{1}{2} [1 \ 0 \ 0 \ 1]^T$ , left-hand circular polarized  ${}^l\mathbf{s}_L = \frac{1}{2} [1 \ 0 \ 0 \ -1]^T$ . These six binary Stokes vectors, since an additional ideal polarizer must be employed to obtain them, have magnitude  $1/2$  [e.g., CO, p 71], distinct from  $|{}^0\mathbf{s}_L| = 1$ . The binary Stokes vector  $\mathbf{s}_L$  can be applied equally well to the laser peak power, i.e.,  $\mathbf{P}_L = P_L \mathbf{s}_L$ .

At least two incident polarization states are produced by the rotated plate or electro-optical modulator depicted in Figure 5.2. With either,  $\mathbf{s}_L$  is the vector of binary Stokes parameters, which matrix-multiplies the volume scattering coefficient matrix  $\mathbf{B}$  to result in the vector form of the **SNR**. Regarding the vector component notation:  ${}^z\text{SNR}_i$  is used to designate **SNR** polarimetric component; superscript is incident polarization state, subscript is row of  $\mathbf{B}$ .

### 5.2.3 Polarimetric SNR Estimates

From Section 2, Eq (2B),  $\mathbf{B}$  is a Mueller matrix made up of 16 elements, at most, but more commonly having not more than eight different non-zero elements—the eight  $\Theta$ -varying volume scattering coefficients  $\beta_{ij}(\Theta)$ . In this report, only four of these:  $\beta_{11}(\Theta)$ ,  $\beta_{21}(\Theta)$ ,  $\beta_{22}(\Theta)$ , and  $\beta_{43}(\Theta)$ , are used to assess SNR for the Table 5.2 biodefense scenarios.

Each element of  $\mathbf{B}$  (as detailed in Section 2.2) depends on: number-concentration, per-particle average scattering ability, and normalized scattering function. Specifically,

$$\beta_{ij}(\Theta) = N [\langle C_{\text{sca}} \rangle / 4\pi] F_{ij}(\Theta) \quad (5D)$$

Clearly, all  $\beta_{ij}$  magnitudes depend directly on the same *total* volume scattering coefficient  $N \langle C_{\text{sca}} \rangle$ , discussed more fully in Section 6.2 and Appendix A.5. What accounts for the difference among the  $\beta_{ij}$ 's is the normalized scattering matrix elements  $F_{ij}$  (expeditiously symbolized as  $a_1$ ,  $b_1$ ,  $a_2$ , etc., in Section 2 and Appendix A), which are determined by the sizes, shapes, orientations, and refractive indices of the scattering particles. The angular variation of any  $F_{ij}(\Theta)$  (and also of any  $\beta_{ij}(\Theta)$ ) is—given incident wavelength—the net effect of all these particle physical properties.

Table 5.5 is a synopsis of  $\mathbf{B}$  ( $\times 10^{-9} \text{ cm}^{-1}$ ), specifically, the magnitudes of the four elements at  $\lambda = 1.50 \mu\text{m}$  taken from Tables 4.1, 4.2, 4.3, and 4.4. Only near-forward or far-backward values are used, specific,  $\beta_{ij}(\Theta = 5^\circ)$  and  $\beta_{ij}(\Theta = 170^\circ)$ . The continental ‘L’ aerosol (Tables 3.1 and 3.2) is the spherical-shaped ambient background aerosol with number-concentration  $N_a = 100 \text{ cm}^{-3}$ . It is combined with the bio-aerosol simulant ‘BS,’ number concentration  $N_b = 1 \text{ cm}^{-3}$ , having either of two shapes—spheres or prolate spheroids with  $\epsilon = 1.0/1.4$ .

The values in Table 5.5 are results of the scattering code computations (refer to Section 4). The overall magnitudes can be crudely reaffirmed from Eq (5D) by using the fact that for small particles the scattering cross section per particle  $\langle C_{\text{sca}} \rangle$  is roughly estimated as  $(\pi r_{\text{eff}}^2)/10$ , which for the ‘L’ aerosol is about  $0.1 \mu\text{m}^2$ , and for large particles as  $(\pi r_{\text{eff}}^2)$ , which for the ‘BS’ aerosol is about  $60 \mu\text{m}^2$ . Thus, the ‘ambient + bio’ combined value is expected to be approximately  $[N_a \langle C_{\text{sca}} \rangle_a + N_b \langle C_{\text{sca}} \rangle_b]/4\pi = 55 \times 10^{-9} \text{ cm}^{-1}$ . Since  $F_{11}(\Theta)$  varies between 20 in forward directions and 0.05 in backward [e.g., MTL, Figure 10.29], the range of  $\beta_{11}$  values in Table 5.5 is of the expected order.

**Table 5.5. Aerosol Volume Scattering Coefficients  $|\beta_{ij}|$  ( $10^{-9} \text{ cm}^{-1}$ ) for  $\lambda = 1.50 \mu\text{m}$ .  
 Continental ‘L’ ambient background aerosol ( $N_a = 100 \text{ cm}^{-3}$ , spherical) plus  
 ‘BS’ bio-aerosol ( $N_b = 1 \text{ cm}^{-3}$ , spherical  $\varepsilon = 1$  or prolate  $\varepsilon = 1.0/1.4$ ).**

'BS' Shape	Vol. Scatter Coefficient	$\Theta = 5^\circ$		$\Theta = 170^\circ$	
		Ambient	Ambient+Bio	Ambient	Ambient+Bio
Sphere	$ \beta_{11} $	199.70	3742.00	2.18	23.24
	$ \beta_{21} $	0.10	8.94	0.15	1.52
	$ \beta_{43} $	0.68	146.00	0.09	9.02
Prolate Spheroid	$ \beta_{11} $	199.96	3948.20	2.18	10.49
	$ \beta_{21} $	0.10	4.69	0.15	0.45
	$ \beta_{11} - \beta_{22} $	0.00	1.00	0.00	3.52
	$ \beta_{43} $	0.68	128.41	0.09	0.06

The Table 5.5 values are the elements of  $\mathbf{B}$  that are used in Eq (13B) to compute the components of SNR in Table 5.6. Pulse-averaging is applied to the individual-pulse values of SNR obtained from Eq (13B). The number of pulses  $K = 100$  provides an integration gain of  $\sqrt{K} = 10$ . Tables 5.6(a), (b), and (c) contain these gain-enhanced SNR values for each biodefense scenario.

As an example of the Table 5.6 computations, at  $\Theta = 5^\circ$  for the indoor auditorium scenario, the  ${}^+ \text{SNR}_4$  determined with the coefficient  $\beta_{43}$  ( $\times 10^{-9} \text{ cm}^{-1}$ ) are:  $[(\sqrt{K})(85 \times 10^3)][\sqrt{0.068/2}] \times 10^{-4} = 15.7$  for the ambient aerosol alone, and  $[(\sqrt{K})(85 \times 10^3)][\sqrt{12.841/2}] \times 10^{-4} = 215.4$  for ambient plus prolate-spheroid bio-aerosol. For the coefficient difference ( $\beta_{11} - \beta_{22}$ ), the SNR is only computed in Table 5.6 for prolate spheroids ( $\varepsilon = 1.0/1.4$ ). It is determined using  $\sqrt{1/2}$  times the average of the two individual ambient-plus-bio  $\beta_{ii}$  absolute magnitudes. In the near-forward direction, therefore,  ${}^P \text{SNR}_{1-2} = \sqrt{1/2} {}^+ \text{SNR}_1$ . In the far-backscatter direction for the indoor auditorium scenario, ambient plus bio as an example, the computation is  ${}^P \text{SNR}_{1-2} = [\sqrt{1/2}] [(\sqrt{K})(85 \times 10^3)][\sqrt{1.049 + 1/2(1.049)} / 4] \times 10^{-4} = 37.7$ . Since from Figure 4.6 (lower left panel, green curve), at  $\Theta = 170^\circ$  the value of  $\beta_{22} \approx \beta_{11}/2$  (recall  $\beta_{11} \sim a_1$  and  $\beta_{22} \sim a_2$ ), the factor of  $1/2$  is thereby explained.

It is noted that the entries in Table 5.6 are estimates of the ideal shot-noise upper limits. Authentic SNR performance for a more detailed system design that includes all noise sources [e.g., AW, Section 28.3; also WO6, pp 24-26] and takes into account actual component efficiencies, losses, and transmittances, could well be half the Table 5.6 values. Accepting this  $1/2$  safety factor and applying the minimum sensing-and-tracking criterion of  $\text{SNR} = 6$  [FM, p 4], then any Table 5.6 value less than 12 is unacceptably low.

Separate conclusions are drawn from Table 5.6 for backscatter versus both back- and forward-scatter situations. It is accepted as given that in the outdoor stadium scenario only backscatter measurements are available, whereas for the indoor auditorium or HVAC system both back- and forward-scatter measurements can be made.

**Table 5.6. Gain-Enhanced Signal-to-Noise Ratios  ${}^7\text{SNR}_i$  (Shot-Noise and Pre-Amp Limited) for 100 Pulses at  $=1.50 \mu\text{m}$  for: Outdoor Stadium, Indoor Auditorium, and HVAC System.**

Superscript is incident polarization; subscript is row of volume scattering coefficient matrix. Ambient background aerosol—continental ‘L’ ( $N_a = 100 \text{ cm}^{-3}$ , spherical), combined with ‘BS’ bioaerosol ( $N_b = 1 \text{ cm}^{-3}$ , spherical  $\varepsilon = 1$  or prolate  $\varepsilon = 1.0/1.4$ ).

(a) Outdoor Stadium

‘BS’ Shape	Polarimetric Component	$\Theta = 5^\circ$		$\Theta = 170^\circ$	
		Ambient	Ambient+Bio	Ambient	Ambient+Bio
Sphere	${}^+\text{SNR}_1$	58.6	253.7	6.2	20.0
	${}^+\text{SNR}_2$	1.3	12.4	1.6	5.1
	${}^+\text{SNR}_4$	3.4	50.1	1.2	12.5
Prolate Spheroid	${}^+\text{SNR}_1$	58.6	260.6	6.2	13.4
	${}^+\text{SNR}_2$	1.3	9.0	1.6	2.8
	${}^p\text{SNR}_{1-2}$	41.4	184.3	3.8	8.2
	${}^+\text{SNR}_4$	3.4	47.0	1.2	1.0

(b) Indoor Auditorium

‘BS’ Shape	Polarimetric Component	$\Theta = 5^\circ$		$\Theta = 170^\circ$	
		Ambient	Ambient+Bio	Ambient	Ambient+Bio
Sphere	${}^+\text{SNR}_1$	268.6	1162.7	28.1	91.6
	${}^+\text{SNR}_2$	6.0	56.8	7.4	23.4
	${}^+\text{SNR}_4$	15.7	229.7	5.7	57.1
Prolate Spheroid	${}^+\text{SNR}_1$	268.8	1194.3	28.1	61.6
	${}^+\text{SNR}_2$	6.0	41.2	7.4	12.7
	${}^p\text{SNR}_{1-2}$	189.9	844.5	17.2	37.7
	${}^+\text{SNR}_4$	15.7	215.4	5.7	4.7

(c) HVAC System

‘BS’ Shape	Polarimetric Component	$\Theta = 5^\circ$		$\Theta = 170^\circ$	
		Ambient	Ambient+Bio	Ambient	Ambient+Bio
Sphere	${}^+\text{SNR}_1$	1224.8	5301.8	128.0	417.8
	${}^+\text{SNR}_2$	27.4	259.1	33.6	106.9
	${}^+\text{SNR}_4$	71.5	1047.2	26.0	260.3
Prolate Spheroid	${}^+\text{SNR}_1$	1225.5	5445.9	128.0	280.7
	${}^+\text{SNR}_2$	27.4	187.7	33.6	58.1
	${}^p\text{SNR}_{1-2}$	866.6	3850.8	78.4	171.9
	${}^+\text{SNR}_4$	71.5	982.1	26.0	21.2

Conclusions regarding far-backscatter  $\text{SNR}_{\text{snpn}}$  values (right columns in Table 5.6) are: 1) In the outdoor stadium scenario, although pulse-averaging improves the SNR, the ambient background aerosol has SNR values that are unacceptably low except for  ${}^+\text{SNR}_1$  in the unrealistic condition that even the bio-aerosols are spherical particles. However, even with this condition, the ambient background aerosols are not reliably monitored in the far-backscatter direction ( ${}^+\text{SNR}_1 = 6.2$ ), which compromises the outdoor standoff detection unless critical system parameters (esp.  $E_L$  in

Table 5.3 or detector specifications in Tables 5.1 and 5.4)) are enhanced. 2) In the indoor auditorium scenario, both intensity  ${}^+SNR_1$  and non-sphericity  ${}^pSNR_{1,2}$  are usable to discriminate between ambient and suspect ‘BS’ aerosols. The non-sphericity measurement is clearly a solid enhancement for standoff detection. 3) In the HVAC applications all polarimetric SNRs are usable, allowing some possibility for detecting changes in specific aerosol properties (discussed in Sections 6.3 and 6.4), especially shape and refractivity.

For applications allowing forward measurements (center pair of columns in Table 5.6), intensity and non-sphericity have acceptable ( $SNR_{snpn} > 12$ ) values for all scenarios and for both bio-aerosol shape options. In both indoor and HVAC scenarios, the retardation SNR is also usable. For the HVAC system, all SNRs—in both background-plus-bio-aerosol and ambient background alone—are acceptable. In the indoor application, there is the possibility of using forward scattering—all of these SNR are significant. In the near-forward direction, enhancement of the retardation quantity,  ${}^+SNR_4$ , is noteworthy. There, it becomes a very viable detection quantity irrespective of bio-aerosol shape, as seen in Figure 4.7,

Overall, these initial SNR results suggest that a more comprehensive investigation is warranted, one which employs specifications of forthcoming higher average power lasers and of very efficient avalanche photodiode detectors [BW and CA].

### 5.3 SIGNAL-TO-NOISE BACKSCATTER-ANGLE PROFILES

The standoff application for polarimetric measurements of aerosol scattered light motivates specific consideration of the far-backscatter region ( $140^\circ \leq \Theta \leq 175^\circ$ ). It is evident from Figures 4.5, 4.6, and 4.7 (oblate, at least) that scattering matrix elements have distinctive features in this region; these are also seen in [MTL, Figures 10.29 and 10.30, center three rows]. As pointed out by [BAK, p 316], scattering matrix elements are most sensitive to any particle non-isotropy in this far-backscatter region. Therefore, backscatter angular profiles of different polarimetric signal-to-noise ratios are now presented to assess reliability of measuring these features.

Thermal-noise limited SNR quantities (also called Johnson-, component-, or amplifier-noise limited) are being dealt with in this section. These are still the ‘voltage,’ ‘current,’ or ‘square-root’ SNR version (refer comments on Eq (12A)), but the predominant noise source now comes from receiver electronic components rather than detector shot-noise. Only traditional detector technology is assumed, not the more promising avalanche photodiode. The average number of detected signal photons per pulse is just Eq (10E) divided by  $hv$ , i.e.,  $\bar{n}_q = E_S/hv = \lambda E_S/hc$  photons. The average number of noise photons is  $\bar{n}_N = (1/e)\sqrt{4kT \tau_D F/R_D}$ ,  $e$  and  $k$  being the elemental electron charge and the Boltzmann constant;  $T$ ,  $F$ , and  $R$  are the temperature, amplifier noise factor, and detector resistance (refer to Appendix D.2). The laser, environment, and receiver component values used here are listed in Table 5.7. In this section, off-the-shelf components are considered that would result in a compact, portable, and unattended SPADE system.

**Table 5.7. Parameters for Thermal-Noise Limited SNR Computations.**

Parameter	Value
<b>Laser:</b>	
Wavelength	$\lambda = 2.12 \text{ } \mu\text{m}$
Energy per pulse	$E_L = 1.00 \text{ mJ}$
Pulse duration	$\tau_L = 10 \text{ ns}$
<b>Environment:</b>	
Temperature	$T = 300 \text{ K}$
Transmittance	$t^2 = 1.00$
Overlap factor	$\xi = 0.70$
<b>Receiver:</b>	
Integration time	$\tau_L = 10 \text{ ns}$
Quantum efficiency	$\eta = 0.50$
Detector resistance	$R_D = 50 \Omega$
Amplifier noise factor	$F = 2$
Aperture area (6" dia)	$A_o = 182.5 \text{ cm}^2$

Applying the Table 5.7 values,  $\bar{n}_N = 1.61 \times 10^4$  photons per pulse. And with Eq (10E), the thermal-noise limited  $\text{SNR}_{tn}$  ( $= \bar{n}_q / \bar{n}_N$ ) equation is

$$\text{SNR}_{tn} \leq \eta [A_o/R^2] [(\lambda\tau_L/2h) \mathbf{B} \cdot \xi t^2 E_L s_L] / [1.61 \times 10^4] = 3.18 \times 10^{11} [\mathbf{B} s_L / R^2] \quad (14A)$$

where the magnitude of the binary Stokes vector, from Eq (13B), is assigned the value of  $1/2$ , some component efficiencies and transmittances (Table 5.1) other than  $\eta$  have cancelled, and the remaining parameters are from Table 5.7. Here the number of pulses integrated is  $K = 1000$  (vs.  $K = 100$  in Section 5.2.3). The gain-enhanced ( $\sqrt{[1000]}$ )  $\text{SNR}_{tn}$  magnitudes are then,

$$\text{SNR}_{tn} \leq 1.00 \times 10^{13} [\text{cm}^3] \beta_{ij} [\text{cm}^{-1}] / R^2 [\text{cm}^2] \quad (14B)$$

Attention is called to the fact, seen in Eq (14A), that with the receiver electronic components as the major noise source, SNR varies as  $(1/R^2)$ , vs.  $(1/R)$  if shot-noise is the limiting source, as in Eq (12C).

Three ranges are considered in Figures 5.3–5.5,  $R = 10, 32, 100 \text{ m}$ , but now the laser and receiver parameters are the same (Table 5.7) for all ranges (vis-à-vis lower portion of Table 5.4). The implication of the  $(1/R^2)$  variation of  $\text{SNR}_{tn}$ , given the constant aperture size, is the reason for the particular selection of  $R$ -values; sets of curves are one decade apart. In spite of differences from the three-range SNR information presented in Section 5.2.3, the more realistic thermal-noise limited receiver profiles of  $\text{SNR}_{tn}(\Theta)$  considered here can enhance understanding of the reliability of polarimetric measurements in the far-backscatter region.

In Figure 5.3 are plotted the two  $\text{SNR}_{tn}$  profiles associated with ‘intensity’ and ‘linearity’ (Table 2.2) in the far-backscatter region, specific,  ${}^+ \text{SNR}_1(\Theta)$  and  ${}^+ \text{SNR}_2(\Theta)$ , for the three sample-volume-to-detector ranges given and at two SWIR wavelengths. The  $(1/R^2)$  dependency is very evident—one-decade separation of SNR-sets due to the three selected ranges along with a constant receiver aperture  $A_o$  (6" diameter). For the ‘voltage’ version of SNRs, values greater than 6 imply probability-of-detection  $> 99\%$ ; this is adopted as the minimum acceptable level for any  $\text{SNR}_{tn}$ .

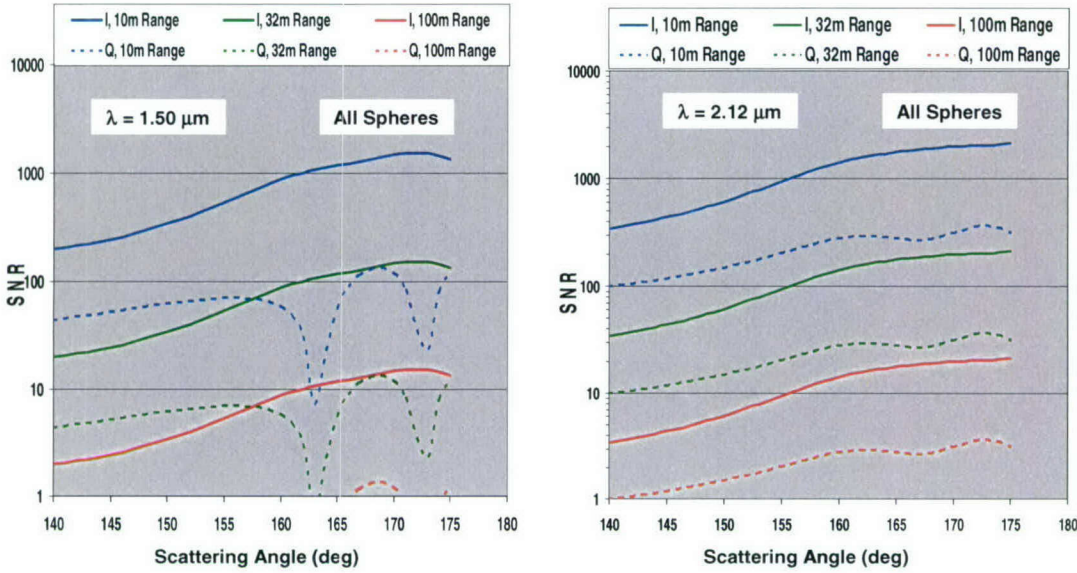


Figure 5.3. Signal-to-Noise Ratio ( $\text{SNR}_m$ ) Profiles at Far-Backscatter Angles ( $140^\circ \geq \Theta \geq 175^\circ$ ) for Laser Wavelengths  $\lambda = 1.50 \mu\text{m}$  (left) and  $\lambda = 2.12 \mu\text{m}$  (right).  $I$  – ‘intensity’ is  ${}^+\text{SNR}_I(\Theta)$  (solid curves) and  $Q$  – ‘linearity’ is  ${}^+\text{SNR}_2(\Theta)$  (dashed curves), as indicated in Table 2.1 and defined in Section 5.2.3. Ranges:  $R = 10 \text{ m}$  (blue),  $32 \text{ m}$  (green),  $100 \text{ m}$  (red). Incident polarization  $+45^\circ$ , with spherical bio-aerosol ( $N_b = 1 \text{ cm}^{-3}$ ) combined with spherical ambient aerosol ( $N_a = 100 \text{ cm}^{-3}$ ).

At wavelength  $2.12 \mu\text{m}$ , both ‘intensity’ and ‘linearity’ SNRs qualify as significant for the shorter two ranges, but only  ${}^+\text{SNR}_1(\Theta)$  with  $\Theta > 150^\circ$ , qualifies for  $100 \text{ m}$  range. At  $\lambda = 1.50 \mu\text{m}$ , only the ‘intensity’ type qualifies with the longer two ranges, and then only for  $\Theta > 155^\circ$  in the  $100 \text{ m}$  case.

The profiles in Figure 5.3 are from volume scattering coefficients computed at  $1^\circ$  increments of  $\Theta$  that capture the fine-scale angular changes in the  ${}^+\text{SNR}_2(\Theta)$  profiles seen at  $\lambda = 1.50 \mu\text{m}$ . However, practical limits on receiver two-dimensional field-of-view angle  $\theta_S$  (as in Table 5.2) may average over such dips in measurement reliability. The mode size of the spherical bio-aerosol relative to the illumination wavelength is responsible for these SNR backscatter angular features for spherical particles. At  $\lambda = 2.12 \mu\text{m}$  the sharp minima have disappeared. In any event, the most important message from Figure 5.3 is the significant increases in SNR values as  $\Theta$  increases;  $155^\circ$  and  $170^\circ$  are especially advantageous for standoff aerosol scattering measurements (see also Table 6.1).

Figures 5.4 and 5.5 are the far-backscatter angular profiles of the non-sphericity SNR, in the terminology of Table 5.6,  ${}^P\text{SNR}_{1-2}(\Theta)$ . Profiles for two axis-ratio spheroid bio-aerosols are used,  $\epsilon = 1.0/1.3$  and  $1.0/2.0$  for prolate (left panels) and  $\epsilon = 1.3/1.0$  and  $1.0/2.0$  for oblate spheroids (right panels). The same three ranges as in Figure 5.3 are employed. Aside from the again-evident  $(1/R^2)$  dependence, the more eccentric spheroid shapes are distinguished by the nearly constant values of all SNRs throughout the far-backscatter region.

Although all far-backscatter  ${}^P\text{SNR}_{1-2}(\Theta)$  values are somewhat larger at  $\lambda = 2.12 \mu\text{m}$  (Figure 5.5) than at  $\lambda = 1.50 \mu\text{m}$  (Figure 5.4), applying the  $\text{SNR} \geq 6$  criterion as before, the longest range SNRs are all unacceptably small.

To summarize reliability of scattering measurements at backscatter angles based on laser parameters given in Table 5.7, thermal-noise limited SNRs of the ‘intensity’ (scattering element  $a_1$ ), ‘linearity’ (scattering element  $b_1$ ), and ‘non-sphericity’ (scattering element difference,  $a_1 - a_2$ ) appear to be usable in detecting the introduction of suspect aerosols out to a range of  $\sim 50$  m. Overall, the  $SNR_{tn}$  values are higher for  $\Theta > 150^\circ$ , but are usable over all far-backscatter angles ( $140^\circ \leq \Theta \leq 175^\circ$ ). Examination of Eq (14A) for system parameters that could increase the operating range results in  $R \sim \sqrt{(A_o P) / (SNR_{tn})}$ . Thus, increasing the laser peak power by a factor-of-10 and doubling the receiver radius results in factor-of-3 and factor-of-2 increases in  $R$ , respectively, even with fixed SNR. This combined factor-of-6 increase applies either to the ranges in Figures 5.3–5.5 (60 m, 192 m, 600 m) or leaving the ranges fixed, to the  $SNR_{tn}$  far-backscatter profiles themselves.

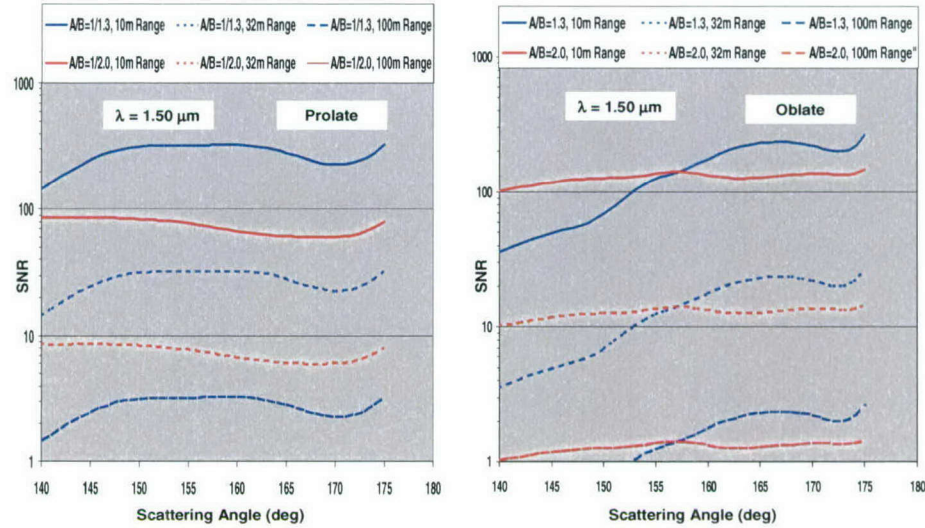


Figure 5.4. ‘Non-Sphericity’ Signal-to-Noise Ratio Profiles  $^P\text{SNR}_{1-2}(\Theta)$  at Far-Backscatter Angles ( $140^\circ \geq \Theta \geq 175^\circ$ ) for Prolate (left) and Oblate (right) Spheroid Bio-Aerosols ( $N_b = 1 \text{ cm}^{-3}$ ) and Spherical Ambient Background Aerosols ( $N_a = 100 \text{ cm}^{-3}$ ) for Laser Wavelength  $\lambda = 1.50 \mu\text{m}$ . Small eccentricity (blue), axis-ratio  $\epsilon = 1.0/1.3$  or  $1.3/1.0$ , and moderate eccentricity (red), axis-ratio  $\epsilon = 1.0/2.0$  or  $2.0/1.0$ . Ranges:  $R = 10 \text{ m}$  (solid),  $32 \text{ m}$  (dotted),  $100 \text{ m}$  (dashed). Incident polarization parallel ( $0^\circ$ ) to scattering plane.

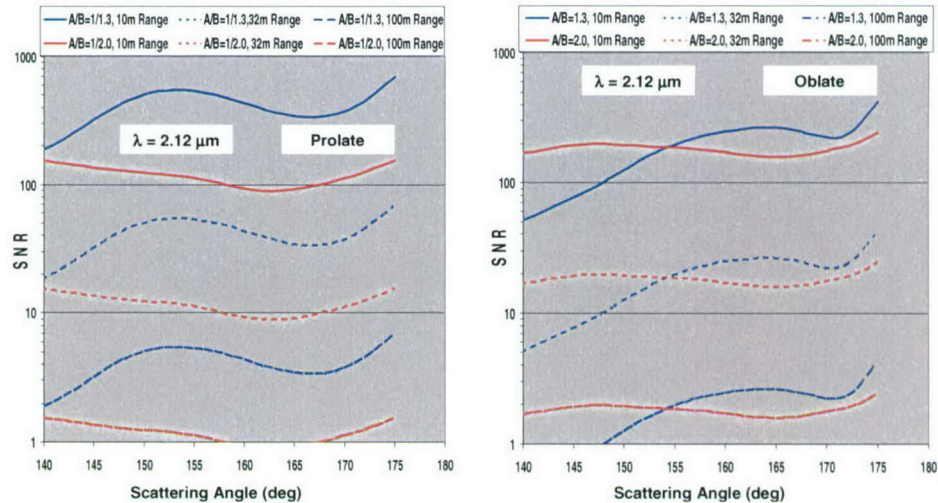


Figure 5.5. Same as Figure 5.4 Except for Laser Wavelength  $\lambda = 2.12 \mu\text{m}$ .

## 5.4 BIODEFENSE CONFIGURATION DESIGNS

Regarding deployment, the separation of the laser transmitter and receiver(s) in the SPADE bistatic lidar system permits two basic standoff bio-aerosol defense configurations—perimeter and area—depending on the deployment and relative coordination of transmitter-receiver pairs. As indicated in Sections 4 and 6, specific scattering angles in the far-backscatter and near-forward scatter directions contain substantial aerosol-discriminating polarimetric information, whereas much less information is contained at side-scatter angles. For standoff bio-aerosol detection it is not necessary, therefore, to make polarimetric measurements over the full range  $0^\circ < \Theta < 180^\circ$ , but rather over more restrictive angle ranges, particularly in the backscatter region.

The detection procedure (discussed in Section 6) relies on continuous monitoring of specific grid-locations at fixed scattering angles. Simple geometric considerations of Section 5.4.1 establish that the locus of constant scattering angle is a circle having the laser-to-detector distance  $L$  as a cord. Unless the derivation of this principle is of interest, the first half of Section 5.4.1 can be ignored. Application of the circular pattern of locations having constant scattering angle is then considered, providing for fixed-angle-monitoring designs that emphasize the most favorable scattering angles. These are the perimeter and area defense designs, detailed in Section 5.4.2.

### 5.4.1 Loci of Constant Scattering Angle

In Figure 5.6 are depicted one laser-transmitter T and one receiver-detector D separated by distance  $L$ . The scattering volume, the source of the scattered radiation, is located at Q. The transmitter beam axis is directed outward along TQ and the receiver field-of-view axis is aligned along DQ. The scattering plane is defined by these two axes.  $\Theta$  is the particular angle through which radiation incident along TQ is redirected.

The geometry of a bistatic lidar system is based on the distance  $L$  between laser-transmitter and receiver-detector, as shown in Figure 5.6,  $TD = L$ . The scattering angle can range from  $0^\circ$  for directly forward scattering to  $180^\circ$ , which is the conventional monostatic lidar direct-backscatter direction. For scaling purposes  $L$  can be taken as unity in order to concurrently include area coverage scenarios from the size of a ventilation duct to a football field.

The angles  $a$ ,  $b$ ,  $c$ ,  $d$ ,  $e$ , and  $f$  in Figure 5.6 are the interior angles of two triangles formed by connecting the points T, Q, and D to the center of the circumscribed circle of radius  $r$ . The center of this circle is located at the intersection of the perpendicular bisectors of the two axes TQ and DQ. Its magnitude can be found from  $r = (L/2)/\sin(\psi/2) = -(L/2)/\sin[\frac{1}{2}(a + b)]$ , since the sum of the apex angles of the two triangles is  $(a + b) = (2\pi - \psi)$ .

That these two triangles are isosceles is confirmed by applying the ‘law of sines’ to each:  $\sin(c)/r = \sin(d)/r$ , and  $\sin(e)/r = \sin(f)/r$ . The conclusion is that  $c = d$  and  $e = f$ , making each triangle,  $(b, c, d)$  and  $(a, f, e)$ , isosceles. In fact, for any and all positions of Q on the circumscribed circle these pairs of base angles are always equal, and both legs being  $r$ , this means that each of the two triangles individually is isosceles. Because these triangles are always isosceles, it follows  $(a + 2e) = \pi$ , and  $(b + 2d) = \pi$ , which when added give  $(d + e) = \pi - (a + b)/2$ .

Further, it is evident from Figure 5.6 that for constant values of  $L$  and  $r$ , the angle  $\psi$  is also constant. But, as already seen,  $(a + b) = (2\pi - \psi)$ , meaning that the apex angle sum  $(a + b)$  is constant; and so  $(d + e)$  is constant. But, the scattering angle is just  $\Theta = \pi - (d + e)$ . Since for any

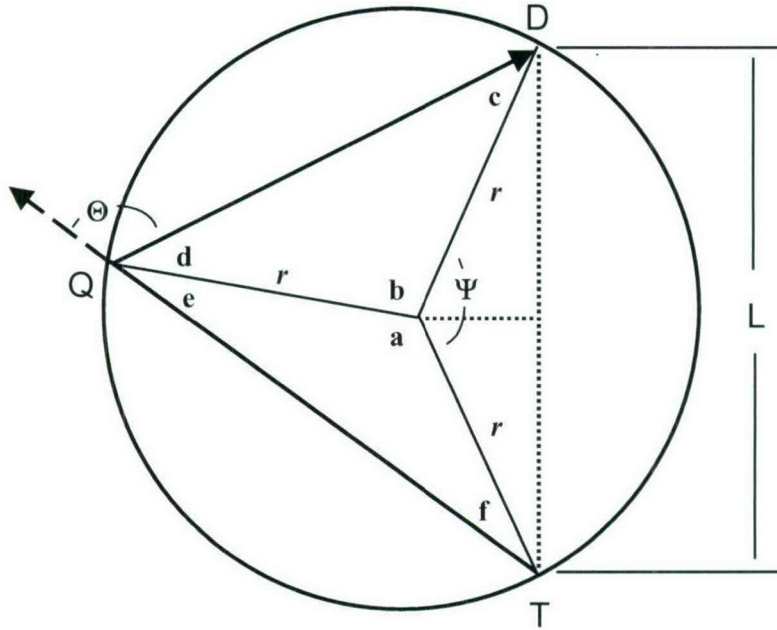


Figure 5.6. Bistatic Lidar Geometry. Laser-transmitter at  $T$  and receiver-detector at  $D$ , separated by  $TD = L$ , monitoring sample volume located at  $Q$ . Perimeter of circle – locus of constant scattering angle  $\Theta$ , constant backscatter angle to left versus constant forward-scatter angle to right of  $TD$  dashed line.

$Q$  on the circle ( $d + e$ ) is constant, the final conclusion is that *the scattering angle  $\Theta$  has a constant fixed value anywhere on the  $(T, Q, D)$  circumscribed circle having  $L$  as a cord.*

Clearly, the ranges  $TQ$  and  $DQ$  will vary depending on the position of  $Q$  on the circumscribed circle; in general the two ranges,  $R_T$  and  $R$  in Section 5.1, are no necessarily equal. The bistatic lidar equation, Eq (10D) or (10E), allows this condition by using the separate path transmittances,  $t(R)$  and  $t(R_T)$ , and overlap factor  $\xi(R, R_T)$ . The implications of this simple circular locus of constant scattering angle are pursued further in Section 5.4.2.

The distinction between backward and forward scattering is now made. The bistatic lidar system axis  $TD$ , the dash vertical chord in Figure 5.6, divides backscattering ( $\Theta > 90^\circ$ ) from forward scattering ( $\Theta < 90^\circ$ ). The longer portion of the circle perimeter (left side) is, therefore, the locus of constant backscatter angle, whereas the shorter portion is the locus of the supplementary forward scattering angle. Figure 5.6 is drawn so that the scattering angle is approximately  $\Theta = 120^\circ$ , a backscatter value that is fixed at any position on the left perimeter. For any position on the perimeter to the right of the system axis  $TD$ , as simple construction can verify, the scattering angle is  $\Theta = 60^\circ$ , a forward scattering angle.

For the singular condition of  $r = TD/2$  ( $= L/2$ ), the center of the circle then lies at the center point of the chord  $TD$  and the locus of constant scattering angle, the circle of diameter  $L$ , is the locus of constant side-scatter angle  $\Theta = 90^\circ$ .

Knowing the pattern of scattering measurements—given transmitter and receiver locations—has implications with regard to the logistics of bio-aerosol defense deployment. This is qualitatively illustrated in Figure 5.7, where various loci of constant scattering angles form an electric-dipole field pattern.

Considering first the larger-than-half-circle arcs to the right of the TD chord in Figure 5.7—these correspond to the loci of constant backscatter angles, the largest depicted being labeled as  $\Theta = 150^\circ$ . Similarly on the left side of TD, the major arcs are again constant backscatter-angle loci. Also, circles have their minor arcs, which are the loci of constant forward scattering angles, the smallest being labeled as  $\Theta = 30^\circ$ .

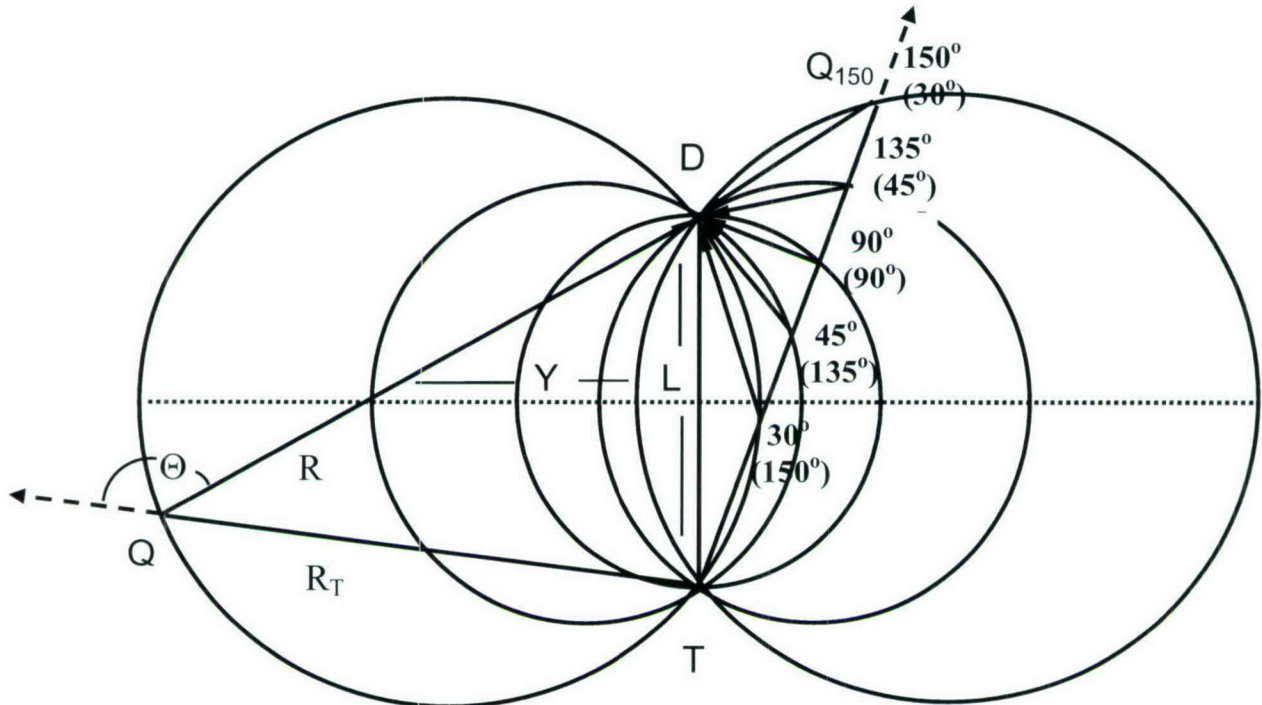


Figure 5.7. Composite Constant- $\Theta$  Coverage. Single transmitter and single receiver (bistatic lidar) loci of constant backward (longer arcs) or forward (shorter arcs) scattering angles. Scattering angles in parentheses apply to corresponding shorter circular arcs. Sample volume  $Q$  (at left) illustrates  $R_T$ ,  $R$ , and  $\Theta$ .

Clearly, to make forward scattering measurements,  $Q$  must be approximately located between the receiver and transmitter. The distance from the center of chord TD along its perpendicular bisector—dotted line in Figure 5.7—at which forward scattering ( $\Theta \leq 90^\circ$ ) is possible, is  $Y \leq L/2$ ; backscattering occurs at  $Y > L/2$ . In any case,  $Y = [L/2][\tan(\Theta/2)]$ . Table 5.7 gives  $Y$ -values for unit transmitter-receiver separation  $TD = L = 1$ .

**Table 5.8. Maximum Perpendicular Distance  $Y$  Scaled by  $L = 1$ , vs. Scattering Angle.**

Forward		Backward		Forward		Backward	
$\Theta$	$Y$	$\Theta$	$Y$	$\Theta$	$Y$	$\Theta$	$Y$
10°	0.04	170°	5.72	40°	0.18	140°	1.37
15°	0.07	165°	3.80	45°	0.21	135°	1.21
20°	0.09	160°	2.84	50°	0.23	130°	1.07
25°	0.11	155°	2.26	60°	0.29	120°	0.87
30°	0.13	150°	1.87	75°	0.38	105°	0.65
35°	0.16	145°	1.59	90°	0.50	90°	0.50

In spite of the negative implications for SNR-values of increased range seen in previous sections, the greater the separation, the greater Y. As before, Table 5.8 indicates that forward scattering ( $\Theta \leq 90^\circ$ ) measurements are possible out to a distance of half the separation,  $L/2$ . Given sufficient laser average power, backscatter measurements (e.g.  $\Theta = 165^\circ$ ) are obtainable out to several times the TD separation distance.

#### 5.4.2 Perimeter and Area Defense Scenarios

Expanding naturally from the discussion relating to Figure 5.7, an elementary two bistatic lidar arrangement for perimeter defense is depicted as the left panel in Figure 5.8. The standoff far-backscattering region of scattering angles is emphasized. (Forward scattering sites are all within the T-R quadrangle.)

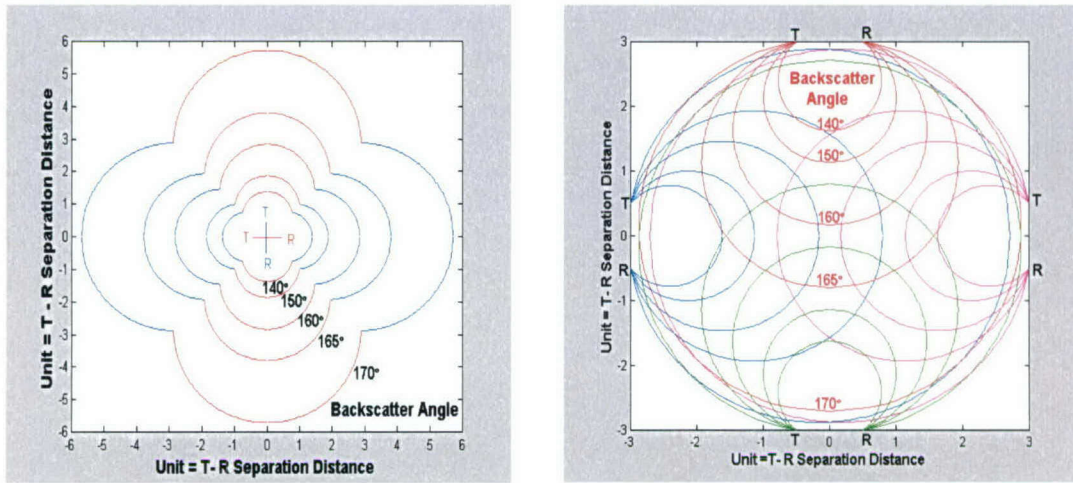


*Figure 5.8. Defense Designs: (Left) Perimeter Defense with Two Bistatic Lidars, (Right) Area Defense with Four Bistatic Lidars. Arcs (color indicates bistatic lidar) of sample sites at constant backscatter angle,  $\Theta = 140^\circ, 150^\circ, 160^\circ, 165^\circ, 170^\circ$ . Design scales with transmitter-receiver separation,  $TR = L$ .*

An arrangement of four bistatic lidars effecting area defense of a circular area is depicted as the right panel in Figure 5.8. A dense network of constant backscatter-angle measurement locations is produced. The maintenance of polarimetric scattering information at each site within the area is an intricate database management procedure alluded to in Section 6.1.

Although conceivable, no design is presented here of a bistatic lidar system made up of a single transmitter and a number of fixed-location receivers.

## 6. DETECTION PROCEDURE

This section outlines a procedure for detecting the introduction of bio-aerosols into an ambient aerosol background. The detection procedure is preliminary and has been neither tested nor implemented.

As indicated in Section 1.2 and detailed in Section 5.4, the detection of bio-aerosol release is accomplished by continually monitoring specific locations (sample volumes) in the area of interest—be it a stadium, auditorium, or air-duct—for changes that are not attributable to expected temporal variations in the ambient background aerosol. Fundamentally, the temporal changes occur in the physical properties of the combination of background and bio-aerosol particles. From the measurement perspective, however, the temporal changes are in the values of the four Stokes parameters of light scattered by all aerosols being irradiated by polarized laser light. These are the two end-points in the information chain—*aerosol properties vs. Stokes parameters*. The detection procedure developed here involves analysis of temporal changes in the Stokes parameters (more correctly, in the polarimetric properties formed from them) and does not involve retrieval of aerosol physical properties per se.

Bispectral incident light is recommended because two separate types of aerosols are combined, ambient background and bio-aerosol, each having its own effective radius (see Table 3.1). The primary wavelength at which measurements are made is dictated by the representative size of the suspected bio-aerosol particles. Specifically, it is such that the effective size parameter is  $x_{\text{eff}} = 2\pi r_{\text{eff}}/\lambda \cong 10$ , where  $r_{\text{eff}}$  is the effective radius (defined in Appendix B.5) of the suspect aerosol size distribution. In this report  $r_{\text{eff}} = 4.36 \mu\text{m}$ . The primary wavelength is, then, in the short-wave infrared (SWIR) wavelength region,  $1.4 \leq \lambda < 3.0 \mu\text{m}$ . The role of the second laser wavelength is to monitor the ambient background aerosols. Given ambient  $r_{\text{eff}}$  and  $m_{\text{real}}$  values dealt with here (Table 3.2), a near-infrared wavelength (NIR),  $0.8 \leq \lambda < 1.4 \mu\text{m}$ , is suggested in order to exploit the first interference maximum in the scattering efficiency function [MTL, Figure 9.12] located roughly within  $4 < x_{\text{eff}} < 6$ .

The bi-spectral illumination format of a SPADE system does not mean that full Stokes-parameter measurements are needed at both the primary and secondary wavelengths. For background monitoring as seen in Section 6.2, any incident polarization state will do and measurements of at most two Stokes parameters are needed. To detect possible bio-aerosols, the primary wavelength has to have a minimum of two incident polarization states and measurements of at least three Stokes parameters.

### 6.1 DATA PROCESSING FUNCTIONS

Figure 6.1 illustrates the detection procedure in the overall context of SPADE components: laser, receiver, and detection procedure. The first two components, the laser-transmitter and receiver, are dealt with in Section 5. The detection procedure, in turn, consists of three data processing functions represented in Figure 6.1 by the three shaded blocks. Each function is briefly described in this section, ending with the prescribed decision process questions themselves. The basic photometric aerosol scattering property is explained in Section 6.2. Analysis details of the aerosol characterization and decision process functions comprise Sections 6.3 and 6.4 – photometric and polarimetric, respectively.

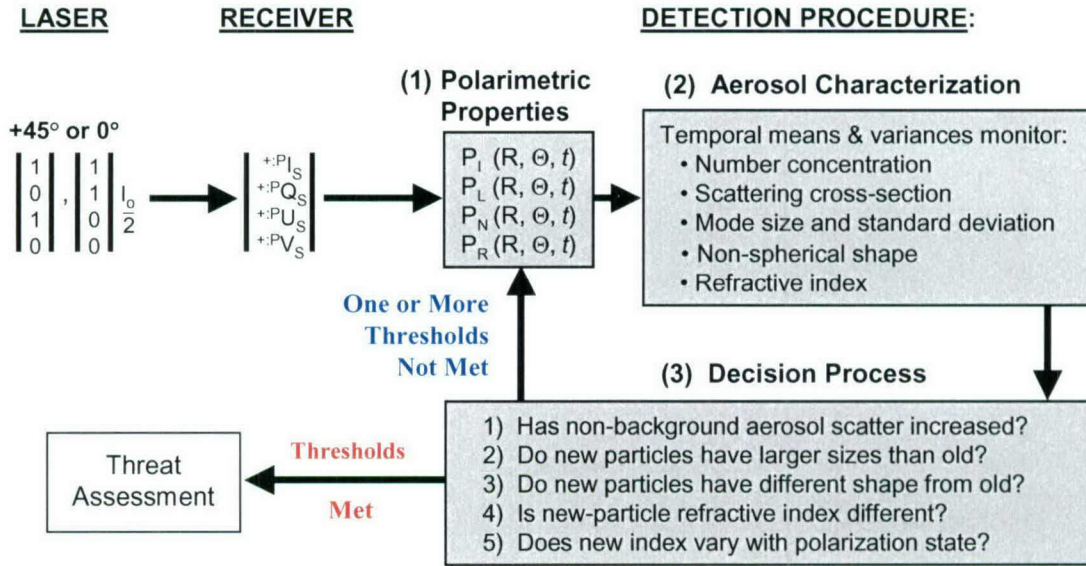


Figure 6.1. Detection Procedure Component of SPADE System. Detection procedure with three data processing functions: (1) Compute polarimetric property values, (2) Maintain database of prevailing aerosol conditions, and (3) Execute bio-aerosol decision process. Two incident polarizations:  $^+$  for  $+45^\circ$  or  $^P$  for parallel ( $0^\circ$ ) to scattering plane. (Range – R, scattering angle –  $\Theta$ , time – t.)

Generally, at any location under surveillance, measurements are made of the four scattered-light Stokes parameters for a minimum of two incident polarization states. In Figure 6.1 only the two states applied in the present study are indicated, linear polarization at  $+45^\circ$  (superscript  $^+$ ) and parallel (superscript  $P$ ) to the scattering plane (details in Section 2.2). In the context of this report specifically, only five of the resulting eight Stokes parameters are utilized, each varying with the scattering angle  $\Theta$ ; these are listed in Table 2.2. Two are always used in combination [ $^P I_{sca}(\Theta)$ – $^P Q_{sca}(\Theta)$ ], reducing to four the number of different polarimetric properties available for the decision process. These four are listed as the first block in the Figure 6.1 detection procedure.

The first function of the detection procedure is computation of the four polarimetric property values ( $P_{I,L,N,R} \sim I_{sca}/I_o$ , Section 2.3) at each location from measured scattered-light signals  $E_s$  (appropriate equation from Section 5.1). The four properties  $P_x$  ( $x$  being intensity, linearity, non-sphericity, or retardation) are monitored in time  $t$  at each location  $(R, \Theta)$ . For the purpose of this discussion the number of different scattering angles is limited to four. With four polarimetric properties there are 16 current location-specific  $P_{x,\Theta}$  values, which can be formed as a 4x4 matrix.

As indicated in Figure 6.1, the second of the three sequential functions is maintenance of the dynamic database of aerosol conditions at each  $(R, \Theta)$  under surveillance. This is not a database of physical aerosol properties, but rather of time-varying scattering characteristics of the combination–ambient background aerosols and potential bio-aerosols. Although not retrieved, the physical and optical parameters of these aerosols are what physically determine the polarimetric property values. Polarimetric properties serve, then, as surrogate information concerning number-concentration, effective size, shape, and refractive index of the combined aerosol population in any specific scattering volume.

The second data processing function is most simply accomplished by continually updating the current value and the first-difference  $[P_X(R, \Theta, t_2) - P_X(R, \Theta, t_1)]/\Delta t \equiv \Delta_t[P_X(R, \Theta)]$ . In the context of this SPADE feasibility study these would constitute a 2<sup>nd</sup> 4x4 matrix of  $\Delta_t[P_X(R, \Theta)]$  values available at each surveillance location ( $R, \Theta$ ). Additionally, the recent means (3<sup>rd</sup> matrix) and variances (4<sup>th</sup> matrix) would be generated and maintained over the most recent (~100 second) time interval. (More sophisticated dynamic trend-extrapolation of property median and range statistics could supplant the simple mean and variance database maintenance suggested here.) The structured arrays of current  $P_X(R, \Theta)$ ,  $\Delta_t[P_X(R, \Theta)]$ , recent means, and variances constitute the information database used in the bio-aerosol decision process—the third function of SPADE detection procedure.

The decision process involves a sequence of questions – five summarized in the lower shaded box in Figure 6.1 – the answers to which determine if a potential bio-aerosol release has occurred. The logic behind the questions is based on the influence of different aerosol physical properties on the scattering of polarized light. A step-wise interrogation of the structured array of measurement-derived information is made to decide if temporal changes are due to the introduction of suspect aerosols or are explainable as natural background variations. Threshold values for specific database items from function (2) are used to decide whether each question is affirmed (threshold met or exceeded) or refuted (threshold not met). In particular, to meet or exceed all five thresholds in series results in threat assessment activities, whereas not meeting any one threshold results in continued monitoring.

The 1<sup>st</sup> question—Has non-background aerosol *scatter* increased?—is answered by comparison of temporal changes at the two spectral wavelengths, specific., the temporal change  $\Delta_t[P_l(R, 155)]_{SWIR}$  versus  $\Delta_t[P_l(R, 155)]_{NIR}$ . (Explicit definition of *scatter* is the topic of Section 6.2.)

The 2<sup>nd</sup> question, regarding size of particles responsible for the temporal change, cannot be resolved in isolation from the two subsequent questions without forward-scatter measurements and without scattering matrix element  $a_3$  or  $a_4$  (Section 2.1 and Appendix E). For the outdoor standoff application (Section 5.2.2) only backscatter measurements are assumed and for this report neither  $a_3$  nor  $a_4$  is available. (The ambiguity of  $a_1$ ,  $b_1$ ,  $a_2$ , and  $b_2$ —the only elements analyzed here—to particle size in the far-backscatter region can be seen especially well in [MTL, Figures 10.29 and 10.30].)

The 3<sup>rd</sup> question—Do new particles have different shape from old?—is definitively answered by making use of the  $P_N$  property; as is detailed in Section 6.3.

The final two questions involve refractive index. While the 4<sup>th</sup>—Is new-particle refractive index different?—is answered using the  $P_R$  property (Section 6.4), the 5<sup>th</sup>—Does new index vary with polarization state?—involves the *dichroic* or *birefringent* [HC, Sections 8.3 and 8.4] characteristics of bio-aerosols and cannot be answered without a circular incident polarization state and a polarimetric measurement of the scattered light that provides information on the  $a_4$  matrix element. In the study reported here, neither condition is met so that in this study the 5<sup>th</sup> question is not resolved.

The specific scattering properties, photometric and polarimetric, used in the SPADE decision process are detailed in Sections 6.3 and 6.4.

## 6.2 TOTAL VOLUME SCATTERING COEFFICIENT

The aerosol characteristic that influences all scattered light measurements, irrespective of scattering angle, is the photometric quantity introduced in Section 4.1.3 – the *total volume scattering coefficient*  $N_c\langle C_{sca} \rangle_c$ , where the subscript signifies a combination of two aerosol types. More commonly, the product-quantity  $N\langle C_{sca} \rangle$  [ $\text{cm}^{-1}$ ] is called simply the *scattering coefficient* [TKD, p 112, eq 3.1.26; or MD, Section 11.3], and is also referred to as the *scatter coefficient* [e.g., TD, p 99]. (In scalar radiative transfer expressions, the total volume scattering coefficient integrated over the physical path length is the scattering optical thickness of the medium [e.g. MD, Section 9.3].) In relation to the directional volume scattering coefficients, the  $\beta_{ij}$ 's of Eq (2B) in Section 2.2,  $N_c\langle C_{sca} \rangle_c$  is the sum of all  $4\pi$  values of the phase-function related coefficient  $\beta_{11,c}(\Theta)$ . The descriptor *total* is significant; it emphasizes the distinction from *directional*.

The combined number-concentration is  $N_c = N_a + N_b$ . (Notation: The number-concentration  $N$  [ $\text{cm}^{-3}$ ] is not the  $N$  [–] used in [MTL, p 68]; these are related as  $N = NV = D$  [–] used in Section 2 of this report.) By itself, any  $N$  provides no information on the physical or optical properties of the scattering aerosols, but it does directly and linearly affect the magnitude of all scattering matrix elements.

The ensemble-average cross-section part  $\langle C_{sca} \rangle$  of the total volume scattering coefficient, explained further in Appendix A.7, is a doubly integrated quantity; it is *total* because all scattering angles are included (Eq A.10A), and is *volume* since it contains the contributions of all  $N_c$  particles per unit of spatial volume. (Ensemble-averaging  $\langle \cdot \rangle$  is defined in Appendix B.4.) As seen in Section 2.2, the combined total volume scattering coefficient is just the sum of the individual total volume quantities of the ambient background and possible bio-aerosol,

$$N_c\langle C_{sca} \rangle_c = N_a\langle C_{sca} \rangle_a + N_b\langle C_{sca} \rangle_b \quad (15A)$$

The environmental quantity that is measured by the bi-static lidar of Section 5.1 is the combined *directional* volume scattering coefficient matrix  $\mathbf{B}_c(\Theta)$ , Eq (4D). It is evident from Eq (5D) in Section 5.2.3 that the spherical-average ( $1/4\pi$ ) of the total volume scattering coefficient is the factor relating the two directional scattering quantities – the normalized scattering matrix  $\mathbf{F}_c(\Theta)$  (given as Eq (2A) in Section 2.1) and  $\mathbf{B}_c(\Theta)$ . Thus, *the total volume scattering coefficient*  $N_c\langle C_{sca} \rangle_c$  is the scalar measure of the overall scattering ability of the aerosols; it is independent of incident laser polarization state [MTL, p 96] and of scattering angle  $\Theta$ . (If non-spherical particles have preferred orientation, then the total volume scattering coefficient would vary with the angle of incidence relative to that orientation and, therefore would be some function of  $\Theta$ ). In developing the detection procedure outlined here it is advantageous to separate the detected environmental quantity into its  $\Theta$ -independent and  $\Theta$ -dependent parts.

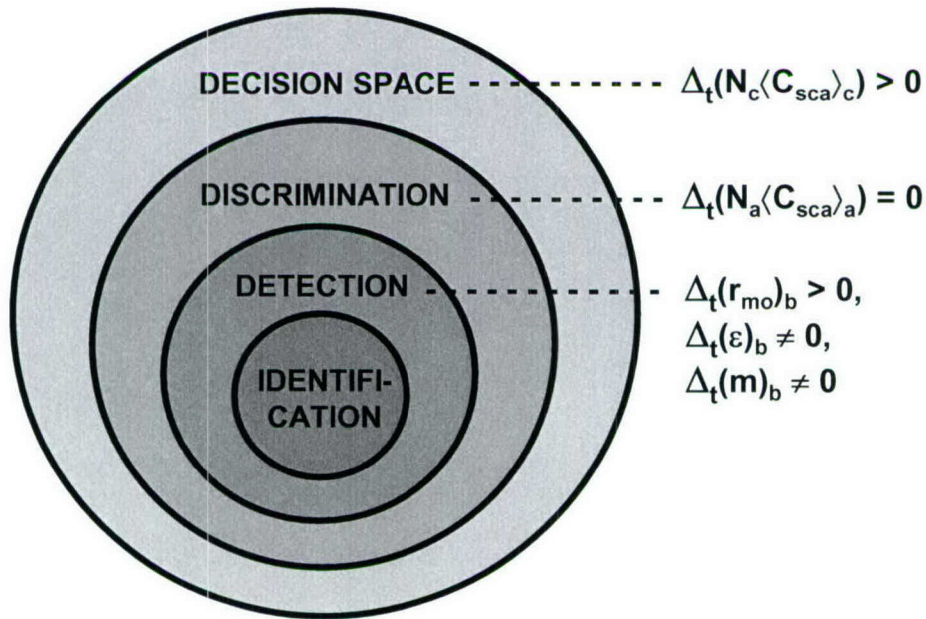
Temporal change in the combined total volume scattering coefficient  $N_c\langle C_{sca} \rangle_c$  at a specific location initiates the decision process by which the likelihood of bio-aerosol introduction is assessed. Temporal change is taken into account for each of the two different aerosol types, i.e.,

$$\Delta_t(N_c\langle C_{sca} \rangle_c) = \Delta_t(N_a\langle C_{sca} \rangle_a) + \Delta_t(N_b\langle C_{sca} \rangle_b) \quad (15B)$$

(The notation  $\Delta_t(\cdot)$  is an abbreviated form of  $\Delta(\cdot)/\Delta t$ , the finite first-temporal difference.) SPADE decision space consists of all measurements that indicate increased aerosol scatter; as in Figure 6.2, all  $\Delta_t(N_c\langle C_{sca} \rangle_c) > 0$ . Within this space, discrimination is made for  $\Delta_t(N_b\langle C_{sca} \rangle_b) > 0$ .

This is accomplished by affirming that  $\Delta_t(N_a \langle C_{sca} \rangle_a)$  is zero or, if not zero, that its value is within recent ambient background variations.

The initial two stages in the Figure 6.2 decision process therefore are based on photometric (polarization indifferent) information. Involved is monitoring only the 1<sup>st</sup> Stokes parameter, the intensity of scattered light, from which is formed  $P_l(\Theta) = {}^+I_{sca}(\Theta)/I_o \sim a_1(\Theta)$ , Eq (6A). (It is noted that  $a_1$  occurs in the 1<sup>st</sup> Stokes parameter no matter what incident polarization state is used. Also, in this study only  $a_1$  appears in  ${}^+I_{sca}$  because all non-spherical particles are assumed to be randomly oriented so that  $b_3 = 0$ ; Appendix A, Eq (A.2C).)



### 6.3 PHOTOMETRIC ANALYSIS

The initial step in the aerosol characterization step is the spectral separation of background from possible bio-aerosol temporal changes. Then the thorough exploitation is made of the scattering-angle profiles of the intensity  $P_l(\Theta) \sim \beta_{11}(\Theta)$  at the primary suspect-aerosol measurement wavelength.

The separation of temporal changes in the two component scattering coefficients,  $\Delta_t(N_a \langle C_{sca} \rangle_a)$  and  $\Delta_t(N_b \langle C_{sca} \rangle_b)$ , is best done spectrally. From Figure 4.1 (red curves), the ambient background particles have their largest total volume scattering coefficient in the NIR ( $\lambda = 1.06 \mu\text{m}$  is shown) over the complete range of scattering angles  $\Theta \in [0^\circ, 180^\circ]$ . The background plus bio-aerosols have their largest total volume scattering coefficient in the SWIR at all scattering angles except  $\Theta < 10^\circ$ . The reason is the enhanced scatter of SWIR light by the bio-aerosols since at such wavelengths (esp. at  $\lambda = 2.12 \mu\text{m}$ ) background scatter is a minimum for all scattering angles (refer to Figure 4.1, red curves). Thus, separate assessment of the two types of scattering aerosols is achieved by monitoring  $\Delta_t(N_a \langle C_{sca} \rangle_a)$  using NIR laser light of any polarization and monitoring  $\Delta_t(N_b \langle C_{sca} \rangle_b)$  using SWIR laser light of a specific polarization state. If a small increase is detected

in the NIR coincident with substantial change in the SWIR, esp. in region  $\Theta > 140^\circ$ , the increase is likely due to new suspect aerosols, i.e., to  $\Delta_t(N_b\langle C_{sca} \rangle_b)$ . If the opposite is true—small SWIR increase, large NIR change—then the combined increase is more likely due to ambient background aerosol change,  $\Delta_t(N_a\langle C_{sca} \rangle_a)$ . This bispectral separation strategy is shown near top of Table 6.1.

**Table 6.1. Synopsis of Bio-Aerosol Detection Procedure.**

Temporal change in:	Assessed by change in:	Wave-length	Incident Pol States	Measured at $\Theta$ :
$N_a\langle C_{sca} \rangle_a$	$P_l$	NIR	1: <sup>+</sup>	$155^\circ$
$N_b\langle C_{sca} \rangle_b$	$P_l$	SWIR	1: <sup>+</sup>	$155^\circ$
$N_b$	$P_l$	SWIR	1: <sup>+</sup>	$140^\circ, 155^\circ, 170^\circ$
$\langle C_{sca} \rangle_b$	$P_l$	SWIR	2: <sup>+</sup> , <sup>P</sup>	$\leq 20^\circ, 155^\circ, 170^\circ$
$r_{mo,b}$	$P_l, P_L$	SWIR	$\geq 2: , , P, R$	$\leq 20^\circ, 155^\circ, 170^\circ$
$\epsilon_b$	$P_N$	SWIR	$\geq 2: , , P, R$	$140^\circ, 155^\circ, 170^\circ$
$m_b$	$P_R$	SWIR	$\geq 2: , , P, R$	$\leq 20^\circ, 155^\circ, 170^\circ$

Subscripts: <sub>a</sub> ambient aerosol, <sub>b</sub> bio-aerosol, <sub>l</sub> intensity, <sub>L</sub> linear polarization, <sub>N</sub> non-sphericity, <sub>R</sub> retardation.

Polarization states: <sup>+</sup> linear at  $+45^\circ$ , <sup>P</sup> parallel ( $0^\circ$ ), <sup>R</sup> right-hand circular.

Next,  $\Delta_t(N_b\langle C_{sca} \rangle_b)$  is separated into its independent components. *The number-concentration N is an absolutely independent environmental quantity; it does not vary with  $\lambda$  or  $\Theta$ , and is independent of all particle optical and physical properties.* On the other hand,  $\langle C_{sca} \rangle$  depends on all particle properties ( $m, r_{mo}, \epsilon$ ), in addition to varying with  $\lambda$ , but it is independent both of  $\Theta$  (unless non-spherical particles are preferentially oriented) and also of the incident polarization state [MLT, p 96]. Because of this particle-property-dependence difference, N and  $\langle C_{sca} \rangle$  are independent of each other. Therefore,

$$\Delta_t(N_b\langle C_{sca} \rangle_b) = \langle C_{sca} \rangle_b \Delta_t N_b + N_b \Delta_t \langle C_{sca} \rangle_b \quad (15C)$$

The time-change term that provides information on the physical properties of the newly added particles is the  $\Delta_t \langle C_{sca} \rangle_b$  term. Whereas the  $\Delta_t N_b$  term can be assessed using intensity ( $P_l$ ) measurements only, evaluation of the  $\Delta_t \langle C_{sca} \rangle_b$  term requires additional polarimetric measures (at least  $P_L, P_N$ , and  $P_R$ ).

In Figure 4.3 (left panels, green vs. blue curves) and Section 4.1.3, it is shown that  $\Delta_t N$  results in the same increase at all  $\Theta \in [0^\circ, 180^\circ]$ . For spherical particles the intensity increases linearly and monotonically with concentration. However, if the added particles are not spherical this simple intensity increase is masked by modifications of its angular profile (the phase function) at all backscatter angles  $\Theta \in [90^\circ, 180^\circ]$  – all except  $\Theta \cong 155^\circ$ , refer to Figure 4.5 (left panels). (In the forward scatter region  $\Theta \in [0^\circ, 90^\circ]$ , non-spherical shape has little effect on the profile.) As the axis ratio departs from unity—for both oblate and prolate spheroids—the intensity ( $I_{sca} \sim \beta_{11}$ ) increases in the backscatter angle range of  $\Theta < 155^\circ$ , but it decreases in the range  $\Theta > 155^\circ$ . The implication is that at backscatter angles—except  $\Theta \cong 155^\circ$ —changes in  $P_l$  and N are not simply correlated. The measured (combined) backscatter  $P_l(\Theta \neq 155^\circ)$  could increase considerably or almost not at all for a given number-concentration increase depending on the shape of the newly added particles. (The identification of the shape-invariant scattering angle  $\Theta \cong 155^\circ$  is convincingly seen in [MLT, plate 10.2, 6 panels of right columns].) In any case, to monitor  $\Delta_t N_b$  it seems essential that intensity be measured at  $\Theta = 155^\circ$ .

In Figure 4.4 (left panels) are illustrated two  $\Delta_t\langle C_{sca} \rangle$  effects –  $r_{mo}$  and  $m$ —on the intensity profile. Comparing the green vs. red curves, the profile shape differences in the far-backscatter  $\Theta \in [140^\circ, 180^\circ]$ , and in the near-forward  $\Theta < 20^\circ$  regions are due to increased  $r_{mo}$ ; as the refractive index is the same for both curves. Conversely, comparing blue vs. green curves in  $\Theta \in [140^\circ, 180^\circ]$ , esp. at 2.12  $\mu\text{m}$  shows the far-backscatter enhancement due to an increased  $m$ -value; specifically from adding ‘BS’ ( $m_{real} = 1.52$ ) particles vs. adding similarly sized large ‘L’ ( $m_{real} = 1.42$ ) particles. Although  $P_l$  in the far-backscatter region does contain information on both  $r_{mo}$  and  $m$ , separation of the two effects using  $P_l$  alone is not clear-cut even for spherical particles. (But as seen in Figure 4.4, in the near-forward direction the  $r_{mo}$  influence dominates and  $m$  has only secondary impact.) For non-spherical particles, as in Figure 4.5 (left panels), non-sphericity of added particles complicates separation of these two effects even further.

For better attribution of any detected backscattered intensity increase to changes in  $N$ ,  $r_{mo}$ , or  $m$ , it is recommended that multi-angle measurements of  $P_l$  be made, in particular at  $\Theta = 140^\circ$ ,  $155^\circ$ , and  $170^\circ$  (provided that possible non-sphericity of particles is independently assessed—as in Section 6.4). An increase in  $P_l(155)$  at SWIR wavelengths means positive  $\Delta_t N_b$  and/or increased  $m$  and possibly increased  $r_{mo}$ , the latter two effects associated with  $\Delta_t\langle C_{sca} \rangle_b$ . However, a concurrent increase in  $P_l(170)$  smaller than produced by spheres, and a larger-than-sphere increase in  $P_l(140)$  indicate that the new particles are non-spherical – then the effect on  $\Delta_t\langle C_{sca} \rangle_b$  of  $\epsilon$  is also present. Without knowing more about at least one of the new particle properties (esp. shape) from other measurements, the final identification of the particular physical property ( $N$  vs.  $m$ ,  $r_{mo}$ , or  $\epsilon$ ) responsible for the increase in  $P_l(155)$  would remain ambiguous. (It is assumed that the form of the size distribution function  $n(r)$  for all particles, old and new, is the same; in this study the modified-gamma distribution, Section 3.2. If  $n(r)$  for either particle is expected to undergo short-term temporal change, then at least one additional angular measurement is needed.) The lower five rows of Table 6.1 summarize specifics of these polarimetric measurements (among others).

To recap the photometric portion of aerosol characterization—use is made of two spectral intensity changes to discriminate between a total volume scattering coefficient increase caused by ambient background  $\Delta_t(N_a\langle C_{sca} \rangle_a)$  vs. new larger potentially bio-aerosols  $\Delta_t(N_b\langle C_{sca} \rangle_b)$ . If the intensity increase is not explainable as due to natural background fluctuations, then the separation of  $\Delta_t N_b$  from  $\Delta_t\langle C_{sca} \rangle_b$  can be done qualitatively (at best) with photometric measurements, especially if the shape of the new particles is non-spherical – as is expected to be the case for weapon aerosols. More information is needed. For the Figure 6.2 decision process to advance to the detection stage, the polarimetric parts of SWIR scattered light measurements need to be utilized.

#### 6.4 POLARIMETRIC ANALYSIS

The first truly polarimetric property analyzed is non-sphericity,  $P_N(\Theta) \sim [\beta_{11}(\Theta) - \beta_{22}(\Theta)]$ . Figure 4.6 provides convincing evidence that non-spherical shape is easily distinguished from spherical shape ( $P_N(\Theta) \equiv 0$ ), throughout the backscatter region  $\Theta \in [90^\circ, 180^\circ]$ . In fact, for spheroid particles at least, the value of the axis ratio  $\epsilon$  can be retrieved from analysis of recent-past vs. present values of  $P_N(140)$ ,  $P_N(155)$ , and  $P_N(170)$ . As pointed out in [BAK, p 316], the angle range  $140^\circ \leq \Theta \leq 175^\circ$  is most sensitive to particle non-isotropic structure esp. to non-spherical shape. (A stepwise analysis procedure, exploiting Figure 4.6 angular profiles, is straightforward.) Table 4.3 confirms the significance of the  $P_N(170)$  environmental signal, esp. at 2.12  $\mu\text{m}$ . Furthermore, from Figure 4.6 (right panels) most signals at  $\Theta = 155^\circ$  and  $140^\circ$  are at least as large as those at  $\Theta = 170^\circ$ .

With even a rough estimate of  $\epsilon$ , the recent and present values of  $P_L(\Theta) \sim \beta_{21}(\Theta)$  at  $\Theta = 155^\circ$  and  $170^\circ$  can be used to specify the form of new particle non-sphericity–prolate vis-à-vis oblate—reference Figure 4.5 (right panels). More comprehensive depictions of the ratio:  $-P_L(\Theta)/P_l(\Theta) = -\beta_{21}(\Theta)/\beta_{11}(\Theta) = -b_1(\Theta)/a_1(\Theta)$ , for both prolate and oblate spheroids having size parameter values  $0 \leq x_{\text{eff}} \leq 30$ , are found in [MTM, plate 3]. The effective size parameter for Figure 4.5 curves (from data in Tables 3.1 and 3.2) is the normalized scatter-weighted sum of the two aerosol type  $x_{\text{eff}}$ 's, specific.  $x_{\text{eff},c} = [N_a \langle C_{\text{sca}} \rangle_a x_{\text{eff},a} + N_b \langle C_{\text{sca}} \rangle_b x_{\text{eff},b}] / [N_a \langle C_{\text{sca}} \rangle_a + N_b \langle C_{\text{sca}} \rangle_b] = [(100)(0.0954)(1.42) + 1(58.88)(12.92)] / [(100)(0.0954) + 1(55.88)] = 11.84$ . (The stepwise procedure to implement the prolate vs. oblate assignment procedure is not presented here; but it is straightforward.)

Knowledge of  $\epsilon$  is materially enhanced by  $P_N$ . With the non-sphericity form–prolate or oblate–of newly added particles now known from  $P_L$  far-backscatter values,  $\epsilon$  could be constrained by a more definitive interpretation of the three  $P_l$  angular values using Figure 4.5 (left panels). But  $\epsilon$  is much more precisely evaluated by the non-sphericity profiles  $P_N(\Theta)$  in Figure 4.6 (right panels). If the dual-angle far-backscatter  $P_L$  test indicates oblate spheroid new particles, then the three-angle  $P_N$  far-backscatter measurements are used to specify the most likely value of  $\epsilon$ , as in Figure 4.6 (upper right). If the  $P_L$  test indicates prolate new particles, the procedure (not detailed here) is the same but uses Figure 4.6 (lower right). Exclusion or acceptance of spheres  $\epsilon = 1.0/1.0$  as a possibility is readily done as the initial step since for spheres  $P_N(140) = P_N(155) = P_N(170) \cong 0$ . (For other size parameters, reference is directed to [MTM, plate 6].)

With  $\epsilon$  known, the differences (like those in Figure 4.5, left panels) in  $P_l(140)$  and  $P_l(170)$ , relative to  $P_l(155)$  are now assignable to changes in either  $r_{\text{mo}}$ , or  $m$ , or both. In any specific sample volume located at  $R$ , the smallest difference among the three  $P_l$ 's ( $\Delta_t[P_l(R, \Theta)]$ ,  $\Theta = 140^\circ, 155^\circ, 170^\circ$ ) is, preliminarily, attributed to  $\Delta_t N_b$ , while the two larger differences are attributed to  $(\Delta_t N_b + \Delta_t \langle C_{\text{sca}} \rangle_b)$  – which means the larger ones include the effects of changes in  $r_{\text{mo}}$  and/or  $m$ .

Given the four polarimetric properties applied in this study, the  $r_{\text{mo}}$  effect is especially difficult to isolate without a near-forward measurement or an additional incident polarization state—both options included in the Table 6.1 listings. Using another polarimetric property based on lower diagonal elements of the volume scattering matrix,  $\beta_{33}$  or  $\beta_{44}$  (Appendix A.5), the variation with representative particle size (here  $r_{\text{mo}}$ ) of the far-backscatter polarimetric properties formed from either of these volume scattering coefficients is sufficient to isolate the effect of an increase in  $r_{\text{mo}}$  from an increase in  $N$ . (The utility of  $\beta_{33}$  and  $\beta_{44}$  in extracting information from light backscattered at  $\Theta = 160^\circ$  by objects is convincingly shown in [ZCT, Figure 2].) Given  $\lambda$ , the size parameter  $x_{\text{eff},c}$  changes with  $r_{\text{mo},b}$  and the consequences in terms of the lower diagonal element values are clearly seen in the far-backscatter portions of [MTM, plates 7 and 8]. In the final analysis, the Table 6.1 polarimetric properties without a near-forward measurement cannot definitive isolate the effect of such a  $r_{\text{mo},b}$  change.

Figure 4.7 depicts angular profiles of the volume scattering coefficient  $\beta_{43}$  forming the retardation polarimetric property  $P_R$ —the different (changed) phase retardance being due primarily to changed refractive index. The ordinate scaling of Figure 4.7 detracts from the importance of the far-backscatter features in  $P_R$ . Furthermore, the Table 4.3 prolate spheroids values at  $\Theta = 170^\circ$  coincide almost precisely with the zero cross-over point of these angular profiles (with  $x_{\text{eff},c} \cong 12$ , refer [MTM, plate 9]). Although not demonstrated here, with  $\epsilon$  known, the three-angle far-backscatter measurements:  $P_R(R, \Theta)$ ,  $\Theta = 140^\circ, 155^\circ, 170^\circ$ , readily determine the impact of changed-refractive-index on the intensity angular profile, esp. on the relative values of the three co-located measurements of  $P_l(R, \Theta)$ .

To summarize the polarimetric portion of aerosol detection (Table 6.1) at the suspect-aerosol primary wavelength—a minimum of three far-backscatter measurements ( $\Theta \cong 140^\circ, 155^\circ, 170^\circ$ ) of at least four polarimetric properties are needed to separate the  $N$ ,  $r_{mo}$ ,  $m$ , and  $\varepsilon$  parts of any detected changes in light intensity backscattered by aerosols. The intensity  $P_l(155)$  is especially useful in monitoring changes in  $N_b$ . At adjacent far-backscatter angles, the physical and optical aerosol properties, esp.  $\varepsilon$ , systematically affect  $P_l$ . But non-sphericity  $P_N \sim [\beta_{11} - \beta_{22}]$  definitively isolates and specifies the  $\varepsilon$  part. Retardation  $P_R$  is a useful measure of the  $m$  part. Without near-forward measurements, the  $r_{mo}$  part can only be isolated if backscatter measurements of  $\beta_{33}$  or  $\beta_{44}$  are available. Finally, in the far-backscatter region, polarization linearity  $P_L$  is minimally useful in the presence of non-spherical particles.

## 7. SUMMARY AND CONCLUSIONS

The feasibility of a standoff polarimetric aerosol detection (SPADE) system is assessed given disperse aerosols (i.e., single-scattering theory is applicable) and current laser and detector component parameters. Four different volume scattering coefficient matrix elements—associated with intensity, degree of linear polarization, aerosol particle non-sphericity, and aerosol particle refractivity—are determined from scattering code computations, not from measurements. Computations are performed twice, once for the background aerosols alone with number-concentration of 100 particles per  $\text{cm}^3$ , and then for the same background aerosols combined with a bio-aerosol simulant having number-concentration of 1 particle per  $\text{cm}^3$ , i.e., for a total number-concentration of  $101 \text{ cm}^{-3}$ , mixing ratio (relative concentration)  $R_N = 1/100$ .

Differences between these two sets of computations are then used to evaluate the signal-to-noise ratios (SNR) for each of the four matrix elements in three application scenarios. The scenarios employed in making the SNR determinations are: outdoor stadium (1600 m), indoor auditorium (50 m), and building HVAC system (1 m), where nominal range from scattering aerosol to detector is in parentheses. Of these, the HVAC application is very feasible using current laser and detector technology – all four elements have large SNR’s. The indoor application is feasible – reliably providing at least two different elements. However, for the outdoor application current SWIR optical components can provide information, within the shot-noise limit  $\text{SNR} > 12$ , on only one matrix element quantity – the scattered intensity. While the intensity measurement is necessary information it is generally not sufficient to detect bio-aerosols introduced into typical background aerosols at relative concentrations  $R_N \leq 1/100$ .

The study documented here is limited to four polarimetric quantities developed from four matrix elements  $a_1$ ,  $b_1$ ,  $a_2$ , and  $b_2$ , which are made available by the two incident linear polarization states employed. Even for randomly oriented homogeneously dispersed particles there are at least two more elements available,  $a_3$  and  $a_4$ ; both occurring in the lower right block and, at backscatter angles, sensitive to particle refractive index. A circular incident polarization state is needed to exploit fully this added information in the scattered light. Further, if suspect aerosols have narrowly distributed sizes or highly irregular shapes, then elements in the off-diagonal blocks of the scattering matrix,  $b_3$  through  $b_6$ , take on very distinctive backscatter profiles.

### 7.1 ENVIRONMENTAL SIGNALS

Four environmental signals (the  $P_X$ ’s; Table 2.2) are formed from the volume scattering coefficient values excerpted from Tables 4.1 – 4.4. The relative rankings of each polarimetric property by strength of signal alone are presented in Table 7.1. Not surprisingly,  $P_I(\Theta)$  has the strongest signal since it is based on the intensity directional volume scattering coefficient  $\beta_{11,b}(\Theta)$ , which is directly associated with the total volume scattering coefficient (Section 6.2). The bio-aerosol total volume scattering coefficient is the product of its concentration  $N_b$  and its average scattering cross-section  $\langle C_{\text{sca}} \rangle_b$ , the latter being especially large. Also, as expected from lidar research, for spheroid bio-aerosol particles the non-sphericity property  $P_N$  is second strongest in the back-scattering region but not in the near-forward scattering directions; there the retardation-related property  $P_R$  is. But in almost all situations – spherical or non-spherical bio-aerosol particles, forward or backward scattering – the retardation property  $P_R$  is a stronger signal than the linearity property  $P_L$ .

**Table 7.1. Relative Rankings of Bio-Aerosol Signal Strengths.**  
**Spherical and spheroidal particle shapes. Bwd – backward,  $\Theta = 170^\circ$ .**  
**Fwd – forward,  $\Theta = 5^\circ$  or  $6^\circ$ . Bio-aerosol ‘BS’, Tables 3.1 and 3.2.**

Bio-Aerosol Shape: Polarimetric ~ Physical	Spherical		Spheroidal	
	Fwd	Bwd	Fwd	Bwd
$P_I \sim N, \langle C_{sca} \rangle$	1	1	1	1
$P_L \sim r_{eff}$ or $r_{mo}$	3	3	3	3
$P_N \sim \epsilon$	---	---	4	2
$P_R \sim m$	2	2	2	4

Since the strengths of all environmental signals vary directly with number-concentration, they will likewise vary with the mixing ratio  $R_N$ , as long as physical properties ( $r_{eff}$ ,  $\epsilon$ ,  $m$ ) of both bio- and ambient aerosols are approximately fixed. Therefore to a considerable extent, the relative rankings in Table 7.1 are expected to be independent of  $R_N$ .

Concisely, of the four polarimetric properties studied, intensity  $P_I$  is the best discriminator in both backward and forward scattering directions. For realistic bio-aerosols, the next-best discriminator is non-sphericity  $P_N$  in backward, but  $P_R$  in forward directions. The readily obtained and much-researched degree of linear polarization  $P_L$  is found to be of only tertiary importance as a bio-aerosol discriminator, in spite of the fact that for spherical particles it has very distinctive far-backscatter (bow) features.

All environmental signals increase directly with number-concentration  $N$ —a quantity independent of other aerosol properties. Similarly all signals vary directly with  $\langle C_{sca} \rangle$ , which is determined by physical and optical properties of the scattering particles, in particular, particle size and real refractive index. Therefore, by utilizing specific polarimetric quantities sensitive to refractivity, the scattering change resulting from the same change in  $N$  for like-sized background aerosols vs. suspect aerosols is readily distinguished. In this study only one such quantity is used – called retardation  $P_R$ . Though its signal is degraded strongly by non-sphericity (and absorption) in the far-backscatter region,  $P_R$  is immune from shape effects at near-forward directions and there it is a sensitive refractivity discriminator. (It is recommended that added polarimetric quantities be employed in any future standoff detection study—supplemental to the four considered in this report; in particular, quantities that exploit the lower right diagonal elements of the scattering matrix, which are known to be index-sensitive in the backscatter region.)

Regarding wavelength sensitivity, SWIR wavelengths enhance bio-aerosol environmental signals at backward scattering angles over visible or NIR. For remote sensing of bio-aerosols employing near-forward scattering directions, the opposite is true; NIR environmental signals are stronger than those at SWIR wavelengths. For monitoring relatively small particles, esp. the ambient background aerosols, visible or NIR wavelengths are preferred in both backward and forward directions. Use of two separate wavelengths is advocated in order to definitively dissociate scattering changes due to background aerosol variations from those caused by the introduction of a new type of aerosol. The primary wavelength is in the SWIR ( $\lambda_1 \approx 2 \mu\text{m}$ ) and the other is toward the visible side of the NIR ( $\lambda_2 \leq 1 \mu\text{m}$ ).

A synopsis of a bio-aerosol physical property detection protocol that results from this study is contained in Table 7.2 (restated from Table 6.1). The initial step is the bispectral discrimination

between changes due to background vs. suspect aerosol. Then two incident polarization states are employed at the primary detection wavelength (SWIR) to provide information related to specific physical properties of the suspect aerosol.

**Table 7.2. Physical vis-à-vis Polarimetric Bio-Aerosol Properties – Detection Protocol.**

Temporal change in:	Assessed by change in:	Wave-length	Incident Pol States	Measured at $\Theta$ :
$N_a \langle C_{sca} \rangle_a$	$P_I : {}^+SNR_1$	NIR	1: ${}^+$	155°
$N_b \langle C_{sca} \rangle_b$	$P_I : {}^+SNR_1$	SWIR	1: ${}^+$	155°
$N_b$	$P_I : {}^+SNR_1$	SWIR	1: ${}^+$	140°, 155°, 170°
$\langle C_{sca} \rangle_b$	$P_I : {}^+SNR_1$	SWIR	2: ${}^+, {}^P$	$\leq 20^\circ, 155^\circ, 170^\circ$
$r_{mo,b}$	$P_L : {}^+SNR_2$	SWIR	$\geq 2: {}^+, {}^P, {}^R$	$\leq 20^\circ, 155^\circ, 170^\circ$
$\epsilon_b$	$P_N : {}^P SNR_{1-2}$	SWIR	$\geq 2: {}^P, {}^+, {}^R$	140°, 155°, 170°
$m_b$	$P_R : {}^+SNR_4$	SWIR	$\geq 2: {}^+, {}^P, {}^R$	$\leq 20^\circ, 155^\circ, 170^\circ$

Subscripts:  $a$  ambient aerosol,  $b$  bio-aerosol,  $I$  intensity,  $L$  linear polarization,  $N$  non-sphericity,  $R$  retardation.

Polarization states:  ${}^+$  linear at  $+45^\circ$ ,  ${}^P$  parallel ( $0^\circ$ ),  ${}^R$  right-hand circular.

To separate different particle property influences, measurements are recommended at multiple backscattering angles, specifically, three in the far-backscatter region:  $\Theta \cong 140^\circ, 155^\circ, 170^\circ$ . At each, a minimum of four polarimetric properties is needed to separate the  $N$ ,  $r_{mo}$ ,  $m$ , and  $\epsilon$  parts of any detected changes in light intensity backscattered by aerosols. The intensity  $P_I(155)$  is especially useful in monitoring changes in  $N_b$ . However, at the adjacent far-backscatter angles,  $P_I$  is also affected by the physical (and optical) aerosol properties, esp.  $\epsilon$ . But non-sphericity  $P_N \sim [\beta_{11} - \beta_{22}]$  definitively isolates and specifies the  $\epsilon$  part. Retardation  $P_R$  is a useful measure of the  $m$  effect (at least in near-forward directions). Isolating the  $r_{mo}$  effect from backscatter measurements can only be done unambiguously if  $\beta_{33}$  or  $\beta_{44}$  are also used. In Table 7.2 an additional polarization state (right circular  ${}^R$ ) is included in the rows of particle properties that it could provide information on (forms of additional polarimetric properties are not given here). As a final note, in the far-backscatter region, polarization linearity  $P_L$  is minimally useful as an information source about non-spherical particles.

## 7.2 SIGNAL-TO-NOISE FOR THREE SCENARIOS

The signal-to-noise (SNR) computations utilize the four environmental signals for the three SPADE applications – outdoor stadium, indoor auditorium, and building HVAC system. State-of-technology laser and receiver specifications are used and, not surprisingly, the range  $R$  from scattering aerosol to detector is a very critical performance constraint. Conclusions are drawn for backscatter versus both back- and forward-scatter applications. Separate types of SNR values are analyzed: Table 5.6 has shot-noise limited  $SNR_{sn}$ 's that vary as  $1/R$ , whereas Figures 5.3–5.5 have thermal-noise (electronic component-noise) limited  $SNR_{tn}$ 's that vary as  $1/R^2$ . (It is accepted as given that in any outdoor longer-range scenario, only far-backscatter data are available.)

Regarding far-backscatter  $SNR_{sn}$  values: 1) In the outdoor stadium scenario, although pulse-averaging improves the SNR, the ambient background aerosol has SNR values that are unacceptably low except for  ${}^+SNR_1$ . Yet even with this condition, the ambient background aerosols may not be reliably monitored in the far-backscatter direction ( ${}^+SNR_1 = 6.2$ ), thus compromising the outdoor standoff detection unless laser power is enhanced. 2) In the indoor auditorium scenario, both intensity  ${}^+SNR_1$  and non-sphericity  ${}^P SNR_{1-2}$  are usable to discriminate between ambient and suspect bio-aerosols. The non-sphericity measurement is a solid

enhancement for standoff detection. 3) In the HVAC applications all polarimetric SNR's are usable, allowing some possibility for detecting changes in specific aerosol properties (Table 7.2), especially changes involving shape and refractivity.

For applications allowing forward measurements, intensity  $P_I$  and non-sphericity  $P_N$  have acceptable ( $\text{SNR}_{\text{sn}} > 12$ ) values for all scenarios and both bio-aerosol shape options. In both the indoor and HVAC scenarios, retardation  ${}^+\text{SNR}_4$  is also usable. For HVAC, all four SNR's are usable for detection. In the near-forward direction, the enhancement of the retardation quantity,  ${}^+\text{SNR}_4$ , is noteworthy; it becomes a very viable detection quantity irrespective of bio-aerosol shape.

To summarize reliability of scattering measurements throughout the far-backscatter region ( $140^\circ \geq \Theta \geq 175^\circ$ ), component thermal-noise limited  $\text{SNR}_{\text{tn}}$ 's based on the laser parameters given as the center values in Table 5.4 are used. The limit on acceptable size is set at  $\text{SNR}_{\text{tn}} = 6$  since the thermal-noise limit is inherently more realistic than the shot-noise limit. The values of  $\text{SNR}_{\text{tn}}$  for the intensity [ $P_I \sim a_1 \sim \beta_{11}$ ], linearity [ $P_L \sim b_1 \sim \beta_{21}$ ], and non-sphericity [ $P_N, \sim (a_1 - a_2) \sim (\beta_{11} - \beta_{22})$ ], appear to be usable in detecting introduction of suspect aerosols out to a range of approximately 50 m, as seen in Figures 5.3–5.5. (The  $\text{SNR}_{\text{tn}}$  for retardation ( $P_R \sim -b_2$ ) is not evaluated in this report.) Overall, the  $\text{SNR}_{\text{tn}}$  values are higher for  $\Theta > 150^\circ$ , but are usable throughout the far-backscatter angle region. In order to extend the range of significant backscatter measurements ( $R > 50$  m), an increase in average laser power from the  $\bar{P} = 1$  W used here is an obvious first recommendation. Increasing the receiver aperture diameter, if feasible, is a second option.

Final comments regarding SNR resulting from this SPADE feasibility study are the following:

- 1) Range is the ultimate limiting factor in any SPADE application. The  $1/R^2$  falloff in  $\text{SNR}_{\text{tn}}$ , the electronic component thermal-noise limited SNR, is especially restrictive.
- 2) For applications where SNR indicates that the SPADE concept is feasible non-trivial challenges remain. Among them are the formulation of the overlap factor (Section 5.1) and the laser-receiver coordination protocol for area or perimeter defense (Section 5.4).
- 3) Among SNR topics that warrant investigation are: (i) Detrimental effect on scattered signal strength of particle absorption ( $m_{\text{imag}} > 0$ ) especially at backscatter directions, (ii) Substantial particle-shape signal in the linearity property ( $P_L$ ) at near-forward directions (see Figure 4.5, right panels), (iii) Possibly large SNR of polarimetric quantities developed from off-diagonal b-elements where radically non-spherical particles are involved, and (iv) Detrimental effect on any SNR relating to all lower-right block elements whenever new suspect aerosols have refractive index little different from that of the ambient background aerosols.

## APPENDIX A SCATTERING MATRIX

The *volume scattering matrix*  $\mathbf{F}(\Theta)$  quantifies the capability of all the particles in a sample volume to redirect and re-orientate incident radiation. It specifies the relative magnitude of and the angular variation in the altered outgoing electromagnetic fields caused by the presence, in our case, of the scattering particles—altered from those of the incident beam. But these fields are not specified here – only the resulting measurable radiation vectors, the  $\mathbf{I}$ 's, are considered. Although  $\mathbf{F}(\Theta)$  depends on wavelength, that variation is not the topic of this appendix. Rather, we take the incident wavelength as given and consider only elastic scattering. The emphasis here is on the appropriate forms of the scattering matrix for optically thin scattering media. In particular, we only discuss characteristics of single-scattering, no radiative transfer protocol is involved that distinguishes a reflection from a transmission type of scattering matrix.  $\mathbf{F}(\Theta)$  specifies the outcome of at most one scattering event per incident photon. It is the single-scattering scattering matrix, referred to as the phase matrix in earlier publications [e.g., HT, eq 2.9]. However, regarding nomenclature, neither the awkward complete name – single-scattering volume scattering matrix – is used, nor the somewhat deceptive name phase matrix [BH, p 66].  $\mathbf{F}(\Theta)$  is here referred to either as the volume scattering matrix or more simply as the *scattering matrix*.

### A.1 SCATTERING EQUATION

The basic scattering relationship expresses the angle-varying scattered light vector as the product of the incident light vector and the volume scattering matrix, i.e.,

$$\mathbf{I}_{\text{sca}}(\Theta) \sim \mathbf{F}(\Theta) \mathbf{I}_{\text{inc}} \quad (\text{A.1A})$$

The incident light vector is expressed using the Stokes parameters as  $\mathbf{I}_{\text{inc}} = [\mathbf{I}_{\text{inc}}, \mathbf{Q}_{\text{inc}}, \mathbf{U}_{\text{inc}}, \mathbf{V}_{\text{inc}}]^T$ , where the superscript indicates the transpose. (Entirely equivalent are the symbols commonly used in polarimetry,  $\mathbf{I}_{\text{inc}} = [\mathbf{S}_0, \mathbf{S}_1, \mathbf{S}_2, \mathbf{S}_3]^T$ .)

The scattering matrix discussed here is the Mueller scattering matrix, specifically, the 4x4 matrix of real quantities (vis-à-vis the 2x2 Jones scattering matrix of complex quantities explained, for example, by Collett [CO, ch 10]). The 16 elements of our volume scattering matrix  $\mathbf{F}(\Theta)$ , each with dimensions of area, completely describe all the scattering properties of the scattering medium, i.e., those of all the particles in the sample volume.

The scattered light vector  $\mathbf{I}_{\text{sca}}(\Theta)$  is the source of information on these particles. More specifically, the information source is measurement, by a suitably configured receiver, of the four scattered-light Stokes parameters,  $\mathbf{I}_{\text{sca}}(\Theta) = [\mathbf{I}_{\text{sca}}(\Theta), \mathbf{Q}_{\text{sca}}(\Theta), \mathbf{U}_{\text{sca}}(\Theta), \mathbf{V}_{\text{sca}}(\Theta)]^T$ .

The volume scattering matrix  $\mathbf{F}(\Theta)$  is one of the Mueller matrices needed to make the Eq (A.1A) scattering relationship into an equality [e.g. MHT, p 50, eq (2)]. This relationship becomes an equation by including the matrices quantifying the various optical components of the illumination laser and the receiver-detector, the geometric size of the sample volume  $V$ , and the range  $R$  from sample volume to receiver. Here, we include  $V$  and  $R$ ; the complete bi-static lidar equation is explained in Section 5 of this research report.

The origin of the scattering matrix formulation is eminently simple. Light scattered by independent particles (many wavelengths apart) is incoherent (phases of the electric fields of light scattered by individual particles are uncorrelated). Therefore, each Stokes parameter of the scattered light is the linear superposition of contributions from each particle separately. But the contributions are

attributable to specific Stokes parameters of the incident light vector. Using Stokes parameter symbols introduced by Walker in 1954 [WA, eqs 1-4] and quoting from the 1942 seminal work of Perrin [PN, p 421], "... this requires that the quantities [ $I_{\text{sca}}(\Theta)$ ,  $Q_{\text{sca}}(\Theta)$ ,  $U_{\text{sca}}(\Theta)$ ,  $V_{\text{sca}}(\Theta)$ ] be linear homogeneous functions of the quantities [ $I_{\text{inc}}$ ,  $Q_{\text{inc}}$ ,  $U_{\text{inc}}$ ,  $V_{\text{inc}}$ ], i.e., that"

$$\begin{aligned} I_{\text{sca}}(\Theta) &\sim F_{11}(\Theta) I_{\text{inc}} + F_{12}(\Theta) Q_{\text{inc}} + F_{13}(\Theta) U_{\text{inc}} + F_{14}(\Theta) V_{\text{inc}}, \\ Q_{\text{sca}}(\Theta) &\sim F_{21}(\Theta) I_{\text{inc}} + F_{22}(\Theta) Q_{\text{inc}} + F_{23}(\Theta) U_{\text{inc}} + F_{24}(\Theta) V_{\text{inc}}, \\ U_{\text{sca}}(\Theta) &\sim F_{31}(\Theta) I_{\text{inc}} + F_{32}(\Theta) Q_{\text{inc}} + F_{33}(\Theta) U_{\text{inc}} + F_{34}(\Theta) V_{\text{inc}}, \\ V_{\text{sca}}(\Theta) &\sim F_{41}(\Theta) I_{\text{inc}} + F_{42}(\Theta) Q_{\text{inc}} + F_{43}(\Theta) U_{\text{inc}} + F_{44}(\Theta) V_{\text{inc}}. \end{aligned}$$

In matrix notation this is concisely Eq (A.1A),  $\mathbf{I}_{\text{sca}}(\Theta) \sim \mathbf{F}(\Theta) \mathbf{I}_{\text{inc}}$ . (Collett [CO, pp 416-418] offers a more analytical proof of Perrin's statement of this linear relationship between  $\mathbf{I}_{\text{sca}}$  and  $\mathbf{I}_{\text{inc}}$ .)

Although the concern is primarily ensembles of particles, we begin the discussion by considering the simplest form of the scattering matrix, that of a single homogeneous (meaning isotropic refractive index) spherical particle. The interaction between the electric fields of an incident plane electromagnetic wave and that emanating from the affected spherical particle – an outgoing spherical-wave form; these comprise the scattered light electric field that is quantified by a diagonal 2x2 amplitude matrix having two well-known Lorentz–Mie elements [esp. BH, eqs (4.74) & (4.75)]. The resulting scattering matrix  $\mathbf{S}(\Theta)$  is, consequently, block diagonal and consists of just three independent elements. Specific., [BH, eq (4.77)],

$$\mathbf{S}(\Theta) = \begin{vmatrix} a_1(\Theta) & b_1(\Theta) & 0 & 0 \\ b_1(\Theta) & a_1(\Theta) & 0 & 0 \\ 0 & 0 & a_3(\Theta) & b_2(\Theta) \\ 0 & 0 & -b_2(\Theta) & a_3(\Theta) \end{vmatrix}$$

where  $[a_1(\Theta)]^2 = [b_1(\Theta)]^2 + [a_3(\Theta)]^2 + [b_2(\Theta)]^2$ . (Notation  $a_i$ ,  $b_i$  is explained in Section A.3. Also, the scattering matrix symbol  $\mathbf{S}$  indicates single spherical particle, whereas  $\mathbf{F}$  refers to populations of particles that may or may not be spheres.) The four scattering matrix elements are readily expressed in terms of the two complex Lorentz–Mie amplitude matrix elements [e.g., MTL, eqs (5.152) – (5.155)]. The simple form and the limited number of readily computed elements [as in BH, p 477] have led to extensive application of the single homogeneous sphere scattering matrix.

However, any finite sized sample volume contains numerous aerosol particles. If all  $\text{D}$  particles in the sample volume  $V$  are the same type, then the concept of the ensemble-average scattering matrix per particle is very useful,  $\langle \mathbf{F}(\Theta) \rangle = (1/\text{D}) \sum_i \mathbf{F}_i(\Theta)$ , sum extending to  $i = \text{D}$ . (Notation:  $\text{D}$  is identical to  $N$  used in [MTL, p 68] so that as used here  $N = \text{D}/V = \text{D}/V$ . Also, the comprehensive ensemble-averaging procedure  $\langle \cdot \rangle$  is explained in Appendix B.4, esp, Eq (B.5B).) These matrix elements  $\langle F_{ij}(\Theta) \rangle$  are independent of number-concentration  $N$  and sample volume size, since  $\text{D}[-] \equiv (N[\text{cm}^{-3}] V[\text{cm}^3])$ . As particles act individually,  $\mathbf{F}(\Theta) = \sum_i \mathbf{F}_i(\Theta)$ . Eq (A.1A) is now,  $\mathbf{I}_{\text{sca}}(\Theta) \sim \text{D} \langle \mathbf{F}(\Theta) \rangle \mathbf{I}_{\text{inc}}$ .

The fraction of  $\text{D}$  actually irradiated and therefore constituting the source of scattered light is taken to be the same as the fraction of  $V$  that is illuminated by the laser pulse, namely the scattering volume  $\xi V$ , where  $\xi \leq 1$  is in lidar research called the *overlap factor* [ME, p 238]. Including also in Eq (A.1A) the reduction in scattered energy flux due to separation  $R$  between receiver-detector and the pseudo-point source of scattered light results in the *basic scattering equation*.

$$\mathbf{I}_{\text{sca}}(R, \Theta) = [\xi/R^2] \text{D} \langle \mathbf{F}(\Theta) \rangle \mathbf{I}_{\text{inc}} \quad (\text{A.1B})$$

## A.2 ENSEMBLE-AVERAGE SCATTERING MATRIX

The *ensemble-average scattering matrix*, defined above as the per-particle-average scattering matrix  $\langle \mathbf{F}(\Theta) \rangle = (1/\mathbb{D}) \mathbf{F}(\Theta)$ , is formally

$$\langle \mathbf{F}(\Theta) \rangle = \begin{vmatrix} \langle F_{11}(\Theta) \rangle & \langle F_{12}(\Theta) \rangle & 0 & 0 \\ \langle F_{21}(\Theta) \rangle & \langle F_{22}(\Theta) \rangle & 0 & 0 \\ 0 & 0 & \langle F_{33}(\Theta) \rangle & \langle F_{34}(\Theta) \rangle \\ 0 & 0 & \langle F_{43}(\Theta) \rangle & \langle F_{44}(\Theta) \rangle \end{vmatrix} \quad (\text{A.2A})$$

In Eq (A.2A) the elements of the off-diagonal blocks are each zero because induced electric fields of individual particles in their ensemble tend to cancel for common aerosol conditions. These conditions are that the scattering media consist of macroscopically homogeneous dispersions of particles that are distributed in sizes (not monodispersed) and, though not necessarily spheres, are rotationally symmetric (i.e., do have some plane of symmetry), and are randomly oriented. Then, all the non-zero values that such individual non-spherical particles can contribute to elements of the off-diagonal 2x2 blocks tend to converge to zero in the ensemble average. (This block-diagonal structure was derived in early studies of polarized light [PN, eq 33A; more recently MTL, eq 4.4].)

Additionally, the eight elements of Eq (A.2A) are not independent for many naturally occurring aerosol populations. If the particles are spheres, the number of different elements reduces to four since  $\langle F_{22}(\Theta) \rangle = \langle F_{11}(\Theta) \rangle$ ,  $\langle F_{21}(\Theta) \rangle = \langle F_{12}(\Theta) \rangle$ ,  $\langle F_{44}(\Theta) \rangle = \langle F_{33}(\Theta) \rangle$ , and  $\langle F_{43}(\Theta) \rangle = -\langle F_{34}(\Theta) \rangle$  [e.g., MTL, eq 4.49]. For randomly oriented non-spherical but rotationally symmetric isotropic-index particles, the number of separate elements is six [e.g., MTL, eq 4.6] – the four different diagonal elements along with  $\langle F_{21}(\Theta) \rangle = \langle F_{12}(\Theta) \rangle$  and  $\langle F_{43}(\Theta) \rangle = -\langle F_{34}(\Theta) \rangle$ . If there is a preferred orientation for such particles, then all eight elements are different and at least the two most-off-diagonal corner elements in Eq (A.2A) are no longer zero, esp. at backscatter angles. But even then, the scattering medium for which Eq (A.2A) applies – while it may change the orientation of linearly polarized incident light – it does not contribute a rotational sense to the scattered beam unless some such sense is already present in the incident light. If these same non-spherical particles possess non-isotropic refractive index, then a rotational sense can be introduced into the scattered beam that is not present in the incident light. This is a distinctive trait that could be exploited in bio-aerosol detection.

Each element of Eq (A.2A) varies with  $\Theta$ , i.e., it constitutes the scattering-angle profile of that scattering characteristic for the ensemble of particles. Here we discuss the meanings of some of the individual elements, but more complete descriptions are in Bohren and Huffman (1983) [BH, pp 65-67, 189, 412-424]. Very thorough descriptions of elements normalized by  $(1/\langle F_{11} \rangle)$  as functions of  $\Theta$  and of the effective size parameter  $x_{\text{eff}} = 2\pi r_{\text{eff}}/\lambda$  (defined in Appendix B.3) are in Mishchenko et al (1996) [MTM, plates 3-9 and figs 5-12].

## A.3 NORMALIZED SCATTERING MATRIX

The ensemble-average scattering matrix  $\langle \mathbf{F}(\Theta) \rangle$  can be separated into its integral photometric part [ $\langle C_{\text{sca}} \rangle / 4\pi$ ], explained in Section A.7, and its normalized directional polarimetric part  $\mathbf{F}(\Theta)$ , specifically,  $\langle \mathbf{F}(\Theta) \rangle = [\langle C_{\text{sca}} \rangle / 4\pi] \mathbf{F}(\Theta)$ . Of particular interest here is the polarimetric part, the matrix  $\mathbf{F}(\Theta)$ , which is referred to as the *normalized scattering matrix* [MTL, p 100; the symbol  $\bar{\mathbf{F}}(\Theta)$  is identical to  $\mathbf{F}(\Theta)$  used here]. The ensemble-average scattering matrix normalized by the integral photometric quantity of the per-solid-angle-average scattering cross-section per particle is  $\mathbf{F}(\Theta) = \langle \mathbf{F}(\Theta) \rangle / (\langle C_{\text{sca}} \rangle / 4\pi)$ . Now, we have separated the effects not only of the number of particles in the sample volume  $\mathbb{D}$ , but also of the overall spherical-average scattering ability of those particles

$[\langle C_{\text{sca}} \rangle / 4\pi]$  from the angle-varying polarimetric effects. In Eq (A.1B) for the purpose of this appendix  $\xi = 1$ , so that the *normalized scattering equation* is

$$\mathbf{I}_{\text{sca}}(\mathbf{R}, \Theta) = [1/R^2] \square [\langle C_{\text{sca}} \rangle / 4\pi] \mathbf{F}(\Theta) \mathbf{I}_{\text{inc}} \quad (\text{A.1C})$$

The normalized directional quantity  $\mathbf{F}(\Theta)$  is dimensionless, which further enhances its usefulness in isolating the directional effects of the scattering particles.  $\mathbf{F}(\Theta)$  is the per-particle-average angular scattering function of all aerosol particles contained in the sample volume. The first element of this 4x4 matrix  $F_{11}(\Theta)$  is identically the single-scattering phase function applied in nearly all atmospheric scattering studies [e.g., DE, p 73; HT, figs 14 & 15; MC, p 199; BH, p 72]. Each of the remaining 15 elements represents a particular scattering characteristic of the scattering medium. For individual non-spherical particles, many of these elements are significant. However, as we indicated above, whenever a population of non-spherical particles has macroscopic random orientation and homogeneous (uniform) dispersion of distributed sizes, and the individual-particles all have some similar axis of symmetry and the same isotropic refractive index, then many of the off-diagonal elements approach zero at all scattering angles (not just at  $\Theta = 0^\circ$  and  $180^\circ$ ).

Clearly, for such particles having Eq (A.2A) as the ensemble-average scattering matrix, the normalized scattering matrix  $\mathbf{F}(\Theta)$  has the same block-diagonal form. Employing the symbols originated by Perrin (1942) [PN, eq 47], the elements of the normalized scattering matrix are without ambiguity abbreviated as single-subscript letter designations (diagonal elements a's, off-diagonal b's), specifically,  $F_{11}(\Theta) \equiv a_1(\Theta)$ ,  $F_{12}(\Theta) \equiv b_1(\Theta)$ ,  $F_{22}(\Theta) \equiv a_2(\Theta)$ , etc. For both spherical particles and spheroidal (i.e., plane-symmetric) particles that are randomly orientated and homogeneously dispersed throughout the sample volume, the block diagonal normalized scattering matrix is,

$$\mathbf{F}(\Theta) = \begin{vmatrix} a_1(\Theta) & b_1(\Theta) & 0 & 0 \\ b_1(\Theta) & a_2(\Theta) & 0 & 0 \\ 0 & 0 & a_3(\Theta) & b_2(\Theta) \\ 0 & 0 & -b_2(\Theta) & a_4(\Theta) \end{vmatrix} \quad (\text{A.2B})$$

Again, the  $a(\Theta)$ 's and  $b(\Theta)$ 's are the normalized directional per-particle-average angular profiles of each scattering quantity for the ensemble population of particles in the sample volume. In this research report, we deal with only the four independent elements  $a_1(\Theta)$ ,  $b_1(\Theta)$ ,  $a_2(\Theta)$ , and  $b_2(\Theta)$ . In particular,  $a_1(\Theta)$  is the familiar single-scattering phase function [MTL, p 101],  $b_1(\Theta)$  is called the polarized phase function [HDD],  $a_2(\Theta)$  is used as a measure of particle non-sphericity, and  $b_2(\Theta)$  allows some assessment of refractive index related scattering effects. All elements in the lower right block are associated with properties of the refractive index, such as dichroism or birefringence [HC, Chapter 8.3, 8.4]. The significant fact is that normalized scattering matrix elements are not only independent of the product  $N\langle C_{\text{sca}} \rangle$  (further explained in Section 6.2 of this report), but are also independent of the polarization state of the incident illumination.

In scattering computations for particle populations made up of randomly oriented, uniformly dispersed, variously sized, similarly shaped isotropic-index spheroids, the six independent elements of the normalized scattering matrix, in Eq (A.2B), are independent of some population parameters and vary only with  $\Theta$ ,  $x_{\text{eff}}$ ,  $\epsilon$ , and  $m$ ; i.e., they vary with the scattering angle and are parametric functions of the effective size parameter  $x_{\text{eff}} = 2\pi r_{\text{eff}}/\lambda$ , the axis ratio  $\epsilon$  and the complex index of refraction  $m = m_{\text{real}} - i m_{\text{imag}}$  [MTL, p 134]. These six elements are then expressible as sums of simple products – each product being a generalized spherical function multiplied by an expansion coefficient [e.g., MTL, pp 103-105]. The generalized spherical functions (esp. associated Legendre polynomials or Wigner functions) take care of the  $\Theta$ -variation of the scattering elements. The

expansion coefficients, in number equal to the number of independent, non-zero scattering matrix elements, are determined by the parameters  $x_{\text{eff}}$ ,  $\varepsilon$ , and  $m$ . The coefficients are computed only once for a specific aerosol population parameter set ( $x_{\text{eff}}$ ,  $\varepsilon$ ,  $m$ ). Thereafter, for any  $\Theta$ , the products are completed and the summations performed by elementary scattering code computations. (Codes to accomplish these computations for non-spherical particles are available on the world-wide-web; addresses are found in Appendix C.)

Many naturally occurring aerosols have scattering matrixes of the form of Eq (A.2B). However, populations of near-uniformly sized non-symmetrically shaped particles, such as those newly generated or artificially prevented from coagulating, will not have all four elements of the off-diagonal blocks tending to zero. In fact, a narrow distribution of such particle sizes may be detected by probing the population with incident radiation that affords the non-zero off-diagonal elements to be sensed. Using the original complete set of Perrin's [PN, eq (47)] single-subscript symbols, explained by van de Hulst [VH, p 50, case 5], the complete normalized scattering matrix is,

$$\mathbf{F}(\Theta) = \begin{vmatrix} a_1(\Theta) & b_1(\Theta) & b_3(\Theta) & b_5(\Theta) \\ b_1(\Theta) & a_2(\Theta) & b_4(\Theta) & b_6(\Theta) \\ -b_3(\Theta) & -b_4(\Theta) & a_3(\Theta) & b_2(\Theta) \\ b_5(\Theta) & b_6(\Theta) & -b_2(\Theta) & a_4(\Theta) \end{vmatrix} \quad (\text{A.2C})$$

Sensing the ten different elements requires multiple – up to six – polarization states of the incident (or scattered) light along with a few – up to three – polarization states of the scattered (or incident) light (more detail in Appendix E.2). For example, if the incident light is horizontally polarized (meaning linearly polarized parallel to the scattering plane,  $\mathbf{I}_{\text{inc}} \sim [1, 1, 0, 0]^T$ ) and if the scattered light is analyzed with an adequate Stokes parameter receiver (polarimeter), then the affect on  $\mathbf{I}_{\text{sca}}(\Theta)$  of  $\mathbf{F}(\Theta)$  as required by Eq (A.2C) is:  $I_{\text{sca}}(\Theta) \sim [a_1(\Theta) + b_1(\Theta)]$ ,  $Q_{\text{sca}}(\Theta) \sim [b_1(\Theta) + a_2(\Theta)]$ ,  $U_{\text{sca}}(\Theta) \sim -[b_3(\Theta) + b_4(\Theta)]$ ,  $V_{\text{sca}}(\Theta) \sim [b_5(\Theta) + b_6(\Theta)]$ . The deficiency of this incident polarization is that no information on  $b_2(\Theta)$ ,  $a_3(\Theta)$ , or  $a_4(\Theta)$  can be extracted no matter how comprehensive the polarimeter. Also, only the sum  $[a_1(\Theta) + b_1(\Theta)]$  is measurable by a simple receiver. To specify  $b_1(\Theta)$  itself at least two measurements are needed – one to isolate  $a_1(\Theta)$ .

Measurement of any scattering matrix element means that it must appear in the first Stokes parameter position of the scattered light vector, specifically in the  $I_{\text{sca}}$  position. Therefore, determination of  $a_4$  requires some circular polarization of the incident light and use of circular analysis in the receiver. (Refer to Appendix E.2, Eq (E.6A).)

The ‘lidar’ configuration  $\Theta = \pi$  (i.e.,  $180^\circ$ ) is useful for monitoring the overall scattering ability of particles. In addition, it is well suited for detecting particle non-sphericity and may also be advantageous for detecting particles of any shape that have narrow size distributions or preferred orientations. (The ‘lidar’ measurement is made either with large separation between the sample volume and the detector, or by rapid-shift time-sharing of the transmitter optical axis.) Near the ‘lidar’ angle, any population of randomly orientated narrowly sized non-spherical particles (each having the same shape parameter) may be expected to have a much-reduced scattering matrix [VH, p 55, case 12a]. Specifically,

$$\mathbf{F}(\pi) = \begin{vmatrix} a_1(\pi) & 0 & 0 & b_5(\pi) \\ 0 & a_2(\pi) & 0 & 0 \\ 0 & 0 & -a_2(\pi) & 0 \\ b_5(\pi) & 0 & 0 & a_4(\pi) \end{vmatrix} \quad (\text{A.2D})$$

The values of the four independent elements of this ‘lidar’ normalized scattering matrix can be evaluated with only two basic polarization states of the incident light; one being a linear polarization at 45° to some otherwise defined plane, the other being circular [ref. SH, table 2.1; or BH, table 2.2]. In practice, the departures of  $b_5(\pi)$  from zero, and of  $a_4(\pi)$  from [ $a_1(\pi) - 2a_2(\pi)$ ] may be sensitive measures of transient departures of particles in the sample volume from a random and homogeneous dispersion [MTL, eqs 4.37 and 4.63].

Finally, a summary of the four directional scattering matrices so far introduced is contained in Table A.1 (the fifth is explained in Section A.5). Table A.1 relates each individual form of the scattering matrix, in particular its elements, to the other forms. For simplicity of notation, the scattering angle variation  $f(\Theta)$  of each element (and matrix) is not explicitly included in Table A.1.

**Table A.1. Various Scattering Matrix Forms.**

All matrices and elements are directional; all vary with scattering angle ( $\Theta$ ).

Descriptor	Symbol	Units	Element:	$= F_{ij}$	$= \langle F_{ij} \rangle$	$= F_{ij}$	$= a_k, b_k$	$= \beta_{ij}$
Volume	<b>F</b>	[cm <sup>2</sup> ]	$F_{ij} \times$	1	1/D	$4\pi/D\langle C_{sca} \rangle$	$4\pi/D\langle C_{sca} \rangle$	N/D
Ensemble-Ave.	$\langle F \rangle$	[cm <sup>2</sup> ]	$\langle F_{ij} \rangle \times$	D	1	$4\pi/\langle C_{sca} \rangle$	$4\pi/\langle C_{sca} \rangle$	N
Normalized	<b>F</b>	[–]	$F_{ij} \times$	$D\langle C_{sca} \rangle/4\pi$	$\langle C_{sca} \rangle/4\pi$	1	1	$N\langle C_{sca} \rangle/4\pi$
Abbreviated	<b>F</b>	[–]	$a_k, b_k \times$	$D\langle C_{sca} \rangle/4\pi$	$\langle C_{sca} \rangle/4\pi$	1	1	$N\langle C_{sca} \rangle/4\pi$
Vol. Scattering Coefficient	<b>B</b>	[cm <sup>-1</sup> ]	$\beta_{ij} \times$	D/N	1/N	$4\pi/N\langle C_{sca} \rangle$	$4\pi/N\langle C_{sca} \rangle$	1

D [–] – number of particles in sample volume V[cm<sup>3</sup>], D = NV, D/N = V. N[cm<sup>-3</sup>] – number of particles per unit physical volume.  $\langle C_{sca} \rangle$  [cm<sup>2</sup> = 10<sup>8</sup> μm<sup>2</sup>] – ensemble-average scattering cross section. Examples (4<sup>th</sup> column element x table entry = header-row element; or inverse):  $F_{ij} = (D\langle C_{sca} \rangle/4\pi)b_k$ ;  $\beta_{ij} = (N\langle C_{sca} \rangle/4\pi)F_{ij}$ ;  $a_k = (4\pi/\langle C_{sca} \rangle)\langle F_{ij} \rangle$ .

#### A.4 COMBINED SCATTERING MATRIX

For the case of two different types of particles co-located in the same sample volume, the possibility of identifying each type individually results from their independent interaction with the incident illumination and depends on the correct formulation of the contribution of each to the combined scattering matrix. The combined volume scattering matrix  $\mathbf{F}_c(\Theta)$  now defines the transformation of the incident light vector into the scattered light vector,  $\mathbf{I}_{sca}(\Theta) \sim \mathbf{F}_c(\Theta) \mathbf{I}_{inc}$ . The combined volume scattering matrix is not simply ensemble-averaged, as before, because there are now two different ensembles within V. Specifically, D = (N<sub>a</sub> + N<sub>b</sub>)V, where the subscripts indicate the ambient background aerosol and bio-aerosol types (these subscripts have nothing to do with the Perrin abbreviated normalized scattering matrix elements.) But the combined matrix is expressible in terms of the number-concentration-weighted ensemble averages of the individual components,  $\mathbf{F}_c(\Theta) = V [N_a \langle \mathbf{F}_a(\Theta) \rangle + N_b \langle \mathbf{F}_b(\Theta) \rangle]$ .

In terms of individual normalized scattering matrices, applying the relationship from Table A.1,  $\mathbf{F}_c(\Theta) = [V/4\pi] [N_a \langle C_{sca} \rangle_a \mathbf{F}_a(\Theta) + N_b \langle C_{sca} \rangle_b \mathbf{F}_b(\Theta)]$ . But, by its definition,  $\mathbf{F}_c(\Theta) = [V/4\pi] [N_a \langle C_{sca} \rangle_a + N_b \langle C_{sca} \rangle_b] \mathbf{F}_c(\Theta)$ , resulting in the *combined normalized scattering matrix*

$$\mathbf{F}_c(\Theta) = [N_a \langle C_{sca} \rangle_a \mathbf{F}_a(\Theta) + N_b \langle C_{sca} \rangle_b \mathbf{F}_b(\Theta)] / [N_a \langle C_{sca} \rangle_a + N_b \langle C_{sca} \rangle_b] \quad (\text{A.3})$$

which is given as eq (4.74) in [MTL, p 103] (where the factors  $1/4\pi$  have canceled; here the factors  $V/4\pi$  have likewise canceled).

The individual elements of the combined normalized scattering matrix are symbolized by the same  $a_1(\Theta)$ ,  $b_1(\Theta)$ , etc, appearing in Eq (A.2B); but it is the expressions (given in Section A.6) for these combined normalized scattering matrix elements that differ from those of a single aerosol type. In scattering computations for commonly occurring aerosol conditions Eq (A.3) is used extensively.

Eq (A.1C) and the definition of  $\mathbf{I}$  result in the scattered light vector produced by each aerosol separately, specific,  $\mathbf{I}_{sca}(R, \Theta) = [V/4\pi R^2][N_a \langle C_{sca} \rangle_a] \mathbf{F}_a(\Theta) \mathbf{I}_{inc}$ , or  $\mathbf{I}_{sca}(R, \Theta) = [V/4\pi R^2][N_b \langle C_{sca} \rangle_b] \mathbf{F}_b(\Theta) \mathbf{I}_{inc}$ . The sum of these is the detected quantity. Similarly, the introduction of Eq (A.3) into the combined form of Eq (A.1C) results in the *combined normalized scattering equation*

$$\mathbf{I}_{sca}(R, \Theta) = [V/4\pi R^2][N_a \langle C_{sca} \rangle_a + N_b \langle C_{sca} \rangle_b] \mathbf{F}_c(\Theta) \mathbf{I}_{inc} \quad (\text{A.1D})$$

Eq (A.1D) specifies the scattered beam (i.e., scattered irradiance vector) produced by two independent but co-located aerosol types.

Although this may appear to introduce redundancy, cf. Eq (A.3), for sensitivity analyses it is convenient to express the scattered irradiance vector  $\mathbf{I}_{sca}(R, \Theta)$  in terms of the combined normalized scattering matrix and the integral (photometric) scattering quantities of each type of aerosol within the sample volume. E.g., the effects on  $\mathbf{I}_{sca}(R, \Theta)$  of a change in either number concentration  $N_a$  or  $N_b$  (or in the number-concentration mixing ratio  $R_N = N_b/N_a$ ) are easily evaluated given  $\mathbf{F}_c(\Theta)$ ,  $\langle C_{sca} \rangle_a$ , and  $\langle C_{sca} \rangle_b$  – these three scattering quantities need only be computed once to evaluate the changes in  $\mathbf{I}_{sca}(R, \Theta)$  that are due to number-concentration changes. The effect is considerably enhanced computational efficiency for sensitivity analyses.

## A.5 VOLUME SCATTERING COEFFICIENT MATRIX

The *volume scattering coefficient matrix*  $\mathbf{B}$  collects all the particle-related quantities in the normalized scattering equation into a single variable. (This matrix is similar in purpose to the extinction matrix defined in [BAK, eq 1.2.33].) The *directional volume scattering coefficient matrix*  $\mathbf{B}(\Theta)$  is the scattering ability of particles in a unit scattering volume to elastically redirect incident radiation through the angle  $\Theta$ . For each type of aerosol and for the combined aerosol it is made up of all particle factors in expressions leading to Eq (A.1D), specifically,

$$\begin{aligned} \mathbf{B}_a(\Theta) &= [1/4\pi][N_a \langle C_{sca} \rangle_a] \mathbf{F}_a(\Theta) \\ \mathbf{B}_b(\Theta) &= [1/4\pi][N_b \langle C_{sca} \rangle_b] \mathbf{F}_b(\Theta) \\ \mathbf{B}_c(\Theta) &= [1/4\pi][N_a \langle C_{sca} \rangle_a + N_b \langle C_{sca} \rangle_b] \mathbf{F}_c(\Theta) \end{aligned} \quad (\text{A.4})$$

It is the combined volume scattering coefficient matrix that we are most interested in. From the expression for  $\mathbf{B}_c(\Theta)$  in Eq (A.4) and Eq (A.3), it is clear that this matrix explicitly includes the effects (both photometric and polarimetric) of all scattering particles within the unit scattering volume. Elements of the volume scattering coefficient matrix are widely applied in active remote sensing of the atmosphere since they are independent of any geometric parameters, in particular, the sample volume  $V$  and the range  $R$ . (In this sense, the volume scattering coefficient is similar to the radiance quantity, which is independent of the source dimensions or distance away.) Given the incident laser wavelength,  $\mathbf{B}_c(\Theta)$  is a function only of the properties of the scattering particles – a

major advantage in remote sensing. Finally, with the  $\mathbf{B}_c(\Theta)$  expression in Eq (A.4), now Eq (A.1D) is concisely written

$$\mathbf{I}_{\text{sca}}(\mathbf{R}, \Theta) = [V/R^2] \mathbf{B}_c(\Theta) \mathbf{I}_{\text{inc}} \quad (\text{A.1E})$$

Explicit expressions for the elements of  $\mathbf{B}_c(\Theta)$ , conforming to the Table A.1 relationships, are given in Section A.6.

For particle conditions that lead to the Eq (A.2B) scattering matrix form, the matrices  $\mathbf{F}_a(\Theta)$ ,  $\mathbf{F}_b(\Theta)$ , and  $\mathbf{F}_c(\Theta)$ , and also  $\mathbf{B}_a(\Theta)$ ,  $\mathbf{B}_b(\Theta)$ , and  $\mathbf{B}_c(\Theta)$  are all likewise block-diagonal. Specifically, each volume scattering coefficient matrix has the form

$$\mathbf{B}(\Theta) = \begin{vmatrix} \beta_{11}(\Theta) & \beta_{12}(\Theta) & 0 & 0 \\ \beta_{12}(\Theta) & \beta_{22}(\Theta) & 0 & 0 \\ 0 & 0 & \beta_{33}(\Theta) & \beta_{34}(\Theta) \\ 0 & 0 & -\beta_{34}(\Theta) & \beta_{44}(\Theta) \end{vmatrix} \quad (\text{A.5})$$

Any particular element of this matrix is referred to by the generic term *volume scattering coefficient*, which has the dimensions of inverse length ( $\text{cm}^{-1}$ ). For the applications made in this report, only four (of six) independent elements of Eq (A.5):  $\beta_{11}(\Theta)$ ,  $\beta_{12}(\Theta)$ ,  $\beta_{22}(\Theta)$ , and  $-\beta_{34}(\Theta)$  are employed. That being said, the specific elements of the volume scattering coefficient matrix that affect each  $\mathbf{I}_{\text{sca}}(\mathbf{R}, \Theta)$  Stokes parameter depend on the polarization state of  $\mathbf{I}_{\text{inc}}$ . For the two incident polarization states dealt with here, linear at  $+45^\circ$  and  $0^\circ$  (parallel) to the scattering plane, the five resulting volume scattering coefficients are:  $\beta_{11}(\Theta)$ ,  $\beta_{12}(\Theta)$ , and  $-\beta_{34}(\Theta)$  for the  $+45^\circ$ , and  $(\beta_{11}(\Theta) + \beta_{12}(\Theta))$  and  $(\beta_{12}(\Theta) + \beta_{22}(\Theta))$  for the  $0^\circ$  incident polarization (see Section A.6).

From Eqs (A.1E) and (A.4) it is evident that the magnitudes of the scattered light Stokes parameters, for a single aerosol type or for a combination, vary directly with number concentration and ensemble-average scattering cross-section. This photometric quantity, the general product  $N(C_{\text{sca}})$  is here called the *total volume scattering coefficient* (see main report Section 6.2). The word *total* is significant. It is a measure of the overall (all-angle average) scattering ability of the aerosol particles irrespective of scattering angle. It can be measured, most readily, using the 1<sup>st</sup> Stokes parameter of the scattered light vector,  $I_{\text{sca}}(\Theta)$ . Since the total volume scattering coefficient is independent of scattering angle, it is directly proportional to the smaller of any two scattering-angle measurements of  $I_{\text{sca}}$ ; whereas the difference between the two measurements can be used to assess the polarimetric quantity  $F_{11}(\Theta)$ , or equivalently  $a_1(\Theta)$ .

## A.6 POLARIMETRIC PROPERTIES

The four angle-varying polarimetric quantities applied in this report, which are called intensity  $P_I(\Theta)$ , linearity  $P_L(\Theta)$ , non-sphericity  $P_N(\Theta)$ , and retardation  $P_R(\Theta)$ , are defined as the measured scattered-radiation Stokes parameters normalized by the magnitude of the incident irradiance (light). However, the  $P_x$ 's need to be expressed in terms of their constituent elements – the scattering particles' scattering properties. When so expressed, the four measurable polarimetric quantities are referred to as *polarimetric properties* because the scattering properties of the particles in the scattering volume are explicitly contained within the elements of the  $\mathbf{B}_c(\Theta)$  matrix. Since the incident laser vector is completely known, it is the inference of the scattering properties of the particles, i.e., the specific terms and factors comprising each element  $\beta_{ij}(\Theta)$ , that enables detection of aerosols and even the retrieval of particle properties from remote polarimetric measurements.

The Stokes parameters of the incident light vector  $\mathbf{I}_{\text{inc}} = [I_{\text{inc}}, Q_{\text{inc}}, U_{\text{inc}}, V_{\text{inc}}]^T$  are known so that, for a single polarization state of  $\mathbf{I}_{\text{inc}}$ , the angular changes in the measured Stokes parameters of the scattered light vector  $\mathbf{I}_{\text{sca}}(\Theta) = [I_{\text{sca}}(\Theta), Q_{\text{sca}}(\Theta), U_{\text{sca}}(\Theta), V_{\text{sca}}(\Theta)]^T$ , up to three of which are independent, are immediately usable to infer as many as three elements of  $\mathbf{F}(\Theta)$ . Using a second polarization state of  $\mathbf{I}_{\text{inc}}$  provides two more elements of  $\mathbf{F}(\Theta)$ . As seen from Eq (A.2B), six of 16 is often the number of independent  $\mathbf{F}(\Theta)$  elements for common aerosol conditions. Thus, the scattering properties of such aerosols could completely be specified using three incident polarization states [e.g. SH, table 2.1] and a full Stokes-parameter receiver.

The four polarimetric properties employed here are summarized in Table A.2 and then each is subsequently explained.

**Table A.2. Polarimetric Properties of Scattered Light.**

All entries vary with  $\Theta$ . Superscript incident polarization:  $^+$  is  $+45^\circ$ ,  $^P$  is parallel to scattering plane ( $0^\circ$ ).

Name	Symbol	Stokes Parameter	Normalized Element*	Vol. Scat. Coefficient*
Intensity	$P_I$	$^+I_{\text{sca}}$	$a_1$	$\beta_{11}$
Linearity	$P_L$	$^+Q_{\text{sca}}$	$b_1$	$\beta_{21}$
Non-Sphericity	$P_N$	$^P I_{\text{sca}} - ^P Q_{\text{sca}}$	$a_1 - a_2$	$\beta_{11} - \beta_{22}$
Retardation	$P_R$	$^+V_{\text{sca}}$	$-b_2$	$\beta_{43}$

\* Valid for spherical particles or for randomly orientated homogeneously dispersed isotropic-index spheroids. Otherwise normalized elements are:  $a_1 \rightarrow (a_1 + b_3)$ ,  $b_1 \rightarrow (b_1 + b_4)$ , and  $-b_2 \rightarrow (b_5 - b_2)$ .

The four polarimetric properties in Table A.2 (out of a larger number of possibilities, e.g. circularity  $P_C \sim a_4$ ) are expressed using four elements of the normalized scattering matrix, Eq (A.2B), for the combination of aerosol types. Three of these properties are defined simply as the angle-varying Stokes parameters themselves when the incident vector is  $+45^\circ$  linearly polarized. Specifically, for the incident radiation vector  $^+I_{\text{inc}} = [1 \ 0 \ 1 \ 0]^T I_o/2$ , of magnitude  $I_o$  that is linearly polarized counterclockwise  $45^\circ$  to the scattering plane when looking into the source, the first polarization property of the scattered light is the angle-varying scattered *intensity*,  $P_I(\Theta) = ^+I_{\text{sca}}(\Theta)/I_o \sim a_1(\Theta)$ . The second, called here the *linearity* is  $P_L(\Theta) = ^+Q_{\text{sca}}(\Theta)/I_o \sim b_1(\Theta)$ , and the last, the *retardation* is  $P_R(\Theta) = ^+V_{\text{sca}}(\Theta)/I_o \sim -b_2(\Theta)$ . The fourth is formed from two scattered light Stokes parameters with incident linear polarization at  $0^\circ$ , parallel to the scattering plane,  $^P I_{\text{inc}} = [1 \ 1 \ 0 \ 0]^T I_o/2$ . The angular profile of depolarization, called here *non-sphericity* is  $P_N(\Theta) = [^P I_{\text{sca}}(\Theta) - ^P Q_{\text{sca}}(\Theta)]/I_o \sim \{[a_1(\Theta) + b_1(\Theta)] - [b_1(\Theta) + a_2(\Theta)]\} = [a_1(\Theta) - a_2(\Theta)]$ .

The simplicity of the polarimetric property expressions recommends the two states of incident linear polarization – at least for an initial study. However, considerable added scattering information can be obtained from right-circularly polarized incident light,  $^R I_{\text{inc}} = [1 \ 0 \ 0 \ 1]^T I_o/2$ . Incorporating Eqs (A.1D), (A.3) and (A.2B) into these definitions, the four polarization properties defined and employed in this research report are:

$$\begin{aligned} P_I(\Theta) &= [V/4\pi R^2][N_a \langle C_{\text{sca}} \rangle_a + N_b \langle C_{\text{sca}} \rangle_b] a_1(\Theta) \\ P_L(\Theta) &= [V/4\pi R^2][N_a \langle C_{\text{sca}} \rangle_a + N_b \langle C_{\text{sca}} \rangle_b] b_1(\Theta) \\ P_N(\Theta) &= [V/4\pi R^2][N_a \langle C_{\text{sca}} \rangle_a + N_b \langle C_{\text{sca}} \rangle_b][a_1(\Theta) - a_2(\Theta)] \\ P_R(\Theta) &= -[V/4\pi R^2][N_a \langle C_{\text{sca}} \rangle_a + N_b \langle C_{\text{sca}} \rangle_b] b_2(\Theta) \end{aligned} \quad (\text{A.6A})$$

In this case of randomly oriented axi-symmetric particles, the first expression in Eq (A.6A) is called a polarimetric property for convenience because  $P_I(\Theta)$  is simply the angular partitioning of scattered light for incident unpolarized light,  $^U I_{\text{inc}} = [1 \ 0 \ 0 \ 0]^T I_o$ , of unit magnitude. Specifically,

$P_l(\Theta) = {}^u I_{\text{sca}}(\Theta)/I_o$  is just the angular profile of scattered intensity, the phase function, which does not conveying any information on the ability of the scattering medium to alter light polarization.

The full expressions for each of the four combined normalized scattering matrix elements are the appropriate forms of Eq (A.3) inserted into Eq (A.1D). For example, the four combination elements  $a_1(\Theta) \equiv F_{c,11}(\Theta)$ ,  $b_1(\Theta) \equiv F_{c,21}(\Theta)$ ,  $a_2(\Theta) \equiv F_{c,22}(\Theta)$ , and  $b_2(\Theta) \equiv F_{c,43}(\Theta)$  are:

$$\begin{aligned} a_1(\Theta) &= [N_a \langle C_{\text{sca}} \rangle_a F_{a,11}(\Theta) + N_b \langle C_{\text{sca}} \rangle_b F_{b,11}(\Theta)] / [N_a \langle C_{\text{sca}} \rangle_a + N_b \langle C_{\text{sca}} \rangle_b] \\ b_1(\Theta) &= [N_a \langle C_{\text{sca}} \rangle_a F_{a,21}(\Theta) + N_b \langle C_{\text{sca}} \rangle_b F_{b,21}(\Theta)] / [N_a \langle C_{\text{sca}} \rangle_a + N_b \langle C_{\text{sca}} \rangle_b] \\ a_2(\Theta) &= [N_a \langle C_{\text{sca}} \rangle_a F_{a,22}(\Theta) + N_b \langle C_{\text{sca}} \rangle_b F_{b,22}(\Theta)] / [N_a \langle C_{\text{sca}} \rangle_a + N_b \langle C_{\text{sca}} \rangle_b] \\ b_2(\Theta) &= [N_a \langle C_{\text{sca}} \rangle_a F_{a,43}(\Theta) + N_b \langle C_{\text{sca}} \rangle_b F_{b,43}(\Theta)] / [N_a \langle C_{\text{sca}} \rangle_a + N_b \langle C_{\text{sca}} \rangle_b] \end{aligned} \quad (\text{A.7})$$

Eq (A.7) makes evident the convenience of the notation  $a_1(\Theta)$ ,  $b_1(\Theta)$ , etc, in spite of the reappearance of the sum of total volume scatters in the denominator, which cancels when entered into Eq (A.6A).

The four polarimetric properties in terms of the Stokes-formatted volume scattering coefficients are

$$\begin{aligned} P_l(\Theta) &= [V/R^2] \beta_{11}(\Theta) \\ P_L(\Theta) &= [V/R^2] \beta_{21}(\Theta) \\ P_N(\Theta) &= [V/R^2] [\beta_{11}(\Theta) - \beta_{22}(\Theta)] \\ P_R(\Theta) &= -[V/R^2] \beta_{43}(\Theta) \end{aligned} \quad (\text{A.6B})$$

For completeness, the relationships  $\beta \sim$  normalized element ( $a_1$ ,  $b_1$ ,  $a_2$ ) are stated. From Eqs (A.6A) and (A.6B), normalized scattering matrix elements, given in Eq (A.7), and elements of the volume scattering coefficient matrix resulting from  $+45^\circ$  and  $0^\circ$  linear incident polarizations, are related as

$$\begin{aligned} \beta_{11}(\Theta) &= [1/4\pi] [N_a \langle C_{\text{sca}} \rangle_a + N_b \langle C_{\text{sca}} \rangle_b] a_1(\Theta) \\ \beta_{21}(\Theta) &= [1/4\pi] [N_a \langle C_{\text{sca}} \rangle_a + N_b \langle C_{\text{sca}} \rangle_b] b_1(\Theta) \\ [\beta_{11}(\Theta) - \beta_{22}(\Theta)] &= [1/4\pi] [N_a \langle C_{\text{sca}} \rangle_a + N_b \langle C_{\text{sca}} \rangle_b] [a_1(\Theta) - a_2(\Theta)] \\ \beta_{43}(\Theta) &= [1/4\pi] [N_a \langle C_{\text{sca}} \rangle_a + N_b \langle C_{\text{sca}} \rangle_b] b_2(\Theta) \end{aligned} \quad (\text{A.8})$$

where the normalized scattering matrix elements,  $a_1$ ,  $b_1$ ,  $a_2$ , and  $b_2$ , are for the combined ambient background plus bio-aerosols expressed above.

## A.7 SCATTERING CROSS SECTION

The scattering cross section  $C_{\text{sca}}$  allows elements of the scattering matrix  $\mathbf{F}(\Theta)$  to be separated into all-angle-average (photometric) and angle-dependent (polarimetric) parts. The separation expedites the analysis of scattering variabilities, e.g., as in sensitivity testing and signal-to-noise computations for varied scattering particle characteristics. The dimensions of both  $C_{\text{sca}}$  and  $\mathbf{F}(\Theta)$  are the same – area; units commonly used are either  $\mu\text{m}^2$  or  $\text{cm}^2$ .

Fundamentally,  $C_{\text{sca}}$  applies to individual particles – it is the cross section the particle presents, i.e., that influences incident radiation. The value of  $C_{\text{sca}}$  always depends on particle size and the wavelength of  $\mathbf{I}_{\text{inc}}$ . But, for orientated non-spherical particles it can also depend on the direction and polarization state of  $\mathbf{I}_{\text{inc}}$  [MTL, p 59]. However for populations of randomly oriented non-spherical scattering particles possessing common symmetries, the ensemble-average value (Appendix B.4) of  $C_{\text{sca}}$  is independent of the  $\mathbf{I}_{\text{inc}}$  propagation direction and polarization state [MTL, pp 95-97]. The ensemble-average scattering cross section  $\langle C_{\text{sca}} \rangle$  is the most useful measure of the scattering ability of a population of particles.

The physical interpretation of  $\langle C_{\text{sca}} \rangle$  involves integration of all scattered radiance over an imaginary sphere surrounding the particles [refer to MTL, pp 57-60; or BH, p 70]. In terms of the elements of the ensemble-average scattering matrix in Eq (A.2A),  $\langle C_{\text{sca}} \rangle$  is the integral of all scattered radiance components transverse to the incident direction for unit incident irradiance [MT3, p 14]. It is for isotropic symmetric particle populations just the integral of all normal components of the azimuth-angle invariant phase function – the first element of the ensemble-average scattering matrix.

$$\langle C_{\text{sca}} \rangle = 2\pi \int_0^{\pi} \langle F_{11}(\Theta) \rangle \sin(\Theta) d\Theta \quad (\text{A.9A})$$

[in particular, MT3, eq 98; or MTL, eq 4.40]. Note that  $\langle F_{11} \rangle$  (vs.  $F_{11}$ , Table A.1) contains specific particle property information.

Since the spherical-average of the integral scattering ability of the ensemble of particles is often the operative quantity needed in scattering computations, the appropriate normalization factor is the complete solid angle, i.e,

$$\langle C_{\text{sca}} \rangle / 4\pi = 1/2 \int_0^{\pi} \langle F_{11}(\Theta) \rangle \sin(\Theta) d\Theta \quad (\text{A.9B})$$

Individual particle values are not practical photometric scattering quantities for populations of particles – the ensemble average  $\langle C_{\text{sca}} \rangle$  is. It is the per-particle average value of the scattering cross section for the  $\text{D}$  particles contained in a specific volume. For any population of particles having concentration low enough so that each particle scatters independently,  $\langle C_{\text{sca}} \rangle$  is the joint scattering cross section—the simple sum of all individual particle cross sections divided by the number of particles. Specifically,  $\langle C_{\text{sca}} \rangle \equiv [1/\text{D}] \sum_i C_{\text{sca},i}$ , where the sum extends to  $i = \text{D}$ . As used here,  $\text{D}$  is the dimensionless number of particles (Section A.1), meaning  $\langle C_{\text{sca}} \rangle$  retains the dimensions of area. In remote sensing applications, the number-concentration  $N[\text{cm}^{-3}]$  is the pertinent population density quantity, which when multiplied by the sample volume size  $V[\text{cm}^3]$  is the number of particles  $\text{D} \equiv NV$ .

In terms of light energy [J],  $\langle C_{\text{sca}} \rangle$  is the amount scattered in all directions per unit of incident energy density [ $\text{J m}^{-2}$ ] [BDS, p 33]. In terms of energy rate, the energy scattered per unit time in all directions by the population of particles is the scattered power  $P_{\text{sca}}[\text{W}]$ . With  $I_o[\text{W m}^{-2}]$  as the magnitude of the incident irradiance, these are related as  $P_{\text{sca}}/\text{D} = (\langle C_{\text{sca}} \rangle / 4\pi) I_o$ . The mathematical interpretation of  $\langle C_{\text{sca}} \rangle$  is therefore that of the factor relating incident light energy flux to per-particle scattered power.

## APPENDIX B

### PARAMETERS OF PARTICLE POPULATIONS

#### B.1 NUMBER-, AREA-, AND VOLUME-CONCENTRATION

Preparatory to defining ensemble averaging and other physical parameters of particle populations, it is useful to define three integral quantities that specify the concentration of particle geometric attributes per unit of physical volume.

The most familiar is *number-concentration*

$$N[\text{cm}^{-3}] = \int n_N(r) dr \quad (\text{B.1A})$$

(also called the number density or particle density), which is the aggregate number of all particles irrespective of size within a unit volume. The general particle size-distribution function is  $n_N(r)$ , units being  $[\text{cm}^{-3} \mu\text{m}^{-1}]$ . It is the number of particles per unit physical (spatial) volume with radii between  $r$  and  $(r + dr)$ . (Particle size is quantified by  $r$ ; simply the radius for a spherical particle. In cases of non-spherical particles,  $r$  is an appropriate equivalent radius considered in Sections B.2 and B.5.) The normalized or unit number-concentration size-distribution function is  $n(r)$ , which is  $n_N(r)$  for the condition  $N = 1 \text{ cm}^{-3}$ , i.e.,  $\int n(r) dr \equiv 1 \text{ cm}^{-3}$ . Furthermore,  $n_N(r) = N n(r)$  meaning that  $n(r)$  is the fundamental quantity describing the manner in which particles are distributed in size. And so,  $n(r)$  is the particle size *probability density function* (pdf). Common analytical forms of  $n(r)$  are referred to in Sect B.5.

The second integral quantity is *area-concentration*, namely, the cross-sectional area-concentration

$$A_P[\mu\text{m}^2 \text{ cm}^{-3}] = \int \pi r^2 n_N(r) dr \quad (\text{B.1B})$$

which is the total geometric cross-section area (also referred to as total projected area [MD, p 396]) of all particles per unit volume. The average geometric cross-sectional area per particle per unit volume is  $A_P/N \equiv \langle G \rangle$  in [MTL, p 161]. For spherical particles the total surface area of all particles per unit physical volume is  $4A_P$ ; the average surface area per particle is  $4A_P/N$ .

The third integral quantity of a population of particles is *volume-concentration*

$$V_P[-] = \int \pi r^3 n_N(r) dr \quad (\text{B.1C})$$

When multiplied by  $4/3$ , it specifies the total volume of spherical particles per unit of physical volume. The quantity  $4/3V_P$  is also called the volume fraction [MD, p 374]. The average particle volume per particle per unit physical volume is  $4/3V_P/N$ .

The integrations are over radius. In theory,  $r \in [0, \infty]$ , but in application the range is limited,  $r \in [r_{\min}, r_{\max}]$ . The meaning of  $r$  for spherical particles is evident, but for non-spherical particles  $r$  requires further explanation.

## B.2 AREA-EQUIVALENT SPHERE RADII OF SPHEROIDS

In particle-radiation physics, particle size is usually quantified by radius  $r$  (in atmospheric chemistry, by diameter  $d$  or  $D$  [SP, Chapter 7]). The meaning of radius as size metric is readily appreciated for spherical particles, but for non-spherical particles two interpretations are customary. For light scattering computations, the size of irregular particles is specified in terms of the *area-equivalent sphere radius*  $r_A$ . For radiation absorption computations (or scattering by very small particles), it is common to use the *volume-equivalent sphere radius*  $r_V$ . The defining equations for both  $r_A$  and  $r_V$  depend on the geometric parameters describing the non-spherical morphology. (The volume-equivalent sphere radius is not applied further here.)

The spheroid morphology, the only non-spherical particle volume treated here, results from complete  $\psi$  rotation of the plane figure given by

$$r(\zeta, \psi) = a/2 [\sin^2(\zeta) + (a^2/b^2) \cos^2(\zeta)]^{-1/2} \quad (\text{B.2})$$

about axis  $b$ , the rotational axis. The distance from the plane-figure center is  $r(\zeta)$ ,  $\zeta$  is the zenith angle relative to the  $b$  axis. The axis  $a$  is the diameter of the plane figure described by Eq (B.2) and is, consequently, the diameter of the circular ‘equatorial’ plane of the three-dimensional spheroid volume. The single parameter specifying the non-spherical shape of these axisymmetric volumes is the axis ratio  $\epsilon = a/b$ . Two distinct types of spheroid particles can occur. For  $b > a$ , the spheroid is roll-shaped, described as *prolate*—in the limit  $a/b \rightarrow 0$  the spheroid is needle-like. For  $a > b$ , the spheroid is bun-shaped, *oblate*—in the limit  $a/b \rightarrow \infty$  this spheroid is a disc-like particle. The sphere is the limiting intermediate case for  $\epsilon = 1$ , as is evident from  $a = b$  in Eq (B.2). In summary, for the non-spherical particles dealt with in this report,

Axis ratio  $\epsilon \equiv a/b$ :  
 Prolate  $\epsilon < 1$ ,  
 Sphere  $\epsilon = 1$ ,  
 Oblate  $\epsilon > 1$ .

The expressions for the area-equivalent-sphere radii for prolate and oblate spheroids are given in [MT4, eq 5 & 6]. The radius of a sphere having the same surface area as a prolate spheroid is

$$r_A = \{[a^2/2] [1 + (\epsilon^2 \eta_{pr})^{-1} \sin^{-1}(\epsilon \eta_{pr})]\}^{1/2} \quad (\text{B.3A})$$

where  $\eta_{pr} = (1/\epsilon^2 - 1)^{1/2}$ . The radius of a sphere having the same surface area as an oblate spheroid, now with  $\eta_{ob} = (\epsilon^2 - 1)^{1/2}$ , is

$$r_A = \{[a^2/2] [1 + (2\epsilon \eta_{ob})^{-1} \ln((\epsilon + \eta_{ob})/(\epsilon - \eta_{ob}))]\}^{1/2} \quad (\text{B.3B})$$

For spheroid particle populations having a single  $\epsilon$ -value, these prolate or oblate  $r_A$  values can be substituted directly for  $r$  in the area-concentration expression Eq (B.1B), and in particle attenuation size parameter expressions, at least the scattering ones—Eqs (B.4A) and (B.4B).

### B.3 PARTICLE ATTENUATION SIZE PARAMETERS

In small particle–radiation interactions the fundamental relationship between particle size and radiation physical dimension is as the ratio of particle circumference to wavelength  $\lambda$  or, equivalently, as the product of particle radius and angular wave number  $2\pi/\lambda$  (also called free-space wave number [BH, p 27], optical wavenumber [HG, p 1114], or wavenumber [TKD, p 2]). The combined quantity is the particle *size parameter*

$$x = 2\pi r/\lambda \quad (\text{B.4A})$$

In scattering computations specifically, the operative variable appears in the combination  $x$ , and not  $r$  or  $\lambda$  separately. Using as scaling the value of  $x$ , scattering regimes are differentiated into: Rayleigh ( $x \ll 1$ ), Mie ( $x \approx 1$ ), and geometric optics ( $x \gg 1$ ). For a population of spherical particles the effective size parameter  $x_{\text{eff}} = 2\pi r_{\text{eff}}/\lambda$  is the appropriate scaling parameter ( $r_{\text{eff}}$  is defined in Section B.5). For non-spherical particles it is the area-equivalent sphere size parameter  $x_A = 2\pi r_A/\lambda$ .

The complete variable appearing in particle–light interaction computations also includes the (relative) refractive index. This variable, the product  $mx$ , is complex as is the relative refractive index  $m = (m_{\text{particle}}/m_{\text{air}}) = (m_{\text{real}} - i m_{\text{imag}})$ . The resulting particle attenuation parameters are the *scattering size parameter*

$$x_{\text{sca}} = 2\pi m_{\text{real}} r/\lambda \quad (\text{B.4B})$$

and the *absorption size parameter*

$$2x_{\text{imag}} = 4\pi m_{\text{imag}} r/\lambda \quad (\text{B.4C})$$

An implication of  $x_{\text{sca}}$  is evident; the scattering regime of high-valued index particles, e.g., aluminum beads, can obey geometric optics rules even though  $x$  may suggest Mie-like behavior.

The reason for the factor 2 in Eq (B.4C) derives from the definition of the bulk (or slab) absorption coefficient  $\beta_{\text{abs}}(\text{cm}^{-1}) = 4\pi m_{\text{imag}}/\lambda$  [BH, eq (2.52)]. The absorption optical thickness for a path of length  $r$  is  $\beta_{\text{abs}}r$ , which is then just Eq (B.4C). It has therefore been proposed that the absorption size parameter be defined as  $2x_{\text{abs}}$ . “Since the average thickness (cord length) of a sphere is  $4(r)/3$  --, a value close to  $(r)$ , it is convenient to simply consider the radius of the particle as the best metric of its thickness” [LM, p 5230], and to consider the quantity  $4\pi m_{\text{imag}} r/\lambda$  as the appropriate particle absorption size parameter.

### B.4 ENSEMBLE AVERAGING

The ensemble-averaging procedure is the appropriate accounting of individual particle contributions to the single-value measurement of light scattered by a population of particles. The ensemble average is, then, the correct per-particle average value of any population scattering quantity. The topic of ensemble averaging over the different particle properties is discussed principally in [MHT, pp 15-17] and in [MTL, pp 72-73].

Measurements of the scattered radiation Stokes parameters are for the total population of particles—diverse as they may be—within a sample volume  $V$ . In this discussion it is assumed that all unit volumes within  $V$  have the same population of particles (and that  $V$  is identical to the scattering volume  $V_T$ .) To meaningfully interpret such measurements in terms of particle property values, ensemble-average values of the scattering matrix elements need to be formed that correctly apportion the effects of each member of the total population of particles. The *ensemble-average scattering matrix*  $\langle \mathbf{F}(\Theta) \rangle$  provides these elements  $\langle F_{ij}(\Theta) \rangle$ . The definition of  $\langle \mathbf{F}(\Theta) \rangle$ , and therefore its elements  $\langle F_{ij}(\Theta) \rangle$ , is the principal topic here.

In general, the particles in a unit volume are a mixture of  $N$  particles having various values of the four quantities: size ( $r$ ), shape ( $\varepsilon$ ), orientation ( $\phi$ ), and refractive index ( $m$ ). (Regarding orientation it is convenient to assign the single angle variable  $\phi$  to represent the three orthogonal Euler angles needed to completely specify particle orientation with respect to the measurement frame of reference; considered further below.) Therefore, the most general un-averaged volume scattering matrix is expected to be of the form  $\mathbf{F}(\Theta; N, r, \phi, m, \varepsilon)$ , where  $\Theta$  is considered a variable and the other arguments can, for the most-part, be treated as parameters. For scattering by spherical particles  $r$  is radius, whereas by spheroid particles  $r$  is an appropriate area-equivalent sphere radius considered in Section B.2.

Since the quantity  $\mathbf{F}$  varies directly with number-concentration  $N$ , the equi-partition per-particle average matrix is simply  $\langle \mathbf{F} \rangle = \mathbf{F}/N$ , with the provision that  $N$  is a single type of particle. In effect, the unbiased probability is  $1/N$  that any one particle contributes to the value of  $\mathbf{F}$ .

The variation in each of the four remaining properties is more formally described by its own *probability density function* (pdf). In the ensemble-averaging procedure each pdf is integrated over its complete domain resulting in 100% likelihood. For example, the pdf for particle sizes is the normalized (unit) number-concentration  $n(r)$ , seen in Sect B.1. The domain of  $n(r)$  is  $r \in [r_{\min}, r_{\max}]$ . The complete-domain integral of the particle size pdf, of necessity, is  $\int_r n(r) dr = 1$ . Integral pdf values of unity are similarly required for any other pdf. From these integrals the value of each pdf is evaluated—the useful end-result of the ensemble-averaging procedure.

It is assumed that the variation in any one of the particle properties, like shape, is statistically independent of all other property variations. Therefore, the total pdf for all properties is just the product (joint) of all pdf's. With the four pdf's:  $n(r)$ ,  $p(\phi)$ ,  $p(m)$ , and  $p(\varepsilon)$ , respectively, the total pdf is  $p(r, \phi, m, \varepsilon) = [n(r) p(\phi) p(m) p(\varepsilon)]$ . The ensemble-averaging procedure entails evaluating  $p(r, \phi, m, \varepsilon)$ —more practically, evaluating its individual pdf's assuming mutual independence—given the multi-domain integral constraint

$$\int_\varepsilon \int_m \int_\phi \int_r p(r, \phi, m, \varepsilon) dr d\phi dm d\varepsilon = \int_\varepsilon \int_m \int_\phi \int_r n(r) p(\phi) p(m) p(\varepsilon) dr d\phi dm d\varepsilon = 1$$

In the case of spheres,  $\varepsilon = 1$  and the shape pdf is a delta function equal to unity only at  $\varepsilon = 1$  and zero at all other  $\varepsilon$ -values. Thus, the domain integral of the shape pdf is also unity. More generally and as assumed here, any population of non-spherical particles has a single fixed shape parameter value,  $\varepsilon (\neq 1)$ , the pdf is again a delta function non-zero only at that  $\varepsilon$ -value, so that the domain integral is again unity. In effect, the shape pdf is known beforehand so that it can be left completely out of the ensemble-averaging procedure. As an example, the spheroid shape parameter  $\varepsilon$  is a

single-valued input parameter to any scattering computation code (listed in Appendix C) and no explicit integration over shapes is carried out.

At most two types of particles—meaning two refractive indices—are present in the sample volume considered here. A unit physical volume may contain a homogeneous mix of different amounts of the two particle types:  $N_a$  of type ‘a’,  $N_b$  of type ‘b’. The pdf for either refractive index is  $p(m_a)$  or  $p(m_b)$ , each pdf being a constant applicable to its type. These index pdf’s are complements, i.e.,  $p(m_a) + p(m_b) = 1$ . Their constant values are thus fractions, specifically, they are the relative number-concentration mixing ratios  $N_a/N$  and  $N_b/N$ , with  $N = N_a + N_b$  as the total number-concentration per unit physical volume. In any event,  $\int_m p(m) = 1$ .

The remaining unspecified pdf is now  $p(r, \phi) = n(r) p(\phi)$ . Orientation is next considered. A triple-angle integral is involved in evaluating the orientation pdf integral, specifically,  $\int_\phi p(\phi) d\phi = \int_{\phi_1} \int_{\phi_2} \int_{\phi_3} p(\phi_1) p(\phi_2) p(\phi_3) d\phi_1 d\phi_2 d\phi_3$ . Here random orientation of all particles is assumed – spheres have no preferred orientation and there is no net external force aligning the spheroid particles. Therefore, any orientation is equally likely in the particle’s frame of reference so that two of the pdf’s are equal and uniform, i.e.,  $p(\phi_1) = p(\phi_2) = \text{constant}$ . The domain of these two orthogonal angles is the full range  $2\pi$ . In order for  $\int_{\phi_1} p(\phi_1) d\phi_1 = \int_{\phi_2} p(\phi_2) d\phi_2 = 1$ , then  $p(\phi_1) = p(\phi_2) = 1/2\pi$ . The third angle accounts for non-coincidence of particle and measurement reference frames. Its pdf is also uniform,  $p(\phi_3) = \text{constant}$ , since randomly oriented particles have no preferred alignment with respect to any reference frame. But the probability that a particular direction between  $\phi_3$  and  $\phi_3 + d\phi_3$  occurs is  $p(\phi_3) \sin \phi_3$ . The domain of  $\phi_3$  is 0 to  $\pi$  for symmetric particles so that the necessary condition  $\int_{\phi_3} p(\phi_3) \sin \phi_3 d\phi_3 = 1$  means that  $p(\phi_3) = 1/2$ . Finally, for randomly oriented spheroid particles  $\int_\phi p(\phi) d\phi = 1$  means that the constant value of the orientation pdf is  $p(\phi) = 1/8\pi^2$  [MTL, eq 3.27].

The ensemble-average scattering matrix, varying with scattering angle  $\Theta$ , is

$$\langle \mathbf{F}_\mu(\Theta) \rangle = 1/N_\mu \int_r \int_\phi \mathbf{F}_\mu(\Theta; r, \varepsilon, \phi, m) n(r) p(\phi) dr d\phi \quad (\text{B.5A})$$

where the subscript  $\mu$  indicates the category of particle, i.e. the specific  $\varepsilon$  and  $m$ ,  $n(r)$ , and  $p(\phi)$  that characterizes the kind of particle. Commonly, integer  $\varepsilon$  and  $m$  values are considered, but only one form of  $n(r)$  is used and only random distributions are allowed. The normalization in Eq (B.5A) makes the ensemble average independent of the number-concentration  $N_\mu$ . For randomly oriented particles  $p(\phi) = 1/8\pi^2$  so that Eq (B.5A) becomes

$$\langle \mathbf{F}_\mu(\Theta) \rangle = 1/(8\pi^2 N_\mu) \int_r \mathbf{F}_\mu(\Theta; r) n(r) dr \quad (\text{B.5B})$$

Eq (B.5B) is the ensemble-averaged scattering matrix for  $\mu$ -type particles in a unit volume. Clearly, since normalized by the number of particles per unit volume  $N_\mu$ , it is the per-particle average for randomly oriented particles. Where two categories of such particles are co-located,  $\mu = a, b$ , then the combined ensemble-averaged scattering matrix is  $\langle \mathbf{F}_c(\Theta) \rangle = N_a \langle \mathbf{F}_a(\Theta) \rangle + N_b \langle \mathbf{F}_b(\Theta) \rangle$ . Eq (B.5B) is repeatedly evaluated by scattering codes, such as those referenced in Appendix C. The scattering code input parameters are  $(\varepsilon, m)_\mu$ , along with the range of the size variable  $r$ . The code output variable is  $\Theta$ .

Next, the ensemble-averaged scattering matrix  $\langle \mathbf{F}_\mu(\Theta) \rangle$  is partitioned into its all-angle average part and the scattering-angle-dependent part. The former is the solid-angle-average ( $1/4\pi$ ) of the photometric scattering quantity, the *ensemble-average scattering cross section*  $\langle C_{\text{sca},\mu} \rangle$  –defined in Appendix A.7 as the per-particle average scattering ability of the  $\mu$ -type particles. The latter part is the polarimetric scattering quantity, the *normalized scattering matrix*  $\mathbf{F}_\mu(\Theta)$ , explained in [MTL, pp 100-103] and in Appendix A.3 (esp. Table A.1). Formally, therefore,

$$\mathbf{F}_\mu(\Theta) = 4\pi \langle \mathbf{F}_\mu(\Theta) \rangle / \langle C_{\text{sca},\mu} \rangle \quad (\text{B.5C})$$

The ensemble-averaged scattering quantities in Eq (B.5C) are bracketed  $\langle \rangle$ , these are per-particle average quantities. Each element  $F_{ij,\mu}(\Theta)$  of the normalized scattering matrix  $\mathbf{F}_\mu(\Theta)$  is therefore a per-particle average quantity, but also a per-unit scattering angle quantity in the direction indicated by  $\Theta$ . For two  $\mu$ -type populations co-located in the unit volume the combined normalized scattering matrix [MTL, eq 4.74] is

$$\mathbf{F}_c(\Theta) = [N_a \langle C_{\text{sca},a} \rangle \mathbf{F}_a(\Theta) + N_b \langle C_{\text{sca},b} \rangle \mathbf{F}_b(\Theta)] / [N_a \langle C_{\text{sca},a} \rangle + N_b \langle C_{\text{sca},b} \rangle] \quad (\text{B.5D})$$

## B.5 EFFECTIVE RADIUS AND EFFECTIVE VARIANCE

Naturally occurring nascent aerosol particles are usually very small ( $r \leq 0.01\mu\text{m}$ ) and are often nearly mono-sized. These aerosol particles reside in the air for days, but not as individual particles. Coagulation among small particles leads to fewer but larger particles that are more broadly distributed in sizes. The resulting particle size distributions take on distinctive forms that are specified by the form of  $n(r)$ , e.g., modified-gamma (refer to Section 3.2), log-normal, etc, [SP, Sections 7.1.8 and 7.1.9; TD, sect. 1.4.1.4.3; or MTL, Section 5.10.1]. These can be characterized by two parameters: a central moment–mean, median, or mode–and a dispersion moment, e.g. standard deviation.

In evaluating scattering effects of such polydispersed aerosol particles, it has been shown [HT, pp 558, 559; MT4, pp 7209, 7210; or MTL, pp 161 & 285] that such distributions can be parameterized by the two moments – *effective radius*  $r_{\text{eff}}$  and *effective variance*  $v_{\text{eff}}$ , defined as

$$r_{\text{eff}} = 1/\langle G \rangle \int_r \pi r^2 r n(r) dr \quad (\text{B.6A})$$

$$v_{\text{eff}} = 1/(\langle G \rangle r_{\text{eff}}^2) \int_r \pi r^2 (r - r_{\text{eff}})^2 n(r) dr \quad (\text{B.7A})$$

where the integration extends from smallest to largest particle,  $r \in [r_{\min}, r_{\max}]$ . The individual-particle cross sectional area is  $\pi r^2$  and the particle-population size pdf is  $n(r)$ . The normalization factor  $\langle G \rangle$  is the average geometric cross-sectional area per particle per unit physical volume; refer to the discussion of Eq (B.1B). Since  $\langle G \rangle = (A_p/N) = \int_r \pi r^2 n(r) dr$ , it is thus seen to be the accumulated geometric cross-sectional area of all particles per unit physical volume  $A_p$  divided by the number-concentration  $N$ , units [ $\mu\text{m}^2 \text{cm}^{-3}$ ], and since the integral in Eq (B.6A) has units [ $\mu\text{m}^3 \text{cm}^{-3}$ ], then the units of  $r_{\text{eff}}$  are indeed [ $\mu\text{m}$ ]. As such,  $r_{\text{eff}}[\mu\text{m}]$  is the cross-sectional-area-weighted mean radius of all particles in the population. Likewise,  $v_{\text{eff}}[-]$  is the cross-sectional-area-weighted

mean variance of all particles normalized by  $r_{\text{eff}}^2$ , which makes this measure of the size range dimensionless.

It is the ratio of the individual-particle dimension to the wavelength of light that determines the optical effectiveness of particles, specifically it is the size parameter  $x = 2\pi r/\lambda$ , given as Eq (B.4A). Similarly, for an ensemble of variously sized particles, their net efficiency in scattering light incident on them varies as the effective size parameter  $x_{\text{eff}} = 2\pi r_{\text{eff}}/\lambda$ . In fact,  $x_{\text{eff}}$  is now nearly universally used in quantifying the scattering characteristics of polydispersed particles [e.g., MTL, Figures 9.12, 9.20-22, 9.26-28].

As demonstrated, for example by [MTL, Table 10.1 and Figure 10.6], both the photometric and polarimetric scattering (and absorption) quantities of typical distributions of aerosols are remarkably insensitive to the specific form of  $n(r)$  and can be more simply parameterized by  $r_{\text{eff}}$  and  $v_{\text{eff}}$ . The physical reason for this insensitivity is that all distributions approximate the numbers of the optically effective particles similarly; e.g., [MTL, Figure 10.7]. From visible through short-wave-infrared wavelengths, the optically effective (active) particles have sizes comparable to or larger than the illumination wavelength, specifically,  $r > 0.1 \mu\text{m}$ . The different analytical forms for  $n(r)$  do influence attenuation in the optically ineffective (passive) particle-size range, i.e.,  $r < 0.1 \mu\text{m}$  (ZZK, p 13). Notwithstanding, the analytical form of  $n(r)$  can materially affect the execution time of scattering computations.

The relationships between the more common statistical moments of distributions, specifically the mode radius  $r_{\text{mo}}$  and standard deviation  $\sigma$  (or variance  $\sigma^2$ ) do depend on the analytical form of  $n(r)$ . For the modified-gamma distribution applied herein (Section 3.2), the relationships are here obtained numerically only for  $\gamma \neq 1$ . For  $\gamma = 1$ , the distribution is the standard gamma distribution [see HH, p 1140]. As such,

$$r_{\text{mo}} = r_{\text{eff}} (1 - 3v_{\text{eff}}) \quad (\text{B.6B})$$

$$\sigma = r_{\text{eff}} [v_{\text{eff}} (1 - 2v_{\text{eff}})]^{1/2} \quad (\text{B.7B})$$

As a final note, development of the effective radius and effective variance has presumed populations of spherical particles. Very often ambient background aerosol particles in the atmosphere are spherically shaped because they are dilute aqueous acid or salt solutions. In low humidity conditions and in desert environments, even background aerosols may be non-spherical. Man-made weapon aerosol particles are also typically non-spherical. Approximations that apply to the scattering ability of spheroid particles are straightforwardly developed by using the  $r_A$  expressions, Eqs (B.3A) and (B.3B), for  $r$  in Eqs (B.6A) and (B.7A).

## APPENDIX C

### SCATTERING CODES AND CODE COMPARISONS

By scattering code is meant the collection of interrelated mathematical algorithms that is used to compute the photometric and polarimetric quantities specifying radiative interactions between incident radiation and small-particle populations. In particular, the values of the Mueller scattering matrix elements as functions of scattering angle are computed, given the value of the physical and optical properties of the scattering particles and the wavelength of illumination. The relevant properties for individual particles are particle size, shape, orientation (if non-spherical), and complex index of refraction. For ensembles of particles the additional population parameters of mean size and variance are needed, along with the analytical form of the particle size distribution.

#### C.1 PARTICLE SCATTERING CODES

A number of such codes are publicly available in printed format, e.g., [BH, pp 477-497] or [TD, pp 136-147]. In electronic format there are increasing numbers of available codes, e.g., at the following internet sites:

1. Various scattering codes of M.I. Mishchenko are available through –  
<http://www.giss.nasa.gov/~crmim>
2. A Fortran77 version of the Mie code by M.F. Modest is available at –  
<http://www.academicpressbooks.com/companions/0125031637>  
(On the Elsevier lead-page, click on “in North America”, then scroll down list of radiative transfer programs to mmmie.f.)
3. The original Bohren and Huffman [BH, pp 479-482] Mie code is available at web site of B.T. Draine –  
<http://www.astro.princeton.edu/~draine/scattering.html>  
(Scroll nearly to end and click on “bhmie”.)
4. “A well tested and widely used Mie code is (W.J.) Wiscombe’s MIEV0 code in Fortran.” [DU, p 1951]. It is reputed to be available at –  
[ftp://climate.gsfc.nasa.gov/pub/wiscombe/Single\\_Scatt/Homogen\\_Sphere/Exact\\_Mie/NCARMie\\_Report.pdf](ftp://climate.gsfc.nasa.gov/pub/wiscombe/Single_Scatt/Homogen_Sphere/Exact_Mie/NCARMie_Report.pdf)

A recent more comprehensive listing (including European and Russian sources) of light scattering codes is given in [BAK, Appendix E].

Although all codes carry out essentially the same computations, the mathematical methods, the conditions of application, and the analytical forms available for the scattering particle size distribution vary among the available codes. A progression of codes is briefly described here; from the Rayleigh condition (particle sizes much smaller than wavelength), to single sphere (particle size comparable to wavelength), to numbers of same-sized spheres, to spheres having distributed sizes, and finally to non-spherical (but axi-symmetric) particles having distributed sizes.

The simplest scattering condition is that of so-called Rayleigh scattering, in which case the scattering molecules, particles, or droplets are much smaller in size than the wavelength of the illuminating radiation (size parameter  $x \ll 1$ ). Single dipoles are induced in such cases and

variations in the size or shape of such very small particles do not affect the scattering computations. The normalized scattering matrix elements (refer to Appendix A.3, Eq (A.2B)) are then simple trigonometric functions of the scattering angle  $\Theta$ . Specific, the diagonal elements are  $a_1(\Theta) = a_2(\Theta) = \frac{1}{2} (1 + \cos^2 \Theta)$ ,  $a_3(\Theta) = a_4(\Theta) = \cos \Theta$ , and there are only two non-zero off-diagonal elements  $b_1(\Theta) = \frac{1}{2} (\cos^2 \Theta - 1)$ , since  $b_2(\Theta) = 0$ , and due to the symmetry of the point-like Rayleigh scattering sources, all other  $b$ 's (Eq A.2C) are also zero. The resulting scattering matrix is that of a polarizer, given in Appendix E, Eq (E.3C). Ideally, the degree of linear polarization for Rayleigh scattering, observed at  $\Theta = 90^\circ$  is simply  $-b_1(\pi/2)/a_1(\pi/2) = 1.00$ , i.e., 100 % vertically polarized, which means perpendicular to the scattering plane. Directly forward  $\Theta = 0^\circ$  or backward  $\Theta = 180^\circ$ , the degree of linear polarization is zero. Scattering computations are, clearly, simple analytical exercises for the Rayleigh condition.

As the scattering particle sizes become comparable with the illumination wavelength ( $x \approx 1$ ), then the scattering pattern increases in complexity due to the increased number and complexity of dipole modes induced in the scattering particles by the incident light. Physically, as particles increase in size the number of radiation redirection processes available increases (e.g., reflections and refractions within and around the scattering particle), and consequently the scattering pattern becomes more complex.

The most basic and well-researched situation, when wavelength and particle sizes are comparable, is the single sphere to which the Lorenz-Mie theory (often called simply Mie theory) applies. As discussed in Appendix A.1, this scattering matrix is block-diagonal, containing only four non-zero elements, all of which are analytical functions of the two complex Lorentz-Mie electric field (amplitude) matrix elements.

Perhaps the most widely available and most easily understood code for this single-sphere scattering situation has been the Bohren and Huffman (1983) code, called by the authors BHMIE, available in print format as [BH, Appendix A]. It uses the nomenclature introduced by van de Hulst [VH, Chapter 9] that is now almost always used [e.g., DU]. The extension of such single-sphere code results to a dispersion of same-sized (mono-dispersed) spheres is simply accomplished by multiplying all values by  $N$ , the number-concentration.

The straightforward enhancement of the BHMIE code to include poly-dispersed spheres is provided by the Thomas and Duncan (1993) code, called by the authors MIEGEN, available in print format as [TD, Table 1.41]. Although a single form of particle size distribution is provided in the MIEGEN code, the so-called modified gamma size distribution [DE, p 75], which is given in Section 3.2 of this report as Eq (7B), other analytical particle size-distribution functions can readily be edited-in.

A more general poly-disperse spherical particles Mie scattering code is that by M.I. Mishchenko [M00] available at: <ftp://ftp.giss.nasa.gov/pub/crmim/spher.f>. This scattering code applies the Lorenz-Mie theory for spherical particles to any one of six different types of particle size distribution: modified gamma, log-normal, power-law, gamma, modified power-law, and bimodal log-normal. It is referred to here as the MIMSPH code. In Section C.2, the results of MIEGEN and MIMSPH are compared.

The more realistic, yet basic situation is polydispersed non-spherical but axi-symmetric particles (having a circular equatorial plane, i.e., an axis of rotation), randomly oriented particles of sizes comparably to the wavelength of illumination. A practical strategy to quantify the scattering properties in this situation involves expanding the incident, internal, and scattered electromagnetic fields in vector spherical wave functions that are related through a transition (T) matrix. In particular, the  $(2 \times 2)$  incident-to-scattered electric field (amplitude) matrix is known

as the T-matrix, from which the computation method for the scattering matrix itself takes its name [MTM; also MTL, pp 115-119]. Probably the best documented and most versatile T-matrix scattering code, applicable to “polydispersed, randomly oriented particles of identical axially symmetric shape”, is that of Mishchenko [M93], which is written in FORTRAN with double (d) or extended (q) precision and is available, respectively, at:

<ftp://ftp.giss.nasa.gov/pub/crmim/tmd.new> and <ftp://ftp.giss.nasa.gov/pub/crmim/tmq.new>

The double-precision T-matrix scattering code is referred to here as the MIMTMD code.

The input parameters needed for both the spherical and non-spherical T-matrix scattering code computations, using MIMSPH and MIMTMD, are listed and well explained both as comments to the codes and in [MTL, Sections 5.10 and 5.11]. All of the results presented in this research report (esp. Sections 4.2 and 4.3) are obtained using the MIMTMD scattering code.

## C.2 MIE CODE COMPARISONS

The purpose here is to document an inter-comparison of two scattering codes for polydispersed spheres: Thomas and Duncan (MIEGEN) [TD, table 1.41] vis-à-vis Mishchenko (MIMSPH) [M00], as applied to the same scattering medium of spherical particles. Both codes are applied first to the mono-modal distribution of ambient background aerosols and then to the bi-modal distribution of two types of particles combined—the same ambient background aerosols plus bio-aerosols. The size-distribution form for both types of particles is the same—modified gamma—but each type has different distribution parameters and refractive indices (given in Tables 3.1 and 3.2). Figure C.1 are the resulting angular profiles ( $0^\circ \leq \Theta \leq 180^\circ$ ) of the first two volume scattering coefficients,  $\beta_{11}(\Theta)$  and  $\beta_{21}(\Theta)$ , as computed by the two spherical scattering codes.

Clearly, the two codes are evaluating the scattering matrix elements for polydispersed particles equivalently, in spite of different approximations, ensemble-averaging methods, limits on integrations, etc. The largest differences ( $\approx 1 \times 10^{-10} \text{ cm}^{-1}$ ) are found in off-diagonal elements near  $\Theta = 175^\circ$  (indiscernible in Figure C.1, bottom plots). Irrespective—MIEGEN or MIMSPH, all results are equivalent and intercomparable.

A word of caution is in order for users of available scattering codes: The input parameter lists that are required to produce the close comparative results shown in Figure C.1 may not be identical. This applies in particular to the range limits on particle size integration.

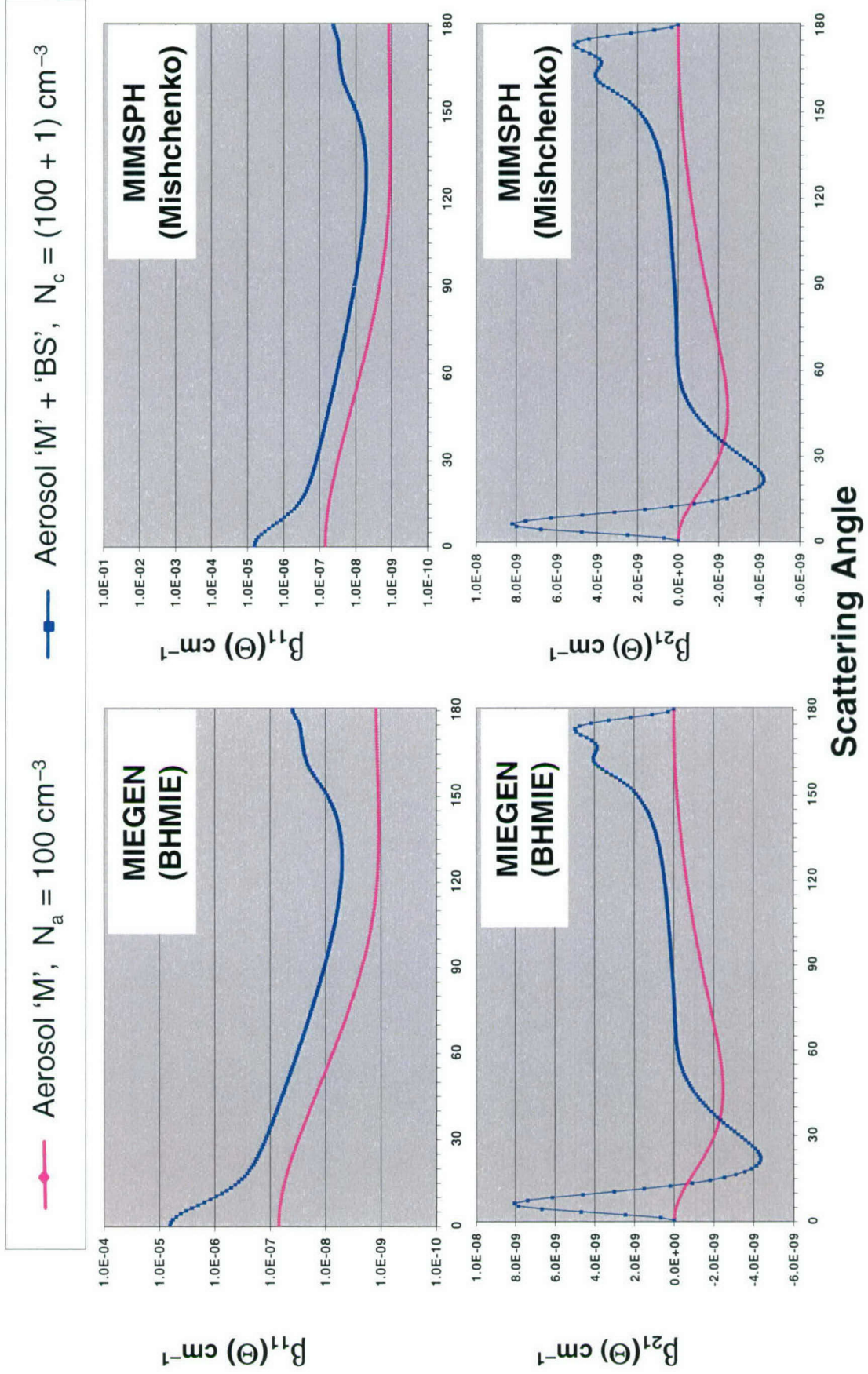


Figure C.1. Comparative Spherical Scattering Code Computations of Profiles of Intensity (Top) and Linear Polarization (Bottom) Volume Scattering Coefficients at  $l = 2.12 \text{ mm}$ ; MIEGEN-BHIE Code (Left), MIMSPH Code (Right). (Red) Ambient background aerosol–continental ‘L’ in Table 3.1 with  $N_a = 100 \text{ cm}^{-3}$ , distributed as in Figure 3.1. (Blue) Combination of same ‘L’ ambient background plus ‘BS’ aerosol in Table 3.1 with  $N_b = 1 \text{ cm}^{-3}$ , distributed as ‘Bio-Aerosol’ in Figure 3.1. MIEGEN-BHIE –Thomas and Duncan enhancement of Bohren and Huffman spherical particle scattering code. MIMSPH: M.I. Mishchenko spherical particle code.

## APPENDIX D SIGNAL-TO-NOISE RATIOS

The abbreviated discussion presented here is mostly heuristic; more rigorous developments are found in [DKB, chapters 5 & 6; KI, chapters 2 & 4; HA, chapters 4 & 8]. Expressions for two basic noise types – shot-noise and thermal-noise – are used to produce the signal-to-noise ratios (SNR) for each. Here the current form of SNR [e.g. DKB, eq 6.2] is developed versus the power form [e.g., KI, p 12].

### D.1 SHOT-NOISE SNR

Fundamental to photon detection is the linear relationship between the incident photon flux, more specifically the signal radiant power  $P_S$ , and the resulting detector current  $i_S$ , i.e.,

$$i_S \sim P_S \quad (\text{D.1})$$

The corollary to Eq (D.1) is that one photon can produce, at most, one free electron, which can then transport its charge and thereby contribute to the signal current. However, every incident photon does not free-up one electron. Some photons may be absorbed and only heat the detector, others may be reflected, etc. The result is that even for steady  $P_S$ , the measured signal  $i_S$  changes with time. The temporal fluctuation of  $i_S$  about the mean signal current  $\bar{i}_S$  is called the *shot-noise current*  $i_N = |i_S - \bar{i}_S|$ . The shot-noise limited maximum value of the signal-to-noise ratio is

$$\text{SNR}_{\text{sn}} \leq \bar{i}_S / \langle i_N \rangle \quad (\text{D.2})$$

where  $\langle i_N \rangle$  is a shot-noise current temporal mean compatible with  $\bar{i}_S$ .

The development of an expression for the maximum (ideal) value of  $\text{SNR}_{\text{sn}}$  proceeds by defining  $P_S$  in terms of the number of incident photons  $n_p$ , and  $i_S$  in terms of the number of free electrons  $n_e$  made available; both within a finite (not instantaneous) time interval  $\tau$ . The number of free electrons is the number of detected photons  $n_q$ , specific.  $n_q \equiv n_e$ ; as in this report Section 5.2.1. The efficiency of the photo-detector in converting the interval-averaged number of incident photons into free electrons is the detector quantum efficiency  $\eta < 1$ ,

$$\bar{n}_e = \bar{n}_q = \eta \bar{n}_p \quad (\text{D.3})$$

(Caution: Here subscript  $p$  indicates incident photons,  $e$  free electrons, and  $q$  detected photons. Eq (D.3) is the same as [DKB] eq (5.50) except there subscript  $q$  indicates incident photons.)

On the radiation side of the detector, photons are incident. Since the energy per photon is  $h\nu$  ( $= h\lambda/c$ ), and assuming a narrow enough spectral bandwidth so that all photons are assigned the same optical frequency  $\nu$ , then the incident signal power is

$$P_S^* = (h\nu/\tau) \bar{n}_p \quad (\text{D.4A})$$

where  $\bar{n}_p$  photons are expected to arrive within any one of the time intervals of duration  $\tau$  – the detector integration time or the laser pulse duration. And so  $P_S^*$  is interpreted as the average radiant power arriving during any  $\tau$ . Although  $P_S^*$  and, more fundamentally,  $n_p$  comprise Stokes

vector components (as in this report Section 5, Eqs (10D) and (12A)) for the development here the scalar magnitude is sufficient. The average detected radiant power is

$$P_S = \eta P_S^* = (hv/\tau) \bar{n}_q \quad (D.4B)$$

Furthermore, the radiation quantities signal energy and signal power are related as  $E_S = \tau P_S$ , so that Eq (D.4B) is equivalently  $E_S = (hv) \bar{n}_q$ .

On the electronic side of the detector, electrons are liberated. The signal current during any  $\tau$ -interval tracks the fluctuating number of electrons  $n_e$  free to transport their individual charge  $e$ , specific,

$$i_S = (e/\tau) n_e \quad (D.5A)$$

The set of  $\tau$ -duration individual values of  $n_e$  constitute a random variable, and so too does the set of associated values of  $i_S$ . This random process is Poisson distributed [DKB, Sect 5.2.1; also KI, p 10].

The mean over a number of  $\tau$ -intervals is the *signal current* (the d.c. current)

$$\bar{i}_S = (e/\tau) \bar{n}_e \quad (D.5B)$$

Individual current departure from the  $\tau$ -mean is the fluctuating shot-noise current  $i_N = | i_S - \bar{i}_S |$ , which is quantified in terms of its mean-square variation – its variance

$$\langle i_N^2 \rangle = \langle (i_S - \bar{i}_S)^2 \rangle = (e^2/\tau^2) \langle (n_e - \bar{n}_e)^2 \rangle \quad (D.6A)$$

over many independent time intervals, all of the same duration  $\tau$  [KI, p 13]. The bracket  $\langle x \rangle$  indicates averaging over an ensemble of  $\tau$ -intervals, all having the same mean  $\bar{x}$ . Any variable  $x$  that is Poisson distributed has its variance equal to its mean  $\bar{x}$  (vs. if  $x$  is Gaussian distributed – its variance is equal to its mean squared). But  $n_e$  is so distributed, meaning that Eq (D.6A) becomes, using Eq (D.5B),

$$\langle i_N^2 \rangle = (e^2/\tau^2) \bar{n}_e = (e/\tau) \bar{i}_S \quad (D.6B)$$

which is the same as [KI, eq 2.3].

From Eq (D.5B), with Eq (D.3),  $\bar{n}_e = \eta \bar{n}_p$ , and Eq (D.4A),

$$\bar{i}_S = \eta (e/hv) P_S^*$$

Substitution into Eq (D.2) with Eq (D.6B) results in

$$\text{SNR}_{\text{sn}} \leq \bar{i}_S / \sqrt{\langle i_N^2 \rangle} = \bar{i}_S / \sqrt{(e/\tau) \bar{i}_S} = \sqrt{(\tau/e) \bar{i}_S} = \sqrt{[\eta (\tau/hv) P_S^*]}$$

The effective bandwidth of the receiver is  $b = 1/2\tau$  [e.g. KI, p 13] so that

$$\text{SNR}_{\text{sn}} \leq \sqrt{[\frac{1}{2}(\eta/bhv) P_S^*]} \quad (D.7)$$

Eq (D.7) is equivalent to Eq (12A), Section 5.2 of this report, where  $E_S (= \tau\eta P_S^*)$ . (The symbol  $T$  appearing in the  $E_S$  expression, Eq (10E), Section 5.1, incorporates  $\eta$ .)

## D.2 THERMAL-NOISE SNR

The average number of incident signal photons per pulse, as in Section D.1, is  $\bar{n}_p = (1/\eta)E_S/h\nu = (1/\eta)\lambda E_S/hc$  photons, and the average number of detected signal photons from Eq (D.3) is

$$\bar{n}_q = E_S/h\nu$$

Using a current generator analog [e.g. DKB, fig 5.10; or KI, fig 4.1 (left)] for the current fluctuations caused by the random agitation of participating electrons in the detector resistance  $R_D$ , the average thermal-noise current, often called the Johnson noise current, is

$$\bar{i}_N = \sqrt{[4kT\tau_D F/R_D]}$$

and the number of noise photons is  $\bar{n}_N = (\tau/e) \bar{i}_N$ , giving

$$\bar{n}_N = (1/e)\sqrt{[4kT\tau_D F/R_D]} \quad (D.8)$$

with  $e$  and  $k$  as the elemental electron charge and the Boltzmann constant;  $T(K)$ ,  $\tau_D$ , and  $F$  are the temperature, detector integration time, and amplifier noise factor. The resulting thermal-noise, also called Johnson- or amplifier-noise) limited maximum SNR is

$$SNR_{tn} \leq \frac{\bar{n}_q}{\bar{n}_N} = (e/h\nu)E_S/\sqrt{[4kT\tau_D F/R_D]} \quad (D.9)$$

where  $E_S$ , as in Eq (10E), Section 5.1 of this report, is the detected pulse energy.

## APPENDIX E

### SCATTERING MATRIX ELEMENT INTERPRETATIONS

The topic here is the physical meaning of the individual elements of the aerosol scattering Mueller matrix. The deduction arrived at in this appendix is summarized as follows: The structure of the scattering matrix for the standard (spherical and homogeneous) aerosol is equivalent to a combination of the two optical devices, a polarizer and a wave plate (retarder). Also, four-member blocks of matrix elements for general aerosols are describable in terms of optical devices.

The general form of the per-particle-average scattering matrix – the normalized scattering matrix – with the convenient Perrin (1942) [PN, eq 47] single-subscript symbols explained by van de Hulst (1957) [VH, p 50, case 5], is

$$\mathbf{F}(\Theta) = \begin{vmatrix} a_1(\Theta) & b_1(\Theta) & b_3(\Theta) & b_5(\Theta) \\ b_1(\Theta) & a_2(\Theta) & b_4(\Theta) & b_6(\Theta) \\ -b_3(\Theta) & -b_4(\Theta) & a_3(\Theta) & b_2(\Theta) \\ b_5(\Theta) & b_6(\Theta) & -b_2(\Theta) & a_4(\Theta) \end{vmatrix} \quad (\text{E.1A})$$

Eq (E.1A) is identically the same as Bohren and Huffman (1983) [BH, eq 13.20]. It is the scattering matrix for the aerosols in general.

For homogeneous spheres  $\mathbf{F}(\Theta)$  simplifies to only four non-zero elements [e.g., BH, p 112], considered below. The 10-element Eq (E.1A) form applies to optically active individual spheres or to populations of variously sized optically active spheres. The term *optically active* means polarization-dependent (non-isotropic also called inhomogeneous) refractive index, in particular, one index  $m^L$  for left-handed polarization, another  $m^R$  for right-handed. Different imaginary part is called *dichroism*; different real part, *birefringence* [HC, Chap 8.3, 8.4; BH, pp 185, 190-194].

Eq (E.1A) also applies to randomly oriented similarly shaped spheroids, whether optically active or not [BH, pp 409, 413]. Finally, it applies to any uniformly distributed set of particles, i.e., to “any medium with (ensemble) rotational symmetry even if all the particles are not identical in shape or composition.” [BH, p 413]. Optically active sphere constraints are  $b_{jk} = |b_{kj}|$ , meaning equal off-diagonal pairs of  $b_1$ ,  $b_5$ , and  $b_6$  in Eq (E.1A), and the equal-but-opposite off-diagonal pairs  $b_2$ ,  $b_3$ , and  $b_4$  [BH, p 190, eq 8.16].

The matrix that represents the angular scattering characteristics of a population of randomly oriented spheroidal particles (each having an internal plane of symmetry and all having a similar axis ratio  $\epsilon$ ) that may be optically active, is known to be block diagonal [PHH, eq 4; MTL, pp 87, 100; BH, p 413; or VH, p 50, case 6] having the form

$$\mathbf{F}(\Theta) = \begin{vmatrix} a_1(\Theta) & b_1(\Theta) & 0 & 0 \\ b_1(\Theta) & a_2(\Theta) & 0 & 0 \\ 0 & 0 & a_3(\Theta) & b_2(\Theta) \\ 0 & 0 & -b_2(\Theta) & a_4(\Theta) \end{vmatrix} = \begin{vmatrix} (\text{A}) & (\text{B}) \\ (\text{C}) & (\text{D}) \end{vmatrix} \quad (\text{E.1B})$$

The four Blocks (A) – (D), as defined in Perry et al (1978), [PHH, eq 7], expedite discussion. The all-zero off-diagonal Blocks (B) and (C) indicate that there is no preferred orientation of similarly-shaped polydispersed isotropic-index particles. Such particles are incapable of

introducing rotation to the preferred polarization state of incident light [PN, eq 47A], reconsidered below as item 3). For one, a few, or for many homogeneous (not optically active) spheres, these two blocks must always be all-zeros. For a single non-spherical particle, or for populations of similar non-spherical particles having some form of non-isotropy—preferred orientation of particles or angle-dependent index—Blocks (B) and (C) are no longer all-zeros. As will be seen, Block (A) is associated primarily with particle size and shape, whereas Block (D) with particle index of refraction. The associations between the scattering matrix blocks and the general properties of the scattering particles are:

(A) size & shape	(B) non-isotropy
(C) non-isotropy	(D) refractive index

## E.1 OPTICAL DEVICES AND AEROSOL ANALOGS

The polarization state of the incident light is changed by any scattering medium – in particular the medium of aerosol particles. The change that is observed in the scattered light polarization state is specified by the values of the elements in the scattering matrix. The incident polarization state can be modified in three different ways:

- 1) Change the magnitude of one or both (unequally) orthogonal intensity components into which the incident light can be separated. (Basically, this is due to unequal changes in the two associated electric field amplitude components),
- 2) Change the phase angle between the two orthogonal incident intensity (or amplitude) components, or
- 3) Change the orientation angle, relative to the scattering plane, of the orthogonal axis-pair associated with incident light intensity, i.e., rotate the incident polarization angle.

The classic optical devices that effect the first two scattered-light changes are the *polarizer* (aka *analyzer*) and *retarder* (aka *wave plate*), respectively. The device for achieving the third change is the *rotator*, which as will be seen is usually a special form of polarizer or wave plate.

Aerosols scattering incident light can, to an exploitable extent, be regarded as functioning like analogs of these optical devices. Therefore, preliminary to interpreting individual elements of the scattering matrix, it is useful to consider the Mueller matrices for these optical devices. Explanation of the optical device Mueller matrices follows that of Collett (1993) [CO, Chap 5].

### 1) Polarizer –

The *polarizer* attenuates the magnitude of one orthogonal component of the incident light intensity more than the other. If such attenuation is part of the light detector, vis-à-vis part of the light source, this same optical device is referred to as an *analyzer*. (The generic symbol for either used here is **A**.) The *ideal* polarizer attenuates completely all but one component, i.e., it is absolutely linear. The *perfect* polarizer attenuates not-at-all the component that it does transmit. Thus, one of the two orthogonal component directions into which unpolarized incident light can be divided is completely attenuated if the polarizer is ideal, whereas the other component is unaffected if the polarizer is perfect. It can therefore be expected that the attenuation of any

polarizer is scaled by 1/2, the fraction of unpolarized incident intensity (e.g., sunlight) emerging from an ideal-perfect polarizer, referred to here as a perfect linear polarizer.

Real polarizers are neither ideal nor perfect; their attenuation of the electric field amplitude is quantified by the attenuation factor  $0 \leq p \leq 1$  and the transmission orientation angle  $\theta$ . The magnitude of attenuation of light intensity affected by such a polarizer is  $0 \leq p^2 \leq 1$  (vs. attenuation of the electric field amplitude,  $p$ ). Although the polarization angle of the intensity is  $2\theta$ , it is most convenient to employ the transmission angle  $\theta$ , which is physically measurable orthogonal to and up from the scattering plane. The Mueller scattering matrix for the generic polarizer [CO, p 72] is

$$\mathbf{A}(\theta) = p^2/2 \begin{vmatrix} 1 & \cos 2\theta & 0 & 0 \\ \cos 2\theta & 1 & 0 & 0 \\ 0 & 0 & \sin 2\theta & 0 \\ 0 & 0 & 0 & \sin 2\theta \end{vmatrix} \quad (\text{E.2A})$$

Whenever  $(\sin 2\theta) = 0$ , the polarizer (or analyzer) is *linear*, since transmitted light is linearly polarized, meaning the third and fourth Stokes parameters are zero, specific.  $\mathbf{I}_{\text{tra}} = [I_{\text{tra}}, Q_{\text{tra}}, 0, 0]$ . In particular, for  $\theta = 0^\circ$  it is a *linear horizontal polarizer*, and for  $\theta = 90^\circ$  it is a *linear vertical polarizer*. For  $0^\circ < \theta < 45^\circ$  and  $45^\circ < \theta < 90^\circ$ , the polarization state of the transmitted light is other than linear. For  $\theta = 45^\circ$ , the polarizer  $\mathbf{A}(45^\circ)$  is a *neutral density filter*, attenuating incident intensity by  $p^2/2$  but unable to change the polarization state of the incident light since the matrix is unit-diagonal and all off-diagonal elements are zero.

A necessary condition for the *perfect* polarizer (indicated by \*), in the notation of Eq (E.2A), is  $p^2 = 1$ . Therefore, the perfect linear horizontal and vertical polarizers are:

$$\mathbf{A}^*(0^\circ) = 1/2 \begin{vmatrix} 1 & 1 & 0 & 0 \\ 1 & 1 & 0 & 0 \\ 0 & 0 & 0 & 0 \\ 0 & 0 & 0 & 0 \end{vmatrix}, \quad \mathbf{A}^*(90^\circ) = 1/2 \begin{vmatrix} 1 & -1 & 0 & 0 \\ -1 & 1 & 0 & 0 \\ 0 & 0 & 0 & 0 \\ 0 & 0 & 0 & 0 \end{vmatrix} \quad (\text{E.2B})$$

Since every scattering event is a polarizing event, aerosols always function as a polarizer (analyzer) to some extent. Specifically, for even the most symmetric and isotropic aerosols Eq (E.1A) is never reduced to a unit diagonal matrix (the neutral density filter).

Therefore, aerosol particles naturally occurring in the atmosphere act like a polarizer (analyzer) insofar as they are able to polarize by scattering incident unpolarized sunlight,  $[1 \ 0 \ 0 \ 0]^T I_o$ . Even so, nearly all environmental-satellite measurements are non-polarimetric and aerosol property retrieval algorithms employ only one non-zero element,  $a_1(\Theta)$ . For any real aerosol population, some off-diagonal element is non-zero. Even with unpolarized incident illumination, at least  $b_1(\Theta)$  affects the polarization state of the scattered light and could be utilized in aerosol property retrieval if the most basic polarimetric measurement (two orthogonal linear analyzers) were made.

For spherical particles acting as an aerosol polarizer (or analyzer), the number of non-zero normalized elements in Eq (E.1A) and even Eq (E.1B) is reduced since: 1) diagonal elements then possess two equalities,  $a_2 = a_1$ ,  $a_4 = a_3$ , and 2) off-diagonals are either symmetric, as are  $b_1$

and  $b_2$  in Eq (E.1B), or are zero. The spherical aerosols Mueller matrix  $\mathbf{F}_{sph}$  has four elements – only three of which are independent since  $a_1^2 = b_1^2 + a_3^2 + b_2^2$  [BH, pp 112, 113]. It is

$$\mathbf{F}_{sph}(\Theta) = \begin{vmatrix} a_1(\Theta) & b_1(\Theta) & 0 & 0 \\ b_1(\Theta) & a_1(\Theta) & 0 & 0 \\ 0 & 0 & a_3(\Theta) & b_2(\Theta) \\ 0 & 0 & -b_2(\Theta) & a_3(\Theta) \end{vmatrix} \quad (\text{E.3A})$$

There is structural similarity of this matrix to Eq (E.2A) at least for conditions of  $b_2 \approx 0$  (spherical particles at forward scattering directions [MLT, Plate 10.6, top right panel], i.e.,

$$\mathbf{A}_{sph}(\Theta) = a_1(\Theta) \begin{vmatrix} 1 & b_1(\Theta)/a_1(\Theta) & 0 & 0 \\ b_1(\Theta)/a_1(\Theta) & 1 & 0 & 0 \\ 0 & 0 & a_3(\Theta)/a_1(\Theta) & 0 \\ 0 & 0 & 0 & a_3(\Theta)/a_1(\Theta) \end{vmatrix} \quad (\text{E.3B})$$

The  $b_2 = 0$  means that the analyzer cannot change the phase angle between components of the incident electric field or light intensity [e.g., BH, 407].

The similarity between Eq (E.3B) and Eq (E.2A) is not straightforward, e.g., the scattering angle  $\Theta$  is not easily related to the transmission angle  $\theta$ . The first matrix element  $a_1(\Theta)$ , which is the aerosol single-scattering angular function (most often called the phase function), is equivalent to a polarizer attenuation magnitude  $p^2/2$ ; but a magnitude that varies with scattering angle  $a_1(\Theta)$ . The off-diagonal ratio  $b_1/a_1$  is called the degree of linear polarization of the aerosol. Insofar as  $b_1/a_1$  varies as  $\cos 2\theta$  the spherical aerosol appears to act like a generic polarizer. The ratio  $a_3/a_1$  has apparently not been named, but insofar as it varies as  $\sin 2\theta$ , again, the spherical aerosol acts like a generic polarizer.

It is the scattering angle variation that is emphasized in Eq (E.1A) and expressed in Eq (E.3A). The scattering angle variation in general is quite complicated and involves scattering code computations (Appendix C). Our attempt here is only to deduce first-order angle dependence of aerosol scattering that resemble characteristics of optical devices.

The simple dipole approximation, the condition of Rayleigh scattering (size parameter  $x = 2\pi r/\lambda \ll 1$ ,  $x \approx 0.002$ ), has well known scattering angle variation. The Rayleigh scattering matrix [e.g., CO, pp 171, 380] is

$$\mathbf{A}_{ray}(\Theta) \sim 1/2 \begin{vmatrix} 1+\cos^2\Theta & -\sin^2\Theta & 0 & 0 \\ -\sin^2\Theta & 1+\cos^2\Theta & 0 & 0 \\ 0 & 0 & 2\cos\Theta & 0 \\ 0 & 0 & 0 & 2\cos\Theta \end{vmatrix} \quad (\text{E.3C})$$

The structure of Eq (E.3C) is evidently that of a generic polarizer; in fact at any position normal to the incident direction, i.e.,  $\Theta = 90^\circ$ , it is a perfect linear vertical polarizer. Directly ahead  $\Theta = 0^\circ$ , it becomes a perfect neutral density filter (unit diagonal matrix) that does not alter the polarization state of incident light. At intermediate scattering angles,  $0^\circ < \Theta < 90^\circ$  and  $90^\circ < \Theta < 180^\circ$ ,  $\mathbf{A}_{ray}(\Theta)$  is a partial vertical polarizer. For  $\Theta = 180^\circ$ , the two lower members of the diagonal are negative, suggesting direction reversal and possible attenuation recovery. Eq (E.3C) applies

to atmospheric molecules – these function like such a polarizer. (It is noted that Eq (E.3C) is normalized to one molecule and does not include the molecular average scattering cross section,  $\sim x^4(m^2-1)/(m^2+2)^2$  [e.g., BH, p 132], which results in familiar Rayleigh relationship  $I_{sea} \sim 1/\lambda^4$ , as long as absorption is not excessive.)

Granted that, for visible radiation, individual diatomic molecules and also populations of such molecules function as vertical polarizers, do aerosols particles act likewise? Even given incident light of  $\lambda \approx 2.0 \mu\text{m}$ , the scattering angle variation specified in Eq (E.3C) would only apply to very small aerosol particles ( $r \leq 0.01\mu\text{m}$ ). For aerosol particle sizes of interest here ( $r \geq 0.2 \mu\text{m}$ ), Rayleigh scattering conditions are met only when long wavelength, esp.  $\lambda \approx 1 \text{ mm}$ , is used as illumination. Of primary interest are the polarimetric properties of larger aerosol particles, specifically, the scattering angle variation for the conditions commonly called Mie scattering (size parameter  $x > 1$ ), i.e., of  $\mathbf{A}_{\text{mie}}(\Theta)$ . Under these conditions the  $\Theta$  dependence is not simply formulated and the relationship with transmission angle  $\theta$  is not clear-cut. Nonetheless, the valid conclusion can be made that very small aerosol particles tend to function like a vertical polarizer; specifically, near  $\Theta = 90^\circ$  the polarization of scattered radiation is perpendicular to the scattering plane and  $b_2$  is small.

It is well known that the phase function depends strongly on the size parameter ( $2\pi r/\lambda$ ) of the scattering situation [e.g., MTL, figs 10.8–10.11]. Given illumination wavelength,  $a_1$  therefore varies with particle size. Also, for particles that are not spheres the  $a_2$  element no longer equals  $a_1$ , implying that the  $a_2$  element can be associated with particle shape. Comparing Eqs (E.1B) and (E.2A), it is concluded that *the scattering aerosol in so far as it acts like a polarizer is specified by the elements in Block (A)*.

## 2) Wave Plate –

The *wave plate*, generic term for phase-shifter, retarder, or compensator; [CO, p 74] shifts the phase (the temporal phase of the electric field amplitude) of one component of the incident light vector relative to the other. The retardation can be considered as occurring along an orthogonal set of axes, between which the phase shifting is maximum; these are called the ‘fast’ axis and the ‘slow’ axis, [e.g., CO, p 74]. The angle between this set and the scattering plane is the wave-plate orientation angle  $\psi$  [BH, p 55]—distinct from the wave-plate retardation angle, introduced presently. Unlike the polarizer, the wave plate has no inherent intensity loss [CO, p 75].

The scattering matrix for the wave plate is [ON, p 143, eq (9-28),  $2\delta$  is here  $\delta$ ; CO, p 75, eq 27]

$$\mathbf{W}_{\delta/2\pi}(\psi) = \begin{vmatrix} 1 & 0 & 0 & 0 \\ 0 & 1 & 0 & 0 \\ 0 & 0 & \cos \delta & -\sin \delta \\ 0 & 0 & \sin \delta & \cos \delta \end{vmatrix} \quad (\text{E.4A})$$

where  $\delta$  is the retardation angle, also called the *retardance* [BH, p 55]. For  $\delta = 90^\circ$  the optical device is called a *quarter-wave plate*; for  $\delta = 180^\circ$  it is a *half-wave plate*.

The retardance  $\delta$  is a function of the integrated influence of the particle medium on the incident radiation – the opacity of the medium. Since only single scattering is considered here,  $\delta \sim 2r$ , the linear extent (diameter) of the scattering particle. More specifically,  $\delta$  varies with the representative particle size  $r_{\text{eff}}$  in relation to the wavelength of the incident radiation—with the

effective size parameter,  $\delta \sim 4\pi r_{\text{eff}}/\lambda$  [e.g., BH, p 418]. But, it is the index of refraction  $m = m_{\text{real}} - i m_{\text{imag}}$ , relative to that of the propagation medium ( $\cong 1$ ) that effects the phase change; specific the factor  $(m - 1) = [(m_{\text{real}}^2 + m_{\text{imag}}^2)^{1/2} - 1]$ . Only rays that have traversed the aerosol particle can experience phase shifting. These are refracted or internally refracted/reflected rays. So, a reasonable expression is  $\delta \sim (j + 1)(m - 1)\pi r_{\text{eff}}/\lambda$ ,  $j$  being the number of internal reflections. Modulation in time, e.g.,  $\sin \omega t$ , is essential for retardation to occur so that  $\delta = (j + 1)(m - 1)(\pi r_{\text{eff}}/\lambda) \sin \omega t$  is a realistic model, from which  $\sin \delta$  and  $\cos \delta$  are generated via Bessel functions [BH, p 418].

By similarity to Eq (E.4A), the aerosol whose general form of scattering matrix is Eq (E.1A), functions as a wave plate if it has  $a_4 = a_3$ , a spherical particle condition. The resulting aerosol wave-plate Mueller matrix is

$$\mathbf{W} = \begin{vmatrix} 1 & 0 & 0 & 0 \\ 0 & 1 & 0 & 0 \\ 0 & 0 & a_3 & b_2 \\ 0 & 0 & -b_2 & a_3 \end{vmatrix} \quad (\text{E.4B})$$

For such a wave plate,  $a_3 \sim \cos \delta$ , and  $b_2 \sim -\sin \delta$ . Only for the null conditions of either very small size parameter,  $r/\lambda \cong 0$ , or no refractive index difference  $(m - 1) \cong 0$ , does  $\delta \cong 0^\circ$ ; this is the condition for  $\mathbf{W}$  to degenerate into perfect neutral density filter. Regarding scattering angle variation in the Eq (E.4B) Block (D) elements only refracted and internally reflected photons can be phase shifted – not diffracted and surface reflected rays. Since the latter two ray types are preferentially directed near  $\Theta \cong 0^\circ$  and  $\Theta \cong 180^\circ$ , the scattering angle modulation that suggests itself for the Block (D) elements is  $\sim \sin \Theta$ . Since the off-diagonal elements are odd functions of the scattering angle it is anticipated that  $b_2 \sim \sin \Theta$ , in addition to  $\sim -\sin \delta$ .

Aerosols, it appears, always have some wave-plate influence on incident light. The essential feature of the aerosol acting like a wave plate is that  $b_2 \neq 0$ . For non-spherical particles, i.e., for  $a_4 \neq a_3$ , the aerosol does not act precisely like the conventional wave plate specified by Eq (E.4B) but does act somewhat like it. Even if acting as both wave plate (Eq (E.4B)) and polarizer (Eq (E.2A in general, Eq (E.3B) for spheres), this analog scattering aerosol does not allow for  $a_4 \neq a_3$ .

In any event, it is concluded that *the scattering aerosol in so far as it acts like a wave plate is specified by the elements in Block (D)*.

### 3) Rotator –

A *rotator* is a physically rotated optical device (analyzer, wave plate, or combination thereof). The physical rotation brings about reorientation of the transmission angle of elliptically polarized incident light (relative amplitude change) by the angle  $\theta$ . Mathematically, the rotator is the Mueller matrix [CO, p 78; ON, p 146],

$$\mathbf{R}(2\theta) = \begin{vmatrix} 1 & 0 & 0 & 0 \\ 0 & \cos 2\theta & \sin 2\theta & 0 \\ 0 & -\sin 2\theta & \cos 2\theta & 0 \\ 0 & 0 & 0 & 1 \end{vmatrix} \quad (\text{E.5A})$$

The rotation per se does not impose intensity loss. The rotator function is to change the plane of polarization by  $\theta$  (by  $2\theta$  in any coordinate system mapping orthogonal change into  $\pi$  radians, such as the Poincare' sphere) [ON, p 146]. Intrinsically, rotators incorporate other optical devices; they are in fact rotated linear polarizers or rotated wave plates. The concept of rotator is that of a mathematical expedient for quantifying rotated optical devices. (The expedient is especially useful when devices are continuously rotated about an optical axis; see Section E.2.)

In particular, the *rotated linear polarizer*  $\mathbf{A}(\theta)$  changes the transmission angle of linearly polarized light by  $+\theta$  (counterclockwise viewed along direction of propagation). For the horizontal linear polarizer ( $\theta_0 = 0^\circ$ ), the rotation to  $+\theta$  is formulated as the triple matrix product, specifically,  $\mathbf{A}(\theta) = \mathbf{R}(-2\theta) \mathbf{A}(\theta_0 = 0^\circ) \mathbf{R}(2\theta)$  [e.g., WA, eq 31; BH, eq 2.87; or CO, pp 80,81]. The  $\mathbf{R}(-2\theta)$  rotation is needed to retain reference to the original (horizontal,  $\theta_0 = 0^\circ$ ) coordinate. Resulting is the Mueller matrix for the rotated linear polarizer,

$$\mathbf{A}(\theta) = p^2/2 \begin{vmatrix} 1 & \cos 2\theta & \sin 2\theta & 0 \\ \cos 2\theta & \cos^2 2\theta & \cos 2\theta \sin 2\theta & 0 \\ \sin 2\theta & \sin 2\theta \cos 2\theta & \sin^2 2\theta & 0 \\ 0 & 0 & 0 & 0 \end{vmatrix} \quad (\text{E.2C})$$

Two rotated linear polarizers have already been considered, viz. Eq (E.2B), the perfect horizontal and vertical polarizers:  $\mathbf{A}^*(0^\circ) = \mathbf{R}(-0^\circ) \mathbf{A}^*(0^\circ) \mathbf{R}(0^\circ)$  and  $\mathbf{A}^*(90^\circ) = \mathbf{R}(-180^\circ) \mathbf{A}^*(0^\circ) \mathbf{R}(180^\circ)$ . Physically placing such linear polarizers in series together, perfect or not, totally attenuates the incident light,  $\mathbf{A}^*(0^\circ) \mathbf{A}^*(90^\circ) = \mathbf{A}(0^\circ) \mathbf{A}(90^\circ) \equiv 0$ .

Also of interest is the perfect  $45^\circ$  linear polarizer  $\mathbf{A}^*(45^\circ) = \mathbf{R}(-90^\circ) \mathbf{A}^*(0^\circ) \mathbf{R}(90^\circ)$  that is physically rotated  $+45^\circ$  (clockwise looking back onto the source) relative to the originally horizontal  $\theta_0 = 0^\circ$  direction.

$$\mathbf{A}^*(45^\circ) = 1/2 \begin{vmatrix} 1 & 0 & 1 & 0 \\ 0 & 0 & 0 & 0 \\ 1 & 0 & 1 & 0 \\ 0 & 0 & 0 & 0 \end{vmatrix}$$

Surprisingly, the  $\mathbf{A}^*(45^\circ)$  inserted between a completely attenuating pair of two orthogonal perfect linear polarizers recovers 1/8th of originally unpolarized intensity, specifically,

$$\mathbf{A}^*(0^\circ) \mathbf{A}^*(45^\circ) \mathbf{A}^*(90^\circ) = 1/8 \begin{vmatrix} 1 & -1 & 0 & 0 \\ 1 & -1 & 0 & 0 \\ 0 & 0 & 0 & 0 \\ 0 & 0 & 0 & 0 \end{vmatrix} = \mathbf{A}^*(90^\circ) \mathbf{A}^*(45^\circ) \mathbf{A}^*(0^\circ)$$

This is quite remarkable since any other (of six in total) possible arrangements of the same three linear polarizers attenuates totally, e.g.,  $\mathbf{A}^*(0^\circ) \mathbf{A}^*(90^\circ) \mathbf{A}^*(45^\circ) = \mathbf{A}^*(45^\circ) \mathbf{A}^*(90^\circ) \mathbf{A}^*(0^\circ) \equiv 0$ .

As with the polarizer in Eq (E.2C), the wave plate can also be combined with rotations. In particular for the quarter-wave plate ( $\delta = 90^\circ$ ) the triple product  $\mathbf{R}(-2\theta) \mathbf{W}_{1/4}(\psi = 0^\circ) \mathbf{R}(2\theta)$  is the *rotated quarter-wave plate* [BB, p 470; BH, p 55].

$$\mathbf{W}_{1/4}(\theta) = \begin{vmatrix} 1 & 0 & 0 & 0 \\ 0 & \cos^2 2\theta & \cos 2\theta \sin 2\theta & -\sin 2\theta \\ 0 & \sin 2\theta \cos 2\theta & \sin^2 2\theta & \cos 2\theta \\ 0 & \sin 2\theta & -\cos 2\theta & 0 \end{vmatrix} \quad (\text{E.4C})$$

In association with a linear polarizer the diagonally rotated quarter-wave plate  $\mathbf{W}_{1/4}(\pm 45^\circ)$  is used to produce or to detect circular polarization [e.g., BB, Fig 2]. For such rotation all cosine-containing elements in Eq (E.4C) are zero and the signs of remaining off-diagonal ( $\sin 2\theta$ )-elements reverse for  $\theta = -45^\circ$

From Eq (E.5A), the form of the equivalent three-element aerosol rotator Mueller matrix is

$$\mathbf{R} = \begin{vmatrix} 1 & 0 & 0 & 0 \\ 0 & a_2 & b_4 & 0 \\ 0 & -b_4 & a_2 & 0 \\ 0 & 0 & 0 & 1 \end{vmatrix} \quad (\text{E.5B})$$

where  $a_2 \sim \cos 2\theta$ , and  $b_4 \sim \sin 2\theta$ , which does conform to the off-diagonal symmetries in Eq (E.1A). Since all off-diagonals must go to zero at  $\Theta = 0^\circ$  and  $\Theta = 180^\circ$ , the implication is that, like  $b_2$  earlier,  $b_4 \sim \sin \Theta$ . Aerosols acting like a rotator implies that  $|\sin 2\theta| > 0$ .

The distinguishing characteristic of the rotator matrix is the off-diagonal elements in Blocks (B) and (C). If  $b_4 = 0$ , the remaining non-zero elements are indistinguishable from polarizer and/or wave-plate functions. Therefore, it is deduced that *the scattering aerosol in so far as it acts like a rotator is specified by the corner elements, those in Blocks (B) and (C)*.

Summarizing the similarities between scattering particles acting as optical devices and the elements of the scattering matrix, the block vs. device associations are

$$\begin{vmatrix} (\text{A}) \text{ polarizer} & (\text{B}) \text{ rotator} \\ (\text{C}) \text{ rotator} & (\text{D}) \text{ wave plate} \end{vmatrix}$$

Comparison of the general form of the (normalized) scattering matrix Eq (E.1A) with the optical device matrices – in so far as aerosols might be interpreted as acting like such devices – i.e., as polarizer Eq (E.3B), as wave plate Eq (E.4B), or as rotator Eq (E.5B), provides some interpretation of certain off-diagonal elements. It is first noted that the matrix elements  $b_3$ ,  $b_5$ , and  $b_6$  in Eq (E.1A) are zero for all three devices. Also, only the aerosol polarizer contributes to non-zero value of  $b_1$ , only the aerosol wave plate to non-zero  $b_2$ , and only the aerosol rotator to non-zero  $b_4$ . Further, the equal magnitude and sign conventions for these off-diagonal  $b$ 's in Eq (E.1A) are the same as in the basic optical device matrices Eqs (E.2A), (E.4A), and (E.5A). The optical device, the non-zero off-diagonal element, and the associated polarimetric effect that is expected in the scattered light vector relative to the incident vector are, then:

- Polarizer:  $b_1$  – extent of linear polarization
- Wave plate:  $b_2$  – circular polarization component
- Rotator:  $b_4$  – reorientation of polarization angle

Combinations of device matrices, e.g., the matrix multiplication  $\mathbf{WA}$  (or  $\mathbf{AW}$ ), or  $\mathbf{RA}$ , etc. might better correspond to actual aerosols but here such arrangements are not considered further.

#### 4) Absorber –

The *absorber* is an optical device that only indirectly influences scattering light measurements – obviously; radiation absorbed cannot be remotely sensed. Nonetheless, for completeness the Mueller matrix for the absorber is included here [see esp. ON, Table 9-2].

$$\mathbf{M}_\beta = \begin{vmatrix} \exp(-2\beta^+) \cosh 2\beta^- & -\exp(-2\beta^+) \sinh 2\beta^- & 0 & 0 \\ -\exp(-2\beta^+) \sinh 2\beta^- & \exp(-2\beta^+) \cosh 2\beta^- & 0 & 0 \\ 0 & 0 & \exp(-2\beta^+) & 0 \\ 0 & 0 & 0 & \exp(-2\beta^+) \end{vmatrix} \quad (\text{E.6})$$

where the subscript is the volume absorption coefficient  $\beta \equiv \beta_{\text{abs}} = (1/4\pi)N\langle C_{\text{abs}} \rangle$ ,  $\langle C_{\text{abs}} \rangle = \sqrt{[\langle C_{\text{abs}} \rangle_{\parallel}^2 + \langle C_{\text{abs}} \rangle_{\perp}^2]} \sim 4\pi m_{\text{imag}}/\lambda$ , where different ensemble-average absorption cross sections are allowed for polarization parallel  $\parallel$  or perpendicular  $\perp$  to the scattering plane. Furthermore,  $\beta^+ = \frac{1}{2}(\beta_{\parallel} + \beta_{\perp})$ , and  $\beta^- = \frac{1}{2}(\beta_{\parallel} - \beta_{\perp})$ ,  $\beta_{\parallel} = \beta_{\text{abs}}(\theta = 0^\circ)$ ,  $\beta_{\perp} = \beta_{\text{abs}}(\theta = 90^\circ)$ .

## E.2 ELEMENT DETERMINATION

Determination of the four Stokes parameters of the scattered light requires a versatile receiver generally referred to as a *polarimeter*. Figure E.1 is an idealized component diagram of such a receiver that could use a single time-shared detector preceded in each optical path, in turn, by one linear analyzer (polarizer) and two flat diagonal mirrors. Post-detector summing or differencing of the measurements from two orthogonal analyzers determines the first three Stokes parameters separately. The fourth requires the addition of a quarter-wave plate between the two flat mirrors. More sophisticated polarimeters employing continuously rotating optical devices and/or multiple detectors are available.

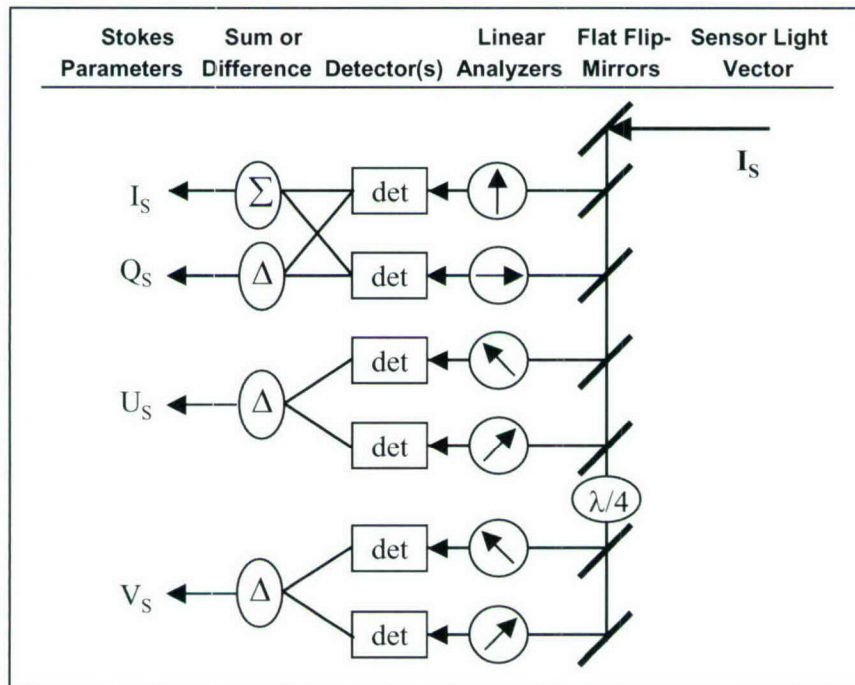


Figure E.1. Stokes Parameter Receiver (Polarimeter) – Conceptual Design. Signal light vector  $\mathbf{I}_S = [I_S, Q_S, U_S, V_S]$ , detector ‘d’, summation  $\Sigma$ , and difference  $\Delta$

Determination of individual elements (or of certain two-element combinations) in the scattering matrix is usually the objective of polarimetric measurements. In any measurement the incident light has a known polarization state and the scattered light is investigated using various optical devices. In Figure E.2 is shown a polarimetric measurement design that provides for an extensive selection of incident polarization states and four analysis polarization states. (The equivalence of more extensive analyzers – a full Stokes-parameter polarimeter – with more limited incident polarization options is easily demonstrated.)

Employment of specific polarizer-analyzer combinations permits determining individual elements of the scattering matrix with minimum attenuation of incident light intensity. Of the scattered light vector  $\mathbf{I}_{\text{sca}}$ , only the 1<sup>st</sup> Stokes parameter of the light vector reaching the sensor,  $\mathbf{I}_S$  in Figure E.2, is measurable. Therefore, the scattering-matrix element to be determined must appear within the first Stokes parameter of  $\mathbf{I}_S$ , the  $I_S$  measurement in Figure E.1.

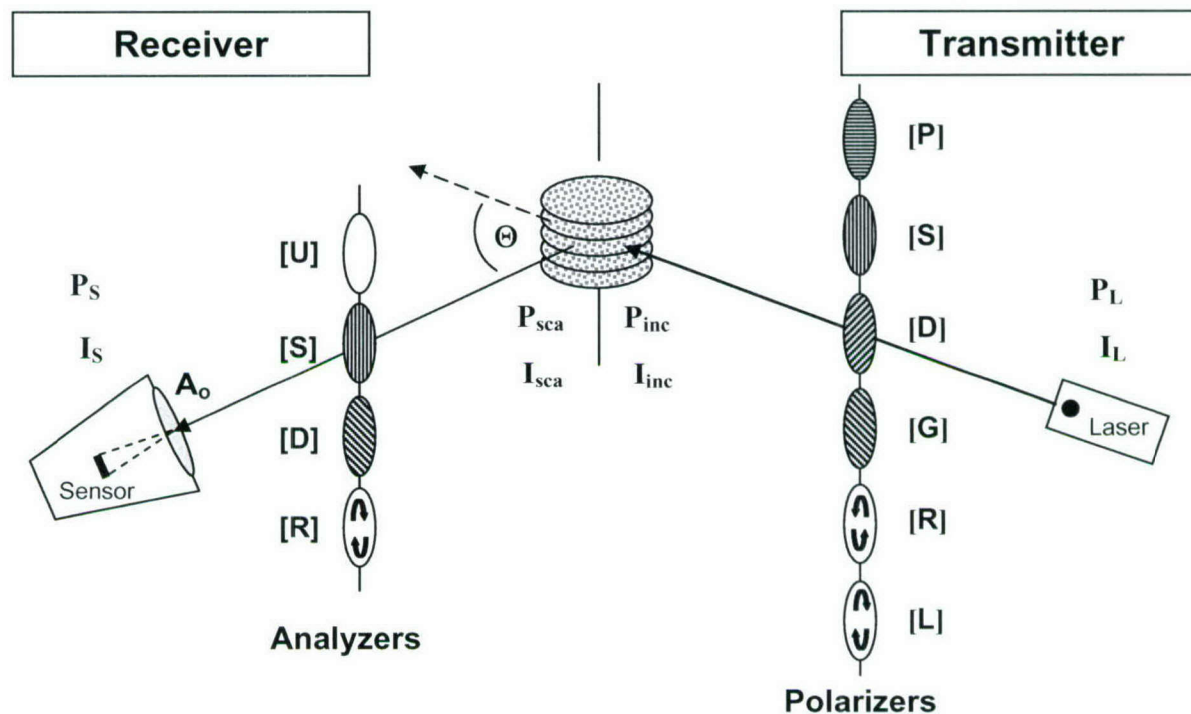


Figure E.2. Polarimetric Measurement Employing Variable Incident Polarization States. Irradiances ( $\text{W m}^{-2}$ ) or powers (W): laser-output  $I_L$  or  $P_L$ , incident on scattering volume  $I_{\text{inc}}$  or  $P_{\text{inc}}$ , leaving sample volume  $I_{\text{sca}}$  or  $P_{\text{sca}}$ , and reaching sensor  $I_S$  or  $P_S$ . Polarizers or analyzers: parallel [P], perpendicular [S], plus 45° [D], minus 45° [G] to scattering plane, right-hand circular [R] or left-hand circular [L], and unpolarized (depolarized) [U]. Scattering angle  $\Theta$ , receiver aperture  $A_o$ .

As originally detailed by Bickel and Bailey (1985) [BB, Fig 5] and as recently (2003) summarized in matrix form by Kokhanovsky [KO, eq (3.14)], the optical devices associated with the incident light (left letter) and scattered light (right letter) that are needed to insure that each individual element of the scattering matrix is present in the measured intensity, the  $I_S$  Stokes parameter, are:

$$\begin{vmatrix} U:U & P:U & D:U & R:U \\ U:P & P:S & D:P & R:P \\ U:D & P:D & D:D & R:D \\ U:R & P:R & D:R & R:L \end{vmatrix} \quad (E.7A)$$

The letter-pairs (incident illumination : sensed scattered light) indicate the following optical devices: U – un-polarizer (commonly called depolarizer), P – parallel linear polarizer (parallel,  $0^\circ$  to scattering plane), S – perpendicular (senkrecht; German) linear polarizer (orthogonal  $90^\circ$  to scattering plane), D – diagonal linear polarizer at  $+45^\circ$  to scattering plane, R – right-hand circular polarizer (clockwise rotation looking into source-beam), L – left-hand circular polarizer (clockwise rotation looking in direction of propagation). Unpolarized (U) for the source is like sunlight; depolarizer (U) for the receiver is an open hole, no analyzer at all. The various two-polarizer sets in Eq (E.7A) place specific scattering matrix elements in the 1<sup>st</sup> Stokes parameter position – the intensity position – of the sensed light  $I_S$ . These 1<sup>st</sup>-position elements, using the Perrin-normalized-element notation of Eq (E.1A), are displayed in Eq (E.7B) as a 4x4 matrix corresponding to Eq (E.7A).

$$\frac{1}{4} \begin{vmatrix} 4a_1 & 2(a_1+b_1) & 2(a_1+b_3) & 2(a_1+b_5) \\ 2(a_1+b_1) & (a_1-a_2) & (a_1+b_1+b_3+b_4) & (a_1+b_1+b_5+b_6) \\ 2(a_1-b_3) & (a_1+b_1-b_3-b_4) & (a_1+a_3) & (a_1+b_2-b_3+b_5) \\ 2(a_1+b_5) & (a_1+b_1+b_5+b_6) & (a_1-b_2+b_3+b_5) & (a_1-a_4) \end{vmatrix} \quad (E.7B)$$

(A comparable array expressed in terms of general scattering matrix elements can be extracted from [BB, Fig 5] by adhering to the polarization states indicated in Eq (E.7A).) Only the phase function  $a_1$ , obtained with unpolarized illumination and depolarized detected beam, appears alone and unattenuated. All other elements of the first row, the first column, and the diagonal need to be compensated for the presence of the phase function as part of the measurement, i.e., two measurements are needed. The remaining off-diagonal elements require at least three elements other than themselves be separately known, meaning four measurements.

Clearly, to isolate individual elements other than  $a_1$ , more than a single measurement is needed. Although the combinations in Eq (E.7A) are not the only ones usable to determine individual elements, single measurements indicated there provide the Eq (E.7B) diagonal elements. These are, for the two upper left diagonal members, the phase function and the non-sphericity. When normalized by the phase function  $a_1$ , the third diagonal is an indicator of the real refractive index at backscatter angles [MT7, Plate 4; KO, Figure 3.22(d)], and the fourth diagonal is an indicator of the optical activity.

### E.3 ELEMENT ASSOCIATIONS

Rough associations between each normalized scattering matrix element and individual or *population* scattering-particle properties are the following:

size <sup>F&amp;B</sup>	size <sup>B</sup> /shape <sup>F</sup>	<b><i>oriented</i></b>	shape <sup>B</sup> / <b><i>width<sup>B</sup></i></b>		(E.8)
size <sup>B</sup> /shape <sup>F</sup>	shape <sup>B</sup>	asymmetry	<b><i>oriented</i></b>		
<b><i>oriented</i></b>	asymmetry	index <sup>2B</sup>	<b><i>median<sup>F</sup></i></b> /index <sup>B</sup>		
shape <sup>B</sup> / <b><i>width<sup>B</sup></i></b>	<b><i>oriented</i></b>	<b><i>median<sup>F</sup></i></b> /index <sup>B</sup>	index <sup>2B</sup>		

Upright print – individual particle physical property

***Bold italics*** – particle-population characteristic

Superscript – <sup>F</sup> forward, <sup>B</sup> backward, <sup>2</sup> multiple

Consolidating information from numerous technical references results in the various associations presented in Eq (E.8). Of these, the following references are especially informative: [PHH, pp 2706-2708], [MTL, p 272, plates 9.4-6, 10.1-4, figs 10.29-33], [QHH, p 529], and [VH, pp 46-55]. Some Eq (E.8) associations need modification if birefringence (optical activity) is present [VJL].

## GLOSSARY OF SYMBOLS [Units]

$a_k$	normalized scattering matrix diagonal element k, [-]
$A$	particle size-distribution coefficient, [ $\text{cm}^{-3} \mu\text{m}^{-(\alpha+1)}$ ]
$A_o$	aperture area of receiver, [ $\text{cm}^2$ ]
$A_s$	cross-sectional area of sample volume, [ $\text{m}^2$ ]
$A_t$	cross-sectional area of transmitted beam, [ $\text{m}^2$ ]
$A_p$	particle area-concentration, [ $\text{cm}^{-1}$ ]
APD	avalanche photodiode detector
$\alpha$	particle size-distribution exponent, [-]
$b_k$	normalized scattering matrix off-diagonal element k, [-]
$b$	bandwidth, [Hz]
B	particle size-distribution coefficient, [ $\mu\text{m}^{-\gamma}$ ]
BS	symbol for Bacillus subtilis bio-aerosol simulant
<b>B</b>	volume scattering coefficient matrix, [ $\text{cm}^{-1}$ ]
$\beta_{abs}$	bulk absorption coefficient, [ $\text{cm}^{-1}$ ]
$\beta_{ij}$	volume scattering coefficient ij, [ $\text{cm}^{-1}$ ]
$c$	speed of light, $2.998 \times 10^8$ , [ $\text{m s}^{-1}$ ]
$\langle C_{abs} \rangle$	ensemble-average absorption cross section, [ $\text{cm}^2$ ]
$C_{sca}$	scattering cross section, [ $\text{cm}^2$ ]
$\langle C_{sca} \rangle$	ensemble-average scattering cross section, [ $\text{cm}^2$ ]
dB	decibel, [-]
D	symbol for desert background aerosol
D	receiver-detector location
$\delta$	optical dimension, [-]
$e$	electron charge, $1.602 \times 10^{-19}$ , [C]
$\varepsilon$	spheroid particle axis ratio, equatorial radius/polar radius, [-]
$E_L$	laser output energy per pulse [J]
$E_S$	signal energy per pulse, [J]
$\eta$	detector quantum efficiency, [-]
f	receiver parameter, [cm]
<b>F</b>	volume scattering matrix, [ $\text{cm}^{-2}$ ]
$F_{ij}$	volume scattering matrix element ij, [ $\text{cm}^{-2}$ ]
$\langle F \rangle$	ensemble-average scattering matrix, [ $\text{cm}^{-2}$ ]
$\langle F_{ij} \rangle$	ensemble-average scattering matrix element ij, [ $\text{cm}^{-2}$ ]
<b>F</b>	normalized scattering matrix, [-]
$F_{ij}$	normalized scattering matrix element ij, [-]
$\Gamma$	gamma function, [-]
$\gamma$	particle size-distribution exponent, [-]
$h$	Planck constant, $6.626 \times 10^{-34}$ , [J s]
$I_{inc}$	incident light (irradiance) vector, [ $\text{W m}^{-2}$ ]
$I_{sca}$	scattered light (irradiance) vector, [ $\text{W m}^{-2}$ ]
$I_L$	laser-leaving pulse irradiance, [ $\text{W m}^{-2}$ ]
$I_S$	signal irradiance per pulse, [ $\text{W m}^{-2}$ ]
$I_o$	magnitude of incident light, [ $\text{W m}^{-2}$ ]
$I_{inc}$	1 <sup>st</sup> Stokes parameter of incident light vector – intensity, [ $\text{W m}^{-2}$ ]

$I_{\text{sca}}$	1 <sup>st</sup> Stokes parameter of scattered light vector – intensity, [W m <sup>-2</sup> ]
$J_{\text{sca}}$	scattered irradiance per unit of range, [W m <sup>-3</sup> ]
$k$	Boltzmann constant, $1.381 \times 10^{-23}$ , [J K <sup>-1</sup> ]
$K$	number of laser pulses, [-]
$\kappa$	atmospheric path extinction coefficient, [m <sup>-1</sup> ]
$L$	symbol for continental background aerosol
$L$	transmitter to receiver distance, [m]
$L_L$	laser pulse spatial length, [m]
$\lambda$	wavelength of light, [ $\mu\text{m}$ ]
$m$	complex index of refraction, $m = m_{\text{real}} - i m_{\text{imag}}$ , [-]
$m_{\text{imag}}$	imaginary part of refractive index, [-]
$m_{\text{real}}$	real part of refractive index, [-]
$M$	symbol for maritime background aerosol
$\mu$	modified-gamma distribution combined parameter, $(\alpha+1)/\gamma$ , [-]
$n(r)$	unit particle size-distribution function, [cm <sup>-3</sup> $\mu\text{m}^{-1}$ ]
$n_p$	number of photons in a polarization state, [-]
$n_N(r)$	general particle size-distribution function, [cm <sup>-3</sup> $\mu\text{m}^{-1}$ ]
$N$	number-concentration of all aerosol particles, [cm <sup>-3</sup> ]
$N_a$	number-concentration of ambient background particles, [cm <sup>-3</sup> ]
$N_b$	number-concentration of bio-aerosol particles, [cm <sup>-3</sup> ]
$D$	number of particles in sample volume, [-]
NIR	near infrared wavelength, approx. 0.8 to 1.4 [ $\mu\text{m}$ ]
$\nu_{\text{eff}}$	effective variance, [-]
$\nu$	laser (optical) frequency, [Hz]
pdf	probability density function, [-]
$p(\chi)$	probability density function of quantity $\chi$ , [-]
$P_I$	intensity polarimetric quantity or property, [-]
$P_L$	linearity polarimetric quantity or property, [-]
$P_N$	non-sphericity polarimetric quantity or property, [-]
$P_R$	retardation polarimetric quantity or property, [-]
$P_L$	laser peak power, [W]
$P_S$	signal power at detector, [W]
PD	probability of detection, [%]
PFD	probability of false detection, [%]
PRF	pulse repetition frequency, [Hz]
$\phi$	general orientation angle, [-]
$q$	polarizer or analyzer efficiency factor, [-]
$Q$	sample volume location
$Q_{\text{inc}}$	2 <sup>nd</sup> Stokes parameter of incident light vector – linearity, [W m <sup>-2</sup> ]
$Q_{\text{sca}}$	2 <sup>nd</sup> Stokes parameter of scattered light vector – linearity, [W m <sup>-2</sup> ]
$r$	particle radius, [ $\mu\text{m}$ ]
$r$	radius of constant- $\Theta$ circle, [m]
$r_{mr}$	reflectance of mirror component, [-]
$r_o$	aperture radius, [cm]
$r_A$	area-equivalent sphere radius, [ $\mu\text{m}$ ]
$r_{\text{eff}}$	effective radius of particles, [ $\mu\text{m}$ ]

$r_{\max}$	maximum particle radius, [ $\mu\text{m}$ ]
$r_{\min}$	minimum particle radius, [ $\mu\text{m}$ ]
$r_{\text{mo}}$	mode radius of particles, [ $\mu\text{m}$ ]
$r_V$	volume-equivalent sphere radius, [ $\mu\text{m}$ ]
$R$	range from sample volume to detector, [m]
$R$	electrical resistance, [ $\Omega$ ]
$R_T$	range from transmitter to scattering volume, [m]
$R_N$	number-concentration mixing ratio, $N_b/N_a$ , [-]
$s_L$	laser binary Stokes vector, [-]
$S_{\text{jm}}$	sum over angles of polarimetric property, [ $\text{W m}^{-2}$ ]
$\text{SNR}$	signal-to-noise ratio, [-]
$\text{SWIR}$	short-wave infrared wavelength, approx. 1.4 to 3.0 [ $\mu\text{m}$ ]
$\sigma$	standard deviation, [ $\mu\text{m}$ ]
$t$	atmospheric transmittance, [-]
$t$	time, [s]
$t_{xy}$	transmittance of receiver component xy, [-]
$T$	receiver transmission loss parameter, [-]
$T$	laser-transmitter location
$T$	temperature, [K]
$\tau_D$	detector integration time, [ns]
$\tau_L$	laser pulse duration, [ns]
$\theta_S$	receiver plane field-of-view angle, [deg]
$\theta_T$	transmitter plane divergence angle, [deg]
$\Theta$	scattering angle measured in scattering plane, [-]
$U_{\text{inc}}$	3 <sup>rd</sup> Stokes parameter of incident light vector – ellipticity, [ $\text{W m}^{-2}$ ]
$U_{\text{sca}}$	3 <sup>rd</sup> Stokes parameter of scattered light vector – ellipticity, [ $\text{W m}^{-2}$ ]
$V$	sample volume, [ $\text{cm}^3$ ]
$V_P$	particle volume-concentration, [ $\text{cm}^3 \text{ cm}^{-3}$ ]
$V_T$	scattering volume, [ $\text{cm}^3$ ]
$V_{\text{inc}}$	4 <sup>th</sup> Stokes parameter of incident light vector – circularity, [ $\text{W m}^{-2}$ ]
$V_{\text{sca}}$	4 <sup>th</sup> Stokes parameter of scattered light vector – circularity, [ $\text{W m}^{-2}$ ]
$x$	size parameter, $2\pi r/\lambda$ , [-]
$x$	horizontal grid coordinate, [m]
$x_c$	combined aerosol size parameter, [-]
$x_{\text{eff}}$	effective size parameter, $2\pi r_{\text{eff}}/\lambda$ , [-]
$x_{\text{imag}}$	half of absorption size parameter, $4\pi m_{\text{imag}}r/\lambda$ , [-]
$x_{\text{sca}}$	scattering size parameter, $2\pi m_{\text{real}}r/\lambda$ , [-]
$y$	horizontal grid coordinate, [m]
$Y$	distance from transmitter-receiver axis, [m]
$\xi$	lidar overlap factor, [-]
$Z_{\text{jk}}_m$	polarimetric information matrix element, [ $\text{W m}^{-2}$ ]
$\psi$	wave-plate orientation angle, [-]
$\Omega_o$	aperture-from-source solid angle, [ $\text{m}^2/\text{m}^2$ ]
$\Omega_S$	receiver field-of-view solid angle, [ $\text{m}^2/\text{m}^2$ ]
$\Omega_T$	laser divergence solid angle, [ $\text{m}^2/\text{m}^2$ ]

## Subscripts

a	ambient background aerosol
A	area-equivalent or aperture
b	bio-aerosol
bs	beam-splitter
c	combined ambient and bio-aerosols
e	electron
eff	effective value of a distributed variable
fl	filter
i	row designator
I	intensity
imag	imaginary part
inc	incident
j	column designator
k	single-subscript normalized matrix element designator
L	laser or linearity
m	type of polarimetric information designator
mie	Mie-like
mr	mirror
nse	noise
N	noise or non-sphericity
$\mu$	category of particles
mo	mode value of distributed variable
o	normalization designator
ob	oblate
p	photon
pn	preamplifier-noise limited
pr	prolate
P	particle
q	detected photon
R	retardation
ray	Rayleigh-like
real	real part
S	signal, receiver, or sample volume
sn	shot-noise limited
sca	scattered
sig	signal
sph	sphere, spherical
t	time
T	transmitter
tn	thermal-noise limited
tra	transmitted
V	volume-equivalent
x	horizontal plane, scattering plane
y	vertical plane, normal plane

## **Superscripts**

B	backward scattering, $90^\circ < \Theta \leq 180^\circ$
D	diagonal + $45^\circ$ linear polarization
F	forward scattering, $0^\circ \leq \Theta \leq 90^\circ$
G	diagonal - $45^\circ$ linear polarization
h	horizontal linear polarization
l	left-hand circular polarization
L	left-hand circular polarization
P	parallel ( $0^\circ$ ) linear polarization
r	right-hand circular polarization
R	right-hand circular polarization
S	perpendicular ( $90^\circ$ ) linear polarization
T	transpose row into column
u	unpolarized, also called depolarized
U	unpolarized, also called depolarized
v	vertical linear polarization
z	generic polarization
+	diagonal + $45^\circ$ linear polarization
-	diagonal - $45^\circ$ linear polarization
,	instantaneous quantity

## REFERENCES

- [AW] Andresen, B.F., and W.L. Wolfe, 2003: *Infrared Sensors*. Chapter 28 in: Optical Engineer's Desk Reference, W.L. Wolfe, Editor. SPIE Optical Society of America, Bellingham, WA, 738 pp.
- [BAK] Babenko, V.A., L.G. Astafyeva, and V.N. Kuzmin, 2003: Electromagnetic Scattering in Disperse Media. Springer-Verlag, Berlin, 434 pp.
- [BB] Bickel W.S., and W.M. Bailey, 1985: *Stokes Vectors, Mueller Matrices, and Polarized Scattered Light*. Am. J. Phys., 53, 468-478.
- [BH] Bohren, C.F., and D.R. Huffman, 1983: Absorption and Scattering of Light by Small Particles. John Wiley & Sons, Inc., New York, NY, 530 pp.
- [BDS] Borghese, F., P. Denti, and R. Saija, 2003: Scattering from Model Nonspherical Particles. Springer-Verlag, Berlin, 253 pp.
- [BDV] Bronk, P.V., S.D. Druger, J. Czege, and W.P. Van De Merwe, 1995: *Measuring Diameters of Rod-Shaped Bacteria in Vivo with Polarized Light Scattering*. Biophys. J., 69, 1170-77.
- [BW] Bowers, J.E., and Y.G. Wey, 1995: *High-Speed Photodetectors*. Chapter 17 (Vol.I) in Handbook of Optics, 2nd Edition. McGraw-Hill, New York, NY, pp 17.1-17.29.
- [CA] Capasso, F., 1985: *Physics of Avalanche Photodiodes*. Chapter 1 (Vol. 22D) in Semiconductors and Semimetals, Vol 22-D, W.T. Tsang (ed.), Academic Press, New York, 375 pp.
- [CH] Chipman, R.A., 1995: *Polarimetry*. Chapter 22 (Vol. II) in Handbook of Optics, 2<sup>nd</sup> Edition. McGraw-Hill, New York, NY, pp 22.1-22.37.
- [CO] Collett, E., 1993: Polarized Light: Fundamentals and Applications. Marcel Dekker, New York, 581 pp.
- [DKS] d'Almeida, G.A., P. Koepke, and E.P. Shettle, 1991: Atmospheric Aerosols – Global Climatology and Radiative Characteristics. Deepak Publ., Hampton, VA, 561 pp.
- [DE] Deirmendjian, D., 1969: Electromagnetic Scattering on Spherical Poly-Dispersions. American Elsevier Publishing, New York, 290 pp.
- [DKB] Dereniak, E.L., and G.D. Boreman, 1996: Infrared Detectors and Systems. John Wiley & Sons, New York, 561 pp.
- [DU] Du, H., 2004: *Mie-Scattering Calculation*. Appl. Opt., 43, 1951-1956.
- [FM] Friedman, E, and J.L. Miller, 2004: Photonics Rules-of-Thumb, 2<sup>nd</sup> Edition. McGraw-Hill, New York, 418 pp.
- [HA] Haus, H.A., 2000: Electromagnetic Noise and Quantum Optical Measurements. Springer-Verlag, Berlin, 562 pp.

- [HH] Hansen, J. E., and J.W. Hovenier, 1974: *Interpretation of the Polarization of Venus*. J. Atmos. Sci., 31, 1137-1160.
- [HT] Hansen, J.E., and L.D. Travis, 1974: *Light Scattering in Planetary Atmospheres*. Space Sci. Rev., 16, 527-610.
- [HC] Hecht, E., 1987: Optics, 2<sup>nd</sup> Edit. Addison-Wesley, Reading, MA, 676 pp.
- [HDD] Herman, M., J.L. Deuze, C. Devaux, P. Goloub, F.M. Breon, and D. Tanre, 1997: *Remote Sensing of Aerosols Over Land Surfaces Including Polarization Measurements and Application to POLDER Measurements*. J. Geophys. Res., 102, 17,039-17,049.
- [HEM] Hielscher, A.H., A.A. Eick, J.R. Mourant, D. Shen, J.P. Freyer, I.J. Bigio, 1997: *Diffuse Backscattering Mueller Matrices of Highly Scattering Media*. Optics Express, 1, 441-453.
- [HG] Holland, A.C., and G. Gagne, 1970: *The Scattering of Polarized Light by Polydisperse Systems of Irregular Particles*. Appl. Opt., 9, 1113-1121.
- [HPC] Holler, S., Y. Pan, R.C. Chang, J.R. Bottiger, S.C. Hill, and D.B. Hillis, 1998: *Two-Dimensional Angular Optical Scattering for the Characterization of Airborne Microparticles*. Opt. Lett., 23, 1489-1491.
- [KI] Kingston, R.H., 1987: Detection of Optical and Infrared Radiation. Springer-Verlag, Berlin, 140 pp.
- [KO] Kokhanovsky, A.A., 2003: Polarization Optics of Random Media. Springer-Verlag, Berlin, 224 pp.
- [LM] Lynch, D.K., and S. Mazuk, 1999: *Size Parameter for Thermally Emitting Particles*. Appl. Opt., 38, 5229-5231.
- [MA] Macleod, H.A., 2001: Thin-Film Optical Filters. Inst. Phys. Publ, London, 641 pp.
- [MC] McCartney, E.J., 1976: Optics of the Atmosphere – Scattering by Molecules and Particles. John Wiley & Sons, New York, 408 pp.
- [MD] Modest, M.F., 2003: Radiative Heat Transfer, 2<sup>nd</sup> Ed. Academic Press, Boston, MA, 822 pp.
- [ME] Measures, R.M., 1984: Laser Remote Sensing – Fundamentals and Applications. John Wiley & Sons, New York, 510 pp.
- [M91] Mishchenko, M.I., 1991: *Light Scattering by Randomly Oriented Axially Symmetric Particles*. J. Opt. Soc. Am. 'A', 8, 871-882.
- [M93] Mishchenko, M.I., 1993: *Light Scattering by Size-Shape Distributions of Randomly Orientated Axially Symmetric Particles of a Size Comparable to a Wavelength*. Appl. Opt., 32, 4652-4666.
- [M00] Mishchenko, M.I., 2000: Light scattering codes (www addresses in Appendix C).

- [MT4a] Mishchenko, M.I., and L.D. Travis, 1994: *Light Scattering by Polydisperse, Rotationally Symmetric Nonspherical Particles: Linear Polarization*. J. Quant. Spectrosc. Radiat. Transfer, 51, 759-778.
- [MT4b] Mishchenko, M.I., and L.D. Travis, 1994: *Light Scattering by Polydispersions of Randomly Orientated Spheroids with Sizes Comparable to Wavelengths of Observation*. Appl. Opt., 33, 7206-7225.
- [MT7] Mishchenko, M.I., and L.D. Travis, 1997: *Satellite Retrieval of Aerosol Properties Over the Ocean Using Polarization as Well as Intensity of Reflected Sunlight*. J. Geophys. Res., 102, 16,989-17,013.
- [MT8] Mishchenko, M.I., and L.D. Travis, 1998: *Capabilities and Limitations of a Current FORTRAN Implementation of the T-Matrix Method for Randomly Oriented, Rotationally Symmetric Scatterers*. J. Quant. Spectrosc. Radiat. Transfer, 60, 309-324.
- [MT3] Mishchenko, M.I., and L.D. Travis, 2003: *Electromagnetic Scattering by Nonspherical Particles*. In Exploring the Atmosphere by Remote Sensing Techniques, R. Guzzi, Editor. Springer-Verlag, Heidelberg, Germany, 370 pp.
- [MHT] Mishchenko, M.I., J.W. Hovenier, and L.D. Travis, 2000: Light Scattering by Nonspherical Particles – Theory, Measurement, and Applications. Academic Press, San Diego, 690 pp.
- [MTK] Mishchenko, M.I., L.D. Travis, R.A. Kahn, and R.A. West, 1997: *Modeling Phase Functions for Dustlike Tropospheric Aerosols Using a Shape Mixture of Randomly Oriented Polydisperse Spheroids*. J. Geophys. Res., 102, 16,831-16,647.
- [MTM] Mishchenko, M.I., L.D. Travis, and D.W. Mackowski, 1996: *T-Matrix Computations of Light Scattering by Nonspherical Particles: A Review*. J. Quant. Spectrosc. Radiat. Transfer, 55, 535-575.
- [MTL] Mishchenko, M.I., L.D. Travis, A.A. Lacis, 2002: Scattering, Absorption, and Emission of Light by Small Particles. Cambridge Univ. Press, Cambridge, UK, 445 pp.
- [ON] O'Neill, E.L., 1963: Introduction to Statistical Optics. Dover Publications (1992), or original Addison-Wesley Publishing, Reading, MA, 179 pp.
- [PN] Perrin, F., 1942: *Polarization of Light Scattered by Isotropic Opalescent Media*. J. Chem. Phys., 10, 415-427.
- [PHH] Perry, R.J., A.J. Hunt, and D.R. Huffman, 1978: *Experimental Determination of Mueller Scattering Matrices for Nonspherical Particles*. Appl. Opt., 17, 2700-2710.
- [QHH] Quinby-Hunt, M.S., P.G. Hull, and A.H. Hunt, 2000: *Polarized Light Scattering in the Marine Environment*. Chapter 18 in Light Scattering by Nonspherical Particles: Theory, Measurements, and Applications. Academic Press, San Diego, CA, pp 525-554.
- [SA] Sassen, K., 2000: *Lidar Backscatter Depolarization Technique for Cloud and Aerosol Research*. Chapter 14 in Light Scattering by Nonspherical Particles: Theory, Measurements, and Applications. Academic Press, San Diego, CA, pp 393-416.

- [SP] Seinfeld J.H., and S.N. Pandis, 1998: Atmospheric Chemistry and Physics. John Wiley & Sons, New York, 1326 pp.
- [SH] Shurcliff, W.A., 1962: Polarized Light – Production and Use. Harvard Univ. Press, Cambridge, MA, 197 pp.
- [SI] Singham, S.B., 1989: *Theoretical Factors in Modeling Polarized Light Scattering by Arbitrary Particles*. Appl. Opt., 28, 5058-5064.
- [TD] Thomas, M.E., and D.D. Duncan, 1993: *Atmospheric Transmission*. Chapter 1 in Atmospheric Propagation of Radiation, F.G. Smith, Editor of Vol. 2, The Infrared and Electro-Optical Systems Handbook. ERIM, Ann Arbor, MI and SPIE Optical Engineering Press, Bellingham, WA, pp 1-156.
- [TAK] Tuminello, P.S., E.T. Arakawa, B.N. Khare, J.M. Wrobel, M.R. Querry, and M.E. Milham, 1997: *Optical Properties of Bacillus Subtilis Spores from 0.2 to 2.5  $\mu\text{m}$* . Appl. Opt., 36, 2818-2824.
- [TKD] Tsang, L., J.A. Kong, and K.H. Ding, 2000: Scattering of Electromagnetic Waves; Vol. I, Theories and Applications. John Wiley & Sons, New York, 426 pp.
- [VH] Van de Hulst, H.C., 1957: Light Scattering by Small Particles. Dover Publications (1981), of original John Wiley & Sons, New York, 470 pp.
- [VHB] Van De Merwe, W.P., D.R. Huffman, and B.V. Bork, 1989: *Reproducibility and Sensitivity of Polarized Light Scattering for Identifying Bacterial Suspensions*. Appl. Opt., 28, 5052-5057.
- [VJL] Volten, H., J.P. Jalava, K. Lumme, J.F. de Haan, W. Vassen, and J.W. Hovenier, 1999: *Laboratory Measurements and T-Matrix Calculations of the Scattering Matrix of Rutile Particles in Water*. Appl. Opt., 38, 5232-5240.
- [WA] Walker, M.J., 1954: *Matrix Calculus and the Stokes Parameters of Polarized Radiation*. Am. J. Phys., 22, 170-174.
- [WO3] Wolfe, W.L., 2003: *Figures of Merit*. Chapter 25 in: Optical Engineer's Desk Reference, W.L. Wolfe, Edit. SPIE Optical Society of America, Bellingham, WA, 738 pp.
- [WO6] Wolfe, W.L., 1996: Introduction to Infrared System Design. SPIE Optical Engineering Press, Bellingham, WA, 129 pp.
- [WO8] Wolfe, W.L., 1998: Introduction to Radiometry. SPIE Optical Engineering Press, Bellingham, WA, 184 pp.
- [WY] Wyatt, P.J., 1968: *Differential Light Scattering: a Physical Method for Identifying Living Bacterial Cells*. Appl. Opt., 7, 1879-1896.
- [ZCT] Zallat, J., C. Collet, and Y. Takakura, 2004: *Clustering of Polarization-Encoded Images*. Appl. Opt., 43, 283-292.

[ZIK] Zege, E.P., A.P. Ivanov, and I.L. Katsev, 1991: Image Transfer Through a Scattering Medium. Springer-Verlag, Berlin, 349 pp.

[ZZK] Zuev, V.E., A.A. Zemlyanov, Y.D. Kopytin, and A.V. Kuzikovskii, 1985: High-Power Laser Radiation in Atmospheric Aerosols. Kluwer Academic Publishers, Dordrecht, The Netherlands, 291 pp.

# REPORT DOCUMENTATION PAGE

*Form Approved  
OMB No. 0704-0188*

Public reporting burden for this collection of information is estimated to average 1 hour per response, including the time for reviewing instructions, searching existing data sources, gathering and maintaining the data needed, and completing and reviewing this collection of information. Send comments regarding this burden estimate or any other aspect of this collection of information, including suggestions for reducing this burden to Department of Defense, Washington Headquarters Services, Directorate for Information Operations and Reports (0704-0188), 1215 Jefferson Davis Highway, Suite 1204, Arlington, VA 22202-4302. Respondents should be aware that notwithstanding any other provision of law, no person shall be subject to any penalty for failing to comply with a collection of information if it does not display a currently valid OMB control number. PLEASE DO NOT RETURN YOUR FORM TO THE ABOVE ADDRESS.

<b>1. REPORT DATE (DD-MM-YYYY)</b> 1 February 2005			<b>2. REPORT TYPE</b> Project Report	<b>3. DATES COVERED (From - To)</b>	
<b>4. TITLE AND SUBTITLE</b> Standoff Polarimetric Aerosol Detection (SPADE) for Biodefense			<b>5a. CONTRACT NUMBER</b> F19628-00-C-0002		
			<b>5b. GRANT NUMBER</b>		
			<b>5c. PROGRAM ELEMENT NUMBER</b>		
<b>6. AUTHOR(S)</b> J.W. Snow, W.E. Bicknell, A.T. George, H.K. Burke			<b>5d. PROJECT NUMBER</b>		
			<b>5e. TASK NUMBER</b>		
			<b>5f. WORK UNIT NUMBER</b>		
<b>7. PERFORMING ORGANIZATION NAME(S) AND ADDRESS(ES)</b>  MIT Lincoln Laboratory 244 Wood Street Lexington, MA 02420-9108			<b>8. PERFORMING ORGANIZATION REPORT NUMBER</b>  TR-1100		
<b>9. SPONSORING / MONITORING AGENCY NAME(S) AND ADDRESS(ES)</b>  Office of the Secretary of Defense 1000 Defense Pentagon Washington, D.C. 20301-1000			<b>10. SPONSOR/MONITOR'S ACRONYM(S)</b>		
			<b>11. SPONSOR/MONITOR'S REPORT NUMBER(S)</b>  ESC-TR-2004-083		
<b>12. DISTRIBUTION / AVAILABILITY STATEMENT</b> Approved for public release; distribution is unlimited.					
<b>13. SUPPLEMENTARY NOTES</b>					
<b>14. ABSTRACT</b> The polarization of laser light elastically scattered by small particles is investigated for the purpose of remotely detecting bio-aer presence in typical ambient background aerosols. The information source is small-particle scattering code computations, not ac measurements. Two separate types of particles – natural background aerosols vs. bio-aerosols – are combined with a concentration rati 100-to-1. The objective is to assess the feasibility of detecting the introduction of the bio-aerosol into the typical background aeroso analyzing the polarization state of the laser light scattered by the combination of particles. The incident laser light is assigned elementary linear polarizations, oriented parallel to or at + 45° relative to the scattering plane. The state of polarization of the redirected through various scattering angles is specified by polarimetric quantities developed from the scattered light Stokes parame Incoherent laser and receiver specifications are employed to evaluate signal-to-noise for three scenarios: outdoor stadium, in auditorium, and building heating-ventilating-air-conditioning (HVAC) system. Of these, the HVAC application is very feasible conventional laser and detector technology. The indoor application is feasible. Coherent laser and advanced photo-diode dete technologies substantially enhance signal-to-noise especially for the outdoor application.					
<b>15. SUBJECT TERMS</b> Aerosol elastic scattering, bio-aerosol, biodefense, bistatic lidar, heterodyne lidar, incoherent laser, Mie scattering, polarimetric detectio polarization, scattering matrix, standoff, Stokes parameters, T-matrix scattering code, volume scattering coefficient					
<b>16. SECURITY CLASSIFICATION OF:</b>			<b>17. LIMITATION OF ABSTRACT</b>	<b>18. NUMBER OF PAGES</b>	<b>19a. NAME OF RESPONSIBLE PERSON</b>
<b>a. REPORT</b> Unclassified	<b>b. ABSTRACT</b> Unclassified	<b>c. THIS PAGE</b> Unclassified	Same as report	139	<b>19b. TELEPHONE NUMBER (include area code)</b>